Strål
säkerhets
myndigheten
Swedish Radiation Safety Authority

Authors: Tobias Backers
Tobias Meier
Peter Gipper
Ove Stephansson

Technical Note

2014:58

Rock Mechanics - Assessing probability and extent of blind faults and fault-end growth around the KBS-3 repository at Forsmark

Main Review Phase

Report number: 2014:58 **ISSN:** 2000-0456

SSM perspektiv

Bakgrund

Strålsäkerhetsmyndigheten (SSM) granskar Svensk Kärnbränslehantering AB:s (SKB) ansökningar enligt lagen (1984:3) om kärnteknisk verksamhet om uppförande, innehav och drift av ett slutförvar för använt kärnbränsle och av en inkapslingsanläggning. Som en del i granskningen ger SSM konsulter uppdrag för att inhämta information och göra expertbedömningar i avgränsade frågor. I SSM:s Technical Note-serie rapporteras resultaten från dessa konsultuppdrag.

Projektets syfte

Det övergripande syftet med uppdraget är att ta fram synpunkter på SKB:s säkerhetsanalys SR-Site för den långsiktiga strålsäkerheten för det planerade slutförvaret i Forsmark. I uppdraget studeras sannolikheten och omfattningen vad gäller tillväxt av de deformationszoner som når markytan och av de som inte når markytan (”blind faults”) på grund av en istidscykel eller ett jordskalv. Särskilt utreds om deformationszonernas tillväxt möjligen kan leda till att dessa gör intrång i slutförvarsvolymen. Utredningen genomförs med hjälp av numerisk modellering av de relevanta scenarierna och materialegenskaperna i SR-Site. Även frågan om slutförvaret som svaghetsplan i bergmassan analyseras.

Författarnas sammanfattning

För att få en generell förståelse av frågan om förkastnings- eller deformationszonsstabiliteten i Forsmark har analyser av reaktiveringspotentialen genomförts. Med dagens bergspänningar är deformationszonerna stabila och visar inga stora deformationer eller mätbar seismicitet. Alla ändringar i bergspänningsfält, särskilt ökning av differentiella bergspänningar i deformationszoner, kan orsaka skjuvrörelser. Därför har flera modeller för bergspänningsfält beaktats i denna studie. Generellt, för dagens förhållanden, visar brant stupande deformationszoner de lägsta reaktiveringspotentialerna på alla djup, medan de flacka deformationszonerna visar störst reaktiveringspotential på grunt djup.

Under istiden inducerar bergspänningsförändringarna på förvarsdjup stor potential för aktivering av flacka deformationszoner under fasen när istäcket drar sig tillbaka. Stor potential för reaktivering förutses för brant stupande deformationszoner framför isfronten (”forebulge”) medan en stabiliserande effekt förväntas för alla deformationszoner under perioder med maximal istjocklek. Från denna analys identifieras de kritiska deformationszoner som ska analyseras vidare för att bättre förstå de numeriska simuleringsresultaten. Dessutom visar denna reaktiveringspotentialanalys tydligt att en god förståelse av bergspänningsfältet är viktigt för en realistisk mekanisk analys av de geologiska förutsättningarna.

Simulering av påverkan på slutförvaret av den termiska fasen visade att: i) branta deformationszoner parallella med slutförvarets kontur stabiliseras, ii) branta deformationszoner snett mot slutförvarets kontur kan bli mindre stabila, iii) flacka deformationszoner har den högsta reaktiveringspotentialen, t.ex. gäller detta för fallet där termiskt inducerade spänningar kan leda till tillväxt av zon ZFMA2. Följaktligen kan flacka zoner som inte når markytan, och som har liknande riktning inom bergspänningsfältet som ZFMA2, komma att aktiveras.

Numerisk simulering av påverkan av istidscykeln visade en påtaglig variation av reaktiveringspotentialen under istidscykeln. De mest påtagliga förändringarna påverkar zon ZFMA2. Stabiliteten hos deformationszonerna är beroende av deras orientering och av fasen i glaciationscykeln. Flacka deformationszoner visar hög instabilitet när istäcket drar sig tillbaka, på motsvarande sätt som dokumenterade aktiveringar av postglaciala förkastningar i Skandinavien.

Hur mycket stabiliteten hos branta deformationszoner påverkas av olika glaciala faser beror på bakgrundsbergspänningsfältet. Generellt visar analyserna att framför isfronten (”forebulge”) kan de branta deformationszonerna bli instabila beroende på deras orientering gentemot bergspänningsfältet. Singö- och Forsmarkzonen blir i detta fall mest kritiska.

Författarna visar att jordskalvsmagnituderna uppskattade av SKB stämmer väl överens med nya publikationer om skalningsförhållanden mellan jordskalvsmagnitud och zonlängd som finns tillgängliga för specifika tektoniska miljöer. Simuleringarna av tre olika jordskalv på utvalda deformationszoner visar att påverkan på stabiliteten hos sekundära deformationszoner: (a) ökar med magnituden hos jordskalven och (b) minskar med avståndet från skalvområdet till respektive sekundär deformationszon. Även om en påtaglig förändring i deformationszonsstabilitet observerades, är områdena med hög reaktiveringspotential mycket lokala och begränsade till små ytor på de flacka deformationszonerna. Simuleringarna visar också att dessa ytor är avgränsade till grunda djup. Effekten beror på magnituden hos bakgrundsspänningarna som är mycket små vid markytan och i samma storleksordning som de glacialinducerade spänningsbidraget. Utifrån detta kan slutsatsen dras att stabiliteten hos deformationszonerna under ett jordskalv av det simulerade slaget i allmänhet ökar med djupet.

Baserat på brottmekaniska överslagsberäkningar kan slutsatsen dras att potentialen för deformationszonstillväxten, där en deformationszon som slutar mot en annan propageras genom den korsade deformationszonen, är liten och deformationszonstillväxt i slutförvarsvolymen bör inte kunna ske.

Projektinformation

Kontaktperson på SSM: Flavio Lanaro
Diarienummer ramavtal: SSM2011-3630
Diarienummer avrop: SSM2013-3840
Aktivitetsnummer: 3030012-4076

SSM perspective

Background

The Swedish Radiation Safety Authority (SSM) reviews the Swedish Nuclear Fuel Company's (SKB) applications under the Act on Nuclear Activities (SFS 1984:3) for the construction and operation of a repository for spent nuclear fuel and for an encapsulation facility. As part of the review, SSM commissions consultants to carry out work in order to obtain information and provide expert opinion on specific issues. The results from the consultants' tasks are reported in SSM's Technical Note series.

Objectives of the project

The general objective of the project is to provide review comments on SKB's post-closure safety analysis, SR-Site, for the proposed repository at Forsmark. This assignment concerns the evaluation of the likelihood and extent of growth of fault-ends and blind-faults due to a glacial cycle or an earthquake at the repository site at Forsmark. In particular, the possibility that reactivated faults or deformation zones might intrude the repository volume is assessed by means of numerical modelling for relevant scenarios and material properties in SR-Site. The issue of the repository level as a plane of weakness in the rock mass is also analysed.

Summary by the Authors

To get a general understanding of the stability conditions of the fault and deformation zone inventory at Forsmark a reactivation potential analysis was carried out. At present-day stress conditions the deformation zones are stable and show no large deformations or detected seismicity. Any changes in stress, and in particular increase of differential stress on deformation zones, might cause slip. Therefore, several stress field models have been considered in this study. In general, steeply dipping deformation zones show the lowest reactivation potential at all depths, while the gently dipping deformation zones show highest reactivation potential today at shallow depth.

During glaciation, the alterations of stress at repository depth produce a large potential for activation of shallow dipping deformation zones during ice retreat. A large potential for reactivation of steeply dipping deformation zones during forebulge periods is predicted while a stabilizing effect for all deformation zones during maximum ice cover periods is inferred. From this analysis the critical deformation zones could be identified for further analysis to help to better interpret numerical simulation results. In addition, this analysis clearly shows that a good understanding of the stress field is essential for any mechanical analysis of geological system behaviour.

Simulation of the influence of the thermal phase showed that i) sub-vertical deformation zones parallel to the repository contour are stabilised, ii) sub-vertical deformation zones at an angle to the repository contour may become less stable, iii) shallow dipping deformation zones show highest reactivation potential as for the case where thermally induced stresses might lead to growth of ZFMA2. Accordingly blind-faults with similar orientations within the stress field might become reactivated. Simulation of the influence of glaciation showed significant variation of reactivation potential during the cycle. Most pronounced changes are visible on zone ZFMA2. The stability of deformation zones is dependent on their orientation and the phase of the glacial cycle. Shallow dipping deformation zones show high instability during ice retreat phases, corresponding to documented post-glacial faulting in Scandinavia.

For sub-vertical deformation zones, the effect of the different glacial phases on the stability depends on the background stress field. In general the analyses show that during forebulge the vertical deformation zones may become unstable depending on their orientation with respect to the stress field; the Singö and Forsmark deformation zones become most critical.

The Authors show that the earthquake magnitudes estimated by SKB are in agreement with newer publications of scaling relations available for the specific tectonic environment. The simulations of three different earthquakes on chosen host zones reveal that the impact on the stability of secondary deformation zones: (a) increases with the magnitude of the earthquakes and (b) decreases with the distance from the rupture area to the respective deformation zone. While a change in deformation zone stability is observed, it was also observed that the high reactivation potentials are very localised and restricted to small patches on the deformation zones. The simulations show that those patches are restricted to shallow depths. This effect depends on the background stress magnitudes that are very small at the surface and in the same order as the induced stress increments. Thus the conclusion is drawn that stability during any earthquake of the simulated type generally increases with depth.

From a scoping Fracture Mechanics approach analysis, it was concluded that there is little potential for deformation zone jump, i.e. the growth of a deformation zone tip that is truncated against another deformation zone, and for deformation zone intrusion in the repository volume.

Project information
Contact person at SSM: Flavio Lanaro

Strål
säkerhets
myndigheten
Swedish Radiation Safety Authority

Authors: Tobias Backers, Tobias Meier, Peter Gipper and Ove Stephansson
Geomecon GmbH, Potsdam, Germany

Technical Note 73

2014:58

Rock Mechanics - Assessing probability and extent of blind faults and fault-end growth around the KBS-3 repository at Forsmark

Main Review Phase

Date: October 2014
Report number: 2014:58 **ISSN:** 2000-0456
Available at www.stralsakerhetsmyndigheten.se

Contents

1. Introduction

This report documents review work conducted by the Consultants in the context of the Swedish Radiation Safety Authority's, SSM's, Main Review Phase of the SR-Site safety assessment covering the final disposal of spent nuclear fuel at the Forsmark site submitted by SKB, the Swedish Nuclear Fuel and Waste Management Company. Based on the initial phase of SSM's review of SR-Site by SKB, SSM has concluded that SKB's reporting is sufficiently comprehensive and of sufficient quality to justify a continuation of SSM's review to the Main Review Phase.

This assignment concerns the evaluation of the likelihood and extent of the expected growth of fault-ends and blind-faults at the repository site at Forsmark. In particular, the possibility that reactivated faults or deformation zones might intrude the repository volume should be assessed by means of numerical modelling for relevant scenarios and material properties in SR-Site. The issue of the repository level as a plane of weakness in the rock mass is also analysed.

This assignment addresses issues of the isostatic and shear load scenarios considering the scale relevant for the stability and evolution of fault and deformation zones around the KBS-3 repository at Forsmark. The report analyses at first (chapter 2) the general stability of the existing faults and deformation zones based on the existing stress field models and discusses the implications for their extension. In the subsequent chapters, the different loading scenarios throughout the evolution of a repository for spent nuclear fuel at Forsmark are analysed. This includes the thermal phase, glacial phase, and generic earthquakes.

1.1. Comment on the nomenclature used by SKB

In general the term *fault* is used to refer to a deterministically modelled deformation zone, which is defined as an essentially 2D structure along which there is a concentration of deformation, e.g. deformation zones (ZFM), as opposed to the term *fracture*, which is used to refer to small scale discontinuities which are statistically modelled as fracture sets for specific rock volumes, e.g. joints in fracture domains (FFM). The term *fault* is not clearly defined in any of the reviewed SKB reports. However, Stephens et al. (2007, SKB R-07-45) define the term *fault zone* as a brittle deformation zone with known shear sense of movement. A brittle deformation zone without known shear sense is termed *fracture zone*.

Table 1.1 shows a set of definitions provided by Stephens et al. (2007) which is following the nomenclature described in Munier and Hermansson (2001, SKB R-01-15) and Munier et al. (2003, SKB R-03-07). Their definition of brittle structures is based on Andersson et al. (2000, SKB R-00-15).

Table 1.1. Terminology and geometrical description of brittle structures in the bedrock based on Andersson et al. (2000, SKB R-00-15).

Terminology	Length	Width	Geometrical description
Regional deformation zone	> 10 km	> 100 m	Deterministic
Local major deformation zone	1 km - 10 km	5 m - 100 m	Deterministic (with scale-dependent description of uncertainty)
Local minor deformation zone	10 m - 1 km	0.1 m - 5 m	Stochastic DFN (if possible, deterministic)
Fracture	< 10 m	< 0.1 m	Stochastic DFN

This terminology however is not consistently used through SKB’s publications. For example Lund et al. (2009, SKB TR-09-15) use the terms *fracture*, *fracture zone* and *fault zone* as synonymous for deformation zones. In Hökmark et al. (2010, SKB TR-10-23) the terminology seems largely consistent with Stephens et al. (2007, SKB R-07-45). However, features with lengths up to 300 m are considered as fractures, not following the above terminology (Table 1.1).

Fälth et al. (2010, SKB TR-08-11) use the term *fault* for potentially earthquake generating discontinuities and the term *fracture* for receivers and potentially slipping planes in response to movements on faults (also “target fractures“), not following the terminology by Stephens et al. (2007, SKB R-07-45). Referring to this report, the terms *fault* will be used in this report to address deterministically modelled deformation zones (i.e. those are named ZFM…), and *fracture* or *crack* for statistically modelled deformation zones. This definition is independent of any scale, but mapped deformation zones are naturally larger.

1.2. Comments on the used criteria for judgment of the fracture and fault stability

The assessment of stability of brittle discontinuities is carried out by SKB with the same analytical method irrespective of the scale. The most basic approach transfers the Mohr-Coulomb brittle failure criterion to an instability quantity like the Coulomb Failure Stress (*CFS*; e.g. Lund et al., 2009, SKB TR-09-15; Fälth et al., 2010, SK TR-08-11), Factor of Safety (*FoS*; Hökmark et al., 2010, SKB TR-10-23) similar to the reactivation potential (*rp*) that will be used in this report. The informative value of all these expressions is equal. The assumption about the strength, which is the resistance to slip in this context, of the discontinuity of interest, however, is crucial. There are abundant data mostly from laboratory deriving the friction angles of fractures, sealed fractures, fracture domains and even deformation zones. The instability quantities *CFS* and *FoS* solely depend on the choice of this parameter, as they normalise the ratio of shear and normal stress on the plane of interest to the assumed critical value that depend on the friction angle. In this respect, the reactivation potential as used in the context of the present Consultants’ assessment has the advantage of not being normalised to a specific friction angle. However, the disadvantage is that it is not as convenient to use, since one has to compare the reactivation potential with a reference friction angle assumed to relate to slip.

Generally, it is anticipated that laboratory based parameter values need some adjustment for scale applicability. However, the question if and how laboratory derived strength parameters are valid for field application is beyond the scope of this report. Therefore, the parameters reported by SKB are used without further reasoning about the methodology of determination or necessary scaling requirements.

1.3. Comment on fracture and fault propagation

It has to be emphasised that SKB mostly does not actually touch upon the topic of fault or fracture extension, but rather assess the stability and quantify the amount of slip on existent discontinuity planes. Most of the employed models assume linear elasticity and cannot describe inelastic deformation.

2. Stability of the structural inventory at Forsmark

2.1. SKB’s presentation

This Section summarises SKB’s understanding of the stress field models, the deformation zone inventory, and the stability of the deformation zones in the suggested stress field models as relevant for this assessment.

2.1.1. Summary of stress fields

The in situ stresses at the Forsmark site and for the repository depth have been investigated due to their utmost importance for various applications and safety assessments of the planned repository for spent nuclear fuel. They are a prerequisite for the assessment of fault stability under induced stresses during thermal heating, glacial cycles and earthquakes.

A review of the stress field at repository depth has been carried out by geomecon in a previous report on the spalling potential around deposition holes and tunnels (Backers et al., 2014a, SSM Tachnical Note 2014:10). However, for the analysis of large scale structures, the in situ stress at much larger depth is of interest. The following sections provide an overview of the stress fields that have been used by SKB and that extend at least down to 10 km depth.

Orientation of the principal stresses

In general, there are no major disagreements about the orientation of the principal stresses at Forsmark. They can be reasonably approximated to lie within the vertical and horizontal planes. SKB’s site stress model promotes a direction of maximum horizontal stress SH at Forsmark of 145°±15° (SKB TR-08-05, Table 7-7). This is derived from overcoring measurements only. The direction obtained from hydraulic methods suggests values of 124°±6° (Glamheden et al., 2007a, SKB R-07-31, Table 6-2), which falls outside the variability of the overcoring data, just overlapping the overcoring measurements at 130°.

Borehole breakouts, which can be assumed to be quite reliable indicators for stress orientation in unaltered and sparsely fractured rocks such as granites, suggest an orientation of SH of 135°.

Lund et al. (2009, SKB TR-09-15) calculate the theoretical direction of SH to be 123° at Forsmark, assuming that it is aligned with the local direction of plate motion. This direction fits the data from the World Stress Map (Heidbach et al., 2008).

Slunga (1990, SKB TR-90-30) mapped earthquake p-axis directions and came to the conclusion that they fit to the direction of ridge push in South-Central Sweden and gives the dominant direction of maximum horizontal stress as 120°. Data from the 6.5 km deep boreholes in the Siljan impact area (Central Sweden) gave a direction

Table 2.1. Literature review on the azimuth of SH at Forsmark and in Central Sweden.

Publication	Direction of SH [°]	Uncertainty [°]	Location
Slunga (1991)	120		Seismic events Fennoscandia
Lund and Zoback (1999)	108	7	Gravberg-1
	127	9	Stenberg-1
Martin (2007, SKB R-07-26)	145	15	Forsmark
Ask et al. (2007, SKB P-07-206)	122-133	4	Forsmark
Glamheden et al. (2007a, SKB R-07-31)	124	6	Forsmark
Lund et al. (2009, SKB TR-09-15)	123		Plate motion, theoretical
Borehole breakouts (Martin, 2007, SKB R-07-26)	135		Forsmark

of 108°-127° for the maximum compression, this also well in agreement with the ridge push (Lund and Zoback, 1999).
Table 2.1 summarises the obtained directions of maximum horizontal stress from the different measurement techniques, theoretical considerations and data from deep boreholes in the Siljan impact area.

Stress fields at repository depth

At repository depth (about 500 m), the stress magnitudes can be constrained from available stress measurements that have been performed at the Forsmark site. The proposed stress models have been reviewed in an earlier geomecon assessment (Backers et al., 2014a, SSM Technical Note 2014:10) and are summarised for the sake of completeness in Table 2.2.

SKB’s site stress model is presented by Martin (2007, SKB R-07-26) and it is largely based on overcoring stress measurements. It corresponds to a reverse faulting regime throughout the repository volume and down to 600 m depth.

In the course of the independent review of the reported stress data and measurement methods at Forsmark, Backers et al. (2014a) presented their interpretation of the in situ stresses that resulted in a transitional model between strike-slip and reverse faulting at repository depth. An alternative suggested model within SKB’s studies is based on hydraulic testing methods and results in a strike slip faulting regime (Ask et al., 2007, SKB P-07-206).

Table 2.2. Stress magnitudes for different proposed models for Forsmark and the repository depth (500 m).

SH [MPa]	Sh [MPa]	Sv [MPa]	Pp [MPa]	Source
41.0 ± 6.2	23.2 ± 4.6	13.3 ± 0.3	5	Martin (2007, SKB R-07-26)
22.7 ± 1.1	10.2 ± 1.6	13.3	5	Ask et al. (2007, SKB P-07-206)
35.5 ± 5	13.3 ± 2	13.3	5	Backers et al. (2014a, SSM Techical Note 2014:10)

Stress fields up to 10 km depth

Lund et al. (2009, SKB TR-09-15) proposed three “background stress” field models for depths down to 10 km for an assessment of fault stability during a glacial cycle. The stress models were constructed by means of theoretical considerations. They assumed frictional failure equilibrium on optimally oriented faults:

$$\frac{\sigma_1 - P_p}{\sigma_3 - P_p} = \left(\sqrt{\mu^2+1}+\mu\right)^2 \qquad \text{Eq. (2.1)}$$

A coefficient of friction μ equal to 0.6 (corresponding to a friction angle of 31°), hydrostatic pore pressure conditions and a vertical stress corresponding to the weight of the overburden with mean crustal density of 2,750 kg/m^3 were used. A stress difference ratio R equal to 0.5 is used without further reasoning or justification:

$$R = \frac{\sigma_1 - \sigma_2}{\sigma_1 - \sigma_3} \qquad \text{Eq. (2.2)}$$

Additionally, a “local stress” model is used by SKB for comparison. This simply extrapolates the gradients from the site stress model based on Martin (2007, SKB R-07-26), which are valid between 400 and 600 m, and keeps a constant direction of SH (145°) throughout the entire profile. Gradients are not given for any of the final stress fields.

Fälth et al. (2010, SKB TR-08-11) similarly constructed three “synthetic stress” fields in order to evaluate fault stability using a similar set of assumptions. They chose different values for the critical parameters: $R = 0.65$ and $\mu = 0.78$ (38°) are calculated from stress magnitudes at repository depth as given by SKB’s site stress model. The vertical stress corresponds to the theoretical weight of the overburden in each model. The pore pressure is not mentioned. Based on the given values, however, the underlying pore pressure can be back-calculated. It seems that a pore pressure of approximately 8.5 MPa/km, smaller than hydrostatic pore pressure, has been used (Fälth et al. 2010, SKB TR-08-11, p. 125). These three stress models are described in Figure 2.1 and named #1, #2 and #3.

#1 Reverse Stress Model

The assumption of frictional equilibrium as in Lund et al.’s (2009, SKB TR-09-15) model has been used. The frictional coefficient μ and the stress difference ratio R

were calculated using stress magnitudes at repository depth from the stress model by Martin (2007, SKB R-07-26).

#2 Mixed stress field

The stress field maintains frictional equilibrium throughout the profile. The gradient of the minor horizontal stress changes at 1 km depth to equal the vertical stress at 2.4 km depth, where the gradient of the maximum horizontal stress is changed to keep frictional equilibrium between SH and Sh. Sh becomes the smallest principal stress, σ_3, in the strike slip regime below 2.4 km depth. The depths of change of the stress gradient are arbitrarily chosen, taking into account the data from the Siljan borehole that suggests a strike slip regime below 0.5 km depth and according to Glamheden et al. (2007a, SKB R-07-31) that suggest a reverse faulting regime above 1 km depth at Forsmark.

#3 Site model stress field

The site stress model (Glamheden et al., 2007a, SKB R-07-31) gives stress gradients for repository depth for the range 400-600 m and is simply extrapolated down to 10 km depth. This is the same as the local stress field from Lund et al. (2009, SKB TR-09-15).

2.1.2. Deformation zone inventory

The term *deformation zone* as defined by SKB refers to “an essentially 2-dimensional structure (a sub-planar structure with a small thickness relative to its lateral extent) in which deformation has been concentrated (or is being concentrated, in the case of active faults)” (Munier et al. 2003, SKB R-03-07). In the deformation zone model, however, the thickness of the zones is modelled to correspond to a defined volume, conceptually similar to fracture domains. Zones are classified according to the length of their trace on the surface as i) regional deformation zones (length > 10 km), ii) local major deformation zones (1-10 km), iii) local minor deformation zones (0.01-1 km) and iv) fractures (< 0.01 km) (Stephens et al., 2007, SKB R-07-45). The classes correspond to the nomenclature introduced by Andersson et al. (2000, SKB R-00-15).

The deformation zones that have been deterministically modelled are shown in Figures 2.2 and 2.3. The set of deformation zones shown in Figure 2.3 will be used in the following analyses. The orientation data is taken from Appendix 15 in Stephens et al. (2007, SKB R-07-45).

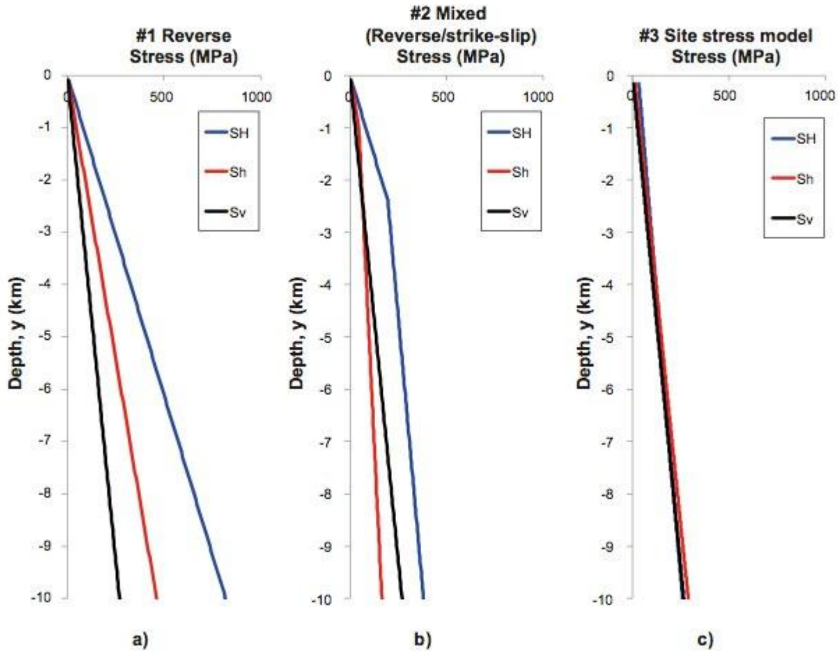

Figure 2.1. Stress models down to 10 km depth as assumed by Fälth et al. (2010, SKB TR-08-11). On the basis of the stress model from the Site Descriptive Model Report (Glamheden et al., 2007a, SKB R-07-31) the stresses have been extrapolated to larger depth using assumptions about the stress ratios and the stress regime (from Fälth et al., 2010, SKB TR-08-11, Figure 7-6).

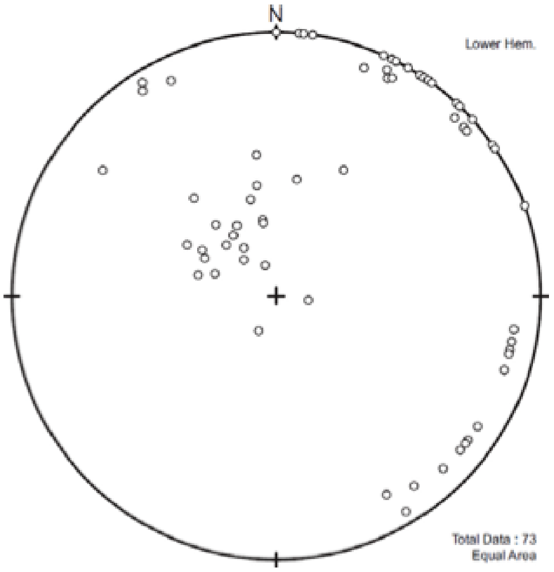

Figure 2.2. Pole plot of the deformation zones with trace length > 3 km that intersect the repository (from Fälth et al., 2010, SKB TR-08-11, Figure 1-10).

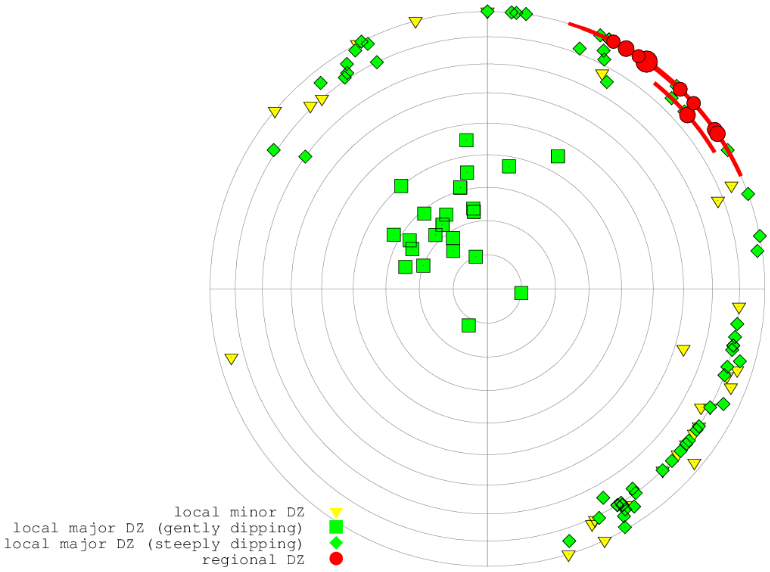

Figure 2.3. Lower hemisphere equal area polar plot showing all deterministic deformation zones (DZ) at Forsmark classified by the length of their trace on the surface. In red: regional deformation zones > 10 km, in green: local major deformation zones between 1 and 10 km, in yellow: local minor deformation zones < 1 km. Furthermore the local major deformation zones are grouped according to their dip angle. The uncertainty of ±10° for the strike direction of the zones (SKB R-07-45, Appendix A15-9) is shown for the regional deformation zones as red arcs. The grey circles denote 10° dip intervals.

2.1.3. SKB's assessment of the stability of deformation zones

Present-day

An evaluation of deformation zone stability at present day has not explicitly been done by SKB. There is, however, a presentation of fracture stability for SKB's "most likely" stress field model (Hökmark et al., 2010, SKB TR-10-23). This is done by means of the Factor of Safety, *FoS*:

$$FoS = \frac{c+\sigma_n \mu}{\tau} \qquad \text{Eq. (2.3)}$$

with cohesion c, normal stress σ_n, coefficient of friction μ, and shear stress τ. Figure 2.4 shows that there is a range of gently dipping planes that are not stable under present-day conditions.

Although this analysis has been done for fractures only, one can draw conclusions for deformation zones, too, since the reported friction coefficients μ are similar for the two according to SKB (0.7 for deformation zones and 0.72 for fractures, respectively). Deformation zones in the approximate range $FoS < 1$ in Figure 2.4 can be regarded as unstable, i.e. planes gently dipping in direction of SH (red domain in Figure 2.4). Those planes are observed at Forsmark as visible from Figures 2.2 and

2.3. These findings are in agreement with the analysis of present-day stress field models in Backers et al. (2014a).

Glacial phase

An evaluation of deformation zone stability has been presented in the SKB report by Fälth et al. (2010, SKB TR-08-11) for elevated stresses during glaciation scenarios taken from Lund et al. (2009, SKB TR-09-15). The stability is evaluated in terms of Coulomb failure stress, *CFS*:

$$CFS = \tau \text{-} \mu(\sigma_n \text{-} P_p) \text{-} c \qquad \text{Eq. (2.4)}$$

with shear stress τ, normal stress σ_n, pore pressure P_p, coefficient of friction μ, and cohesion c.

The coefficient of friction is chosen such that the rock mass is just at the point of frictional equilibrium for the background stress models. The *CFS* is then calculated with the glacially induced stresses at the time of maximum instability added to the background stress field. If the *CFS* value for the orientation of a specific deformation zone lies above the stability margin of -10 MPa, the zone is regarded as unstable. Whether or not a deformation zone becomes unstable strongly depends on the background stress field (Figures 2.5 and 2.6).

It is concluded that the #2 Mixed stress regime appears to be more conservative because more deformation zones become unstable. It is therefore recommended by SKB to count the 5 unstable deformation zones in Figure 2.6 as potentially seismogenic. Those zones are ZFMWNW0809A, ZFMNW1200, ZFMNW0017, ZFMWNW0123 and ZFMA2.

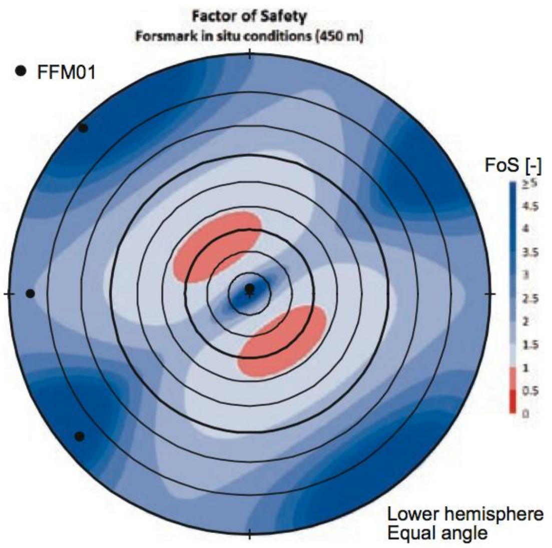

Figure 2.4. Pole plot showing the *FoS* distribution for present-day conditions (from Hökmark et al., 2010, SKB TR-10-23, Figure 6-24).

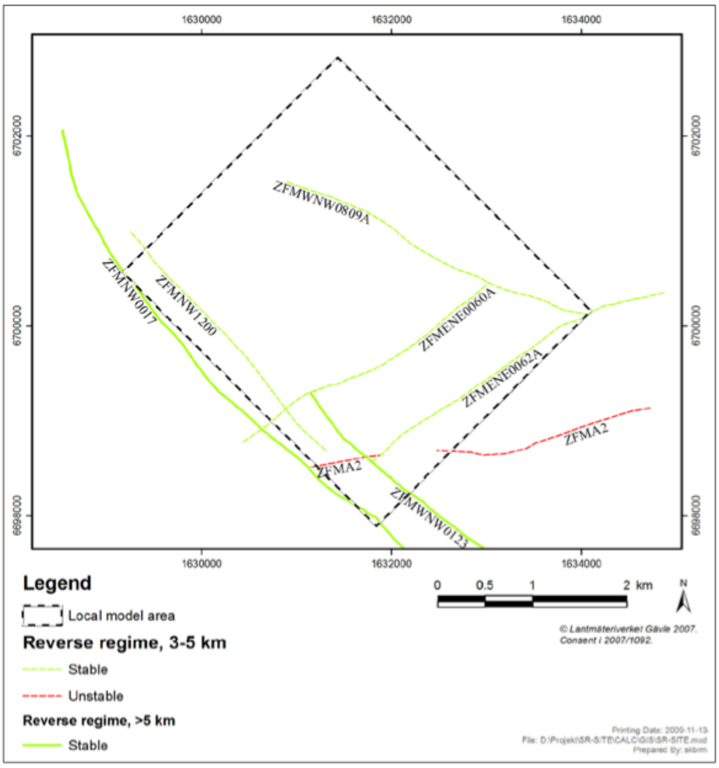

Figure 2.5. Map of the deformation zones at repository depth within the Forsmark local model area. Deformation zones are coded with respect to their stability at 3.5 km depth within the #1 Reverse stress regime (from Figure 7-14, SKB TR-08-11).

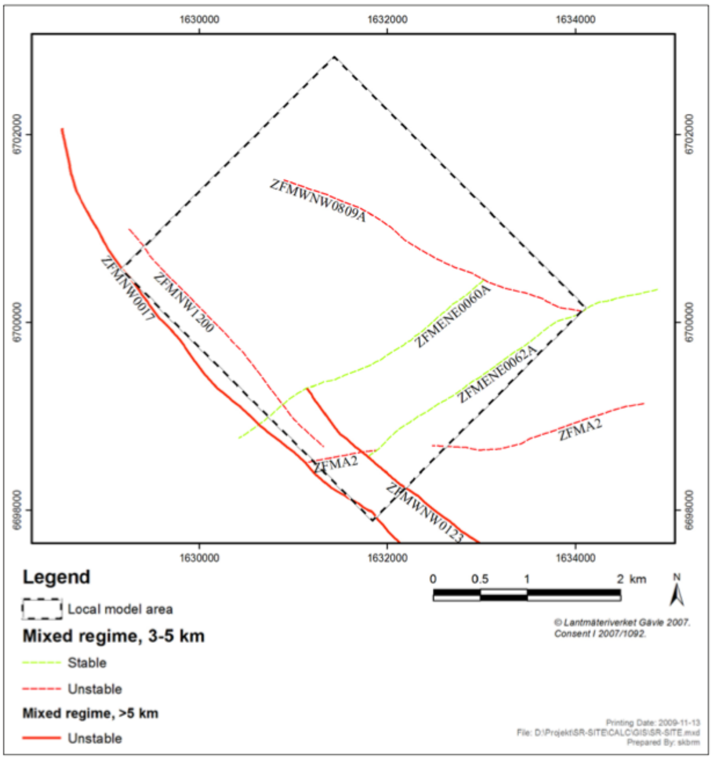

Figure 2.6. Map of the deformation zones at repository depth within the Forsmark local model area. The deformation zones are coded with respect to their stability at 3.5 km depth within the #2 Mixed stress regime (from Figure 7-15, SKB TR-08-11).

The #3 Site model stress field is not considered since it is identical to the other two at repository depth. Below that depth, it is less conservative since the ratio between the principal stresses approach unity and consequently the deviatoric stresses become small.

2.2. Motivation of the Consultants' assessment on the stability of the structural inventory

A good understanding of the stress field and its orientation with respect to the prominent structural features in a geological setting is a prerequisite for any geomechanical analysis. Therefore, this assessment:

- analyses the relevance of the stress models as developed and presented by SKB,
- develops an alternative stress model by reviewing the available data, and
- presents deformation zone stability plots to be able to identify the deformation zones prone to reactivation during different stages of the repository after closure.

This assessment provides a broad understanding of the mechanical behaviour of the system and serves as a starting point for further numerical analyses. In addition, the results of individual simulations can be discussed in the context of the geomechanical system at Forsmark.

2.3. Independent analyses of the stability of the structural inventory

2.3.1. Stress fields

Assessment of the orientation of the principal stresses

The span of data on the orientation of the maximum horizontal stress SH at Forsmark is 118° to 160° (overcoring 145°±15°; hydraulic 124°±6°). The mean directions are consistent with the breakout data. Borehole breakouts, which can be assumed quite reliable indicators for stress orientation in non-layered sparsely fractured rocks such as granites, suggest an orientation of SH of 135°.
Based on the indications of stress orientation from analysis of overcoring, hydraulic and breakout analysis the Authors suggest the direction of the maximum horizontal stress at Forsmark to be 139°.

Assessment of the stress models

Available stress models for larger depth at Forsmark have been presented in Section 2.1. For the analysis of the stability of deformation zones the Authors adopt the more recent large scale models by Fälth et al. (2010, SKB TR-08-11):

#1 Reverse stress field

This stress field might be reasonable at repository depth, but is unlikely to prevail at depths of several kilometres. The resulting stress ratios contradict data from the

Siljan borehole (Lund and Zoback, 1999) and are deviating from the reported observations of decreasing trends of the ratio of mean horizontal to vertical stress magnitudes established by Brown and Hoek (1978) based on data from all over the world.

#2 Mixed stress field

This stress field is reasonable and in agreement with the site stress model at repository depth, with the strike-slip conditions at seismogenic depth as inferred from focal mechanisms (Bödvarsson et al. 2006, SKB R-06-67) and with the mean horizontal to vertical stress ratio decreasing towards larger depth. A change in stress regime at a certain depth is indicated e.g. by data from Siljan boreholes, by the stress model for the Baltic Shield from Stephansson et al. (1991) and even by stress measurements at the Forsmark site (Ask et al. 2007, SKB P-07-206). Earthquake focal mechanism analysis also show dominantly strike-slip faulting (Slunga 1990, SKB TR-90-30).

#3 Site stress field

The stress model has been constructed by extrapolating the site stress model (Martin, 2007, SKB R-07-26) which was established for the depth interval 400-600 m. It is in accordance with the trend of decreasing ratio of mean horizontal to vertical stress (data from Brown and Hoek, 1978). Below 4 km, however, the model appears not realistic, since the least horizontal stress becomes larger than the maximum horizontal stress, which implies a rotation of principal stresses of 90°. In general it is doubtful to extrapolate a stress gradient that was explicitly inferred for the 400-600 m level to a depth of 10 km.

#4 geomecon stress field

geomecon has developed an alternative stress model for Forsmark based on Backers et al. (2014a, SSM Technical Note 2014:10). As the stress models suggested by SKB bare some limitations, the Authors take an approach to develop a stress model based on geomechanical considerations valid for upper to mid-crustal strength conditions.

The approach is based on a decreasing coefficient of friction μ, with depth. The principal stresses are realised as follows:

- the minor horizontal stress gradient Sh as estimated by Stephansson et al. (1991);
- the vertical stress as calculated from the weight of the overburden;
- the maximum horizontal stress according to the theory of frictional failure equilibrium (Jaeger et al., 2007) with a coefficient of friction of 0.7 (e.g. SKB TR-08-05, Table 7-4) down to a depth of 3 km and decreasing beneath.

According to Brown and Hoek (1978) the ratio of mean horizontal stress to vertical stress decreases with depth (Figure 2.7). Assuming a constant gradient for Sv that derives from the weight of the overburden, it follows that the average horizontal stress gradient decreases with depth. In the stress field model proposed by geomecon that bases the maximum differential stress on the theory of frictional failure equilibrium, this is realised by reducing the coefficient of friction μ with increasing depth. The decline of μ with depth is also proposed by Byerlee (1978) who suggests a bilinear function for the shear stress as a function of the normal stress, with the transition from μ equal to 0.85 to 0.6 at a normal stress of 200 MPa. Lundborg

(1967) measured the shear strength of a series of Swedish rocks, including several granitic rocks. Like Byerlee (1978), he found that the ratio of shear stress to normal stress necessary to cause failure in rock mass is decreasing for higher normal stress. In the stress field model proposed here, starting at a normal stress of around 100 MPa, which roughly corresponds to a depth of 3 km, the coefficient of friction is decreasing similar to the data from Lundborg (1967) and reaches a value of 0.42 at 10 km depth (Figure 2.8). At repository depth, the stress model maintains compatibility with the earlier geomecon model for repository depth (Backers et al., 2014a). Figure 2.9 shows the alternative stress model by geomecon together with the SKB models.

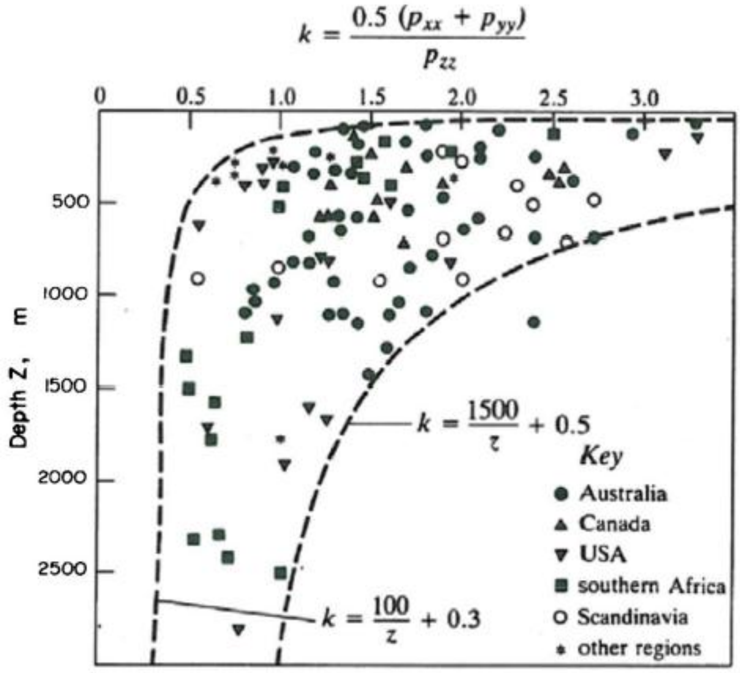

Figure 2.7. Ratio of average horizontal to vertical stress as suggested from worldwide data after Brown and Hoek (1978) (from Fälth et al. 2010, SKB TR-08-11, Figure 7-8).

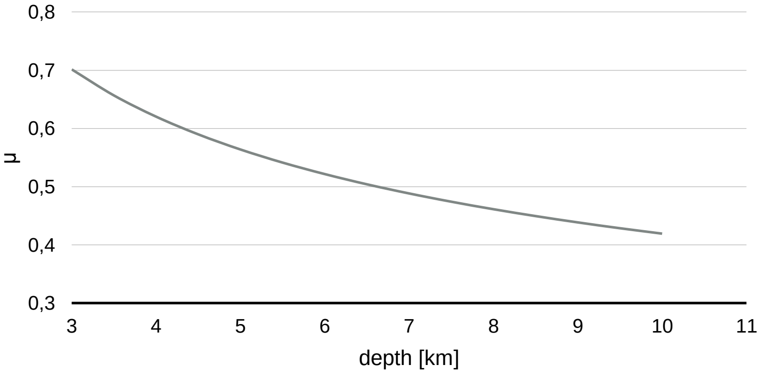

Figure 2.8. Decrease of the coefficient of friction *μ*, as used for the #4 geomecon stress field model.

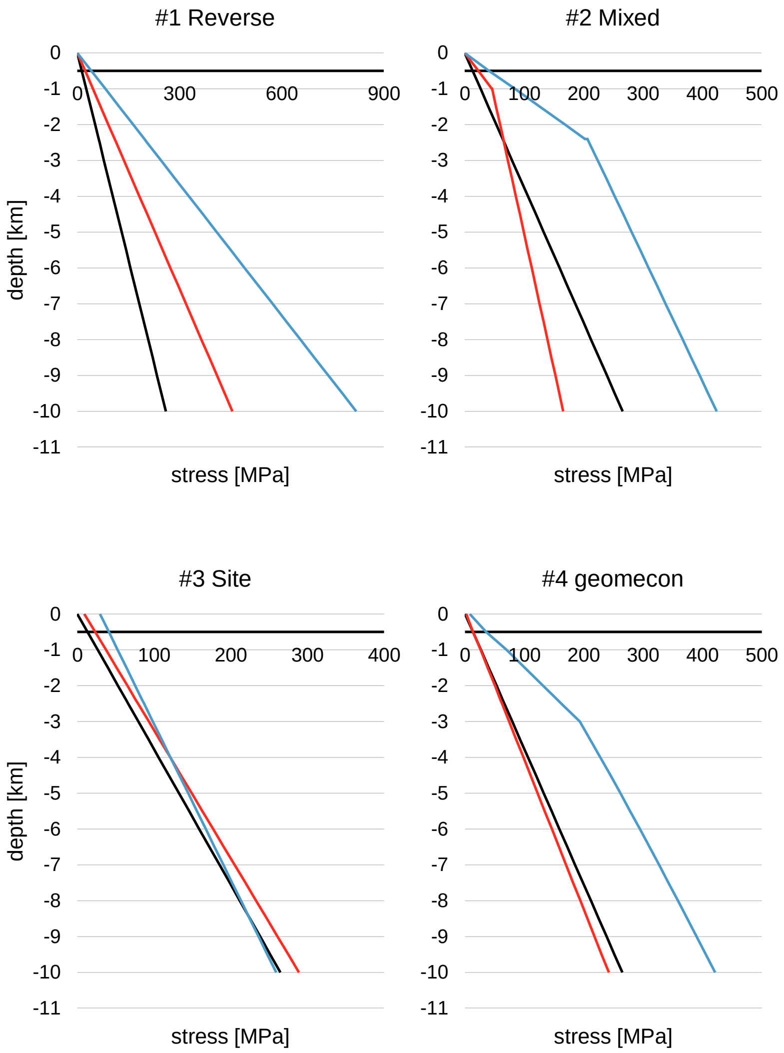

Figure 2.9. Background stress models for depths up to 10 km that are used for the evaluation of fault stability in this report. The vertical stress (black), the maximum horizontal stress (blue) and the minimum horizontal stress (red) are shown for each model.

2.3.2. Analysis of the stability of deformation zones

In the following, not only the stability at present-day stresses is evaluated by an analytical approach, but also the long-term evolution of the repository where heating due to decay of the spent nuclear fuel and glaciation are taken into account. The applied approach estimates the reactivation potential of the deformation zones and discusses it in the light of the tendency for slip on the planes of weakness.

Reactivation potential

In order to evaluate the stability of a fault with a specific frictional coefficient and orientation under a given stress field, the reactivation potential *rp*, which is expressed by the ratio of shear stress to normal stress acting on the fault plane, is calculated:

$$rp = \frac{\tau}{\sigma_n} \qquad \text{(Eq. 2.5)}$$

In order to discuss the deformation zone stability, a threshold for the reactivation potential value of *rp* = 0.7 is used. This value corresponds to the reported residual friction angle of 35° for fractures in deformation zones ($\mu = 0.7$) as obtained from direct shear tests (SKB TR-08-05, Table 7-4). Note that Glamheden et al. (2007a, SKB R-07-31) suggest estimates of 36° ($\mu = 0.72$) for most deformation zones except the Singö deformation zone, which was assigned a friction angle of 31.5° ($\mu = 0.61$) when the zone was modelled as a single fracture plane (Glamheden et al., 2007b, SKB R-07-06).

When assuming a *rp* of 0.7 as threshold, a deformation zone that is judged “unstable” means it has a reactivation potential higher than 0.7. Likewise a “stable” deformation zone has a reactivation potential below 0.7. The threshold does however not indicate if the plane will slip. The analysis will be conducted as such that other thresholds can be assessed later on, i.e. the evaluation will not be normalised to the specific value of 0.7.

Compared to the stability analysis by means of stability quantities like the Coulomb Failure Stress *CFS* (Lund et al., 2009, SKB TR-09-15; Fälth et al., 2010, SKB TR-08-11) or the Factor of Saftety *FoS* (Hökmark et al., 2010, SKB TR-10-23), the reactivation potential has basically the identical explanatory power. A maximum reactivation potential that equals the reported coefficient of friction corresponds to a *CFS* equal to 0 and a *FoS* equal to 1.

A limitation of the proposed approach is that the stress models that are constructed by assuming frictional equilibrium on fractures will naturally reproduce the assumed values of the friction angle as outcome for the maximum reactivation potential at present day. Nevertheless, those models give insight about the most critical orientations and provide information about the impact of long term scenarios. In addition, as the friction coefficients of large deformation zones are not known or reliably determinable anyway, this approach does not suggest predictive capabilities it does not have.

In general, deformation zones in the sense of SKB’s definition may be assumed to have a friction coefficient of between 0.4 and 0.7 (pers. communication Prof. Georg Dresen of Helmholtz Zentrum Potsdam, Germany, 2014). In this case, using the upper limit of that range is justified as SKB has determined the values for fractures within deformation zones. Furthermore, it mirrors the fact that Forsmark is a stable environment with relatively low amounts of documented shear on the faults.

Present-day stresses

The reactivation potential of the deformation zones for the four present-day stress field scenarios is shown in Figures 2.10 through 2.13 for depths of 500, 1,500, 3,500, 5,500, 7,500 and 9,500 m, respectively. The background stress field has a strong influence on the stability of deformation zones.

#1 Reverse Stress Model

For stress model #1 the reactivation potential is distributed the same way throughout all depth levels, which directly results from the model setup with constant gradients

(Figure 2.10). The assumed constant stress ratios based on the coefficient of friction $\mu = 0.78$ lead to this maximum reactivation potential throughout all depth levels.

In theory the reactivation potential for optimally oriented planes should equal the assumed coefficient of friction of 0.78. Due to the fact that a less than hydrostatic pore pressure was presumably used by SKB to construct the model (cf. Sec. 2.1.1) the reactivation potential is calculated here for hydrostatic pore pressure conditions. For this reason, the reactivation potential results to be 0.82, which is higher than the coefficient of friction at all depth.

The regional deformation zones as well as the steeply dipping sets show maximum *rp* smaller than 0.4 for all depth depths, hence they can be assumed to be stable at the assumed present-day conditions. The most critical orientation for stress model #1 is for a strike of 55° and a dip of 25°, which is the orientation of the gently dipping deformation zones at Forsmark. These show a *rp* larger than 0.8. One may assume that those deformation zones would experience reactivation as the reactivation potential is larger than the reported threshold value of 0.7.

#2 Mixed Stress Model

Stress Model #2 (Figure 2.11) results in the same stability pattern as stress model #1 at 500 m since the stresses at repository depth are the same for all SKB models. Between 1,500 and 3,500 m depth, the orientations of most critical planes change when the vertical stress exceeds the minor horizontal stress. In contrast to model #1, the maximum *rp* is increasing with depth although μ has been kept constant; this is due to a relative pore pressure increase with depth that overcomes the increase in principal stresses.

At shallow depth the gently dipping deformation zones are subject to highest *rp* > 0.8, indicating that they are potentially unstable if the *rp* = 0.7 criterion would apply. However, at present conditions they are stable and show no recorded seismicity. With increasing depth the NW-SE regional deformation zones are predicted to be subjected to larger shear stress. At 5,500 m depth the *rp* for the regional deformation zones is about 0.86, which is well above the assumed frictional strength of the fault system.

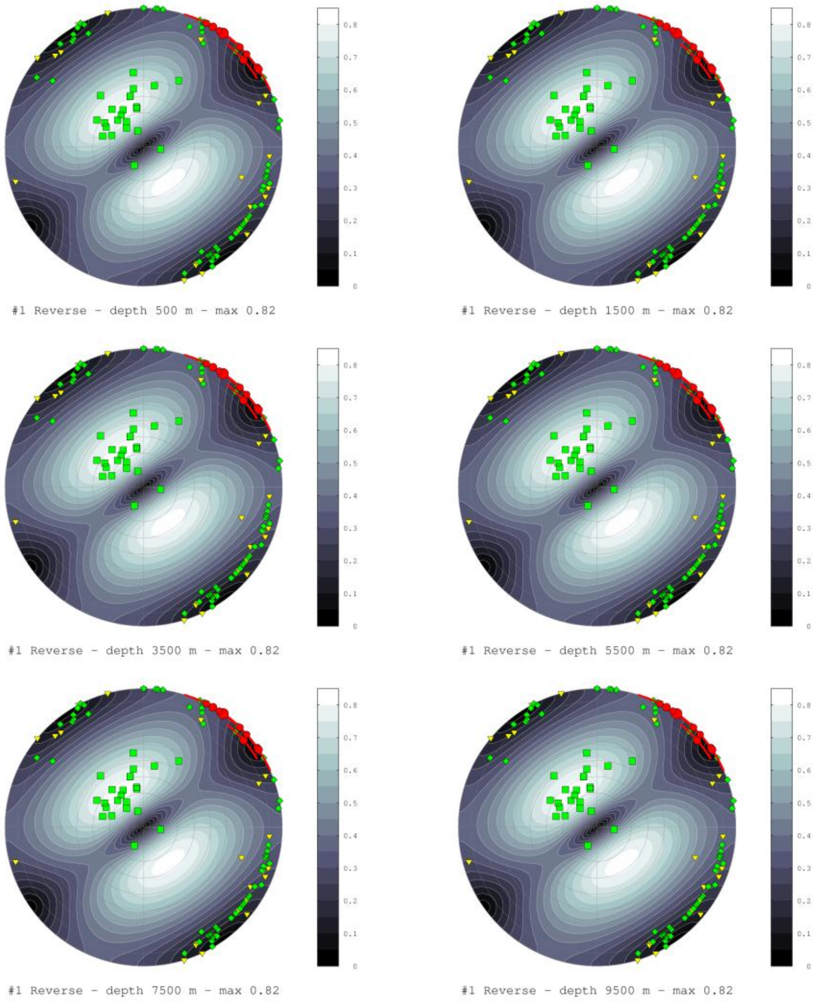

Figure 2.10. Reactivation potential for six depths levels under present-day stress conditions defined by #1 Reverse model. The analysis shows similar results for all depth levels (500 m, 1,500 m, 3,500 m, 5,500 m, 7,500 m, 9,500 m). The gently dipping deformation zones fall into the region of maximum *rp* = 0.82.

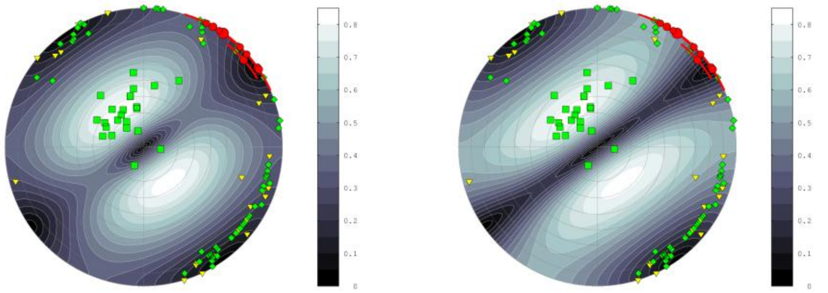

#2 Mixed - depth 500 m - max 0.82

#2 Mixed - depth 1500 m - max 0.82

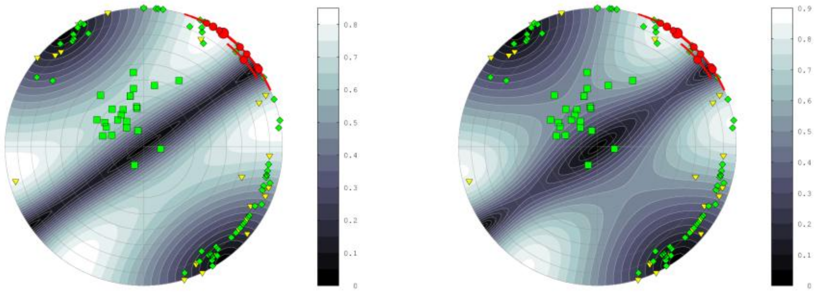

#2 Mixed - depth 3500 m - max 0.84

#2 Mixed - depth 5500 m - max 0.86

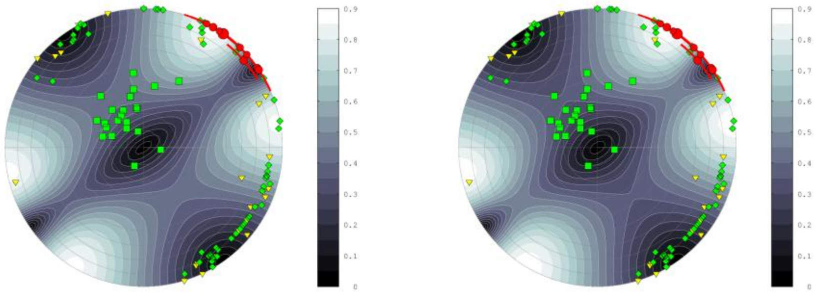

#2 Mixed - depth 7500 m - max 0.87

#2 Mixed - depth 9500 m - max 0.88

Figure 2.11. Reactivation potential for six depths levels (top left to bottom right: 500 m, 1,500 m, 3,500 m, 5,500 m, 7,500 m, and 9,500 m) under present-day stress conditions defined by #2 Mixed model. The analysis shows a change in stability pattern below 1,500 m as the maximum *rp* increases from 0.82 to 0.88. At shallow depth the gently dipping deformation zones fall into the region of maximum *rp*. With increasing depth the NW-SE regional deformation zones become subjected to highest differential stress.

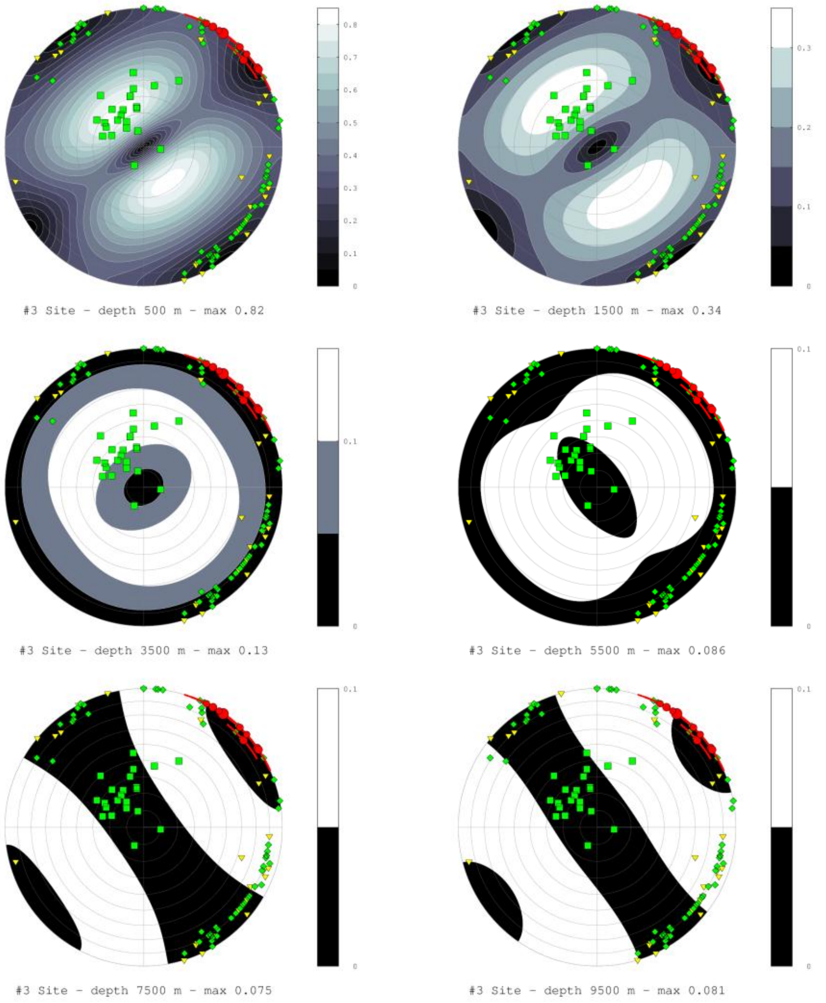

Figure 2.12. Reactivation potential for six depths levels (top left to bottom right: 500 m, 1,500 m, 3,500 m, 5,500 m, 7,500 m, and 9,500 m) under present-day stress conditions defined by #3 Site stress model. The analysis shows increasing stability with depth and predicts little to no reactivation potential.

In addition, at depth larger than 3,500 m, other steeply dipping deformation zones (major and minor) become unstable if their strike is between 95° and 195° (these values consider the uncertainties of ±15° for the stress model and ±10° for the deformation zone model). The most critical orientation between 500 and 1,500 m is for a strike of 55° and a dip angle of 25°; below 3,500 m the most critical orientation is for a strike of between 120° and 170° and a dip angle of 90°.

#3 Site Stress Model

In stress model #3 the maximum reactivation potential decreases significantly with depth because the differential stress decreases (Figure 2.12). The situation for the 500 m level is comparable to stress models #1 and #2. At 1,500 m depth the maximum *rp* = 0.34, which can be assumed to be stable. The reactivation potential analysis predicts for the stress model #3 absolutely stable conditions below 3,500 m with $rp < 0.13$. The regional deformation zones are subject to extremely low shear loads for all depths.

#4 geomecon Stress Model

The results from the newly proposed stress model #4 by geomecon are presented in Figure 2.13. At the 500 m level, the reactivation potential is distributed according to a transitional regime at repository level with the maximum reactivation potential occurring as a band that covers orientations from steep to gently dipping planes. This is similar to SKB’s #2 Mixed stress field model, but more accentuated.

At deeper levels, as the stress model corresponds to a pure strike-slip regime, the maxima are located at the outer rim of the pole plots. The maximum of *rp* mirrors the decreasing frictional coefficient from the model setup. Gently dipping deformation zones are most critical at repository level and become more stable at depth. Regional deformation zones partially lie within the field of maximum reactivation potential at all depth levels if uncertainties and deviations of the strike and direction of SH are taken into account. Consequently, when applying a decreasing coefficient of friction for the model setup, it is implicitly assumed that a smaller ratio of shear stress to normal stress is needed for reactivation of deformation zones. This results from the theory of frictional equilibrium. It is thus difficult to directly compare the results of the different models as they are based on different assumptions about the frictional strength.

In the stress field model #2, regional deformation zones show increasing reactivation potential with depth while in stress field model #4, the reactivation potential is decreasing. The decrease of *rp* in model #4 is caused by the assumption of a decreasing coefficient of friction for the model setup. Following the theory of frictional failure, the deformation zones should actually always be at frictional equilibrium throughout the brittle part of the crust, showing a reactivation potential that mirrors the frictional coefficient.

As mentioned above, the reactivation potential is not normalised to a specific threshold value, and thus it has to be compared to what is assumed to be the frictional strength of the respective plane of weakness. The increase of *rp* in model #2 is caused by the difference in assumed pore pressure for the model setup (8.5 MPa/km) compared to the pore pressure used in the #4 geomecon’s model for calculating the reactivation potential (10 MPa/km).

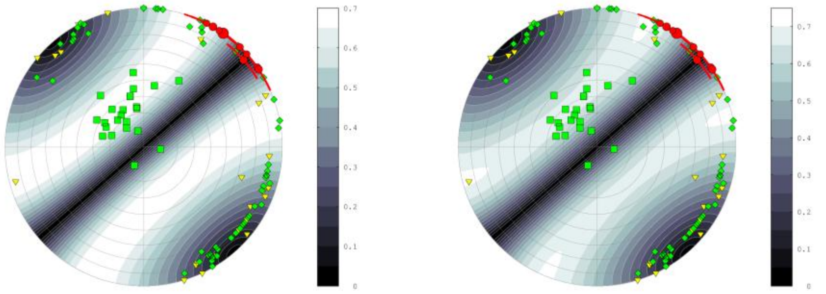

#4 geomecon - depth 500 m - max 0.7

#4 geomecon - depth 1500 m - max 0.71

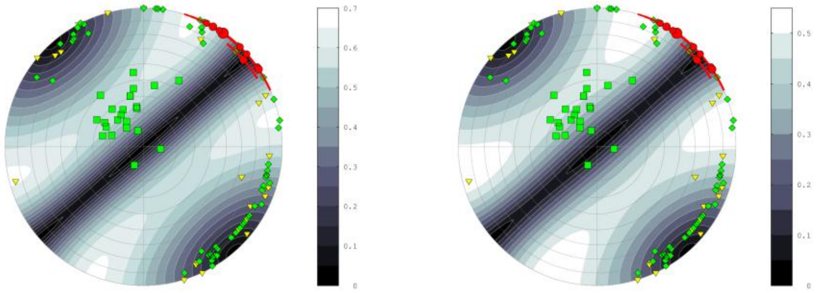

#4 geomecon - depth 3500 m - max 0.66

#4 geomecon - depth 5500 m - max 0.54

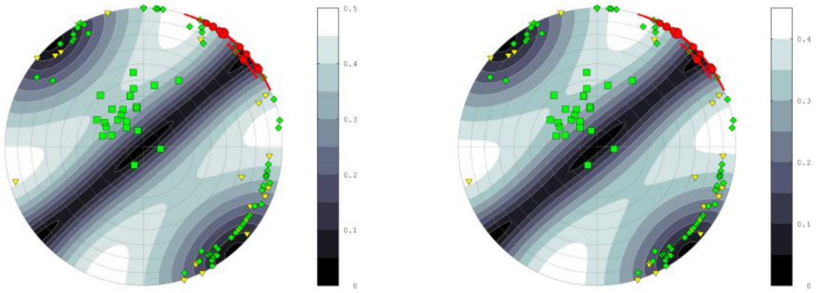

#4 geomecon - depth 7500 m - max 0.48

#4 geomecon - depth 9500 m - max 0.43

Figure 2.13. Reactivation potential for six depths levels (top left to bottom right: 500 m, 1,500 m, 3,500 m, 5,500 m, 7,500 m, and 9,500 m) under present-day stress conditions defined by #4 geomecon model.

Glacial cycle

In the following section, the influence of a reference glaciation scenario on the stability of the set of deformation zones is examined. For this purpose existing glaciation models by SKB are used. Lund et al. (2009, SKB TR-09-15) suggest a series of models based on SKB reference ice model by Näslund (2006, SKB TR-06-23). From the models that fit to GPS data, Model M T9 was chosen by Lund et al. (2009, SKB TR-09-15) as the most realistic, which corresponds to no variation in lithosphere thickness and high glacially induced horizontal stresses. It is the preferred model by Lund et al. (2009) and has frequently been used for further stability analysis by SKB (e.g. SKB TR-08-11, SKB TR-10-49). The discussion of the relevance of glacial cycles and the related stress alterations to expect is beyond the topic of this assessment. The reported results by SKB are taken for granted without further questioning the justification.

From the evolution of glacially induced stresses (Figure 2.14), five points in time are selected for stability analysis (Table 2.3) similarly to Hökmark et al. (2010, SKB TR-10-23). The induced pore pressure is assumed to amount to 50% of the ice load (c.f. intermediate scenario by Lund et al., 2009, SKB TR-09-15). Under present-day stress conditions the stresses predicted by SKB models (#1 to #3) are identical at 500 m depth. The following considerations are valid for all three SKB models and for repository depth.

The phases of maximum ice thickness (at time T1 and T4) stabilise the deformation zones, especially the gently dipping set. As the vertical stress, which is the least principal stress among these stress increments, increases more than the horizontal stresses it counteracts the forces that promote reverse faulting. During the second glacial maximum this effect is especially pronounced since the ice cover is thicker (Figure 2.15).

Table 2.3. Glacially induced stresses from model M T9 by Lund et al. (2009, SKB TR-09-15) at five points in time (see Figure 2.14).

	T1	**T2**	**T3**	**T4**	**T5**
	1st glacial maximum	**Ice margin retreating**	**Stress reductions due to forebulge**	**2nd glacial maximum**	**Ice margin retreating**
SH [MPa]	+16	+7.5	0	+29	+12.5
Sh [MPa]	+14	+5	-5	+27	+9
SV [MPa]	+18	0	0	+28	0
Pp [MPa] (50% Pind)	+9	0	0	+14	0

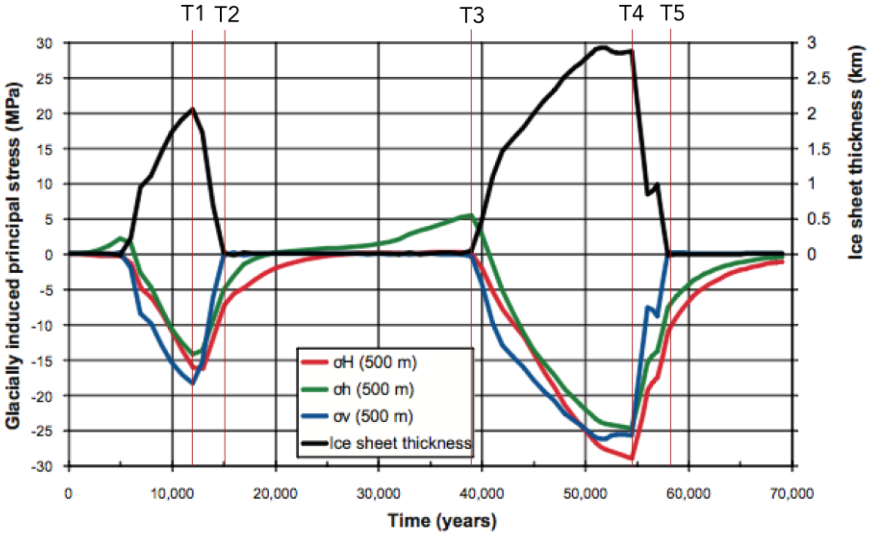

Figure 2.14. Glacially induced stress increments. Vertical red lines mark the points in time T1 to T5 for stability analysis (from Hökmark et al., 2010, SKB TR-10-23, Figure 4-12).

The phases of ice retreat after the maximum ice thickness (T2 and T5), when the ice margin is passing and lateral stresses are still increased but no additional vertical stress is induced, lead to an increase in criticality and thus, reverse faulting is even more likely. Gently dipping deformation zones show massive increase of the reactivation potential.

At T3, when the forebulge of the ice sheet reduces the minor horizontal stress, the maximum reactivation potential is not affected since Sh is the intermediate principle stress and the differential stress is not affected. However, higher values of *rp* are experienced by the SE striking regional deformation zones (between 0.5 and 0.55 compared to 0.35 to 0.4 at present-day conditions).

In the #4 geomecon stress model the present-day conditions have maximum reactivation potential of 0.7 at orientations along a band in the pole plot that ranges from steeply dipping planes with small angles to the maximum horizontal stress, to shallow dipping planes perpendicular to the maximum horizontal stress (Figure 2.16). At times T1 and T4, this transitional regime is shifted towards a strike-slip regime. The maximum reactivation potential is decreased in both cases. In contrast, at T2 and T5, when the ice margin is passing, the faulting regime is shifted towards reverse faulting with increased reactivation potential of gently dipping zones. At T5 the reactivation potential is increased significantly and has a maximum of 0.92.

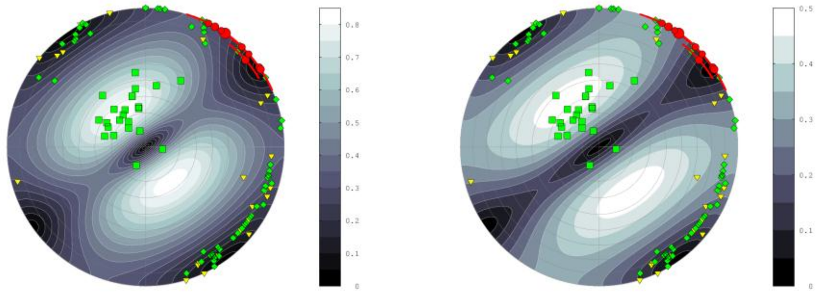

#1 Reverse - depth 500 m - max 0.82

#1 Reverse T1 - depth 500 m - max 0.48

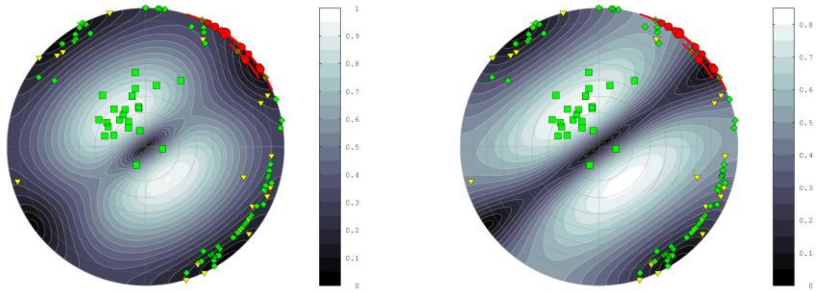

#1 Reverse T2 - depth 500 m - max 0.95

#1 Reverse T3 - depth 500 m - max 0.82

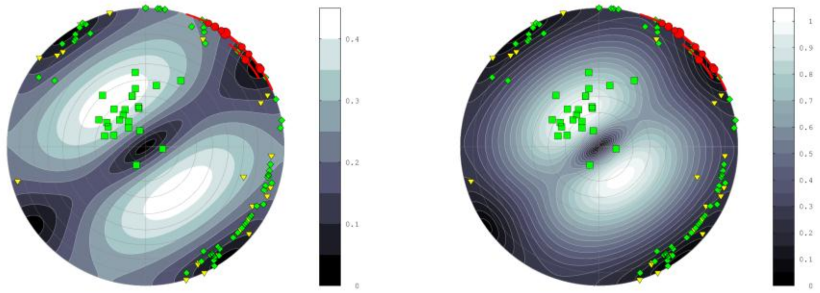

#1 Reverse T4 - depth 500 m - max 0.43

#1 Reverse T5 - depth 500 m - max 1

Figure 2.15. Evolution of reactivation potential at 500 m depth during the reference glacial cycle and SKB's stress model. Results for 500 m coincide for #1 Reverse, #2 Mixed and #3 Site stress model. The orientations of maximum reactivation potential remain the same, but *rp* is massively increased for T2 and T5, corresponding to the passing ice margin post glacial. The upper left pole plot represents the present-day conditions.

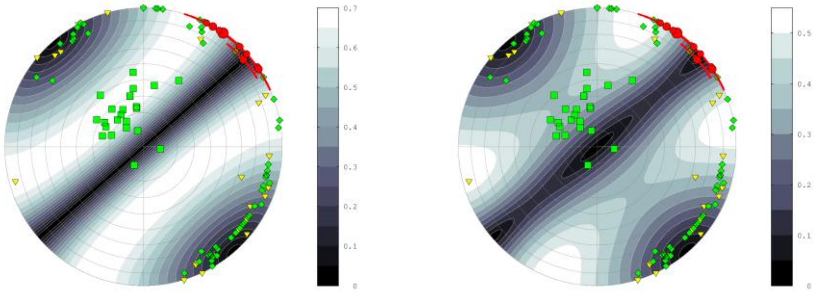

#4 geomecon - depth 500 m - max 0.7

#4 geomecon T1 - depth 500 m - max 0.54

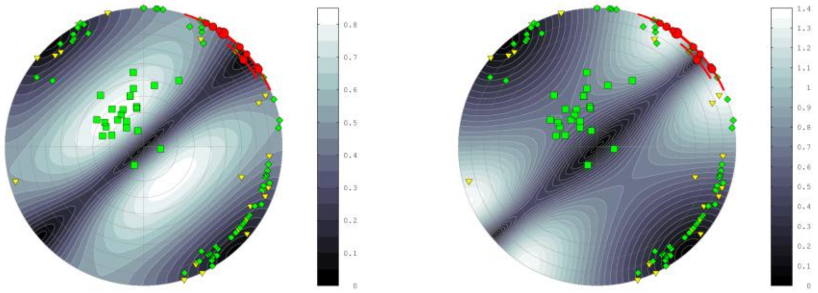

#4 geomecon T2 - depth 500 m - max 0.84

#4 geomecon T3 - depth 500 m - max 1.4

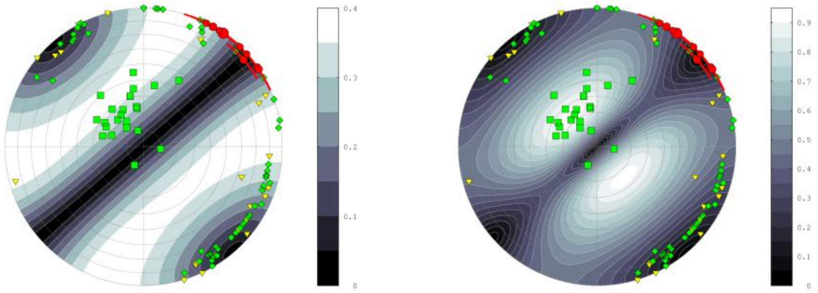

#4 geomecon T4 - depth 500 m - max 0.39

#4 geomecon T5 - depth 500 m - max 0.92

Figure 2.16. Evolution of reactivation potential at 500 m depth during the reference glacial cycle and #4 geomecon's stress model. The upper left pole plot represents the present-day conditions.

Under the forebulge induced stresses at T3, the maximum reactivation potential is extremely high with 1.4, leading to unstable conditions for the sets of steeply dipping deformation zones that strike around ±25-30° with respect to SH, such as some of the regional deformation zones.

The effect of adding the glacial induced stresses as defined by Table 2.2 for the 5,500 m depth level, without discussing the validity for that depth, is shown in Figures 2.17 and 2.18 for #3 SKB Site stress model and #4 geomecon model, respectively. SKB's stress model #3 suggests highest reactivation potential during T2 and T5, which corresponds to the passing of the ice margin after glacial peak. The maximum reactivation potential is confined to gently dipping features, the regional deformation zones lie in the most stable regions. However, the absolute *rp* values are very low, suggesting stable conditions at all times.

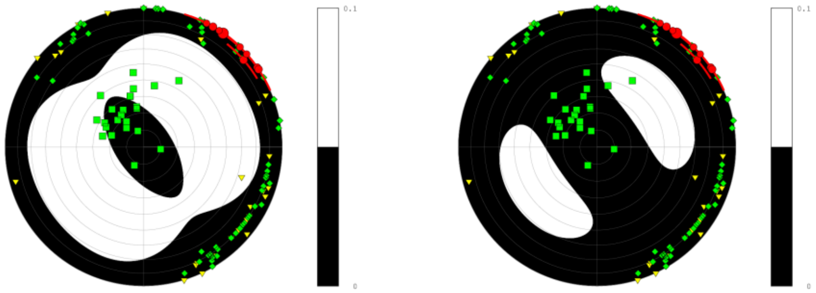

#3 Site - depth 5500 m - max 0.086

#3 Site T1 - depth 5500 m - max 0.061

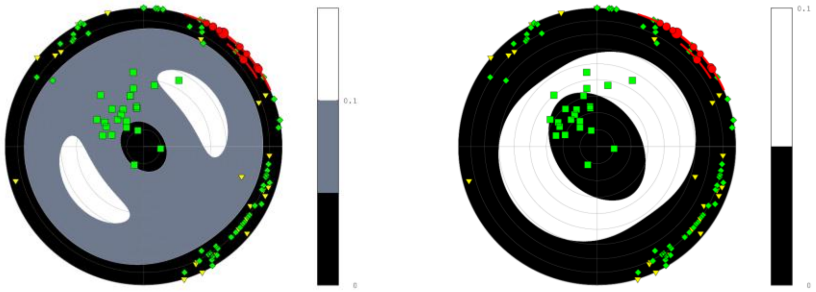

#3 Site T2 - depth 5500 m - max 0.11

#3 Site T3 - depth 5500 m - max 0.062

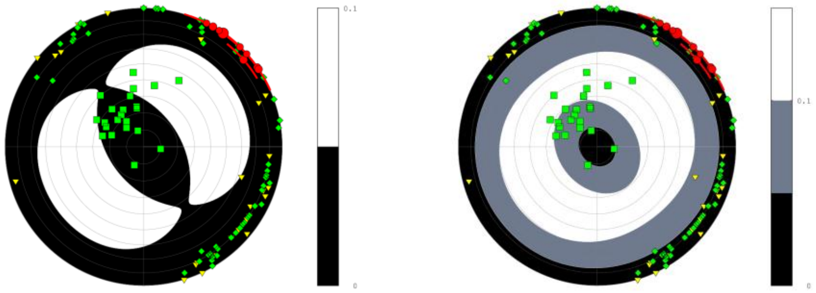

#3 Site T4 - depth 5500 m - max 0.071

#3 Site T5 - depth 5500 m - max 0.13

Figure 2.17. Evolution of reactivation potential at 5,500 m depth during the reference glacial cycle and SKB's #3 Site stress model. The changes in stress as proposed by Lund et al. (2009, SKB TR-09-15) for the M T9 scenario have been applied to 5,500 m. The upper left pole plot represents the present-day conditions.

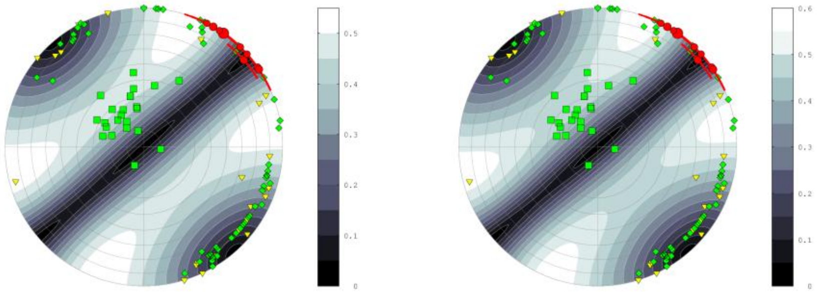

#4 geomecon - depth 5500 m - max 0.54

#4 geomecon T1 - depth 5500 m - max 0.58

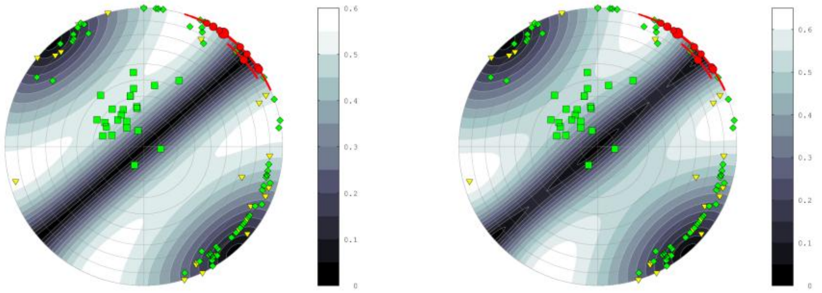

#4 geomecon T2 - depth 5500 m - max 0.58

#4 geomecon T3 - depth 5500 m - max 0.64

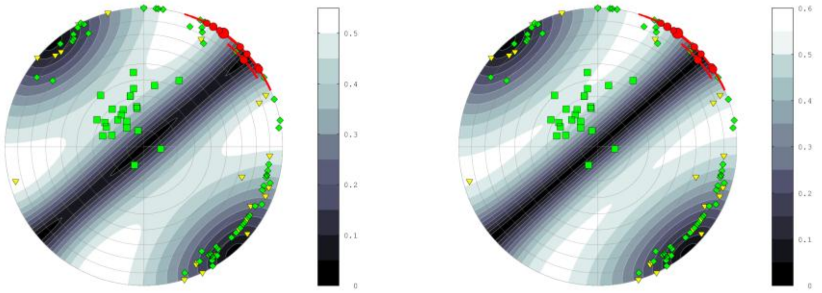

#4 geomecon T4 - depth 5500 m - max 0.55

#4 geomecon T5 - depth 5500 m - max 0.57

Figure 2.18. Evolution of reactivation potential at 5,500 m depth during the reference glacial cycle and #4 geomecon's alternative stress model. The changes in stress as proposed by Lund et al. (2009, SKB TR-09-15) for the M T9 scenario have been applied to 5,500 m depth. The upper left pole plot represents the present-day conditions.

Applied to the geomecon stress model #4, throughout all time the highest reactivation potential of 0.64 is acting on the regional deformation zones. The *rp* is largest, although moderately high, during T3, suggesting largest potential for activation during the forebulge period.

The evolution of the reactivation potential during the glacial cycle is shown again for the two depth levels of 500 and 5,500 m in Figures 2.19 and 2.20 that allow for a direct comparison of the stress field models. At repository depth, the three stress field models by SKB (#1 to #3) equal each other and hence show the same maximum *rp* (black line in Figure 2.19). In contrast to the #4 geomecon model (blue line in Figure 2.19), they reach slightly lower maximum *rp* values but show the same trend of increased stability during times of maximum ice load and decreasing stability during ice retreat. During the forebulge period, however, the reactivation potential is significantly increased with the #4 geomecon model while for SKB's models it is close to the initial value at time T0. At 5,500 m depth the variations in reactivation potential are smaller except for the #3 Site stress model (Figure 2.20), which in turn has very small absolute values.

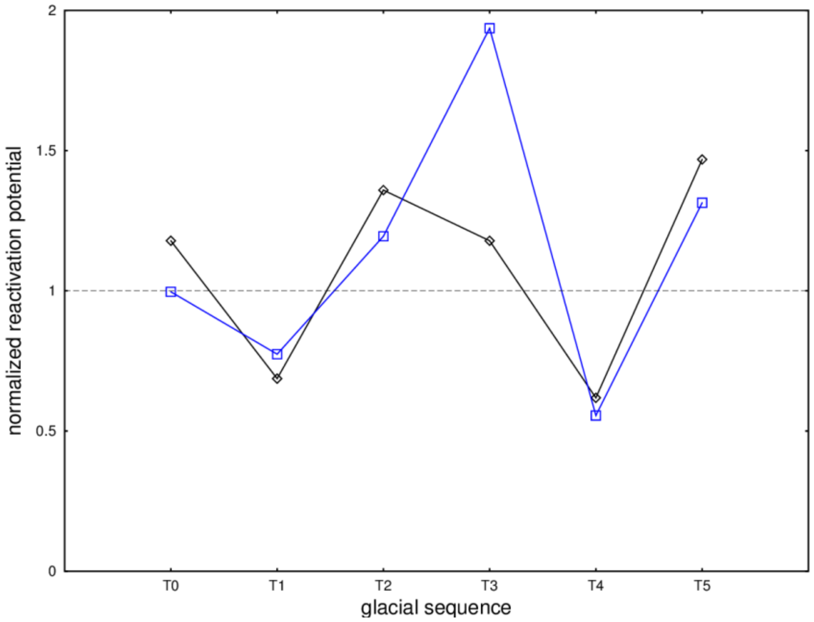

Figure 2.19. Reactivation potential at 500 m for SKB stress field models #1 to #3 (black line) and the #4 geomecon stress field model (blue line). The reactivation potential is normalised to 0.7.

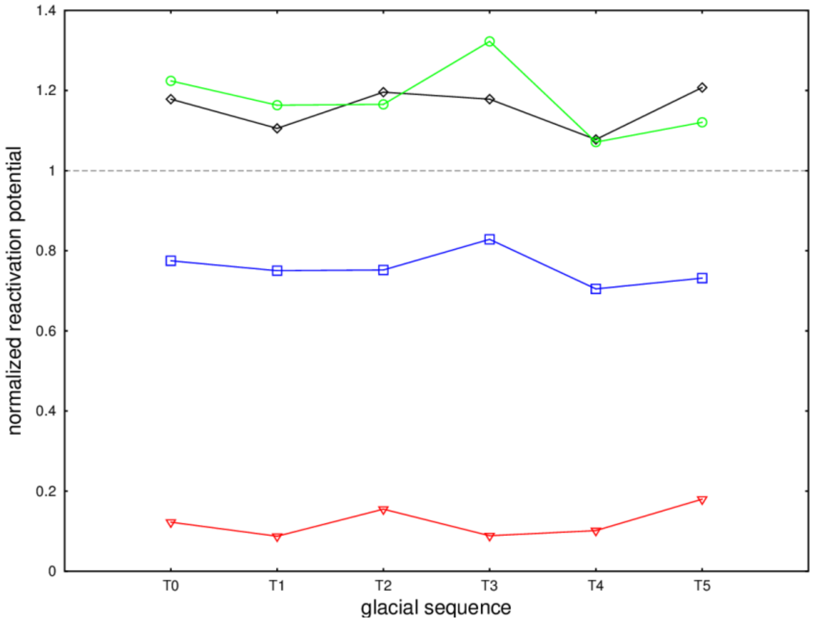

Figure 2.20. Normalised reactivation potential at 5,500 m for stress field models #1 (black line), #2 (green line), #3 (red line) and the #4 (blue line). The reactivation potential is normalised to 0.7.

Figure 2.21 explains how to read the following box plots in Figures 2.22. to 2.45. Figures 2.22 to 2.45 show the evolution of the reactivation potential for each set of deformation zones along with the maximum resulting reactivation potential. The red markers, connected with a straight line, denote the overall maximum *rp*, independently of the presence of deformation zones. The boxes represent the respective set of deformation zones, showing the distribution of the reactivation potential within this population at a certain point in time. The span of deformation zone orientations for each group of deformation zones are shown in Table 2.4.

Table 2.4. Ranges of strike and dip angles for each set of deformation zones. The major deformation zones are split into steeply and gently dipping DZ.

	Strike range [°]			**Dip angle range [°]**		
regional DZ	117	-	146	85	-	90
steeply dipping DZ	33	-	252	70	-	90
gently dipping DZ	15	-	297	10	-	45
minor DZ	40	-	345	63	-	90

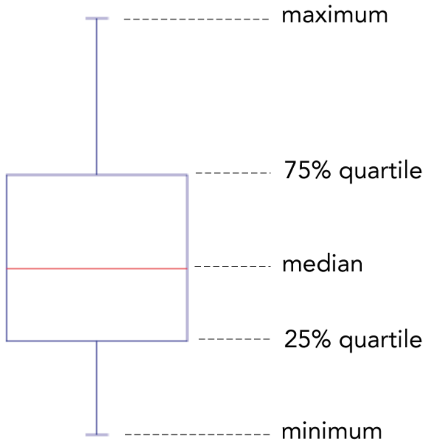

Figure 2.21. The box plots depict the distribution of the reactivation potential within a population of deformation zones. They show the maximum and minimum values, the median, and the lower (25%) and upper (75%) quartiles.

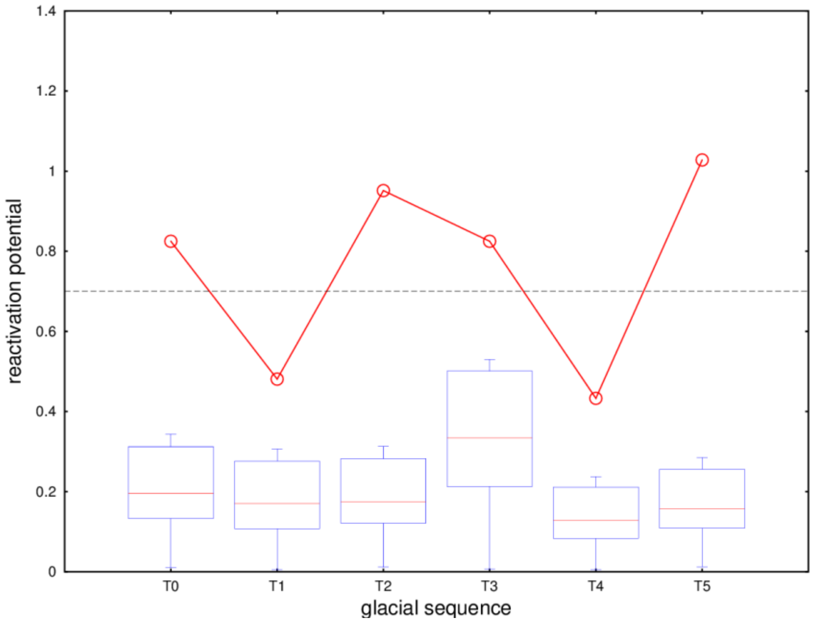

Figure 2.22. Reactivation potential of regional deformation zones (boxes) and maximum reactivation potential (solid red line) throughout the glacial cycle at 500 m for the SKB stress field models (#1 to #3).

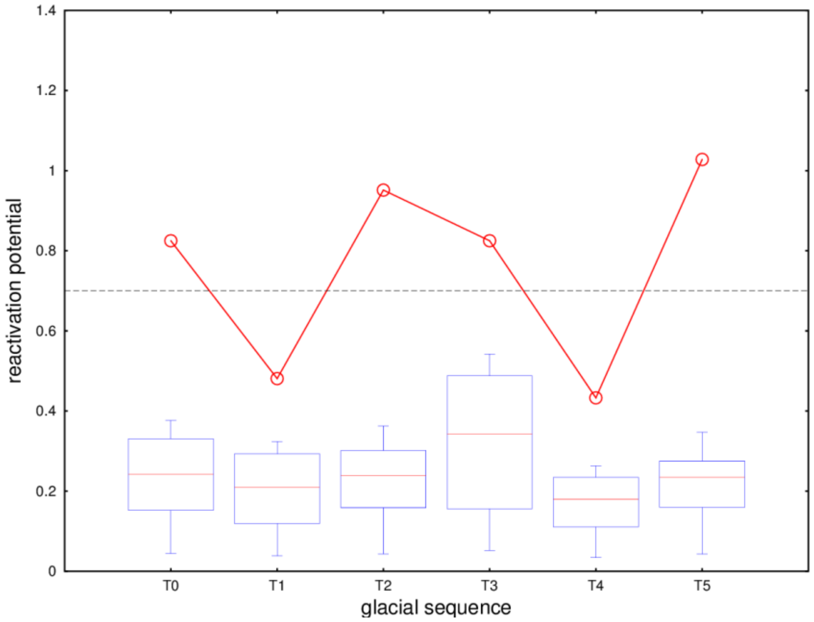

Figure 2.23. Reactivation potential of steeply dipping major deformation zones (boxes) and maximum reactivation potential (solid red line) throughout the glacial cycle at 500 m for the SKB stress field models (#1 to #3).

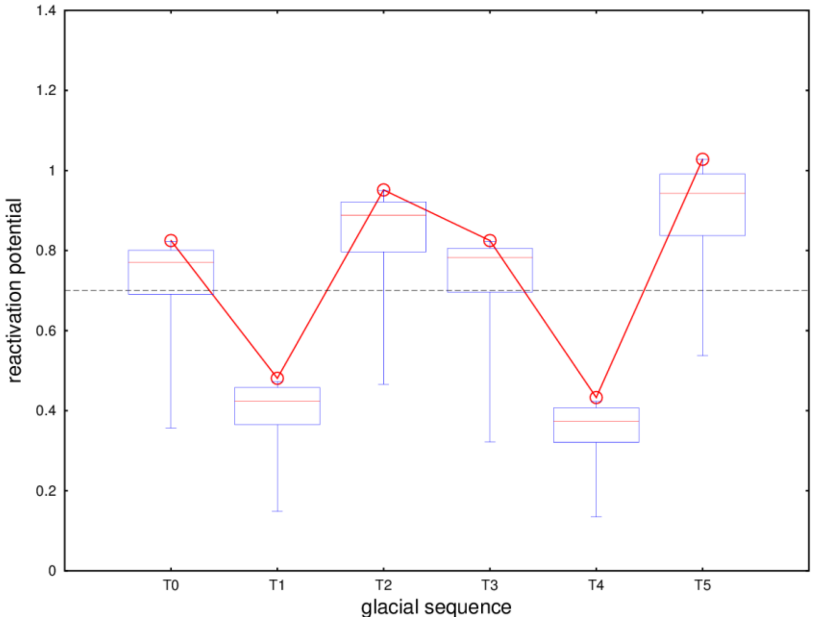

Figure 2.24. Reactivation potential of gently dipping major deformation zones (boxes) and maximum reactivation potential (solid red line) throughout the glacial cycle at 500 m for the SKB stress field models (#1 to #3).

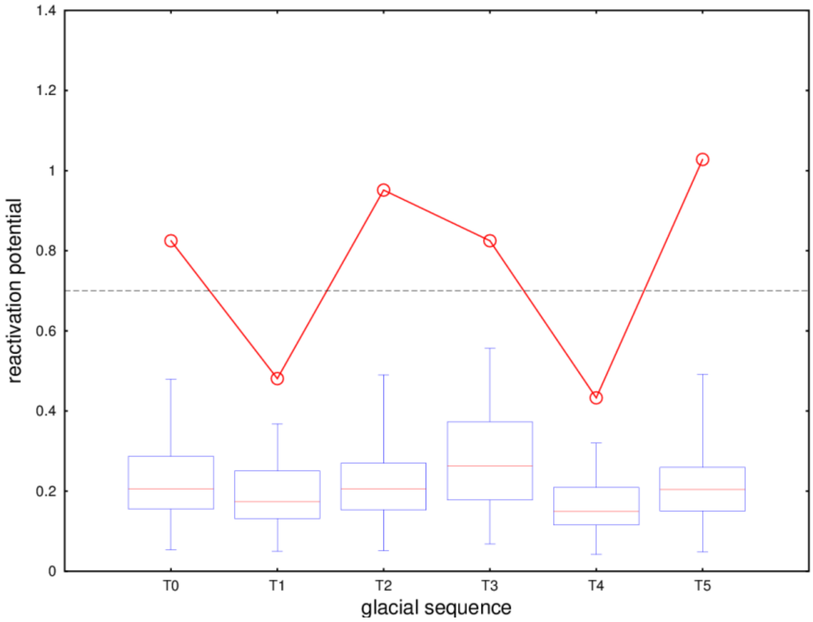

Figure 2.25. Reactivation potential of minor deformation zones (boxes) and maximum reactivation potential (solid red line) throughout the glacial cycle at 500 m for the SKB stress field models (#1 to #3).

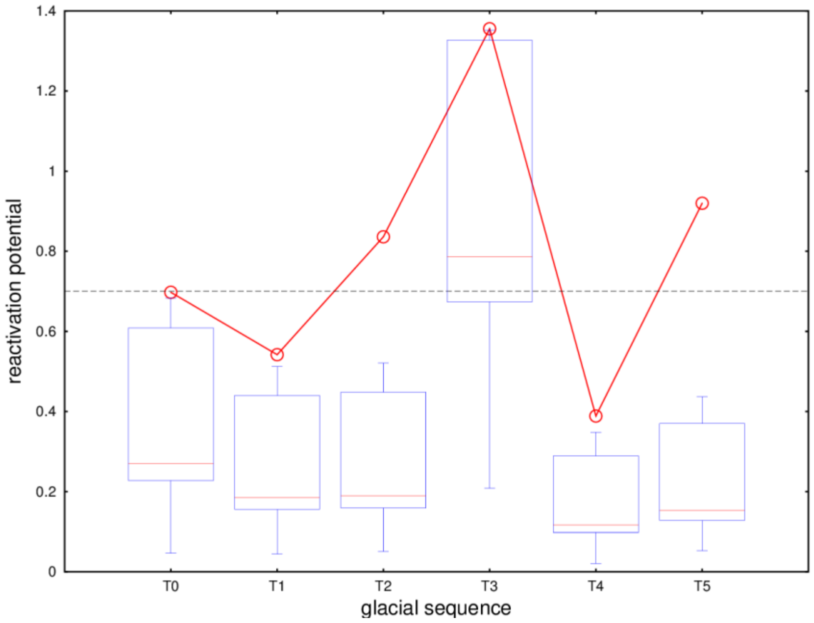

Figure 2.26. Reactivation potential of regional deformation zones (boxes) and maximum eactivation potential (solid red line) throughout the glacial cycle at 500 m for the #4 geomecon stress field model.

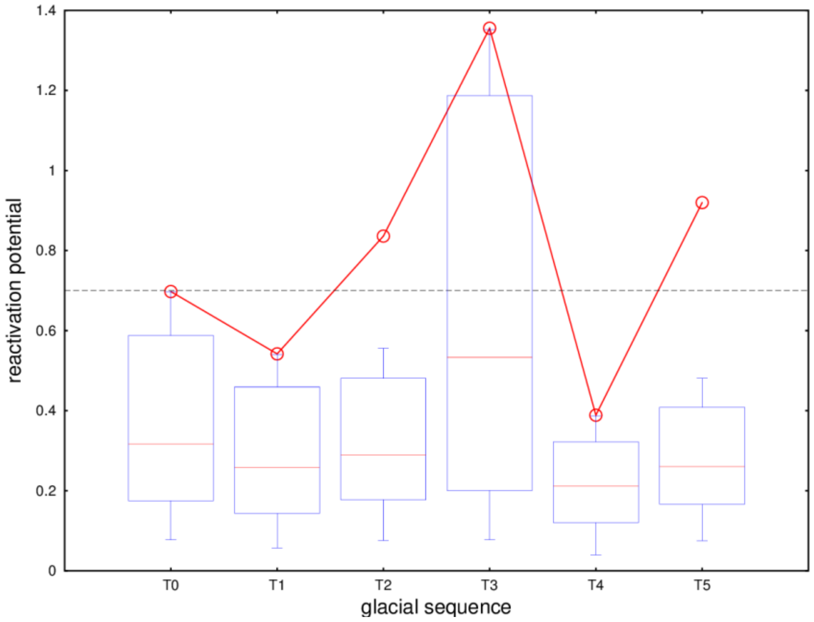

Figure 2.27. Reactivation potential of steeply dipping major deformation zones (boxes) and maximum reactivation potential (solid red line) throughout the glacial cycle at 500 m for the #4 geomecon stress field model.

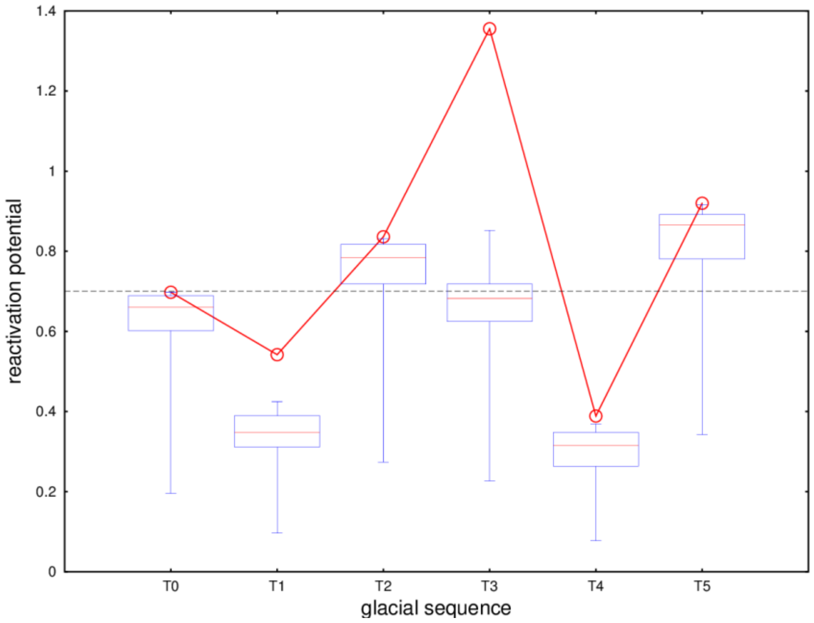

Figure 2.28. Reactivation potential of gently dipping major deformation zones (boxes) and maximum reactivation potential (solid red line) throughout the glacial cycle at 500 m for the #4 geomecon stress field model.

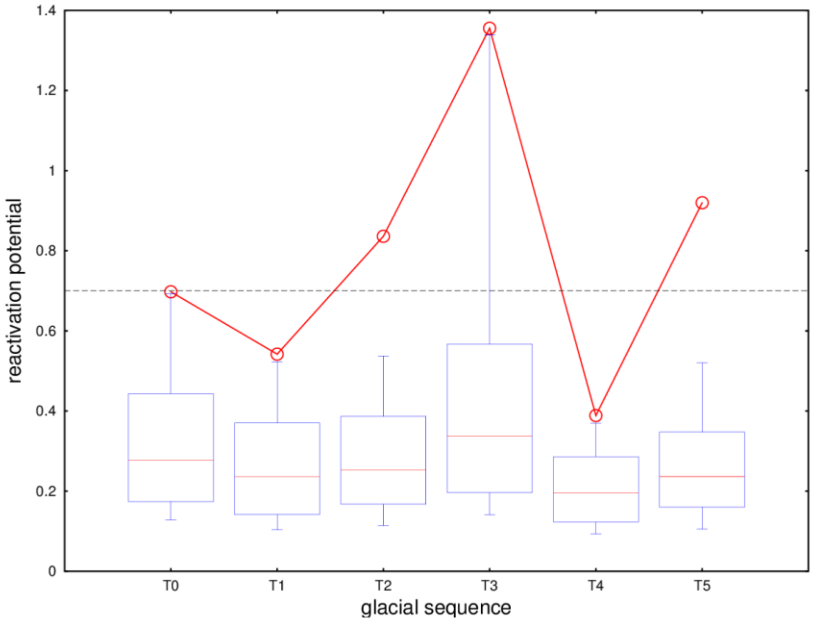

Figure 2.29. Reactivation potential of minor deformation zones (boxes) and maximum reactivation potential (solid red line) throughout the glacial cycle at 500 m for the #4 geomecon stress field model.

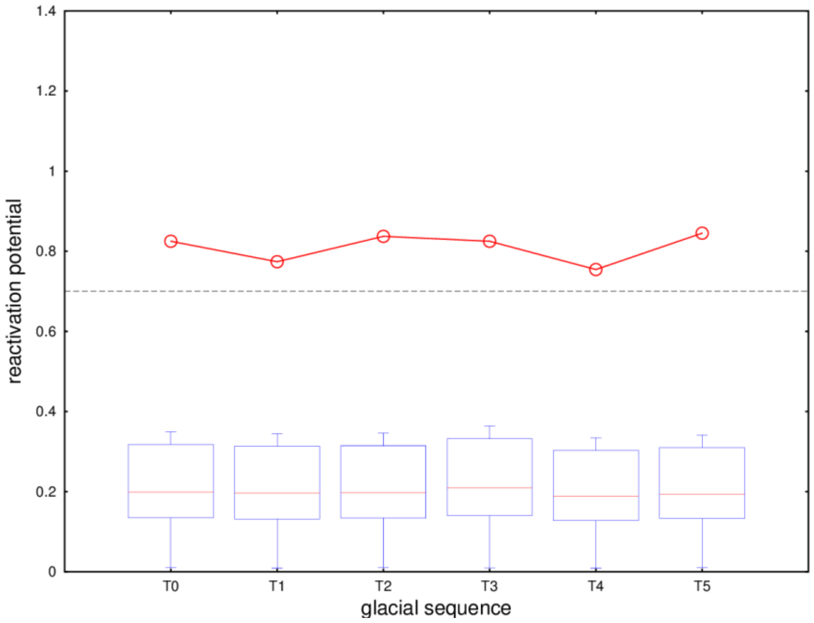

Figure 2.30. Reactivation potential of regional deformation zones (boxes) and maximum reactivation potential (solid red line) throughout the glacial cycle at 5,500 m for the #1 Reverse stress field model.

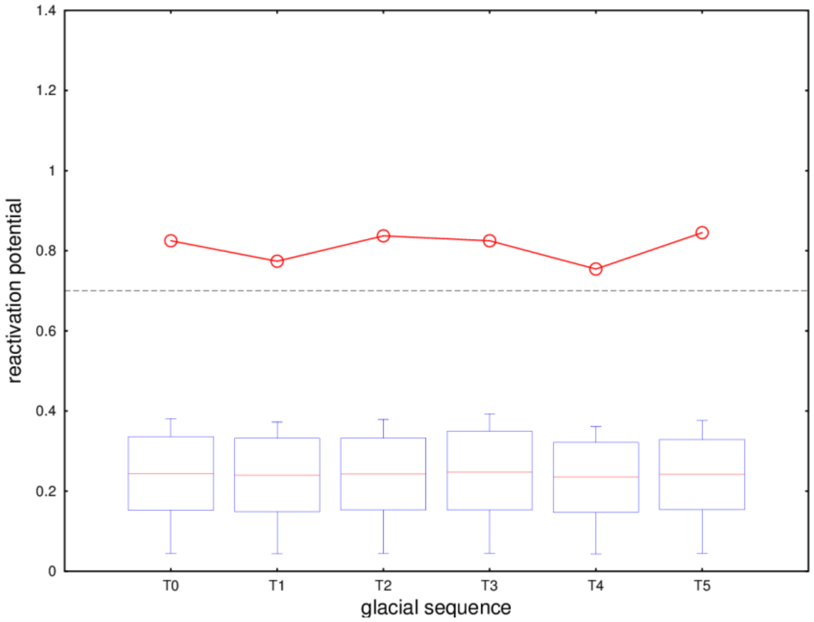

Figure 2.31. Reactivation potential of steeply dipping major deformation zones (boxes) and maximum reactivation potential (solid red line) throughout the glacial cycle at 5,500 m for the #1 Reverse stress field model.

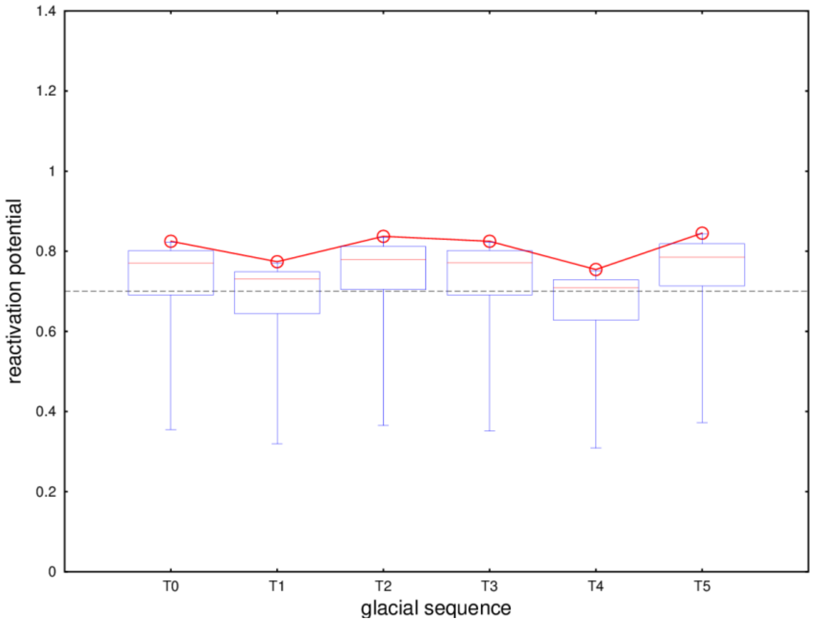

Figure 2.32. Reactivation potential of gently dipping major deformation zones (boxes) and maximum reactivation potential (solid red line) throughout the glacial cycle at 5,500 m for the #1 Reverse stress field model.

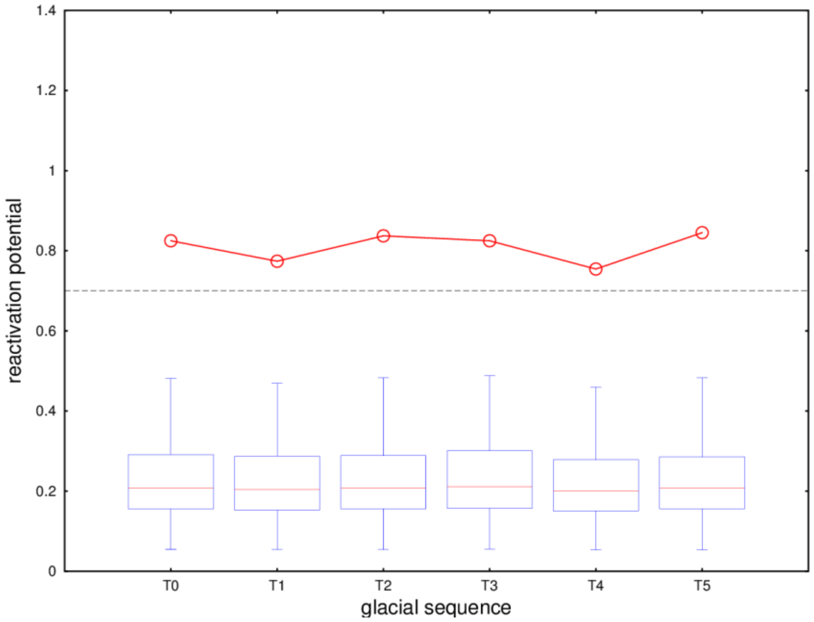

Figure 2.33. Reactivation potential of minor deformation zones (boxes) and maximum reactivation potential (solid red line) throughout the glacial cycle at 5,500 m for the #1 Reverse stress field model.

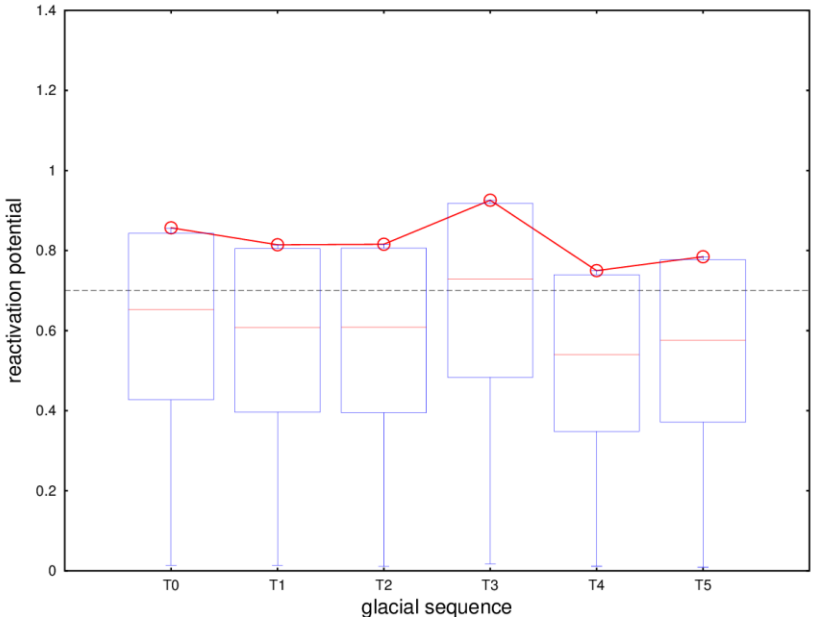

Figure 2.34. Reactivation potential of regional deformation zones (boxes) and maximum reactivation potential (solid red line) throughout the glacial cycle at 5,500 m for the #2 Mixed stress field model.

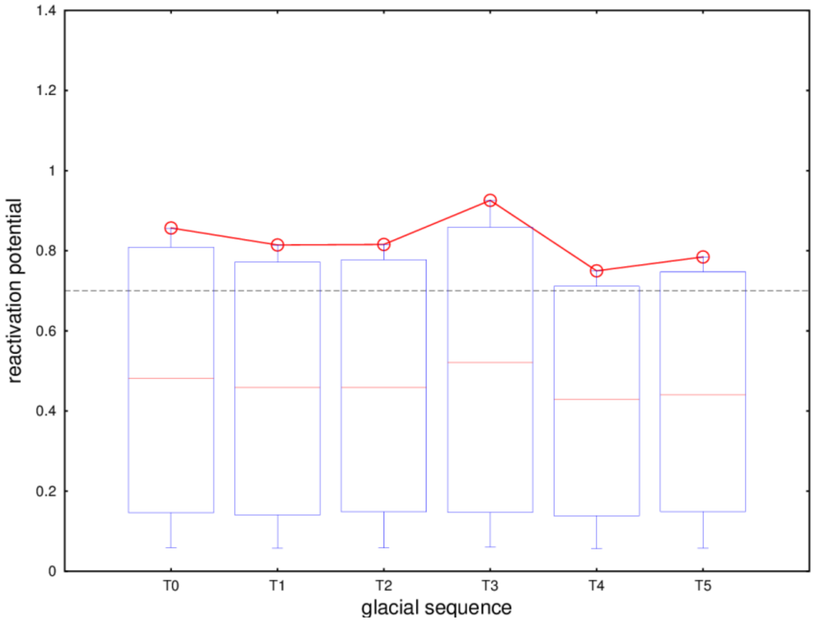

Figure 2.35. Reactivation potential of steeply dipping deformation zones (boxes) and maximum reactivation potential (solid red line) throughout the glacial cycle at 5,500 m for the #2 Mixed stress field model.

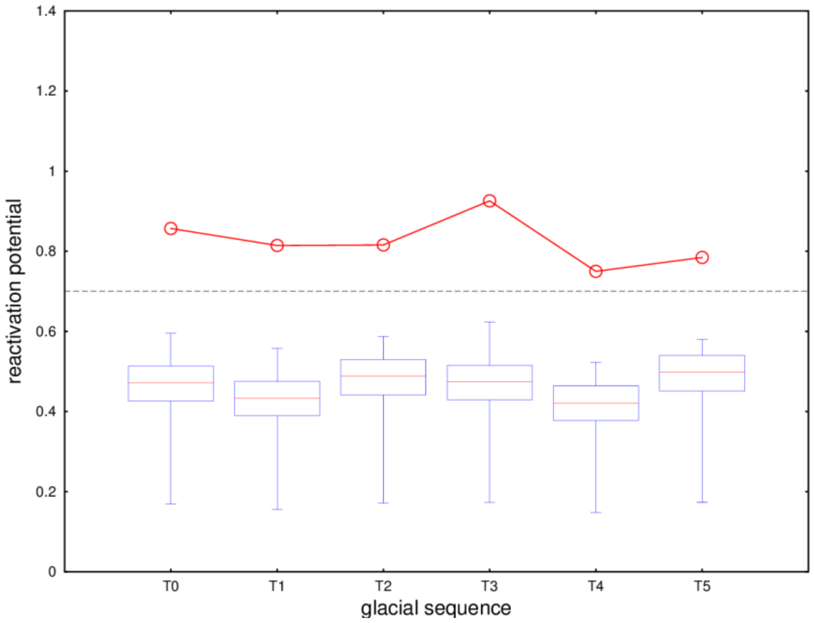

Figure 2.36. Reactivation potential of gently dipping deformation zones (boxes) and maximum reactivation potential (solid red line) throughout the glacial cycle at 5,500 m for the #2 Mixed stress field model.

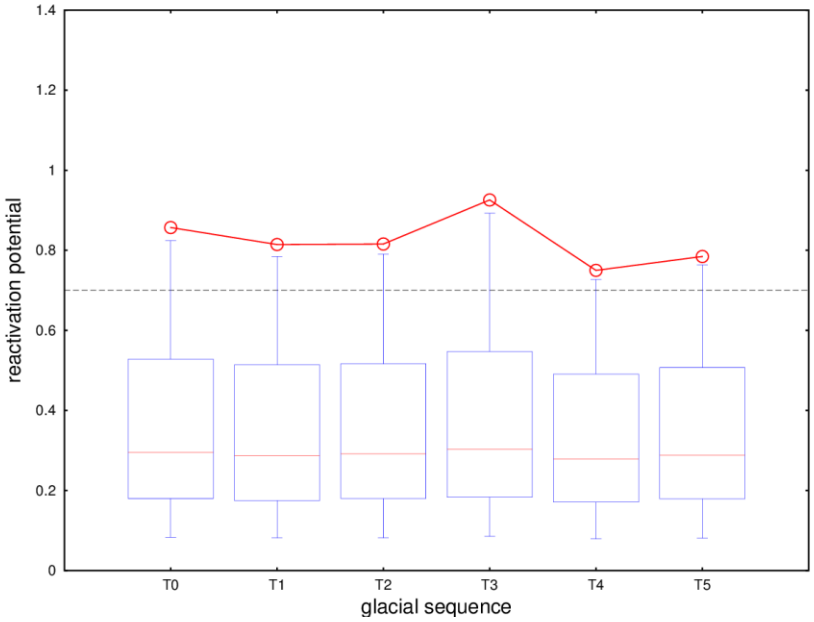

Figure 2.37. Reactivation potential of minor deformation zones (boxes) and maximum reactivation potential (solid red line) throughout the glacial cycle at 5,500 m for the #2 Mixed stress field model.

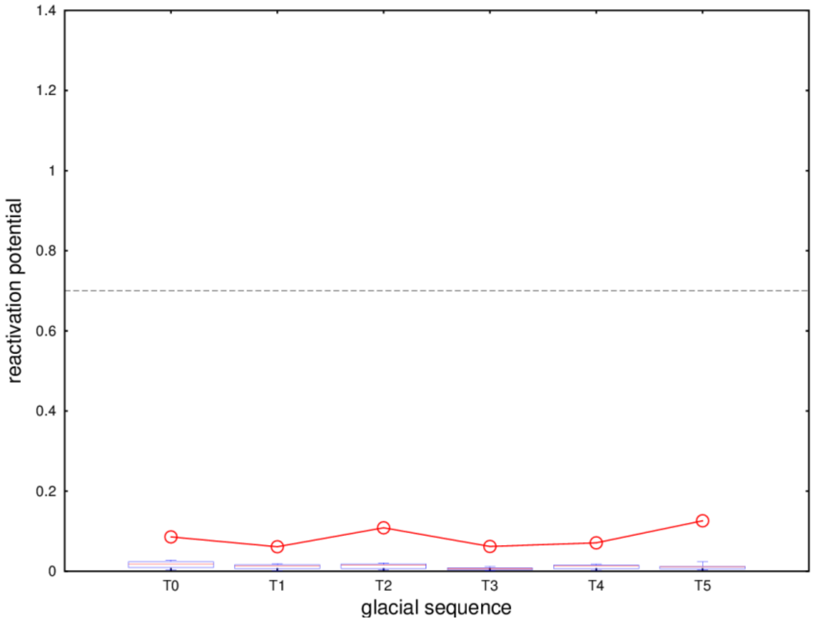

Figure 2.38. Reactivation potential of regional deformation zones (boxes) and maximum reactivation potential (solid red line) throughout the glacial cycle at 5,500 m for the #3 Site stress field model.

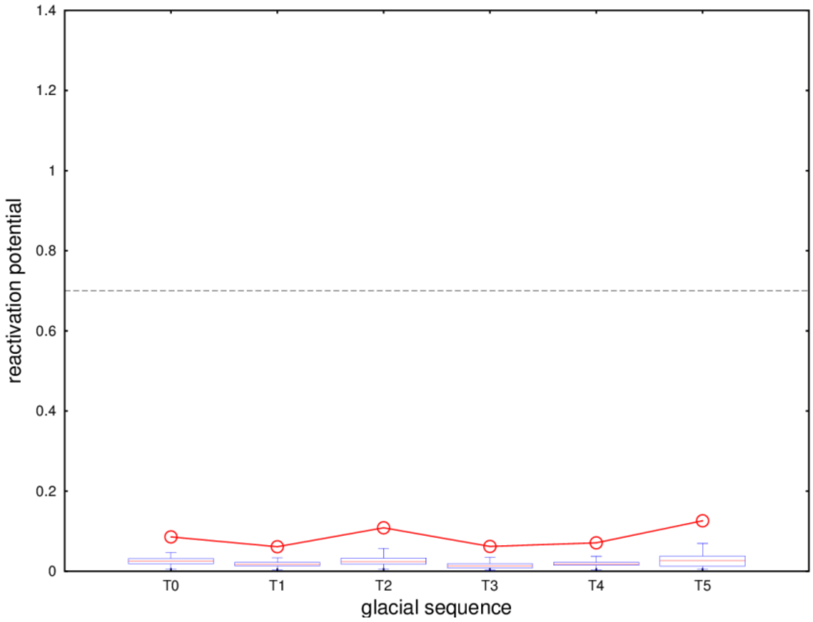

Figure 2.39. Reactivation potential of steeply dipping deformation zones (boxes) and maximum reactivation potential (solid red line) throughout the glacial cycle at 5,500 m for the #3 Site stress field model.

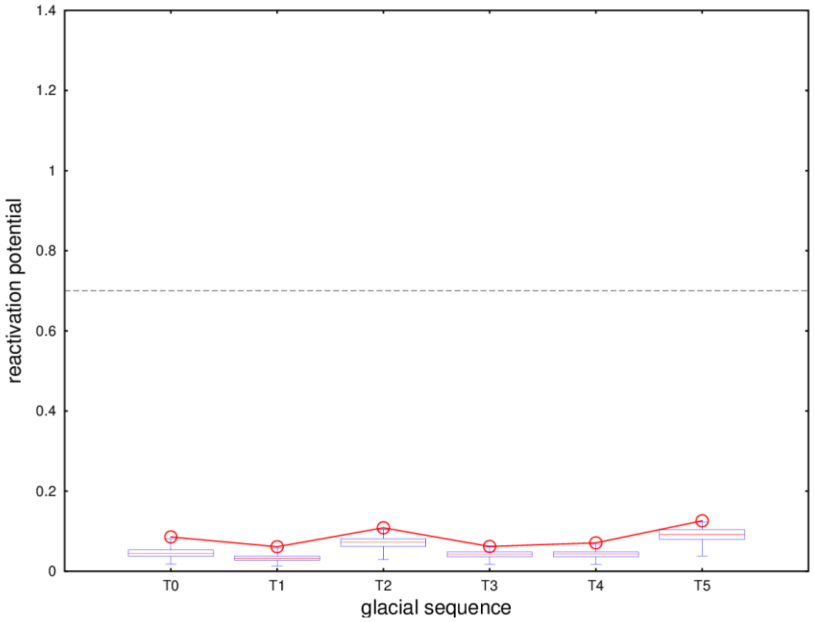

Figure 2.40. Reactivation potential of gently dipping deformation zones (boxes) and maximum reactivation potential (solid red line) throughout the glacial cycle at 5,500 m for the #3 Site stress field model.

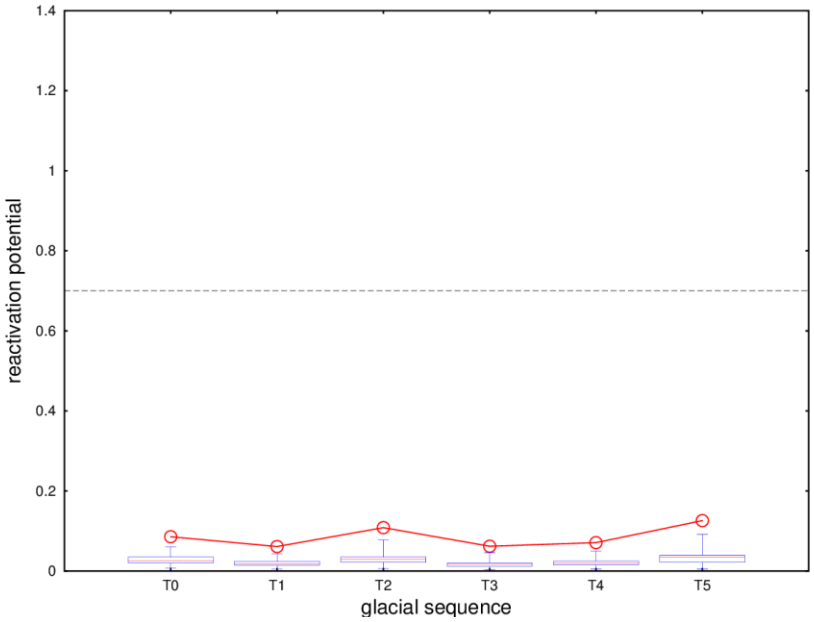

Figure 2.41. Reactivation potential of minor deformation zones (boxes) and maximum reactivation potential (solid red line) throughout the glacial cycle at 5,500 m for the #3 Site stress field model.

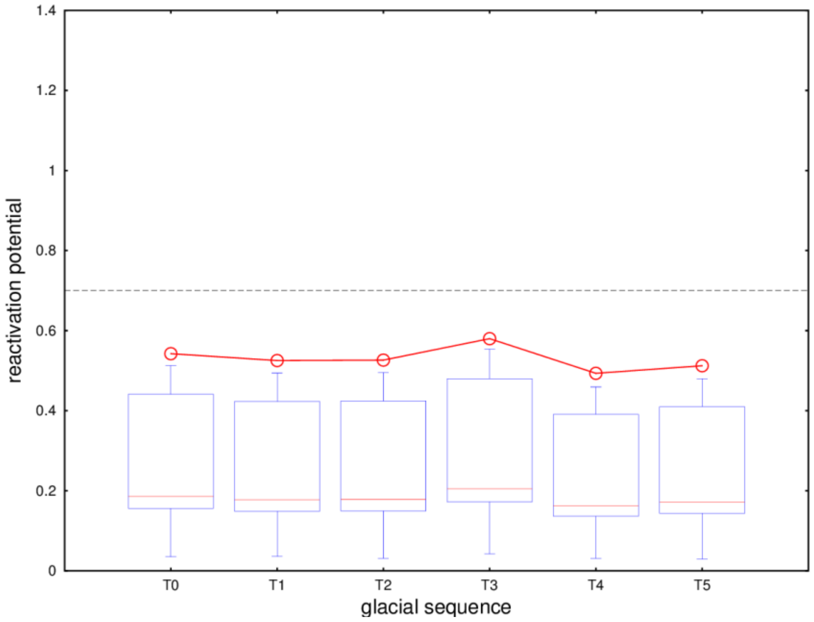

Figure 2.42. Reactivation potential of regional deformation zones (boxes) and maximum reactivation potential (solid red line) throughout the glacial cycle at 5,500 m for the #4 geomecon stress field model.

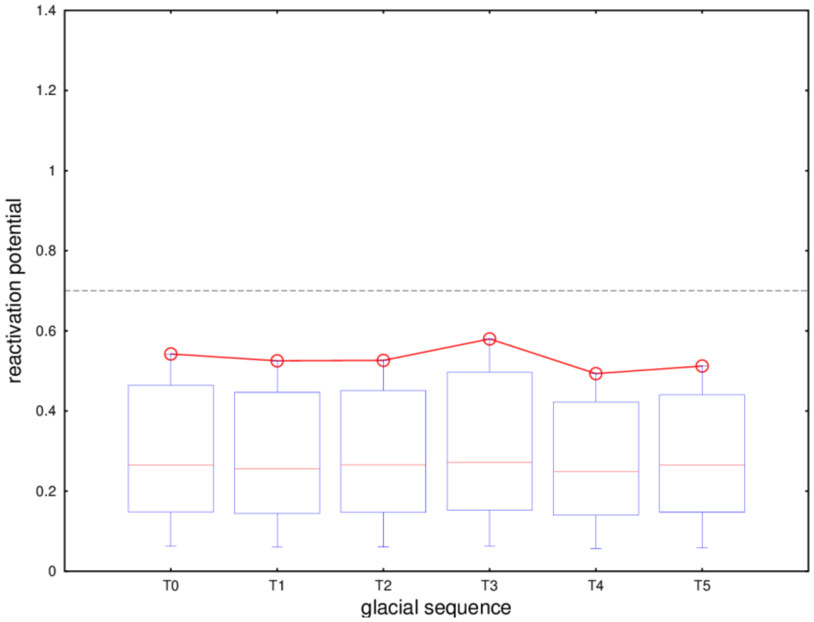

Figure 2.43. Reactivation potential of steeply dipping deformation zones (boxes) and maximum reactivation potential (solid red line) throughout the glacial cycle at 5,500 m for the #4 geomecon stress field model.

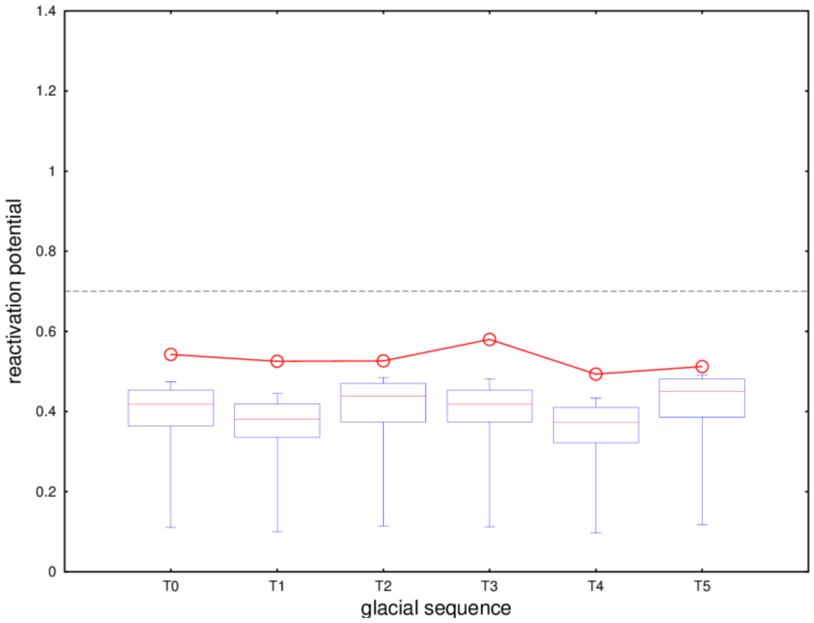

Figure 2.44. Reactivation potential of gently dipping deformation zones (boxes) and maximum reactivation potential (solid red line) throughout the glacial cycle at 5,500 m for the #4 geomecon stress field model.

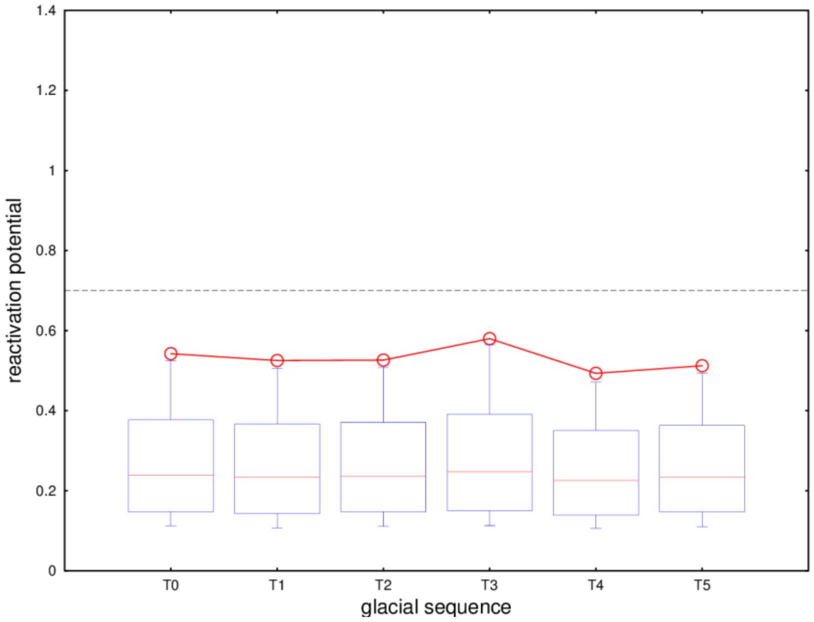

Figure 2.45. Reactivation potential of minor deformation zones (boxes) and maximum reactivation potential (solid red line) throughout the glacial cycle at 5,500 m for the #4 geomecon stress field model.

2.3.3. Analysis of the potential for deformation zone growth

The estimation of the stability by itself will give no indication if a deformation zone will slip. This prediction is possible only if the friction coefficient for the deformation zones is known. If the frictional resistance of the deformation zone is exceeded it can be concluded that there will likely be a displacement along the deformation zone. Such an analysis, which is assumed to be best industry practice, assumes a model with planar singular feature that may be assigned a frictional resistance that can be activated by a superimposed shear and normal load.

However, this does not imply that the deformation zone will grow at the same time. There are no proven methods of assessing the growth of deformation zones. In the following a method for estimation of fracture growth is applied to the deformation zones that represent the highest risk for the repository integrity, i.e. those that immediately surround or crosscut the repository, especially those that have a free end that might extend into the repository volume (Figure 2.46).

Assuming that a deformation zone may be represented by a singular planar feature that can activate friction, the stress concentration at the deformation zone “tip” may be calculated according to Lawn (1993) by means of the expression:

$$K_{II} = (\tau - \mu \sigma_n) \cdot \sqrt{\pi a} \qquad \text{Eq. (2.6)}$$

with stress intensity factor K_{II}, shear stress τ, coefficient of friction μ, normal stress σ_n and fracture effective length a. The analysis will only give an estimate of the resulting stress magnification at the fracture tip due to the superimposed shear loads. As a deformation zone is mostly made up of non persistent fractures, the strain accumulation at the deformation zone tip is overestimated and the analysis may be conservative.

Figure 2.47 shows that the resulting K_{II} values for the deformation zones for varying values of μ and the three present-day stress field models by SKB (#1 to #3) are negative (e.g. stable conditions), except for deformation zone ZFMA2. The resulting K_{II} values for the deformation zones for varying values of μ and the stress model according to Backers et al. (2014a, SSM Technical Note 2014:10) are shown in Figure 2.48. If the stress intensity K_{II} is positive, it is assumed that deformation zones will extend. This is the case for frictional coefficients $\mu < 0.7$ for deformation zones ZFMA2, ZFMWNW0123, and ZFMWNW0809A only.

The extension of zone ZFMA2 would not affect the repository. ZFMWNW0123 terminates against ZFMENE0060A and hence is confined in an arrester position. This configuration will be further discussed in Sec. 5.3.4. ZFMWNW0809A is at the North-East boundary of the repository and may only propagate away from the repository.

For $\mu = 0.7$, none of the deformation zones around the repository at Forsmark is predicted to grow. This coefficient of friction is reported by SKB for the 500 m level of the repository. As today all deformation zones appear to be stable, a coefficient of friction 0.7 seems an appropriate prerequisite for the analysis.

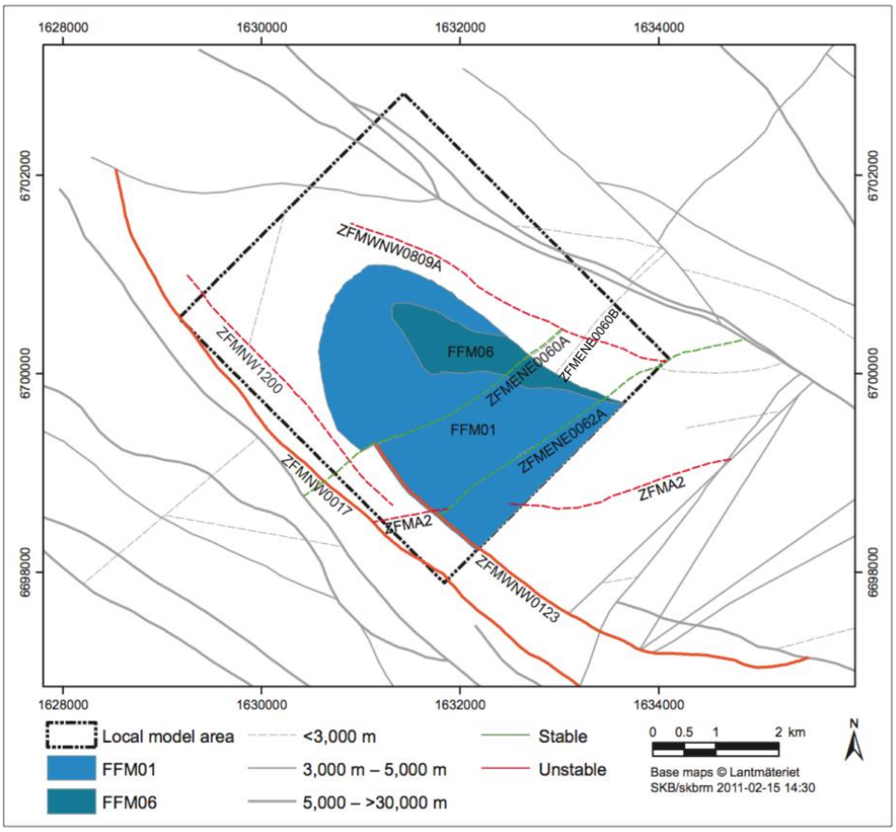

Figure 2.46. Deformation zones in the vicinity of the repository. The labeled deformation zones are analysed in terms of growth with exception of the deformation zone ZFMNW0017 (modified after SKB TR-11-01, Figure 10-118).

In the subsequent chapters the Authors will utilise this type of analysis to analyse the potential growth of those specific deformation zones and stress conditions that occur during the long-term evolution of the repository. An estimation of the length of the potential deformation zone extension is not possible as there is today no sound methodology available for such an analysis.

Limitations of the method

When interpreting the results of this analysis, the reader should bear in mind that the method has some limitations:

- the concept of stress intensity is used in Fracture Mechanics to calculate the growth potential for planar fractures, and applying it to deformation zones violates some basic assumptions;

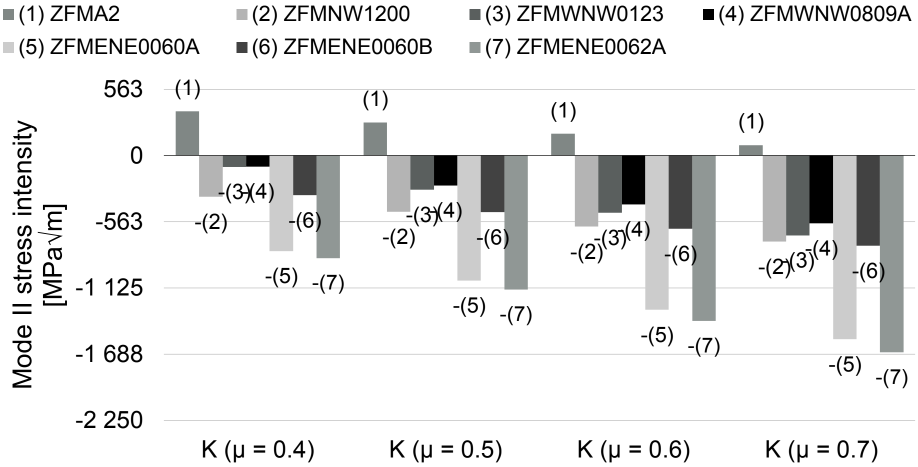

Figure 2.47. K_{II} values for selected deformation zones. Positive values indicate growth. Background stresses are as in the #1 to #3 SKB stress models at 500 m depth. The orientation and length of the deformation zones is taken from Stephens et al. (2007, SKB R-07-45).

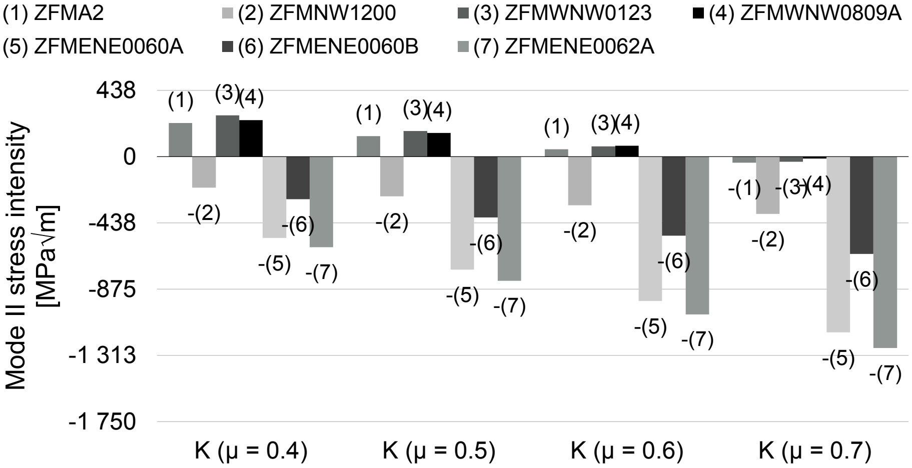

Figure 2.48. K_{II} values for selected deformation zones. Positive values indicate growth. Background stresses are as in the #4 geomecon stress field at 500 m depth. The orientation and length of the deformation zones is taken from Stephens et al. (2007, SKB R-07-45).

- the K_{II} value is calculated for seven deformation zones around the repository as described above. Only one of them (ZFMA2) is a gently dipping deformation zone. For many loading scenarios, especially using SKB's stress models, this is the only deformation zone with growth potential; the figures show that the other six zones would be stable. This should not be mistaken as an indicator for the general tendency towards stable conditions;
- the K_{II} value is calculated for average strike and dip of the deformation zone. Variations are not considered;
- the results represent the growth potential at 500 m depth only.

2.3.4. Estimation of potential earthquake magnitudes

The magnitudes of potential earthquakes on deformation zones at Forsmark have been estimated by SKB following the earthquake scaling relations by Wells and Coppersmith (1994). Table A3.1 in this report shows the maximum estimates by SKB (SKB TR-01-11, Table 10-15) compared to the estimations on the basis of alternative literature consulted by the Authors. SKB estimates are available for deformation zones with trace lengths exceeding 3 km, intermediate to high confidence of existence, and within a circle of 5 km radius centred at Forsmark (cf. Figure 10-117, SKB TR-11-01). The SKB estimates were calculated following Wells and Coppersmith (1994) who provide a correlation of surface rupture length (SRL) with moment magnitude *M* based on 77 seismic events in the magnitude range between 5.1 and 8.1:

$$M = 5.08 + 1.16\, log(SRL) \qquad \text{Eq. (2.7)}$$

Using this equation with the total length of the deformation zone taken as surface rupture length is conservative in the sense that fault segmentation is neglected. The whole deformation zone is assumed to rupture, while in natural cases, faults are often segmented by discontinuities (e.g. step-overs) with each segment reaching its own characteristic magnitude.

The term maximum magnitude, however, is slightly misleading. The estimated magnitudes are in fact mean magnitudes for full fault rupture, and actual magnitudes are normally distributed around the mean (Leonard, 2010). The standard deviation given by Wells and Coppersmith (1994) for their regression database (Eq. 2.7) is 0.28. Therefore, the actual maximum magnitude may be expected to be larger.

On the largest deformation zone, the Forsmark regional deformation zone with 70 km trace length for example, the mean magnitude for full fault rupture estimated after Wells and Coppersmith (1994) is M7.2. The upper limit of the 95% confidence interval lies at M7.8, meaning that 95% of earthquakes can have a magnitude between M6.7 and M7.8. 2.5% of earthquakes can have a magnitude larger than M7.8, assuming that the earthquakes are normally distributed.

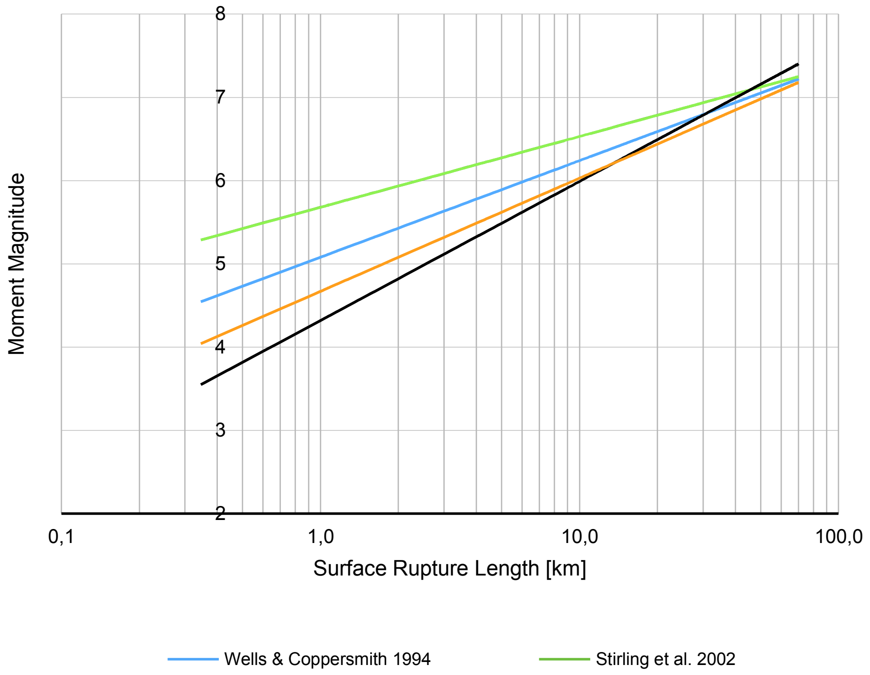

Figure 2.49. Scaling of moment magnitude with surface rupture length according to different authors' databases in the literature.

The regression by Wells and Coppersmith is based on a dataset including interplate and intraplate earthquakes. According to Leonard (2010), the most accepted relation for scaling magnitude and length for stable continental regions (SCR) is that of Johnston (1994), which gives the same or slightly smaller magnitudes than above. However, it is based on only 10 to 12 earthquakes and is therefore not well constrained. Leonard (2010) divides available data in interplate and intraplate earthquakes and proposes a scaling relation for stable continental regions that reaches a larger magnitude for the Forsmark deformation zone, but smaller estimates for the large majority of smaller deformation zones. Moment magnitude estimation following Leonard (2010) reaches M7.4 for full fault rupture of the Forsmark deformation zone (Figure 2.49, Table A3.1).

The three deformation zones that are prone to propagation with an assumed frictional coefficient of 0.6 and lower (ZFMA2, ZFMWNW0123, ZFMWNW0809A, see Sec. 2.3.3) can host earthquakes of magnitudes between M5.7 and M5.9 according to SKB (cf. Table A3.1).

2.3.5. Analysis of the repository as a plane of weakness

By carrying out the same analysis applied to fracture zones to the repository plane, the pole plots consistently show zero *rp* for a plane that is perfectly horizontal. This is valid for all stress models throughout the loading scenarios, since the horizontal plane is aligned parallel to the horizontal stresses and perpendicular to the vertical stress, in theory no shear stresses can develop on that plane. However, should the principal stresses deviate from the horizontal and vertical planes, the reactivation potential will increase with the angle of deviation. The #2 Reverse stress field is the most critical in this regard because *rp* values of more than 0.7 would be reached for a deviation angle between SH and the horizontal plane of about 15° for present-day stresses. During periods of ice retreat (time T2 and T5) this value is reached with an angle of only 10° in this stress field. For all other stress fields the critical angle is larger or, in the case of SKB models at 500 m, equal to 10°.

It is interesting to observe how good the orientation of the principal stress tensor is known. Most discussions about the orientation concern the azimuth of horizontal stresses, but rarely the possible deviation from the horizontal plane. Comprehensive analyses of stress measurements (e.g. Sjöberg et al 2005, SKB R-05-35; Martin 2007, SKB R-07-26) just generally state that the assumption of a principal stress field within the vertical and horizontal planes is reasonable. Ask et al. (2007, SKB P-07-234) report that the vertical direction is a principal direction and that the vertical stress is closely reflected by the theoretical weight of the overburden rock mass.

The largest uncertainty in assessing the risk that the repository itself acts as a plane of weakness with this method is associated with the strength and the equivalent friction angle that has to be assigned to the repository. Such an analysis can, however, not account for the fact that some of the rock volume has been replaced with softer materials and, therefore, the repository should be seen as a volume with soft inclusions.

2.4. The Consultants' assessment on the stability of the structural inventory

The analysis of the reactivation potential for deformation zones cannot deliver a prediction of the probability that the deformation zones get activated, but it can indicate which deformation zones or parts thereof might be or might become most critical. As the critical strength parameters of the deformation zones μ (friction coefficient) are not known, and cannot be determined, any detailed prediction is impossible.

At present-day stress conditions, the deformation zones are stable and show no large deformations or detected seismicity. Any changes in stress, and here in particular increase of differential stress on deformation zones, might cause slip. However, the necessary amount of stress change is not known, and hence it can only be discussed if deformation zones might slip, and what implications this might have.

The stress field models by SKB #1 to #3 and the alternative model #4 by geomecon give at the same time some similar but also quite different indications of reactivation potential for the different deformation zones depending on depth and loading scenario. For present-day conditions:

- the steeply dipping deformation zones striking NW-SE are considered stable in all stress model conditions;
- stress model #3, the extrapolation of Martin's (2007, SKB R-07-26) gradients to large depth, predicts stable conditions for all deformation zones at depth below the repository;
- for stress model #2 (SKB), the regional deformation zones show low stability at all depth;

- the gently dipping deformation zones show highest reactivation potential at shallow depth.

During glaciation the alterations of stress at repository level produce:

- a large potential for activation of shallow dipping deformation zones during ice retreat (post-glacial at time T2 and T5),
- a large potential for activation of steeply dipping deformation zones during forebulge periods, especially for zones that strike NW;
- a stabilising effect for all deformation zones during maximum ice cover periods.

From this analysis, the critical deformation zones could be identified for further analysis and may help to better interpret numerical simulation results.
In addition, this analysis clearly shows that a good understanding of the stress field is essential for any mechanical analysis of geological system behaviour.

It has also been shown, that the earthquake magnitudes estimated by SKB are in agreement with newer publications for scaling relations that apply for the specific tectonic environment at Forsmark (e.g. stable continental regions). SKB’s estimated magnitudes for local major deformation zones with trace length up to 10 km can be considered conservative compared to alternative scaling relations. The estimated “maximum” magnitudes inferred by SKB are actually mean values of the magnitudes for full fault rupture that can be exceeded by single events due to uncertainties associated with the scaling relation.

For all the stress fields, the critical dip angle over which the reactivation potential of a plane gently dipping towards SH across the repository becomes larger than 0.7 is at minimum equal to 10°. This has implications for the tolerable uncertainties of the dip angle of the in situ horizontal principal stresses.

3. Influence of heating on deformation zone stability and growth

3.1. SKB's presentation

The stability of fractures during thermally induced stresses has been evaluated by SKB by means of factor of safety *FoS* (Hökmark et al. 2010, SKB TR-10-23). The findings can also give insights on deformation zone stability if it is considered that reported fracture strengths are somewhat higher than the strength of deformation zones. The extension of the regions with *FoS* > 1 in Figure 3.1 is therefore slightly overerestimated for deformation zones.

3.2. Motivation of the assessment on heating and its influence on deformation zone stability

The thermal effects on the stability of deformation zones have not been directly addressed by SKB. The Consultants assessment consists in analysing the impact by means of numerical modelling and reactivation potential analysis (see Section 2.3.2 for details on the methods). Thereby the stability of specific deformation zones in the vicinity of the repository is examined and visualised.

3.3. Independent analyses on heating and its influence on deformation zone stability

3.3.1. Thermal model

In order to assess the thermally induced stresses and their effect on deformation zones a simplified model of the geological setting at Forsmark was set up and analysed. The FEM software COMSOL Multiphysics was used to evaluate the thermal effects on the proposed repository. COMSOL Multiphysics is well established in Earth Science related academia and industry (e.g. Freeman et al., 2008). The software package is capable of coupling thermo-hydro-mechanical processes, which are expected to affect the repository.

A basic numerical model was set up to calculate the stress changes due to the thermal evolution of the repository and later to study the effect of earthquakes on secondary movements on deformation zones around the repository. The basic geometry of the model is shown in Figures 3.2 and 3.3. For model details, boundary conditions and material parameters, please refer to Appendix 2. The simulations include the initial stress assumptions, but also the long-term thermal evolution due to heating of the spent nuclear fuel canisters and response of the in situ stresses.

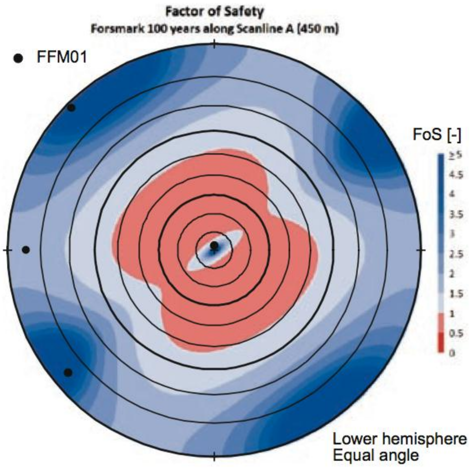

Figure 3.1. Pole plot showing the factor of safety (*FoS*) for planes with $\mu = 0.72$ under peak thermally induced stresses and in most critical regions of the repository (from SKB TR-10-23, Figure 6-25). The background stress field is SKB's most likely stress field from Martin (2007, SKB R-07-26).

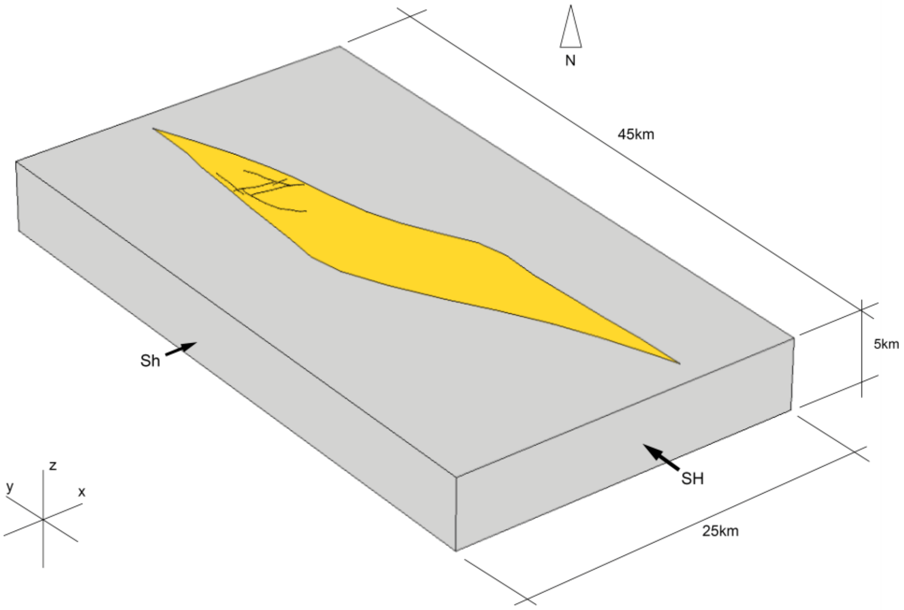

Figure 3.2. COMSOL model set-up with the Forsmark tectonic lens embedded in a rectangular box with its longest axis pointing NW-SE. Black lines within the lens represent the deformation zones in the vicinity of the repository. (See also Figure 3.3).

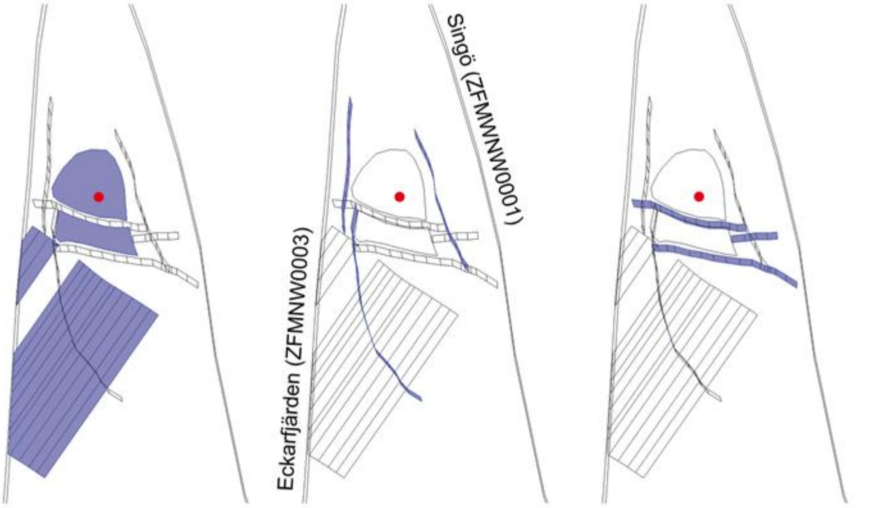

Figure 3.3. View from top of the COMSOL model showing the Forsmark tectonic lens between the regional deformation zones Eckafjärden on the left (ZFMNW0003) and Singö on the right (ZFMWNW0001). (Left picture) Horizontal repository plane and zone ZFMA2 that is divided into a small patch named ZFMA2a, and a larger patch named ZFMA2. (Middle picture) from left to right: zone ZFMNW1200, ZFMWNW0123, ZFMWNW0809A. (Right picture) from top to bottom: zone ZFMENE0060A, ZFMENE0060B, and ZFMENE0062A (cf. Figures 2.5 and 2.6). The red point marks the intersection of the the repository plane with a vertical monitoring line. The gently dipping deformation zone ZFMA2 extends from a depth of 300 m down to a depth of 2200 m.

The temperature field within the model is adjusted to fit the initial measured temperature at repository depth of 11.5°C (Sundberg et al., 2008, SKB R-08-65) with an initial gradient of 13°C/km down to 500 m depth and 13.2°C/km for depths beneath based on Figure 3.4. The upper and lower model boundary have a fixed temperature of 5°C and 78°C, respectively. The outer boundaries follow the temperature gradient of the model. The repository itself features a time-dependent temperature function which is described in the following.

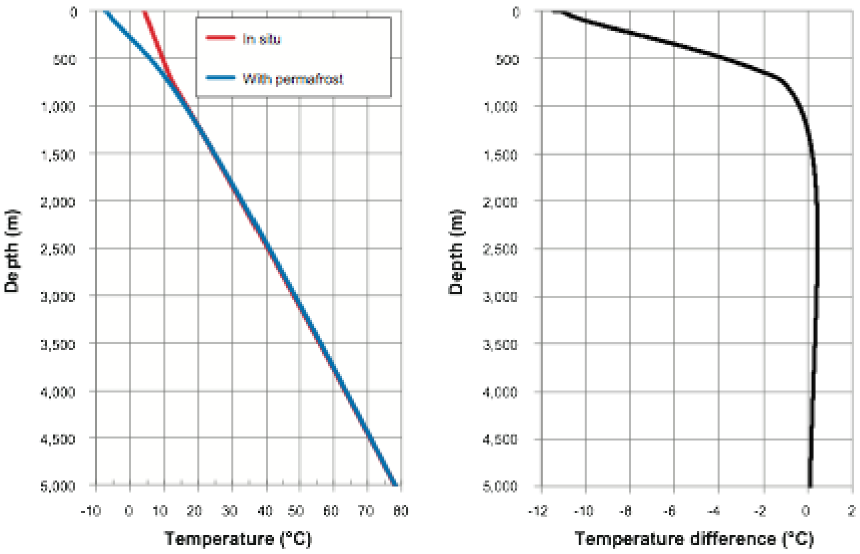

Figure 3.4. Temperature data taken from Hökmark et al. (2010, SKB TR-10-23, Fig. 4-14).

The change in temperature is causing the rock mass to expand or contract, which is controlled by the thermally induced strain, ε_{th}, given by:

$$\varepsilon_{th} = \alpha_{th}(T - T_{ref}) \quad \text{Eq. (3.1)}$$

where α_{th} is the thermal expansion coefficient, T is the temperature and T_{ref} is the strain-free reference temperature. The temperature field induced by the repository at 500 m depth is modelled according to Figure 3.5 with an assigned time-dependent temperature function as given by Hökmark et al. (2010, SKB TR-10-23, see Figure 3.6). Simultaneous heating of the repository is assumed, opposed to sequential heating during operation of the facility.

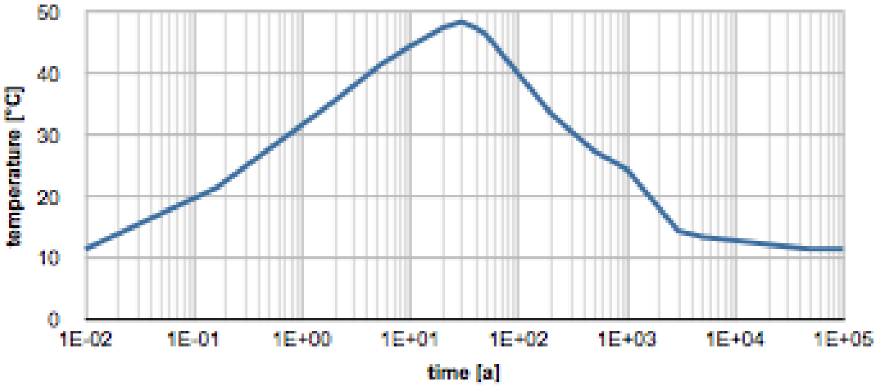

Figure 3.5. Temperature increase of the repository panels versus time as modelled in this study.

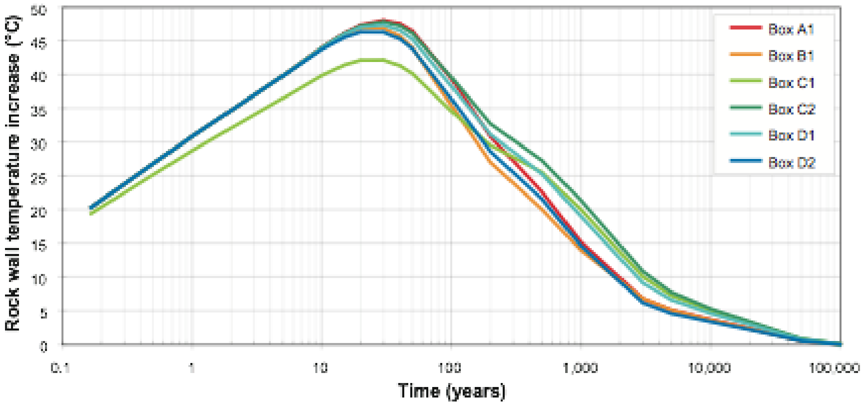

Figure 3.6. Rock wall temperature increase with time as simulated by Hökmark et al. (2010, SKB TR-10-23, Figure 5-14).

3.3.2. Results of the thermal analyses

Along a vertical monitoring line passing through the centre of the repository (cf. Figure 3.3), the stress field changes during the thermal phase are monitored in direction of Sh, SH and SV (Figure 3.7). At peak temperature of about 60°C, the horizontal stresses increase by approximately 20 MPa. Since the upper boundary is free to move, the thermally induced strain changes do not cause a significant increase in vertical stress. The fixed temperature condition at the upper boundary causes a steep temperature gradient from the repository to the surface.

In general, the temperature increase causes an expansion of the rock mass with displacement vectors normal to the temperature isosurfaces. Depending on the orientation of the deformation zones around and within the repository the stability is either increased or decreased. Figures 3.8 shows a contour of 1°C temperature increase from the initial conditions during the thermal phase for selected parts of the repository volume together with the zones ZFMWNW0809A, ZFMENE0060A, and ZFMNW1200.

In particular, deformation zones with strike parallel to the repository outline show an increase of normal stress while the shear stress remains constant. Deformation zones striking with an angle with respect to the contour of the repository feature an increase in shear stresses. Consequently, the *rp* reduces slightly for deformation zones which are directly close to the repository and increases slightly for zones at an angle to the repository edge farther away, e.g. the tip of zone ZFMWNW0809A.

Changes in *rp* are small and localised on small areas of the deformation zones. An exception is ZFMA2, which is not oriented perpendicular to the thermally induced stresses and therefore shows an increase of reactivation potential during heating. Hence, the following explanations relate to the western part of ZFMA2. Note that at the ground surface, the trace of deformation zone ZFMA2 is mapped continuously whereas at repository depth it is divided in two segments. The smaller segment to the West is named ZFMA2a in the following.

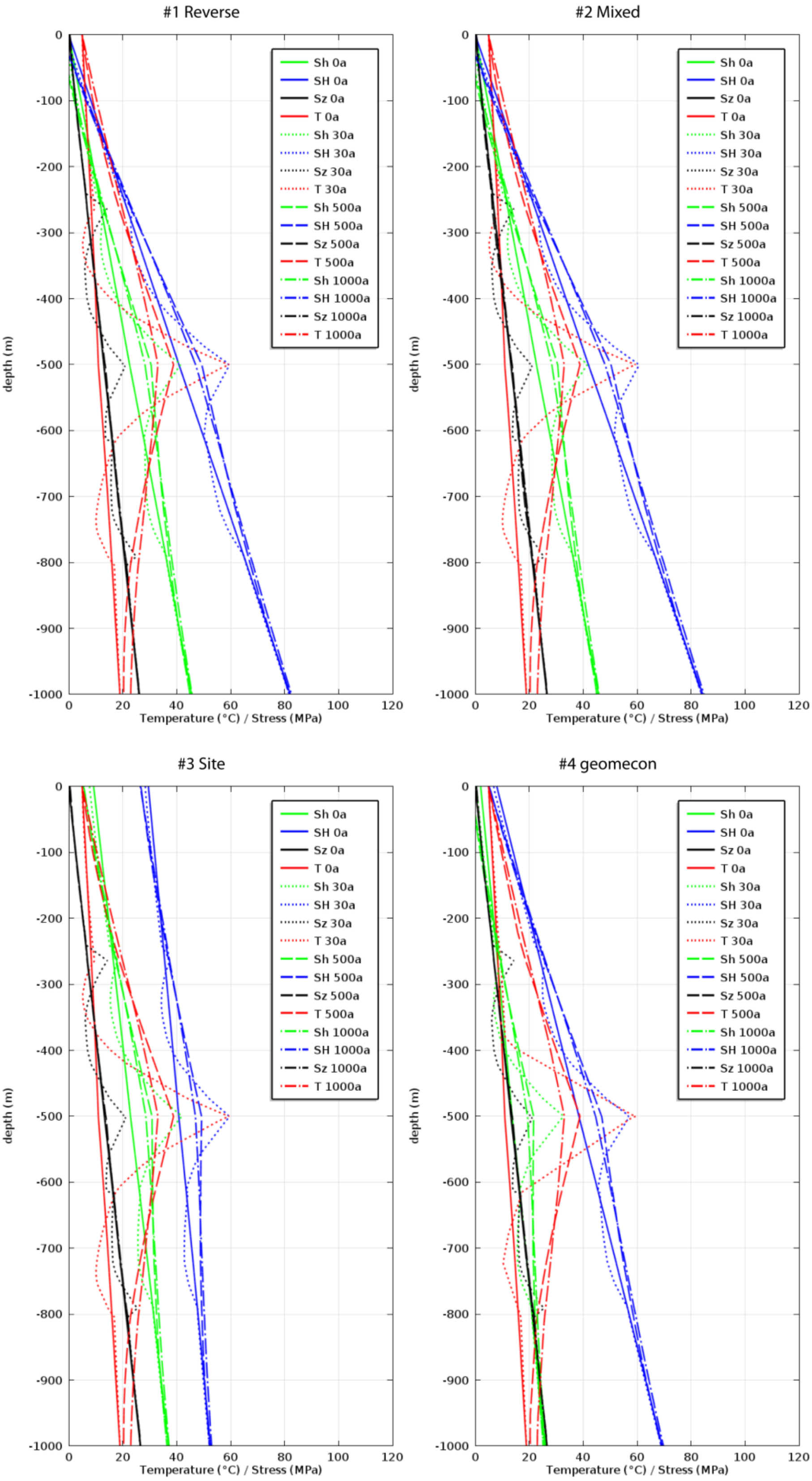

Figure 3.7. Change in stress along a vertical monitoring line through the repository centre at different times for the different stress models.

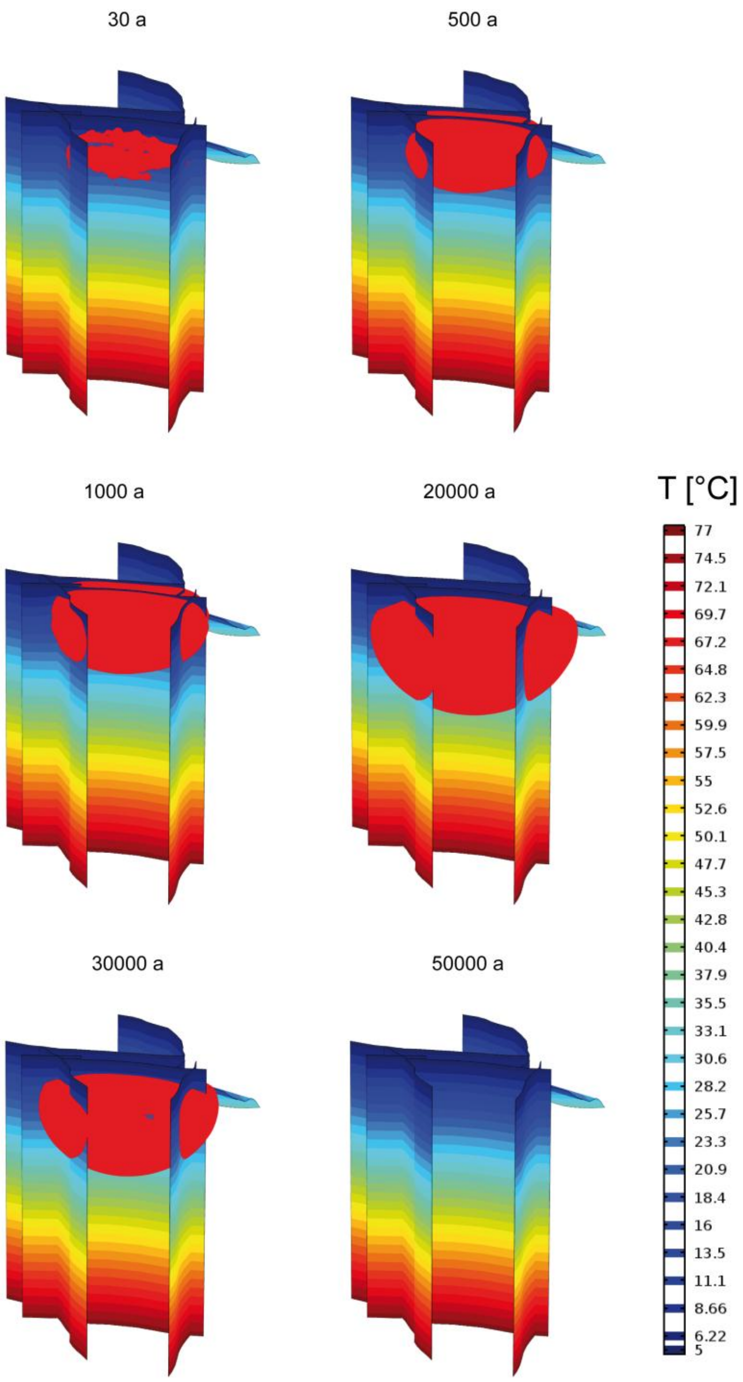

Figure 3.8. The red cloud at repository level shows the volume that has +1°C temperature increase compared to the initial state at different points in time.

#1 Reverse stress field

For the #1 Reverse stress field the evolution of *rp* during the thermal phase is shown in Figure 3.9 and 3.10. The shallow dipping deformation zone ZFMA2a shows an average *rp* of up to 0.74, and a maximum *rp* of 0.91. During the thermal phase, the part of the deformation zone close to the repository is affected the most by the thermally induced stress changes. Figure 3.10 and A2.7 show an initial *rp* distribution resulting from the background stresses with an average value of 0.72, which can be compared with Figure 3.9. Note that the maximum *rp* values in the figures might be higher for the top-views since the regional deformation zones are partly included there.

#2 Mixed stress field

Since the #2 Mixed stress field corresponds to the #1 Reverse stress field within the first 1,000 m, and temperature effects are negligible for depth below 1,000 m, the *rp* is the same as for the #1 Reverse stress field. Hence, similar observations of *rp* are made for ZFMA2a and are not repeated here.

#3 Site stress field

The evolution of *rp* is shown in Figure 3.11 and 3.12. The #3 Site stress field shows the lowest average *rp* among the simulated stress fields. The shallow dipping deformation zone ZFMA2a shows an average *rp* of up to 0.56 and a maximum *rp* of 0.88. Relatively low *rp* values of about 0.6 are observed for the steeply dipping deformation zones above the repository level within the tectonic lens, and decrease with depth.

#4 geomecon stress field

The evolution of *rp* is shown in Figure 3.13 and 3.14. The shallow dipping deformation zone ZFMA2a shows an average *rp* of up to 0.64 and a maximum *rp* of 0.84. The regional deformation zones display a variety of *rp* between 0.2 and 0.75 depending on the strike and depths of the deformation zones. The largest *rp* values are observed in the range between 0 and 3 km depth. Below a depth 3 km, the *rp* reduces slightly.

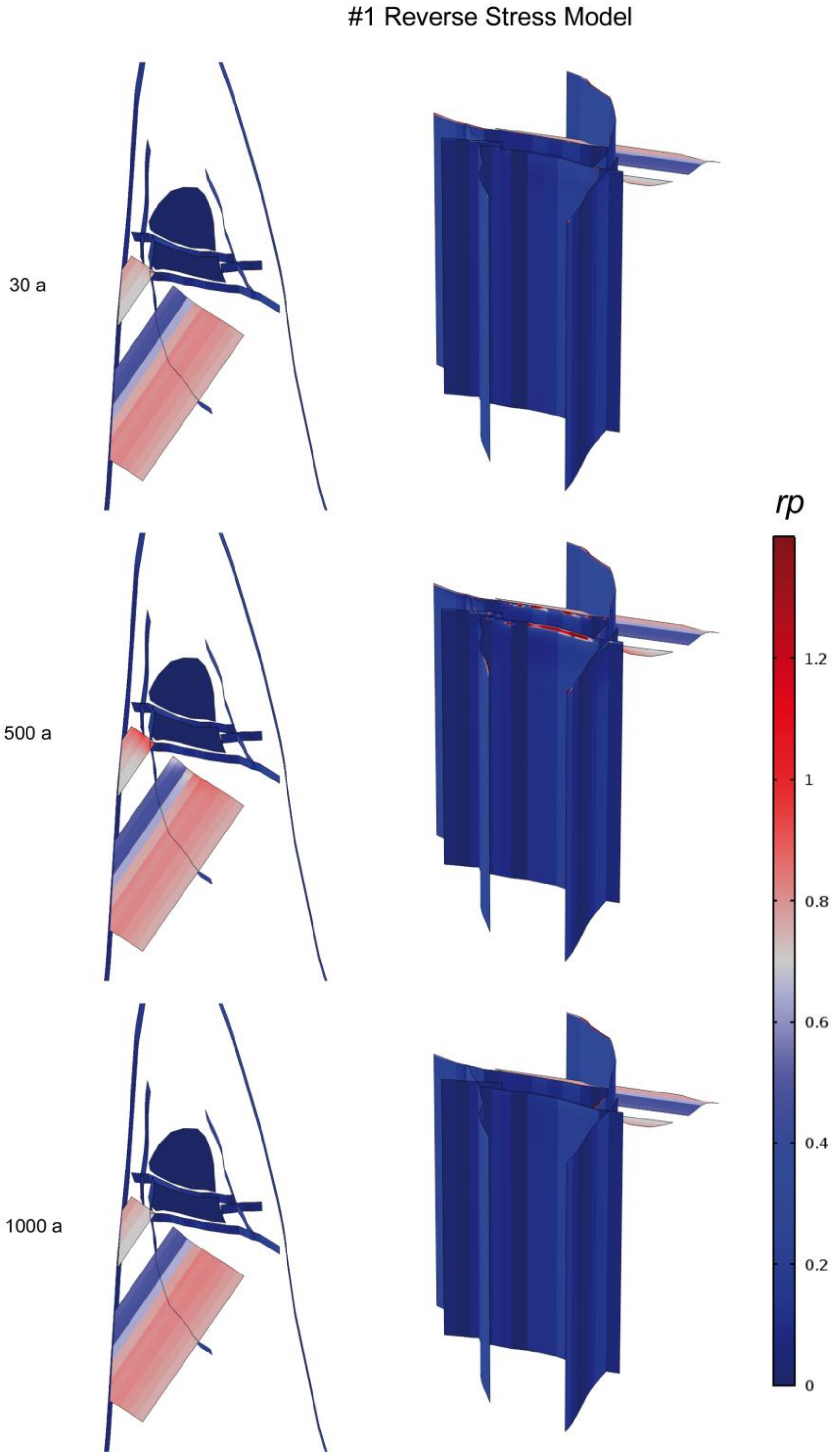

Figure 3.9. Evolution of the *rp* for the #1 Reverse stress model in top view (left column) and view from model north (right column) after (top) 30 years, i.e. at maximum heat, (middle) 500 years, and (bottom) 1000 years, respectively.

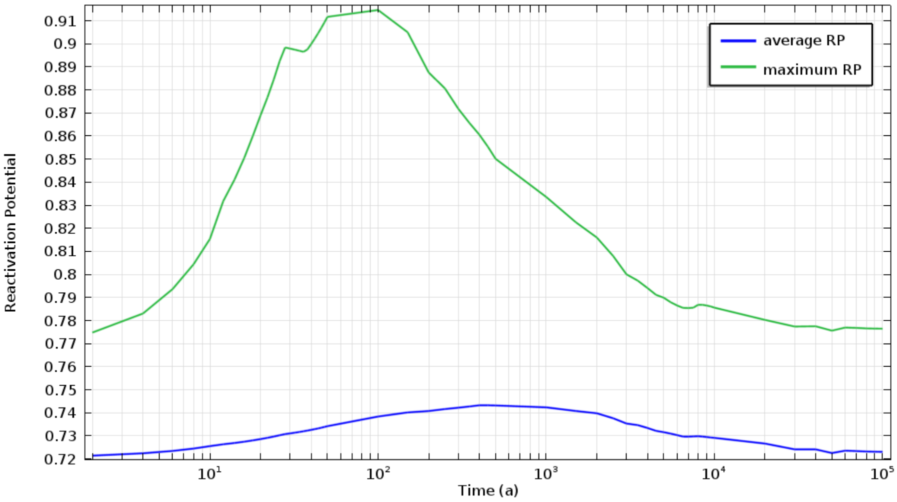

Figure 3.10. Thermally induced changes in maximum and average reactivation potential *rp* versus time for ZFMA2a using the #1 Reverse stress field.

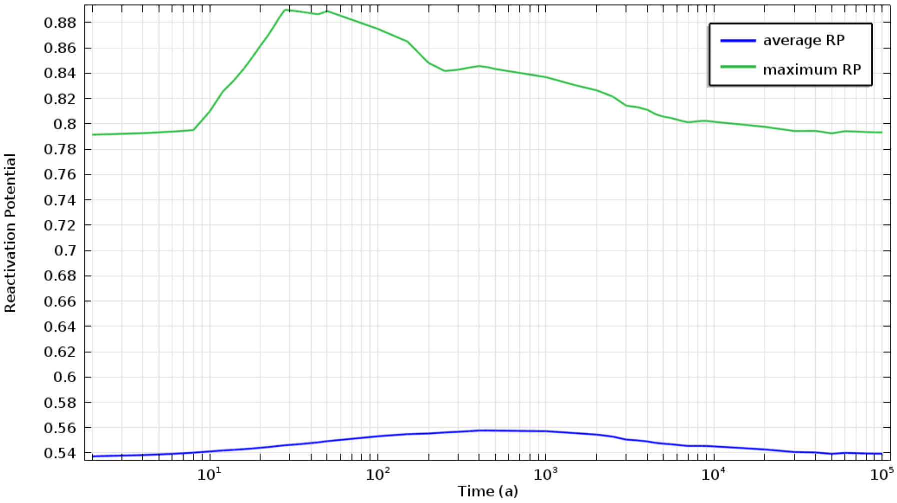

Figure 3.11. Thermally induced changes in maximum and average reactivation potential versus time for ZFMA2a using the #3 Site stress field.

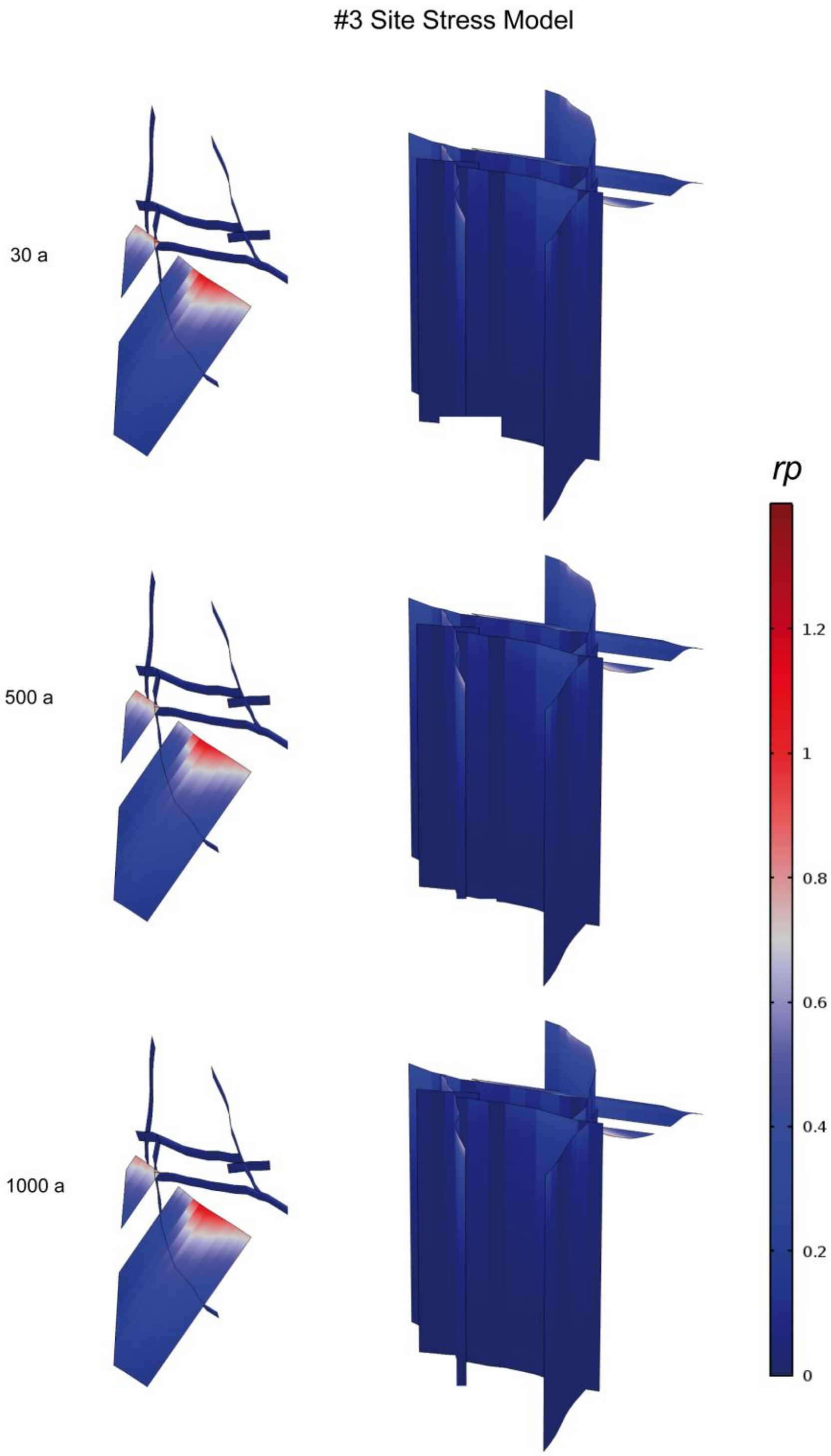

Figure 3.12. Evolution of the *rp* for the #3 Site stress model in top view (left column) and view from model north (right column) after (top) 30 years, i.e. at maximum heat, (middle) 500 years, and (bottom) 1000 years, respectively.

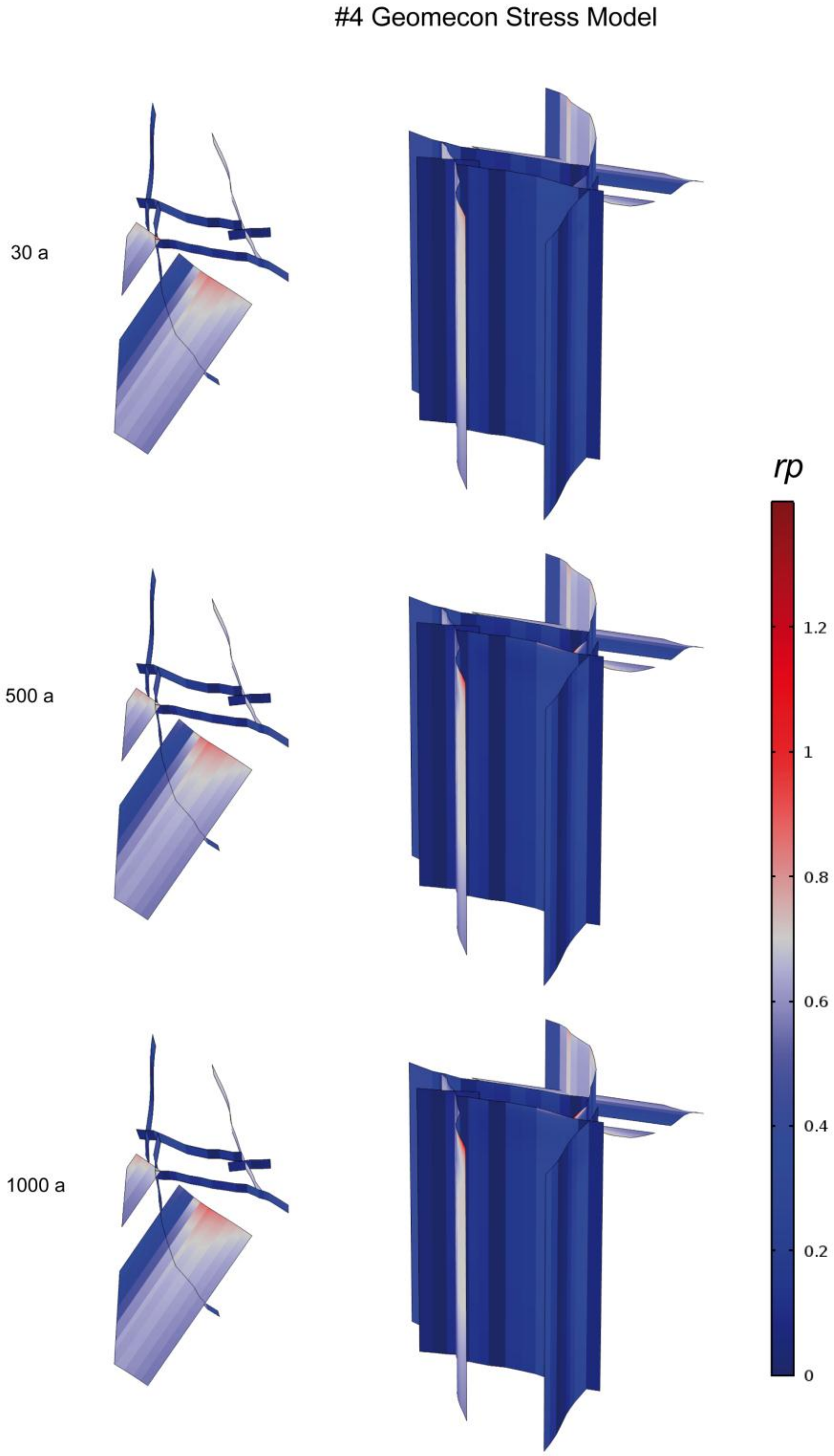

Figure 3.13. Evolution of the *rp* for #4 geomecon stress model in top view (left column) and view from model north (right column) after (top) 30 years, i.e. at maximum heat, (middle) 500 years, and (bottom) 1000 years, i.e. maximum extent, respectively.

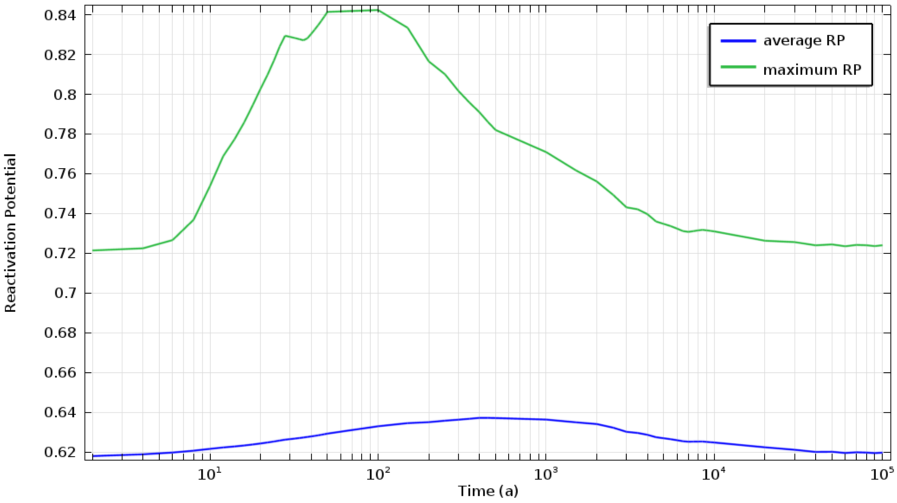

Figure 3.14. Thermally induced changes in maximum and average reactivation potential versus time for ZFMA2a using the #4 geomecon stress field.

3.3.3. Analysis of the potential for deformation zone growth during heating

The analysis of deformation zone growth via the value og the intensity factor K_{II} as in Sec. 2.3.3 shows that, of the selected deformation zones around the repository, only ZFMA2 has potential for growing under peak thermally induced stresses. This is observed for the background stresses according to the #4 geomecon stress model, as well as for the background stresses according to the #1 to #3 SKB models that equal each other at this depth. However, ZFMA2 is truncated towards another gently dipping deformation zone ZFMF1 at its lower edge and towards the ground surface at its upper edge. Any growth of ZFMA2 would therefore be confined to directions along its strike (cf. SKB TR-11-01, Figure 4-12).

Even if the coefficient of friction is as low as 0.4, the vertical deformation zones are not expected to grow in any case.

3.3.4. Analysis of the repository as a plane of weakness

The repository plane consistently shows zero reactivation potential as exemplarily shown in Figure 3.9. This is the result of the assumption that the principal stresses lie in the horizontal and vertical planes, as described in Sec. 2.3.5, and the stress increases due to heatins are mainly restricted to the horizontal stresses.

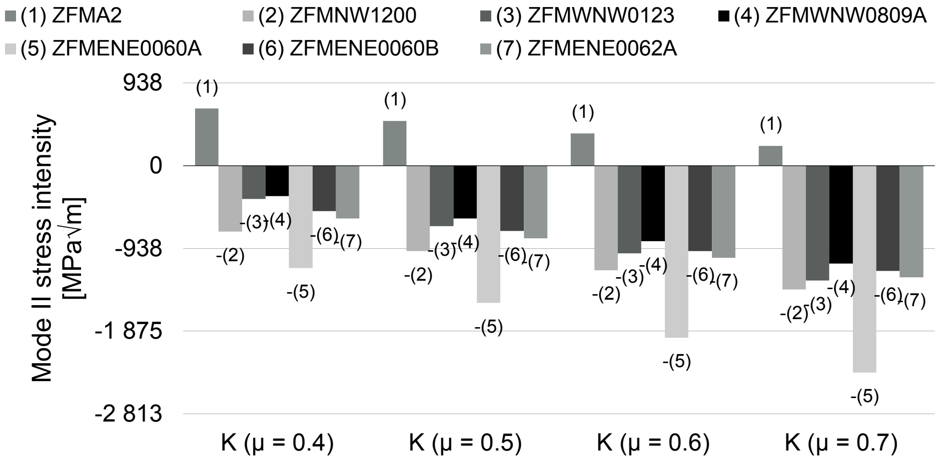

Figure 3.15. K_{II} values for the time of peak thermally induced stresses. Background stresses are as in the #4 geomecon stress model at 500 m depth. Assuming that K_{II} is indicative for growth of deformation zones, it is evident that only the shallow dipping deformation zone ZFMA2 can grow.

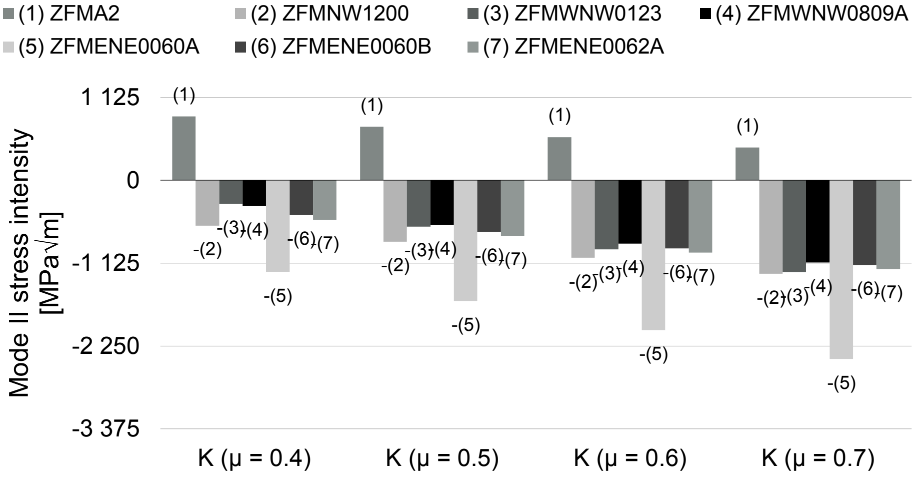

Figure 3.16. K_{II} values for the time of peak thermally induced stresses. Background stresses are as in the #1 to #3 SKB stress models at 500 m depth. Assuming that K_{II} is indicative for growth of deformation zones, it is evident that only the shallow dipping deformation zone ZFMA2 can grow.

3.4. The Consultants' assessment on the influence of heating on deformation zone stability and growth

The thermal phase of the repository leads to a stress increase mainly restricted to the horizontal stresses. The maximum reactivation potential increases during heating by 0.35 to values above 1.1. The average *rp* for ZFMA2a increases by 0.05 for all modelled stress fields during heating. The following can be observed regarding the stability of deformation zones:

- Subvertical deformation zones parallel to the repository contour are stabilised during the thermal phase. This is the case for the largest part of the modelled deformation zones and the present repository layout;
- Subvertical deformation zones striking at an angle to the repository contour may become less stable during the thermal phase. This affects minor areas of the deformation zones. Zone ZFMWNW0809A, for example, shows slightly increased *rp* with maximum values of 0.75 compared to the initial 0.61;
- Shallow dipping deformation zones show increased *rp*, e.g. ZFMA2 reaches maximum values of about 1.15 in some areas and an average value of 0,74. The model predicts that the most critical areas are located on ZFMA2a around 500 m depth. This effect is observed for all stress field models. For the #2 Mixed model, however, the effect is not as pronounced as for the other models;
- The thermally induced stresses might lead to growth of ZFMA2. However, SKB reports the termination of zone ZFMA2 against zone ZFMF1 that would prevent any growth of ZFMA2 towards greater depths.

4. Influence of the glacial cycle on deformation zone stability and growth

4.1. SKB's presentation

An evaluation of deformation zone stability during the glacial cycle has been presented in the SKB report by Fälth et al. (2010, SKB TR-08-11) as already briefly described in Section 2.1.3. The range of the Coulomb Failure Stress *CFS* values and their distribution is shown in Figures 4.1 and 4.2 for the #1 Reverse and #2 Mixed stress field models. Fälth et al. (2010, SKB TR-08-11) consider an additional stress model, the #3 Site stress model, but the results are either the same as for the other two (for 500 m) or not relevant due to unrealistic stress magnitudes and ratios at depth. The *CFS* is calculated with the glacially induced stresses added to the respective background stresses. Additionally, a "worst case scenario" is considered where the differential stress is increased by arbitrarily adding 5 MPa to the maximum horizontal stress. The minimum horizontal stress is increased proportionally. Pore pressures in excess of the hydrostatic pore pressure are added according to: 1 MPa at 500 m depth, 7 MPa at 3,500 m and 10 MPa at 5,500 m, respectively.

Fälth et al. (2010) note that there are large uncertainties concerning the glacial stress additions, the background stresses, the pore pressure evolution and the strength properties of deformation zones during and after the glaciation. However, these uncertainties concern the magnitudes of involved stresses while the stress orientation is rather certain. Therefore, deformation zones that plot in the high stability regions of the pole plots can be considered stable as shown in Figure 2.3. Of all deformation zones that have a trace length larger than 3 km and lie at least within 600 m distance from any canister in the repository, only 2 out of 7 can be considered stable: ZFMENE0060A and ZFMENE0062A.

The long-term safety report (SKB TR-11-01) provides a table with deformation zones located within a 5 km radius centred at Forsmark and exceeding 3 km trace length that are judged to be able to host earthquakes of magnitude M5 or larger (SKB TR-11-01, Table 10-15). The table shows 36 deformation zones with the maximum estimated magnitudes according to Wells and Coppersmith (1994) and with the judgement if they are stable or not in the #2 Mixed stress regime. The same deformation zones are shown in Figure 4.3.

4.2. Motivation of the assessment on the glacial cycle and its influence on deformation zone stability

The analyses by SKB confine themselves to one single point in time, i.e. 11 000 BP, which is stated to be the time of maximum instability during a Weichselian glacial cycle. This point is referring to the ice-retreat after the second and larger glacial peak, T5 in this report.

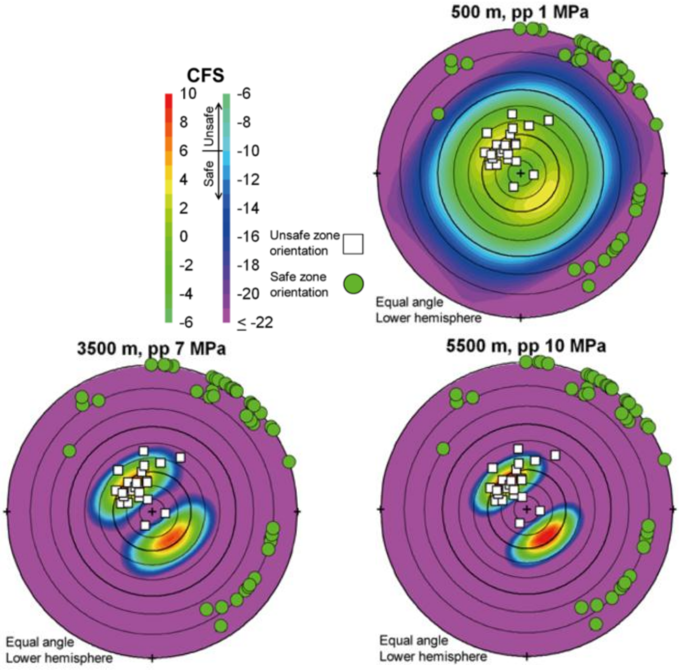

Figure 4.1. Pole plot showing *CFS* contours at three different depths for the time of 11 ka BP (corresponding to the time of the second ice retreat, T5 in this report), with glacial stress increments, excess pore pressure and the background stress field #1 Reverse.

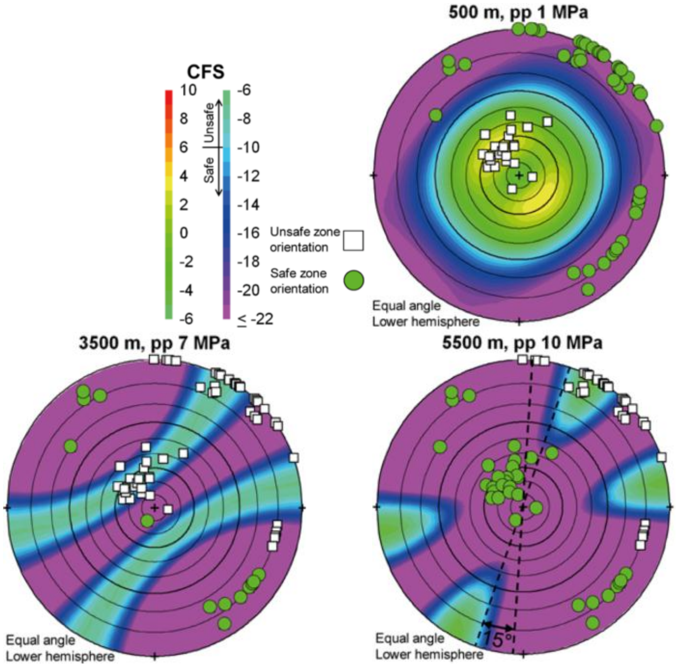

Figure 4.2. Pole plot showing *CFS* contours at three different depths for the time of 11 ka BP (corresponding to the time of the second ice retreat, T5 in this report), with glacial stress increments, excess pore pressure and the background stress field #2 Mixed. The colour code and symbols are the same as in Figure 4.1.

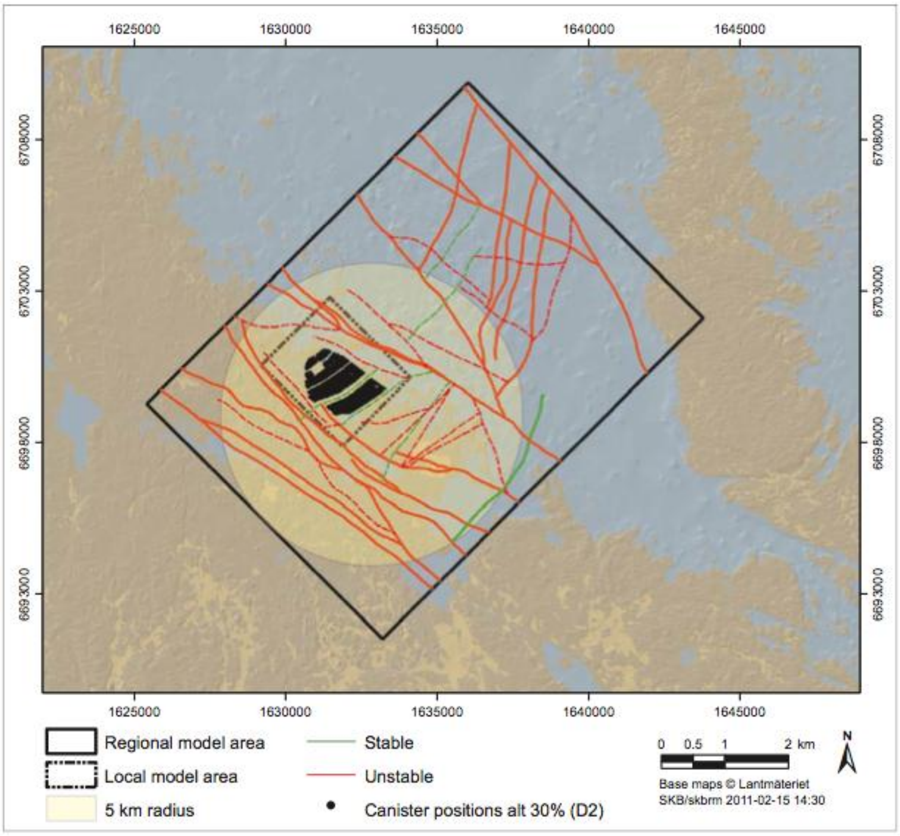

Figure 4.3. Deformation zones at Forsmark classified in terms of stability according to Fälth et al. (2010, SKB TR-08-11; Figure from SKB TR-11-01, Figure 10-117).

As was shown in Chapter 2, the occurrence of maximum instability is not at the same time for different stress regimes. Furthermore, the excess pore pressures assumed by SKB are not explained. They are arbitrarily set to 1 MPa at 500 m, 7 MPa at 3,500 m, 10 MPa at 5,500 m. Although the increase due to the weight of the ice cover should be constant for all depth levels on a first order approximation.

4.3. Independent analyses of glacial cycle and its influence on deformation zone stability

4.3.1. Glaciation model

During glaciation, the load of the ice sheet will induce stress changes which will potentially lead to displacements along deformation zones. SKB's reference ice sheet evolution is derived from the Weichselian ice sheet of Näslund (2006, SKB TR-06-23; Figure 2.11). Lund et al. (2009, SKB TR-09-15) calculated the stress increments during this glacial cycle as in Figure 2.14.

The pore pressure is increased to 50% of a 3 km high water column, corresponding to the maximum ice thickness during glaciation. The increase of the vertical stress directly correlates with the ice sheet thickness. The glacial vertical and horizontal loads are implemented into the numerical COMSOL model by superposing the stress changes onto the initial stress. The mechanical properties of the model are reported in Appendix 2.

4.3.2. Results of the simulations of the glacial cycle

Stress field evolution

Along the vertical monitoring line through the centre of the repository, the stress field changes during the glaciation phase are monitored in direction of Sh, SH and SV (Figure 4.4) for the different stress models by SKB #1 to #3 and geomecon #4.

#1 Reverse stress field model

Since the background stresses usually increase with depth while the stress additions remain constant, the observed effects are larger at shallower depth (Figure 4.6). For the #1 Reverse stress field this is mostly visible for shallow dipping planes since the dominant mode of faulting (reverse) is either promoted or hindered. Figure 4.7 shows the reactivation potential for ZFMA2a, as this deformation zone is most critical in the reverse faulting regime.

T1 - 1st glacial maximum

Vertical deformation zones show constant *rp* with depth that lies below 0.7 (Figure 4.6, top). There are no significant differences of *rp* compared to the initial state. The most critical orientation remains for shallow dipping deformation zones, although with lower *rp* compared to the present-day stress field.

T2 - Ice margin retreating

Compared to the initial state, shallow dipping deformation zones show a significant increase of criticality. The sensitivity to the strike direction of shallow dipping zones as ZFMA2 is illustrated in the Figure 4.6. The criticality should increase towards strike directions perpendicular to SH.

T3 - Stress reductions due to forebulge

For the forebulge period, the criticality is generally not different from the initial state. The forebulge causes a reduction of the minimum horizontal stress. The total differential stress is thus not changed during T3 in this stress field (cf. Chapter 2). The unrealistically high *rp* in the upper 150 m of the model are due to small or negative stresses (cf. Figure 4.6).

T4 - 2nd glacial maximum

During the second glacial maximum, the same observations as for the first glacial maximum (T1) can be made. The stabilising effect of the ice load on shallow dipping planes is even more pronounced, since the stress additions are larger (cf. Table 2.3).

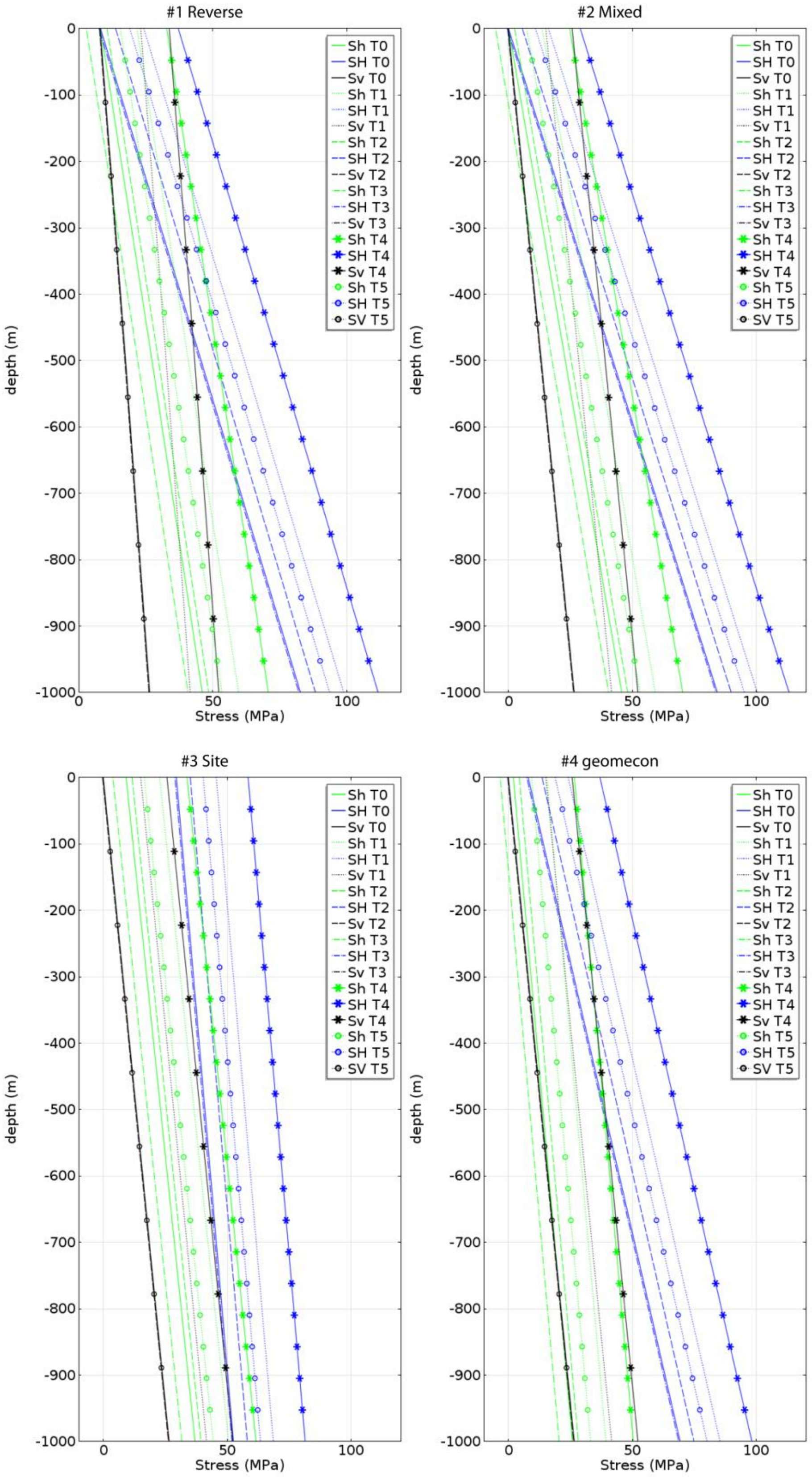

Figure 4.4. Change in stress along a vertical monitoring line through the repository at different times for the four considered stress field models.

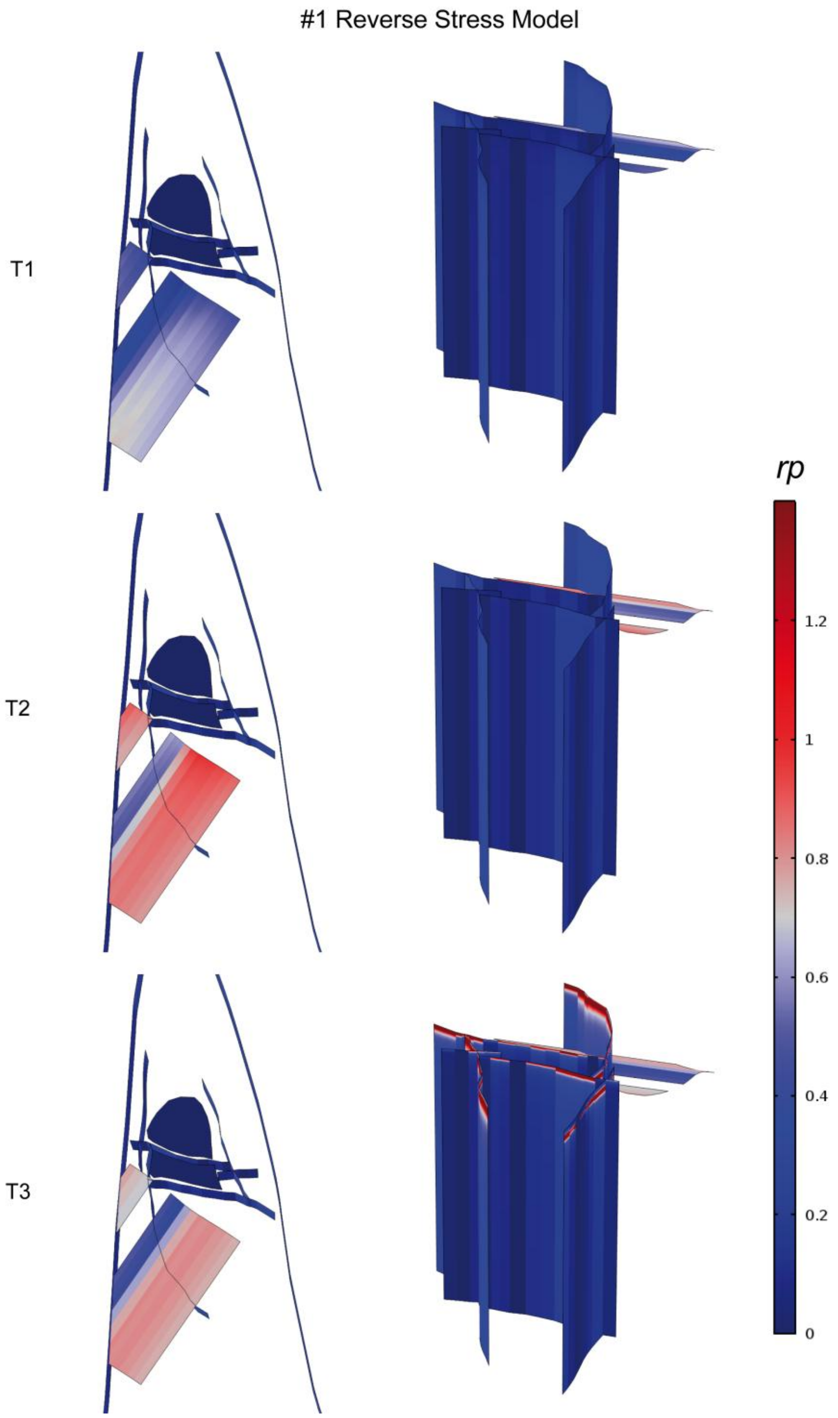

Figure 4.5. Evolution of *rp* for the #1 Reverse stress model in top view (left column) and view from model north (right column) after T1 - 1st glacial maximum, T2 - Ice margin retreating, T3 - Stress reductions due to forebulge, T4 - 2nd glacial maximum, and T5 - Ice margin retreating.

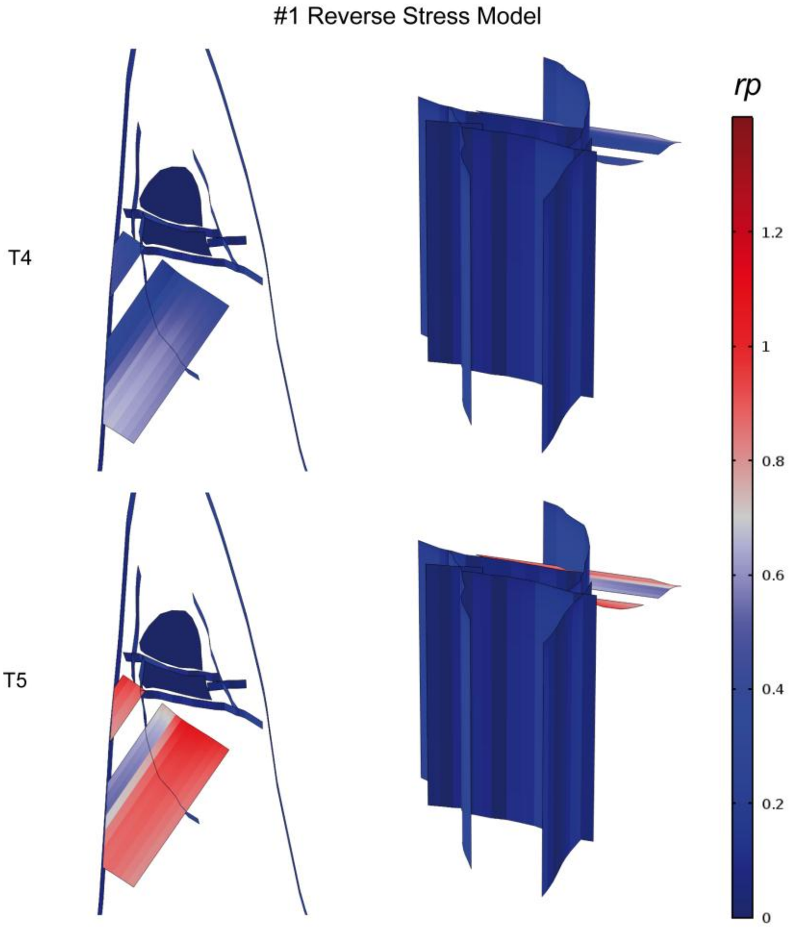

Figure 4.5. (Continued from the previous page.) Evolution of *rp* for the #1 Reverse stress model in top view (left column) and view from model north (right column) after T1 - 1st glacial maximum, T2 - Ice margin retreating, T3 - Stress reductions due to forebulge, T4 - 2nd glacial maximum, and T5 - Ice margin retreating.

T5 - Ice margin retreating

As during T2, the maximum criticality increases during the retreat of the ice margin when only horizontal stresses are increased. This effect is pronounced on shallow dipping planes striking nearly perpendicularly to SH as for ZFMA2, showing that reverse faulting is abetted with maximum *rp* up to 0.99 (Figure 4.6).

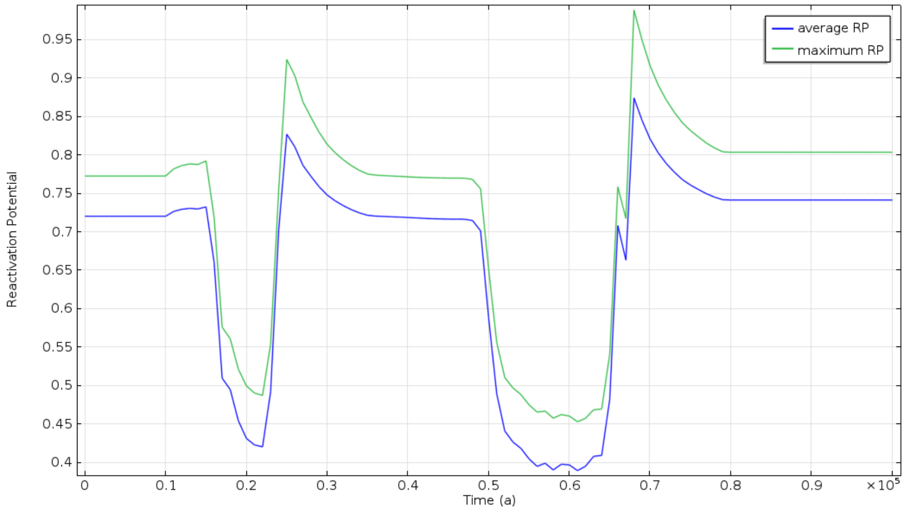

Figure 4.6. Maximum and average reactivation potential *rp* for ZFMA2a during glaciation for the #1 Reverse stress field model and #2 Mixed stress field model.

#2 Mixed stress field model

The shallow dipping deformation zone ZFMA2 is entirely in the upper compartment of the stress field that corresponds to reverse faulting since the regime is changing from reverse faulting to strike-slip at 2,400 m. The *rp* of ZFMA2 is therefore the same as for stress field model #1 and shown in Figure 4.6. The change of the faulting regime with depth is reflected by the sudden increase of *rp* below 2,400 m on vertical planes. The evolution of reactivation potential throughout the glacial cycle is shown in Figure 4.7.

T1 - 1st glacial maximum

The criticality is generally slightly decreased compared to the initial state, on vertical planes as well as on shallow dipping planes. The *rp* reaches values of around 0.8 on ZFMA2 and on vertical planes below 2,400 m.

T2 - Ice margin retreating

After the glacial maximum, the criticality is increased to a value of 0.92 especially on shallow dipping planes in the upper 2,400 m of the model. The changes of *rp* on vertical planes are insignificant.

T3 - Stress reductions due to forebulge

Again, in the first 150 m, the *rp* values shown are high due to very small normal stresses on the deformation zones. Vertical planes in some directions, e.g. as for ZFMWNW0809A and the Singö zone, show increased *rp* below 2400 m with values around 1. There is no effect on shallow dipping planes.

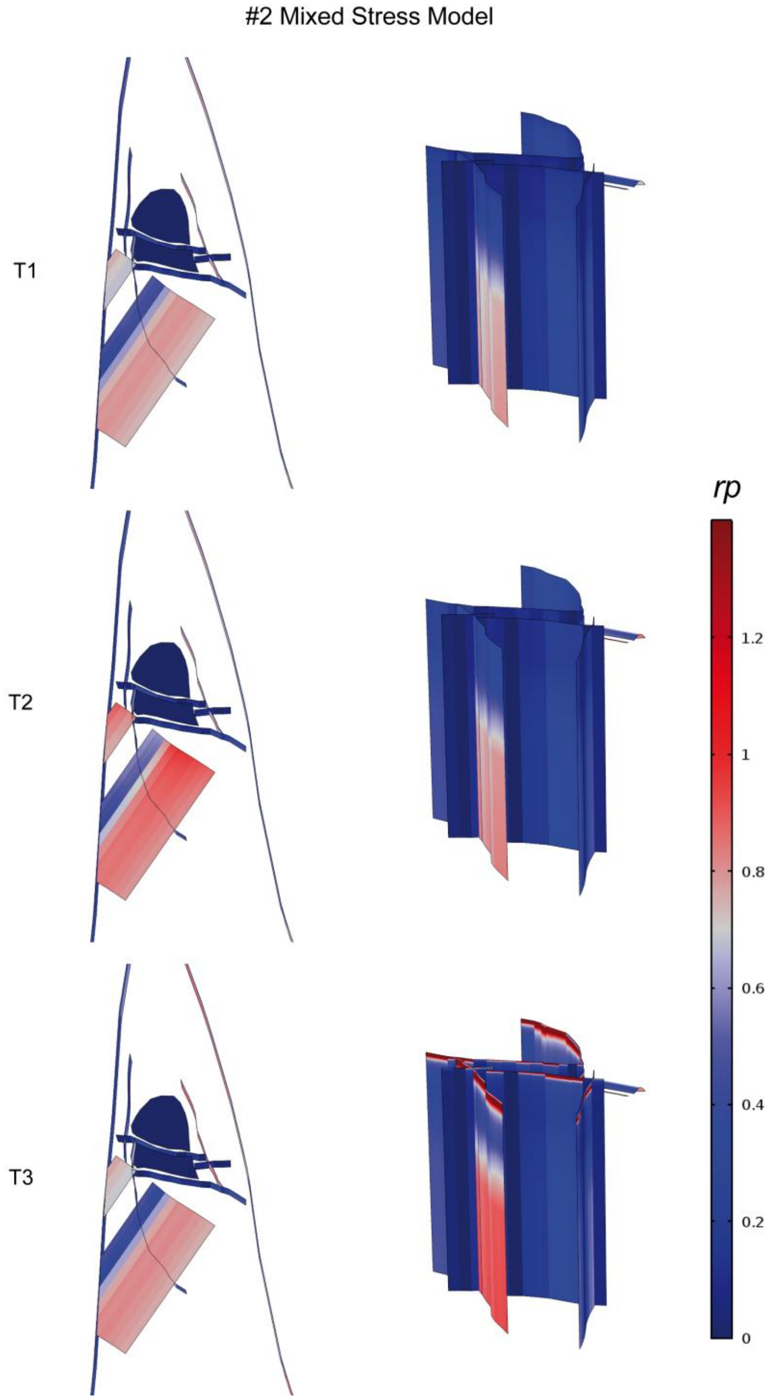

Figure 4.7. Evolution of *rp* for the #2 Mixed stress model in top view (left column) and view from model north (right column) after T1 - 1st glacial maximum, T2 - Ice margin retreating, T3 - Stress reductions due to forebulge, T4 - 2nd glacial maximum, and T5 - Ice margin retreat.

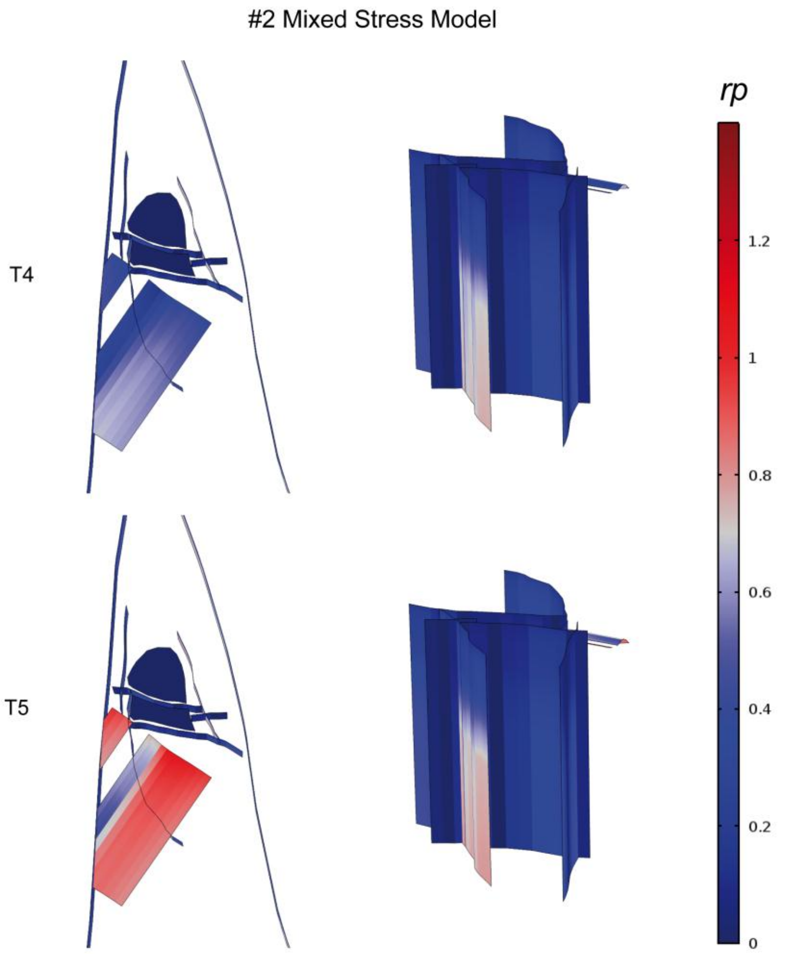

Figure 4.7. (Continued from the previous page.) Evolution of *rp* for the #2 Mixed stress model in top view (left column) and view from model north (right column) after T1 - 1st glacial maximum, T2 - Ice margin retreating, T3 - Stress reductions due to forebulge, T4 - 2nd glacial maximum, and T5 - Ice margin retreating.

T4 - 2nd glacial maximum

Typically for glacial maxima, an increased stability on shallow dipping planes is observed, more pronounced than for the first glacial maximum. The maximum *rp* on ZFMA2 during this stage is 0.65.

T5 - Ice margin retreating

Shallow dipping planes show significantly increased *rp* with values around 1.1 in the highest parts. This represents the increased likelihood of post-glacial deformation zone reactivation via reverse faulting.

#3 Site stress model

The evolution of reactivation potential throughout the glacial cycle for the #3 Site stress model is shown in Figure 4.8. The reactivation potential of ZFMA2a is given in Figure 4.9.

T1 - 1st glacial maximum

Increased stability is shown on shallow dipping planes during the glacial maximum as in the previous models. Mostly, the values of *rp* are well below 0.7.

T2 - Ice margin retreating

There is no significant change of *rp* on vertical planes. It is very low, as in the initial state due to the reverse faulting nature of the stress field in its upper part. Shallow dipping planes however show increased *rp* as visible on ZFMA2 deformation zone of maximum 1.25. The *rp* still rapidly decreases with depth, reflecting converging principal stress magnitudes with depth.

T3 - Stress reductions due to forebulge

There are no significant changes in *rp*. The high *rp* values in the first meters result from horizontal stresses that become very small. The vanishing normal stress acting on the zones produces extremely high *rp* values.

T4 - 2nd glacial maximum

The *rp* of ZFMA2 is reduced and reaches values of no more than 0.6 at 500 m depth. Vertical planes show minor reduction in *rp*.

T5 - Ice margin retreating

Shallow dipping planes show increased *rp* with values around 1 (maximum *rp* on ZFMA2a) at repository level. Vertical planes show minor reduction in *rp*.

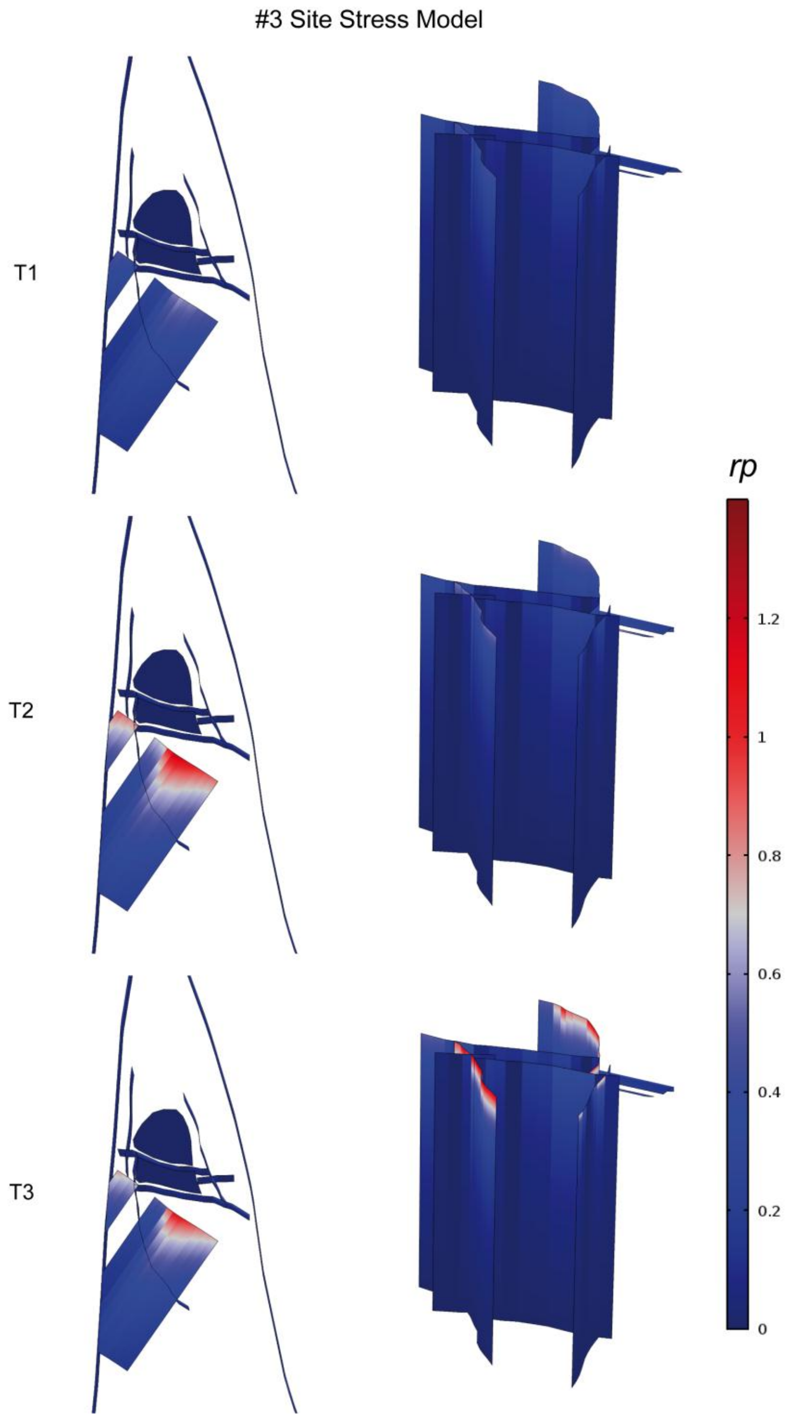

Figure 4.8. Evolution of *rp* for the #3 Site stress model in top view (left column) and view from model north (right column) after T1 - 1st glacial maximum, T2 - Ice margin retreating, T3 - Stress reductions due to forebulge, T4 - 2nd glacial maximum, and T5 - Ice margin retreating.

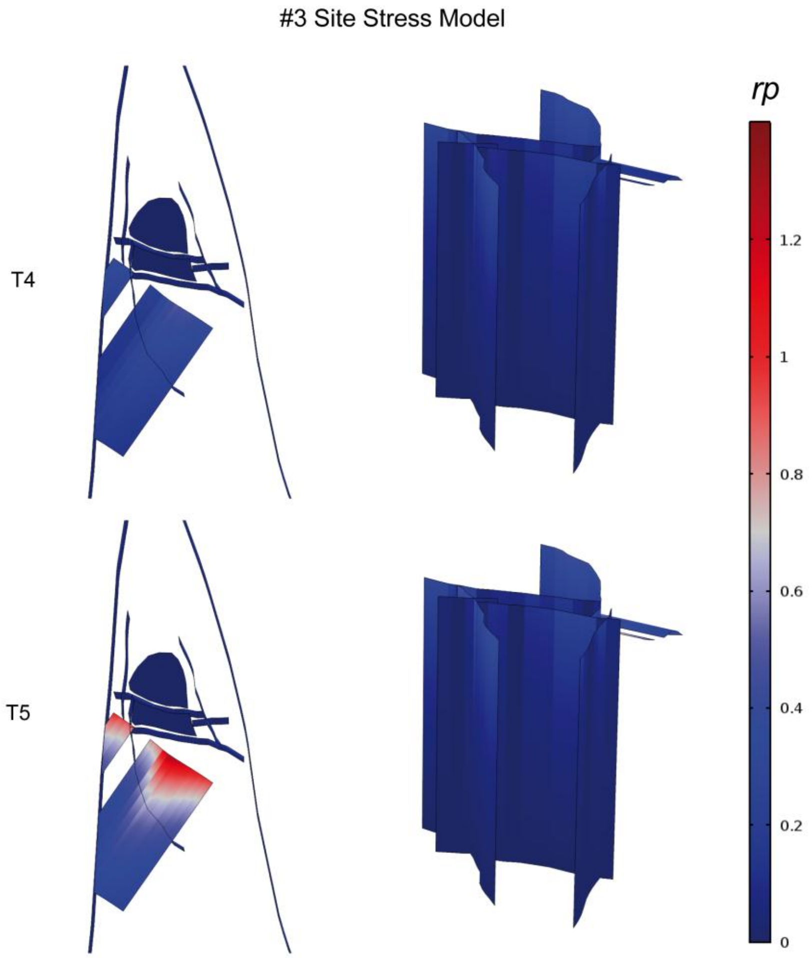

Figure 4.8. (Continued from the previous page.) Evolution of *rp* for the #3 Site stress model in top view (left column) and view from model north (right column) after T1 - 1st glacial maximum, T2 - Ice margin retreating, T3 - Stress reductions due to forebulge, T4 - 2nd glacial maximum, and T5 - Ice margin retreating.

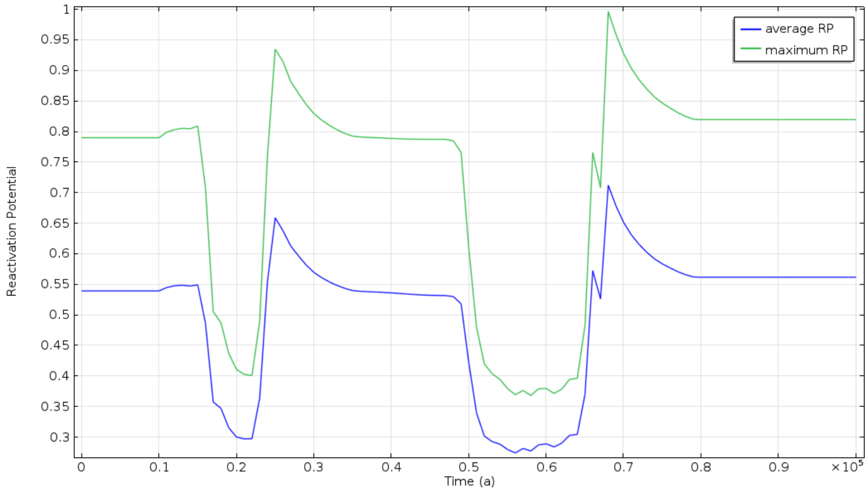

Figure 4.9. Maximum and average *rp* for ZFMA2a during glaciation for the #3 Site stress field model.

#4 geomecon stress model

The evolution of reactivation potential throughout the glacial cycle is shown in Figure 4.10. The reactivation potential of ZFMA2a is given in Figure 4.11.

T1 - 1st glacial maximum

Generally increased stability can be observed on planes of all orientations. At repository depth, the *rp* on ZFMA2 is reduced from initial 0.7 to values around 0.6. On vertical planes with critically striking segments at repository depth, e.g. ZFMWNW0809A, the *rp* is reduced similarly.

T2 - Ice margin retreating

A significant increase of *rp* shows reactivation of shallow dipping planes in reverse conditions at repository depth (for ZFMA2a up to 0.87). The *rp* on vertical planes is slightly reduced in the upper part of the model.

T3 - Stress reductions due to forebulge

While shallow dipping planes show no change in *rp* from the initial state, vertical planes show significant increase in *rp* depending on the strike. The *rp* values in the upper 150 m are unrealistically high due to very small normal stresses as in the previous models for T3. This applies for example for the northernmost part of ZFMNW0017. ZFMWNW0809A on the other hand, below 150 m, shows an increase in *rp* up to values around 1 at repository depth and decreasing below.

T4 - 2nd glacial maximum

Again, the stability is increased during the second glacial maximum on vertical planes as well as on shallow dipping planes. The effect is slightly more pronounced than for the first glacial maximum (T1).

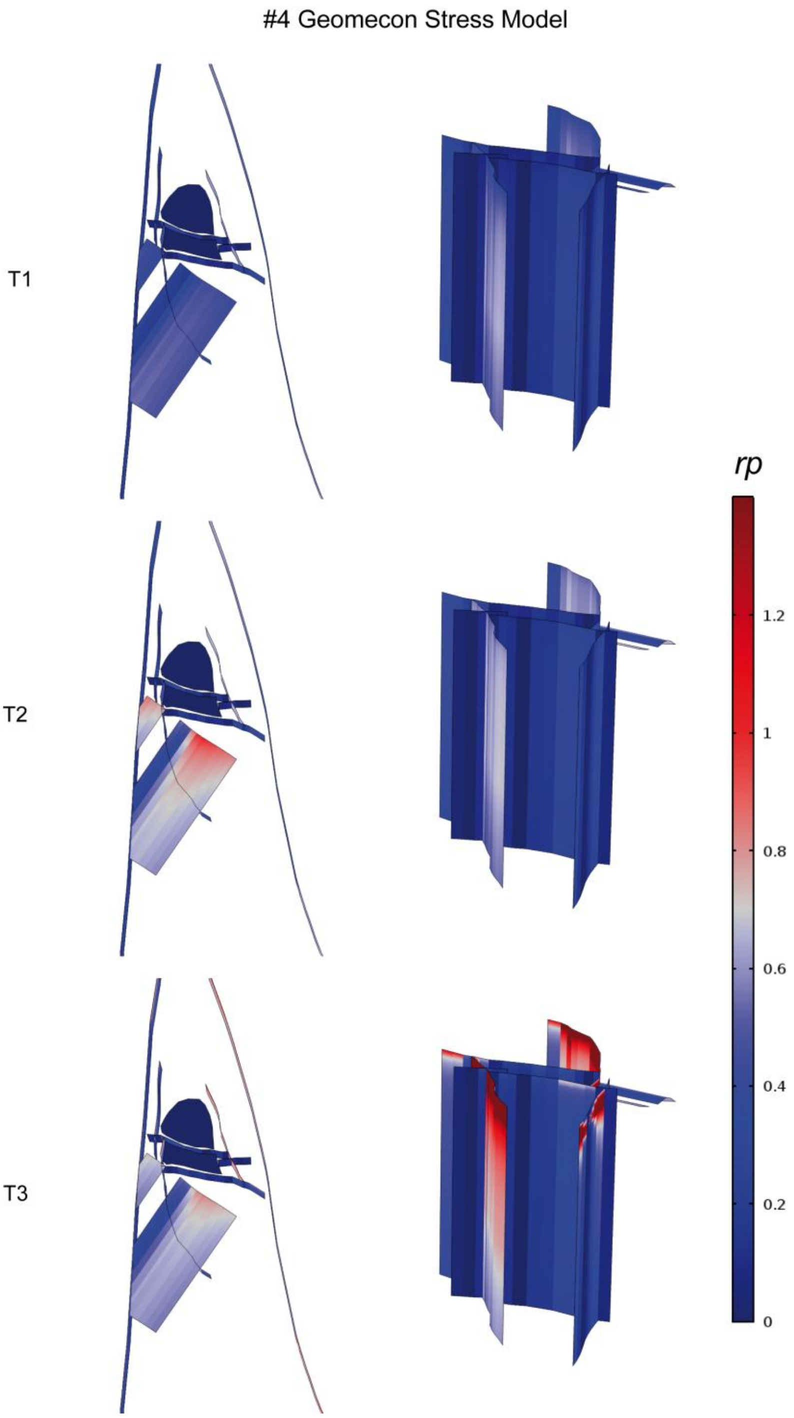

Figure 4.10. Evolution of *rp* for the #4 geomecon stress model in top view (left column) and view from model north (right column) after T1 - 1st glacial maximum, T2 - Ice margin retreating, T3 - Stress reductions due to forebulge, T4 - 2nd glacial maximum, and T5 - Ice margin retreating.

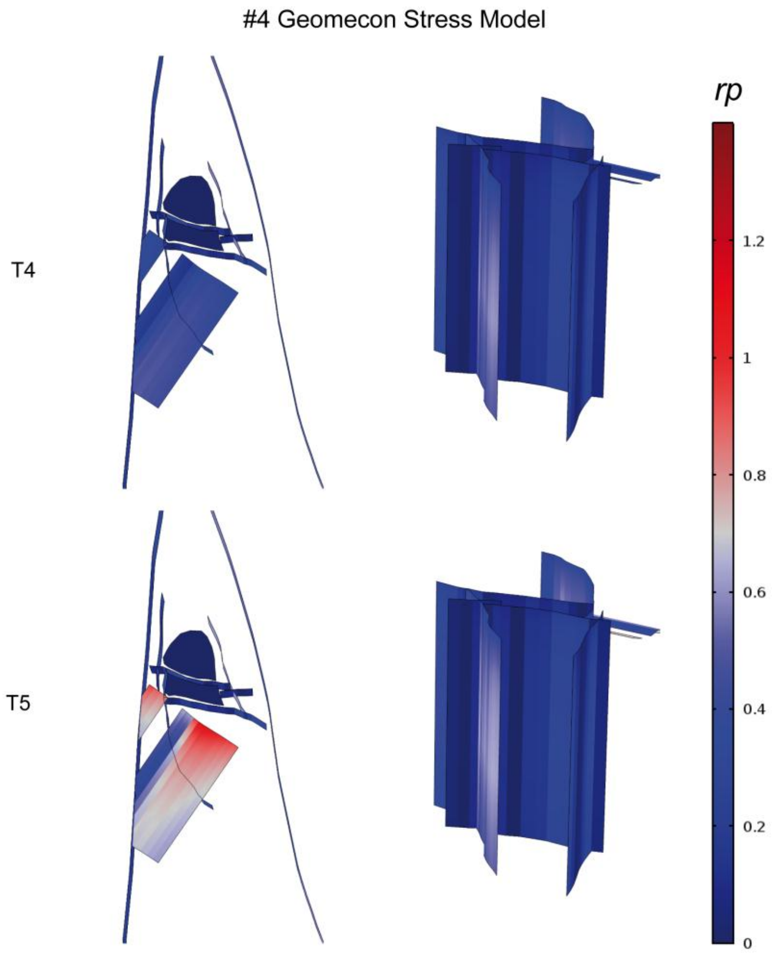

Figure 4.10. (Continued from previous page). Evolution of *rp* for the #4 geomecon stress model conditions in top view (left column) and view from model north (right column) after T1 - 1st glacial maximum, T2 - Ice margin retreating, T3 - Stress reductions due to forebulge, T4 - 2nd glacial maximum, and T5 - Ice margin retreating.

T5 - Ice margin retreating

Reverse faulting is promoted during the phase of a post-glacial retreating ice margin as visible from significantly increased *rp* values on shallow dipping planes. The maximum *rp* for ZFMA2a is close to 1. Vertical planes show a slight decrease in *rp*.

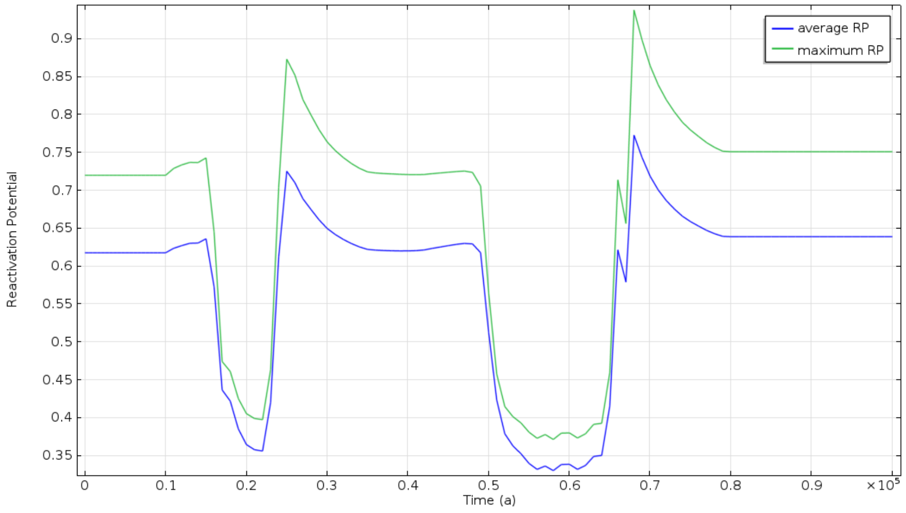

Figure 4.11. Maximum and average *rp* for ZFMA2a during glaciation for the #4 geomecon stress model.

4.3.3. Analysis of the seismicity of the deformation zones

In the previous section it was shown that shallow dipping planes are stabilised during times of maximum ice load, but destabilised during retreat of the ice load (e.g. ZFMA2a). This reflects the phenomenon of post-glacial earthquakes that is documented to have produced magnitudes of up to M8.2 after the last glacial cycle in northern Fennoscandia (Lagerbäck and Sundh, 2008). Post-glacial earthquakes of magnitudes larger than M7 are not thought to have occurred in southern Sweden but the possibility of such large events cannot be completely ruled out.

Gently dipping deformation zones within the geological local model (Stage 2.2, Stephens et al., 2007, SKB R-07-45) at Forsmark are estimated to potentially host magnitudes M5.0 and M5.8 based on their surface trace length (cf. Sec. 2.3.4). ZFMA2 is the largest of those zones and could potentially host an earthquake of magnitude M5.8.

Steeply dipping deformation zones with WNW strike have been shown to partly become unstable during times of a glacial forebulge within the #2 Mixed stress model and the #4 geomecon stress model. The results from the COMSOL simulations show that the critical area on ZFMWNW0809A does not extend over the whole deformation zone for neither the stress models during T3. Assuming that the rupture area corresponds to the area of the deformation zone where the reactivation potential is larger than 0.7, the estimated maximum magnitudes for the deformation zones would not be reached according to modelling results. Steeply dipping deformation zones have been estimated to potentially host earthquakes of magnitudes up to M7.2 (cf. Sec. 2.3.4). That is including the regional deformation zones and assuming full fault rupture.

4.3.4. Analysis of the potential for deformation zone growth

Figures 4.12 to 4.21 show the values of the intensity factor K_{II} as defined in Sec. 2.3.3 for selected deformation zones during the times T1 to T5. The results are consistent with the general analysis of the reactivation potential in Sec. 4.3.2. No growth is expected during T1 for coefficients of friction equal to 0.6 or higher. Similarly, during T4, no growth of deformation zones is expected for both of the applied background stress models. During T2 and T5, ZFMA2 has potential to grow; for very low coefficients of friction also some vertical deformation zones may grow if the #4 geomecon background stresses are applied. During T3, the most prominent difference between the applied stress models can be observed. While for the #4 geomecon stress model, growth is predicted for deformation zones ZFMWNW0123 and ZFMWNW0809A if the coefficient of friction is 0.7, for the background stresses as in the #1 to #3 SKB stress models, growth potential is predicted for zone ZFMA2. For low coefficients of friction also ZFMA2 may grow with the #4 geomecon stress model, and WNW striking deformation zones for the #1 to #3 SKB stress models at 500 m depth.

4.3.5. Analysis of the repository as a plane of weakness

The repository plane consistently shows zero reactivation potential as shown in Figures 4.5, 4.7, 4.8 and 4.10. This is the result of the assumption that the principal stresses lie in the horizontal and vertical planes as described in Sec. 2.3.5, where the limitations of the approach are also discussed.

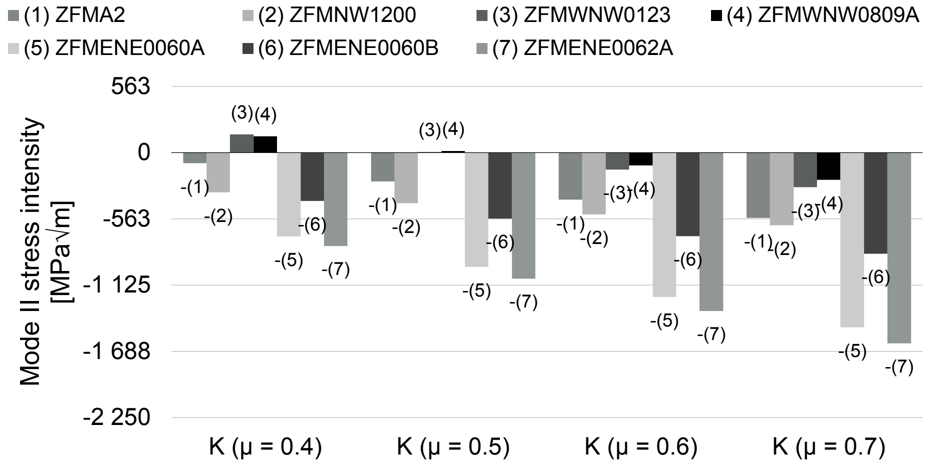

Figure 4.12. K_{II} values for the time T1 during the glacial cycle for selected deformation zones around the repository. Background stresses are as in the #4 geomecon stress model at 500 m depth.

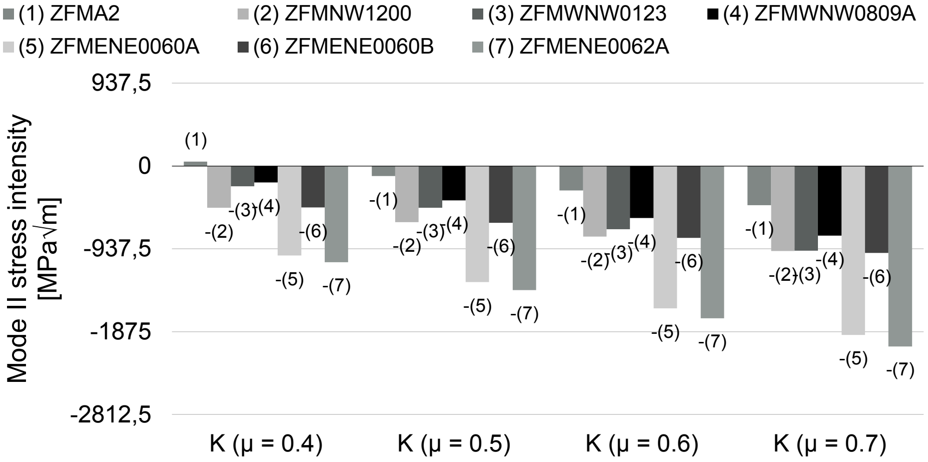

Figure 4.13. K_{II} values for the time T1 during the glacial cycle for selected deformation zones around the repository. Background stresses are as in the #1 to #3 SKB stress models at 500 m depth.

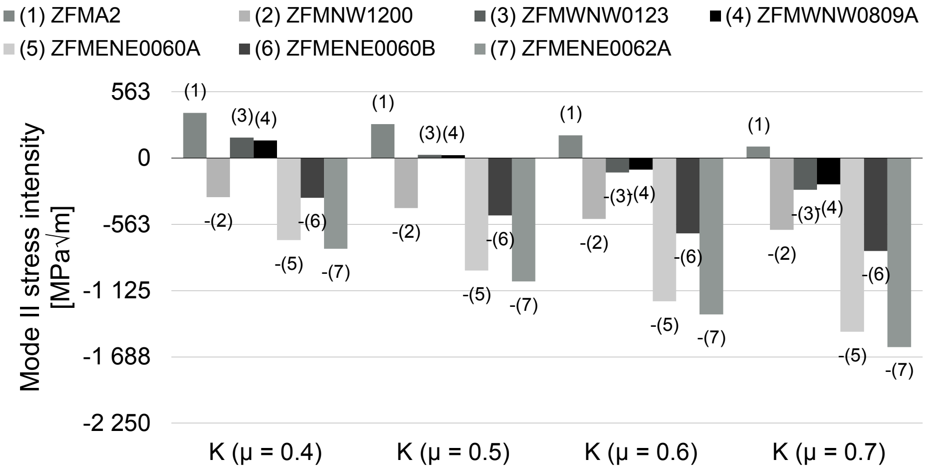

Figure 4.14. K_{II} values for the time T2 during the glacial cycle for selected deformation zones around the repository. Background stresses are as in the #4 geomecon stress model at 500 m depth.

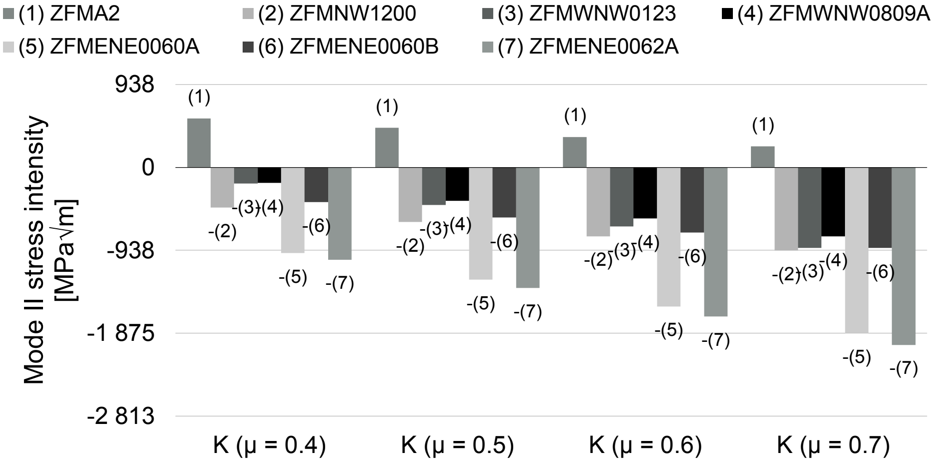

Figure 4.15. K_{II} values for the time T2 during the glacial cycle for selected deformation zones around the repository. Background stresses are as in the #1 to #3 SKB stress models at 500 m depth.

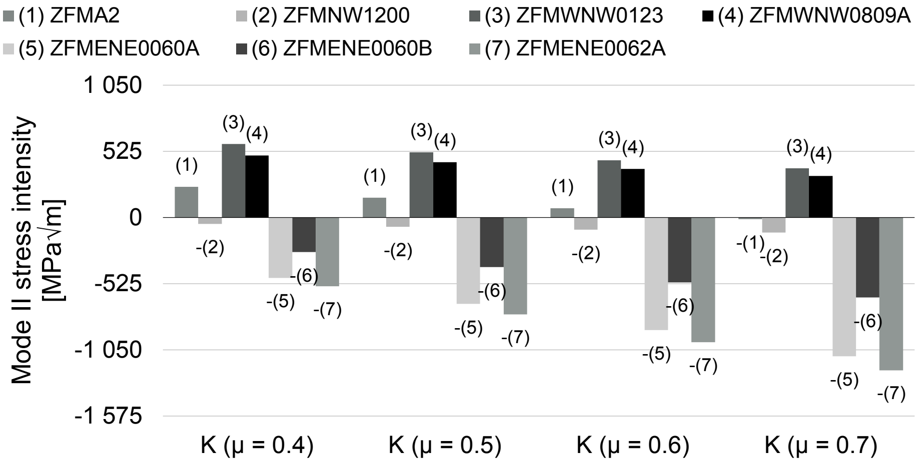

Figure 4.16. K_{II} values for the time T3 during the glacial cycle for selected deformation zones around the repository. Background stresses are as in the #4 geomecon stress model at 500 m depth.

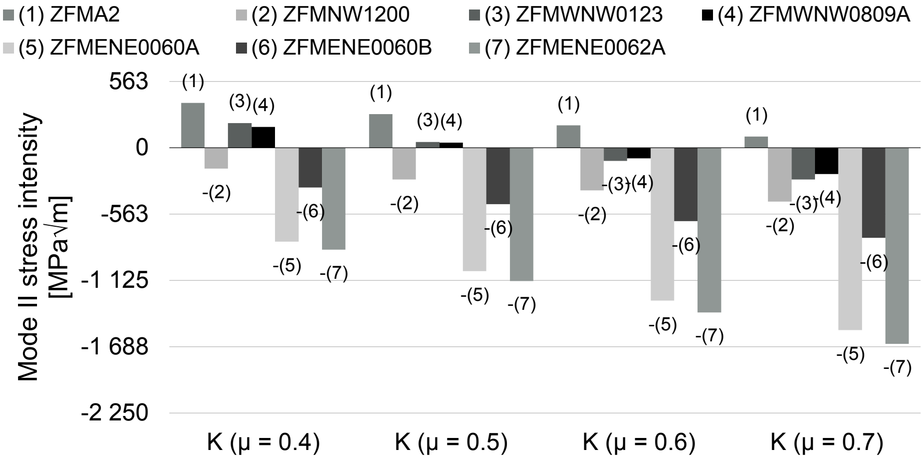

Figure 4.17. K_{II} values for the time T3 during the glacial cycle for selected deformation zones around the repository. Background stresses are as in the #1 to #3 SKB stress models at 500 m depth.

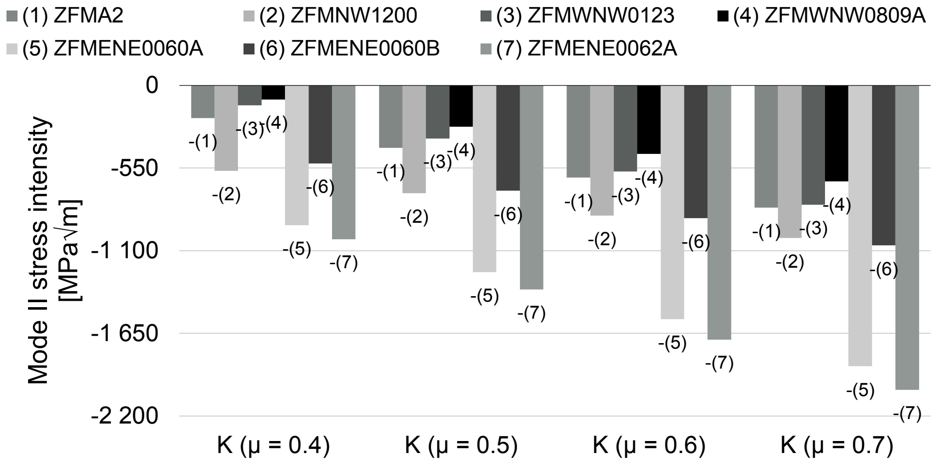

Figure 4.18. K_{II} values for the time T4 during the glacial cycle for selected deformation zones around the repository. Background stresses are as in the #4 geomecon stress model at 500 m depth.

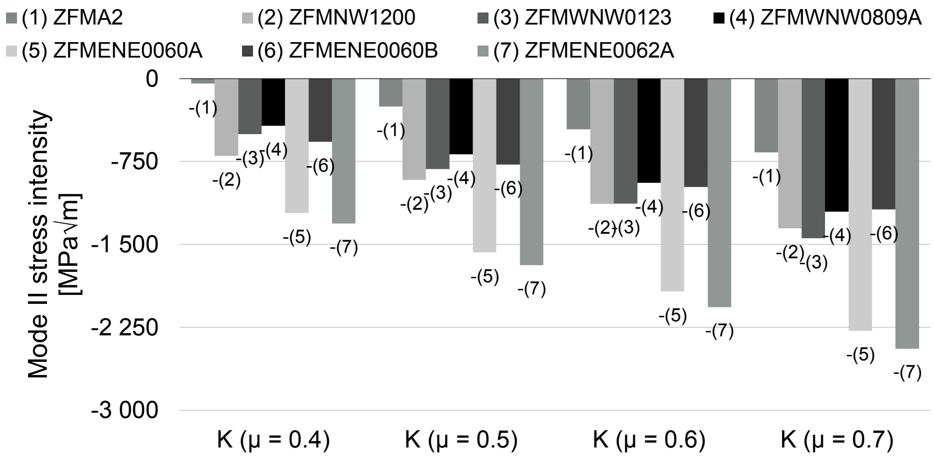

Figure 4.19. K_{II} values for the time T4 during the glacial cycle for selected deformation zones around the repository. Background stresses are as in the #1 to #3 SKB stress models at 500 m depth.

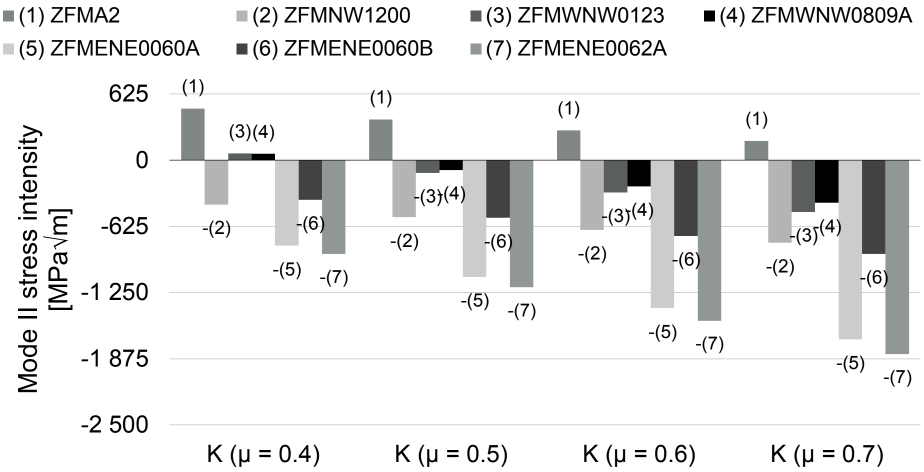

Figure 4.20. K_{II} values for the time T5 during the glacial cycle for selected deformation zones around the repository. Background stresses are as in the #4 geomecon stress model at 500 m depth.

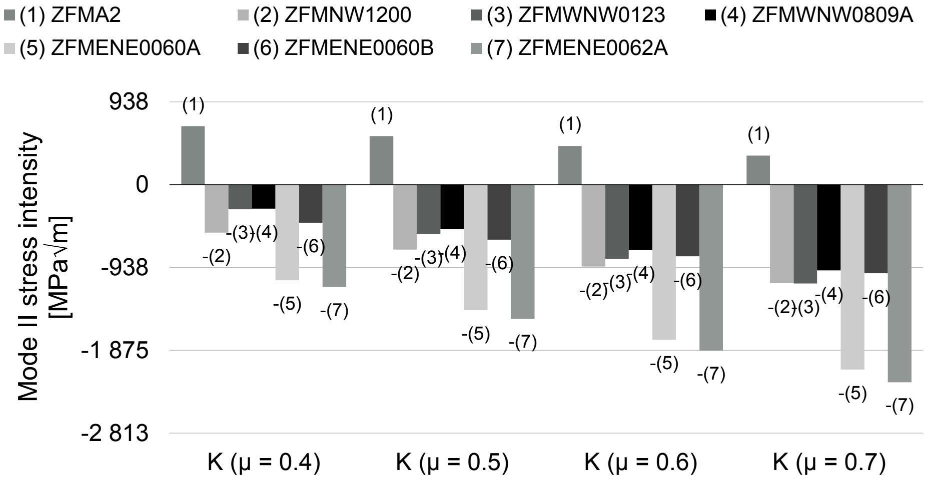

Figure 4.21. K_{II} values for the time T5 during the glacial cycle for selected deformation zones around the repository. Background stresses are as in the #1 to #3 SKB stress models at 500 m depth.

4.4. The Consultant's assessment on the influence of the glacial cycle on deformation zone stability and growth

The maximum reactivation potential *rp* varies (both increases and decreases) significantly during the glaciation cycle. Most pronounced changes are visible on ZFMA2a. The stability of deformation zones depends on their orientation and the phase of the glacial cycle.

- *Shallow dipping deformation zones* become more stable during phases of direct ice load with increased vertical stress (T1 and T4), which is reflected by decreasing *rp* values. During phases of retreating ice margins, when the vertical load disappears while horizontal stresses are still increased (T2 and T5), shallow dipping deformation zones show significantly increased reactivation potential. This corresponds to the phenomenon of activation of Post-Glacial Faults (PGF). The horizontal stress changes during forebulge periods (T3) do not affect the stability of shallow dipping deformation zones, this irrespective of the background stress field.
- *For subvertical deformation zones*, the effect of the different glacial phases on the stability depends on the background stress field and the orientation of the zone with respect to the stress field.

  If the #1 Reverse stress model is applied, there are no significant stability changes. Subvertical planes are stable in the initial state and do not become critical during the whole glacial cycle.

  With the #2 Mixed stress model, vertical deformation zones show initial *rp* values around 0.8 below 1,000 m. During the glacial cycle, the most prominent effect is observed during forebulge periods (T3), when the vertical deformation zones become highly unstable. This is valid for depth ranges below 2,400 m due to a change in the stress regime from reverse to strike-slip. Those parts of the deformation zones that strike with an angle of 122° or 168° become most critical. Some deformation zones that belong to the WNW and NW clusters are therefore especially imperilled. Out of the deformation zones within the numerical model, this is the case forthe zones ZFMWNW0809A and ZFMWNW0123. The WNW and NW clusters are believed to represent the oldest deformation zones in the area that have formed during the late Svecokarelian orogeny (Stephens et al., 2007, SKB R-07-45), including the confining faults of the Forsmark tectonic lens Forsmark, Singö, Eckarfjärden. The Singö fault (average strike 120°) and the Forsmark fault (average strike 125°) belong to the more critical WNW cluster. Other than for T3, the stability is not changed (for T2 and T5) or slightly increased (for T1 and T4). Above 1,000 m, the same conclusions as for the #1 Reverse model apply.

  For the #3 Site stress model, vertical deformation zones show *rp* ranges well below 0.6 for all glacial phases, which therefore should be stable.

  Applying the background stresses defined by the #4 (geomecon) stress model, vertical deformation zones become highly unstable during the forebulge period (T3) and reach *rp* values above 1. Their stability is unaffected during phases of retreating ice (T2 and T5) and sightly stabilised during phases of ice load (T1 and T4).

Vertical planes oriented perpendicularly to the maximum horizontal stress SH are continuously stable and unaffected by glacially induced stress changes as it has also been shown by the analysis of growth potential. This is in accordance with SKB's presentation regarding the stability of deformation zones during the glacial cycle. Deformation zones such as ZFMENE0060A, ZFMENE0060B and ZFMENE0062A are stable under all conditions.

5. Influence of an earthquake on deformation zone stability and growth

5.1. SKB's presentation

There is a series of SKB reports concerning the seismically induced slip on fractures (e.g. La Pointe et al., 1997, SKB TR-97-07; La Pointe et al., 2000, SKB TR-00-08; Bäckblom and Munier, 2002, SKB TR-02-24; Börgesson and Johannesson, 2003, SKB TR-04-02; Fälth and Hökmark, 2006, SKB R-06-48; Fälth et al., 2010, SKB TR-08-11). There are no reports on the subject of seismically induced slip on deformation zones. This is conceivable, since the major concern of SKB is the potential slip of a target fracture that intersects a canister position. Deformation zones are avoided in the present repository layout by applying respect distances to deposition tunnels and holes.

5.2. Motivation of the assessment on earthquake influence on deformation zones stability

Potential slip on deformation zones itself appears to bear no risk for the planned repository if the guidelines for respect distances and avoidance of canister positions intersecting long fractures are followed (Fälth et al., 2010, SKB TR-08-11). However, the risk of potential growth of deformation zones into the repository due to an earthquake on the zones themselves or on another zone has to be addressed. The Authors will therefore focus on:

- evaluating the reactivation potential of deformation zones due to an earthquake in general;
- identifying the most critical orientations of deformation zones, and consequences for the possibility of critically oriented faults that might grow into the repository due to seismic activity;
- studying the possibility of propagation of blind faults (e.g. zones that today do not reach the ground surface);
- studying the effect of the distance from the active zone on the secondary effects of the earthquake on other zones.

In contrast to the simulation of earthquakes by SKB, the approach that is pursued in this chapter is non-generic and approximates the geometry of the large deformation zones at Forsmark.

5.3. Independent analyses of the influence of an earthquake on deformation zone stability

5.3.1. Earthquake model

The seismic phase is simulated in this study as a prescribed slip on a fault along the contour of the Forsmark tectonic lens (Figure 5.1). The confining deformation zones of the tectonic lens are modelled as juxtaposed planar vertical segments of approximately 2 km surface length. A time- and location-dependent displacement can be prescribed onto each segment, simulating the seismic slip along a potentially unstable part of the deformation zone.

As presented in the previous chapters, there are good arguments for expecting seismic events due to reverse faulting after the future glacial maxima at Forsmark. Nevertheless, it has also been shown that there are interglacial stages that also promote strike-slip faulting. The Authors chose to simulate the earthquakes for this assessment as resulting from strike-slip faulting because the vertical deformation zones are the largest in the vicinity of the planned repository and therefore have the potential of hosting the largest earthquakes.

The threshold for allowed displacements along target fractures in the repository that intersect canister positions was initialy set to 100 mm by SKB, and has later been reduced to 50 mm (SKB TR-11-01). SKB has shown that such displacements can be obtained on target fractures if the active fault zone hosts earthquakes of magnitude larger than M5.5 (Fälth et al., 2010, SKB TR-08-11). Therefore, larger earthquakes of moment magnitudes M6 and M7 will be modelled in this study. In order to yield realistic displacements and rupture areas, earthquakes are located on the regional deformation zones (with length >10 km) surrounding the repository. Those have been shown to potentially be able to host earthquakes of magnitudes above M7.0 in Sec. 2.3.4. Three earthquake scenarios have been simulated that differ in terms of distance to the repository, rupture area and displacements (Table 5.1). The magnitude M6 events are hosted on those parts of the deformation zones that were shown to become most critical during glaciation (see Chapter 2 and 4). The modelled earthquakes in Table 5.1 plot in agreement with the regressions based on the data by Wells and Coppersmith (1994) in Figure 5.2.

The size of the COMSOL model for earthquake simulations had to be enlarged compared to the model used for simulations in the previous chapters (Figure 3.2) in order to prevent the seismic wave reflection and interference during the initial and most critical time after rupture. The outer model boundaries enclose a volume of $80 \times 50 \times 15$ km^3. The mechanical properties of the model are reported in Appendix 2. No attenuation or alteration of the static properties has been included in the model, which may be considered a conservative approach.

The earthquake magnitudes and the sizes of the rupture areas lie within reasonable ranges for natural earthquakes according to the database by Wells and Coppersmith (1994; see Figure 5.2). The displacements and the rupture area are larger than average for the two M6 events. This is similar to the earthquake simulations presented by Fälth et al. (2010). The seismic stress increments and the displacements resulting from the simulations are monitored, and the different stress field models for the background stresses are superposed to the seismic stress increments to evaluate the reactivation potential on the deformation zones.

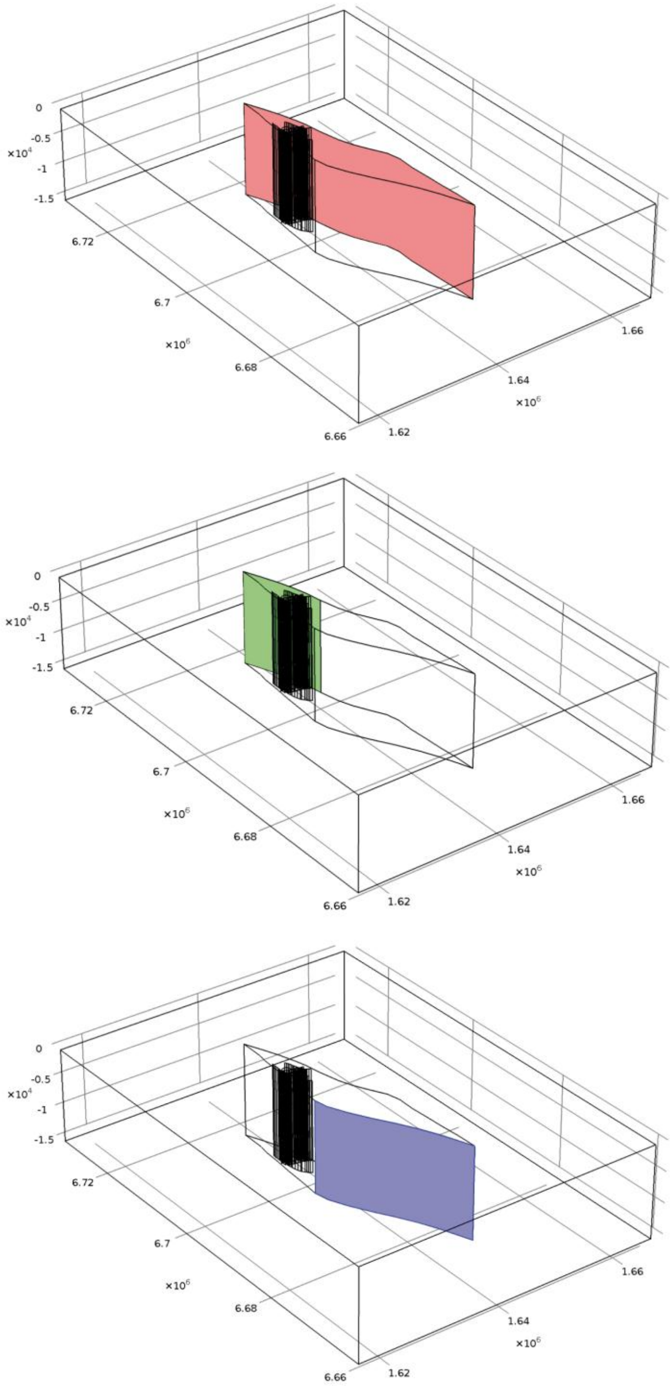

Figure 5.1. Modelled rupture areas for the three earthquake simulations that are located on the regional deformation zones that define the Forsmark tectonic lens. The top case (red) corresponds to the M7 earthquake, the middle (green) and the bottom case (blue) areas correspond to the proximal and distal M6 earthquakes to the repository, respectively. The respective sizes of the rupture area and assigned displacements can be found in Table 5.1.

Table 5.1. Rupture area and displacements as realised for the earthquake simulations.

	Moment magnitude	Rupture area [km^2]	Maximum displacement [m]	Surface rupture length [km]
🔴	M7	643.8	9.0	42.92
🟢	M6 (proximal)	205.7	0.9	13.71
🔵	M6 (distal)	373.7	0.5	24.91

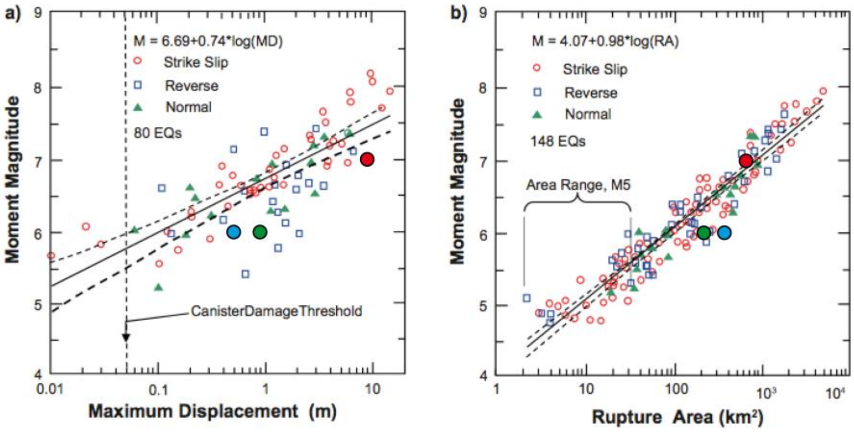

Figure 5.2. Comparison of the earthquake characteristics simulated in this study with the database and regressions by Wells and Coppersmith (1994). The simulations lie in reasonable ranges within the database. The displacements and the rupture area are larger than average for the two M6 events. (Figure redrawn after Fälth et al., 2010, SKB TR-08-11, Figure 1-6).

The moment magnitude M_W (same as M in Eq. 2.7) is calculated via the seismic moment M_0 which is the product of shear modulus G, rupture area A and average displacement d as in:

$$M_0 = G\, d\, A$$ Eq. (5.1)

$$M_W = \frac{2}{3} \log(M_0) - 6.07$$ Eq. (5.2)

The displacement is distributed along the slipping part of the deformation zone as a triangular function with its peak in the middle of the rupture area. The slip velocity is modelled as an uprising sinusoidal function. The displacement is in horizontal direction without vertical component, tangential to the deformation zone.

5.3.2. Results of the earthquake analyses

M7 earthquake

The earthquake of magnitude M7 (red rupture area) is realised by simulating a displacement on a part of the Singö deformation zone that defines the North-Eastern boundary of the Forsmark tectonic lens. The maximum displacement amounts to 9 m in the centre of the rupture area and is decreased to zero displacement at the edges of the activated surface. The total surface rupture length is 42.92 km. Figure 5.3 and 5.4 show the resulting displacements and stress increments in the direction of the principal stresses as monitored at a central point on the repository plane (cf. Figure 3.3). The stress in direction of Sh decreases by 14 MPa and increases by a maximum of around 9 MPa due to the earthquake. The stress in SH direction increases by 7.5 MPa and decreases by 16 MPa within the first two seconds after the earthquake. The vertical stress does not change as significantly as the horizontal stresses. It varies less than 1 MPa around its initial value. This is due to the prescribed displacement on the rupture area that has no vertical component.

The resulting maximum, minimum and average stresses in each direction of the background principal stresses within the whole repository plane are shown in Figure 5.5. The figure shows that the most critical time is likely to be 1.0 s after the rupture. This is confirmed by an evaluation of the overall reactivation potential, which becomes largest at this point in time (Figure 5.6). On the modelled deformation zones, the maximum *rp* values are constantly in the order of 10^3 for the first two seconds after the rupture. This is caused by Sh values that are close to or below zero, causing the normal stress to reduce significantly in parts of deformation zones.

This in turn leads to extremely high *rp* values and significant instability of the local deformation zones in the model. It has to be noted that this effect is mostly localised on small areas that shift along the deformation zones with time, according to the propagation of the seismic waves. Thereby it is striking that the critical areas of the vertical deformation zones are confined to very shallow depths near the surface, where the absolute background stress magnitudes are small enough to lead to those extreme *rp* values when the the seismic stress increments are added.

The shallow dipping deformation zone ZFMA2 is one of the most critical fault zones during the earthquake. It terminates at around 300 m depth in the model at its shallowest point and therefore does not show this extreme instability in the upper 100 m. However, it does reach maximum *rp* values of around 1.0 (Figure 5.6) and average values of 0.72 (ZFMA2a in Figure 5.7).

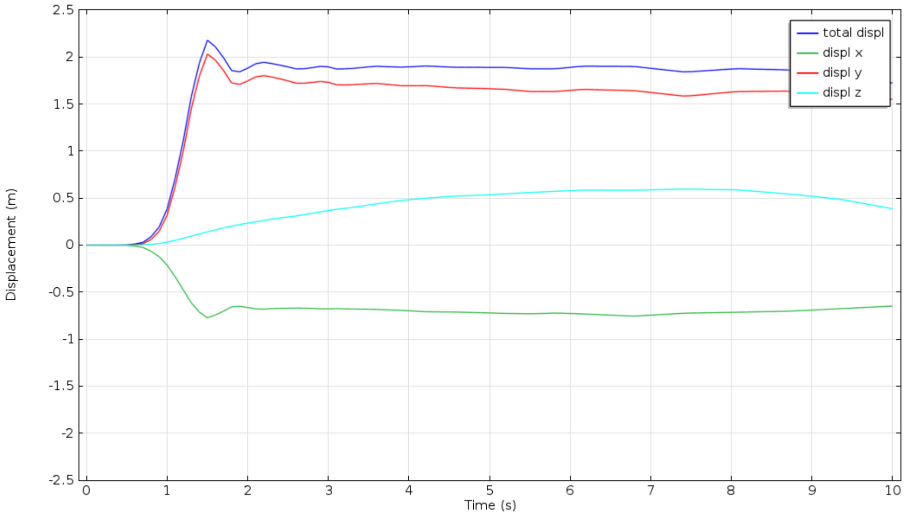

Figure 5.3. Displacements in the direction of the background principal stresses as monitored in the repository plane at 500 m depth.

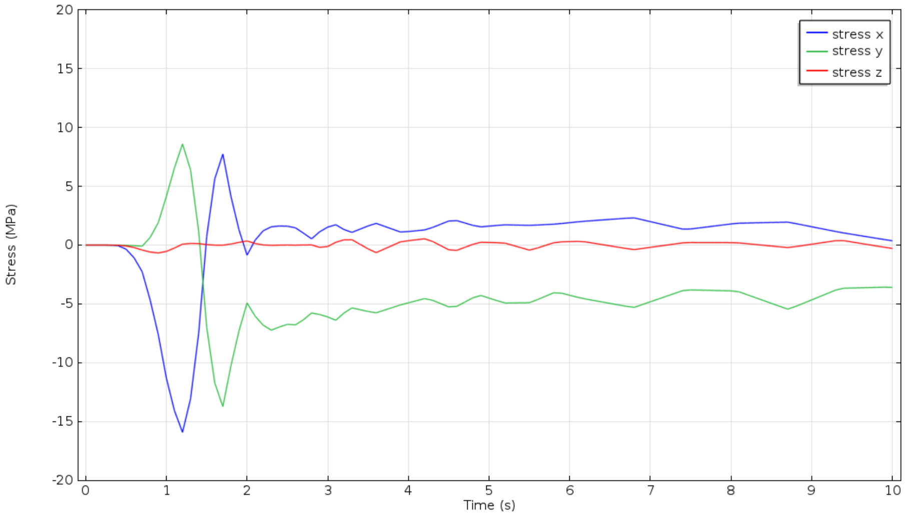

Figure 5.4. Stress increments in the direction of the background principal stresses as monitored in the repository plane at 500 m depth.

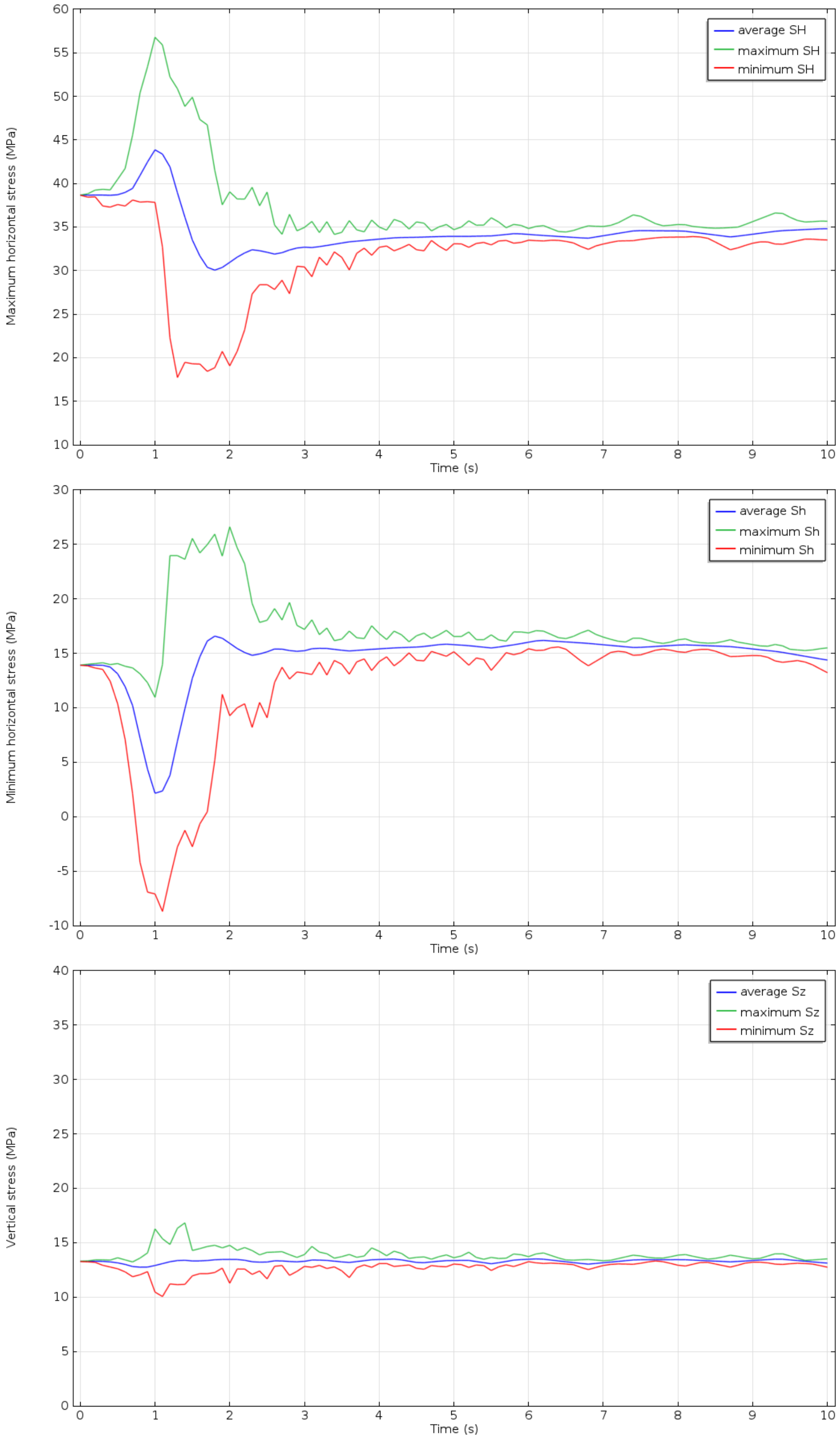

Figure 5.5. Maximum, minimum and average stresses in direction of the background principal stresses (Sh, Sh and Sv) as monitored in the repository plane at 500 m depth during the M7 earthquake (red rupture area) and superposed to the background stresses according to the #4 geomecon stress model.

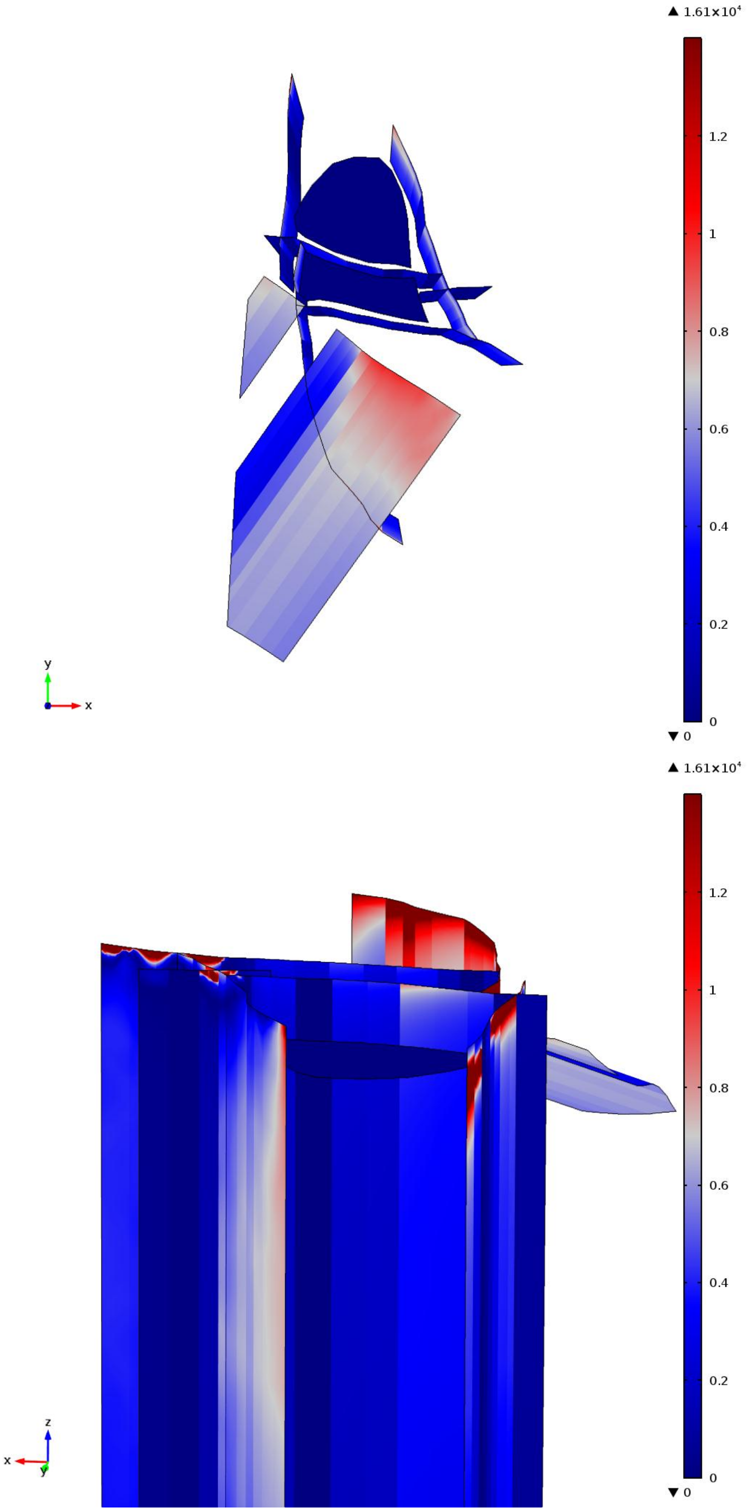

Figure 5.6. Reactivation potential at 1.0 s after the M7 earthquake (red rupture area) in: (top) a view from the top on the model, and (bottom) a view from NW. Background stresses are according to the #4 geomecon stress model.

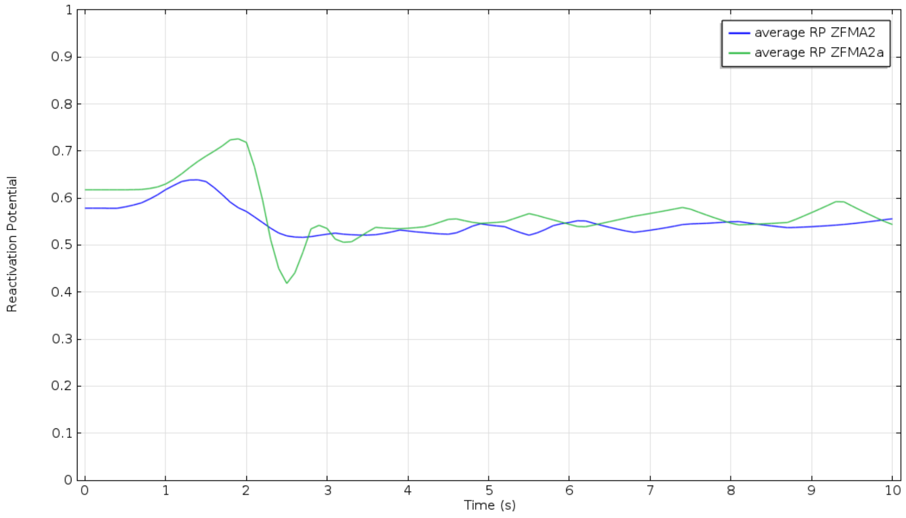

Figure 5.7. Average *rp* for ZFMA2 and ZFMA2a during the M7 earthquake (red rupture area) and background stresses according to the #4 geomecon stress model.

Proximal M6 earthquake

This earthquake of magnitude M6 (green rupture area) close to the repository is realised by simulating a displacement on a part of the Singö deformation zone that defines the North-Eastern boundary of the Forsmark tectonic lens. The maximum imposed displacement amounts to 0.9 m in the centre of the rupture area and is decreased to zero displacement at the edges of the rupture area. The total length of the rupture area on the surface is 13.71 km. Figures 5.8 and 5.9 show the resulting displacements and stress increments, respectively, in direction of principal stresses as monitored at a central point on the repository plane (cf. Figure 3.3). The stress increments are considerably smaller than for the M7 earthquake. The stress increments amount to a maximum of around 2 MPa within the first two seconds after rupture. They are constantly below 0.1 MPa for the vertical stress.

The resulting maximum, minimum and average stresses in each direction of the background principal stresses within the whole repository plane are shown in Figure 5.10. The evaluation of the resulting reactivation potential reveals values between 1.0 and around 2.0 for the time span between 2 and 3 seconds after rupture. The maximum *rp* value was found on deformation zone ZFMWNW0809A and amounts to 2.14 at 2.9 s after rupture (Figure 5.11). Again, the maximum value is found close to the model surface, and it generally decreases with depth. Figure 5.12 shows that for the shallow dipping deformation zone ZFMA2, the average *rp* does not increase significantly. As visible from Figure 5.11, the maximum *rp* on ZFMA2 is basically the same as for the initial state (cf. Figure A2.13).

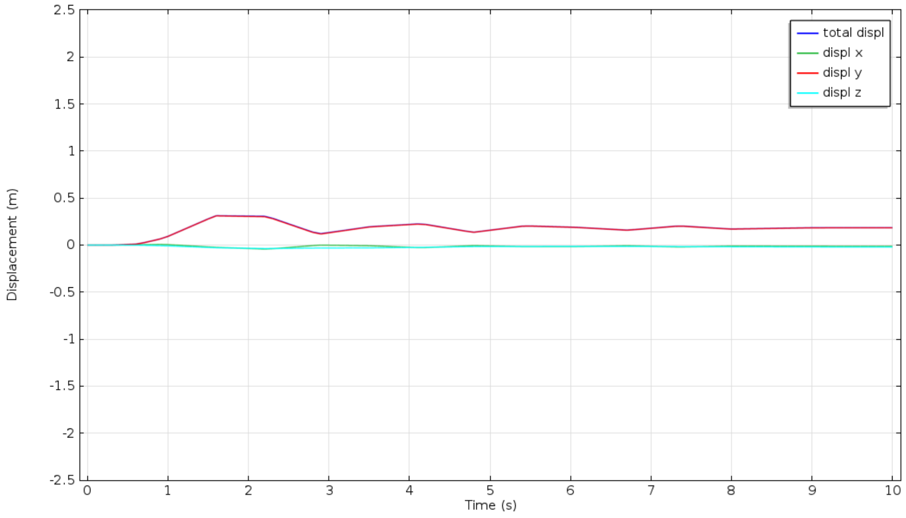

Figure 5.8. Displacements in the direction of the background principal stresses as monitored in the repository plane during the proximal M6 earthquake (green rupture area) and background stresses according to the #4 geomecon stress model.

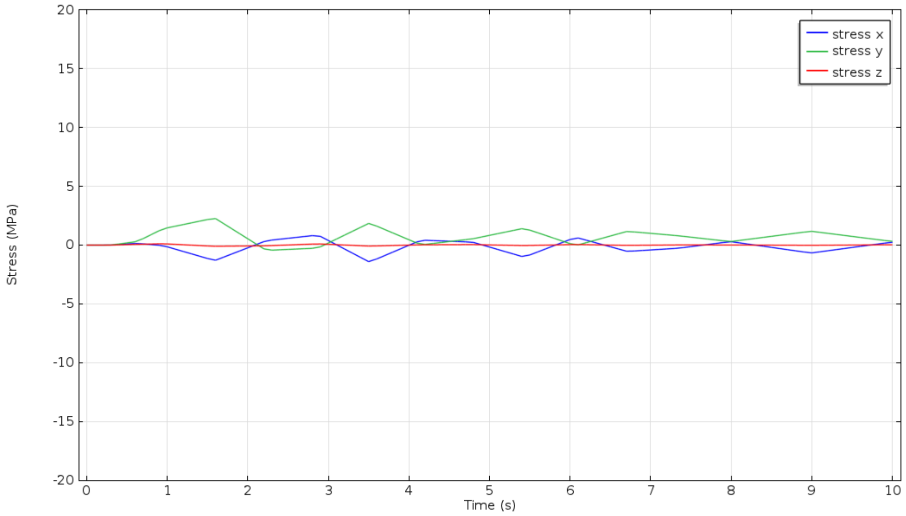

Figure 5.9. Stress increments in the direction of the background principal stresses as monitored in the repository plane during the proximal M6 earthquake (green rupture area) and background stresses according to the #4 geomecon stress model.

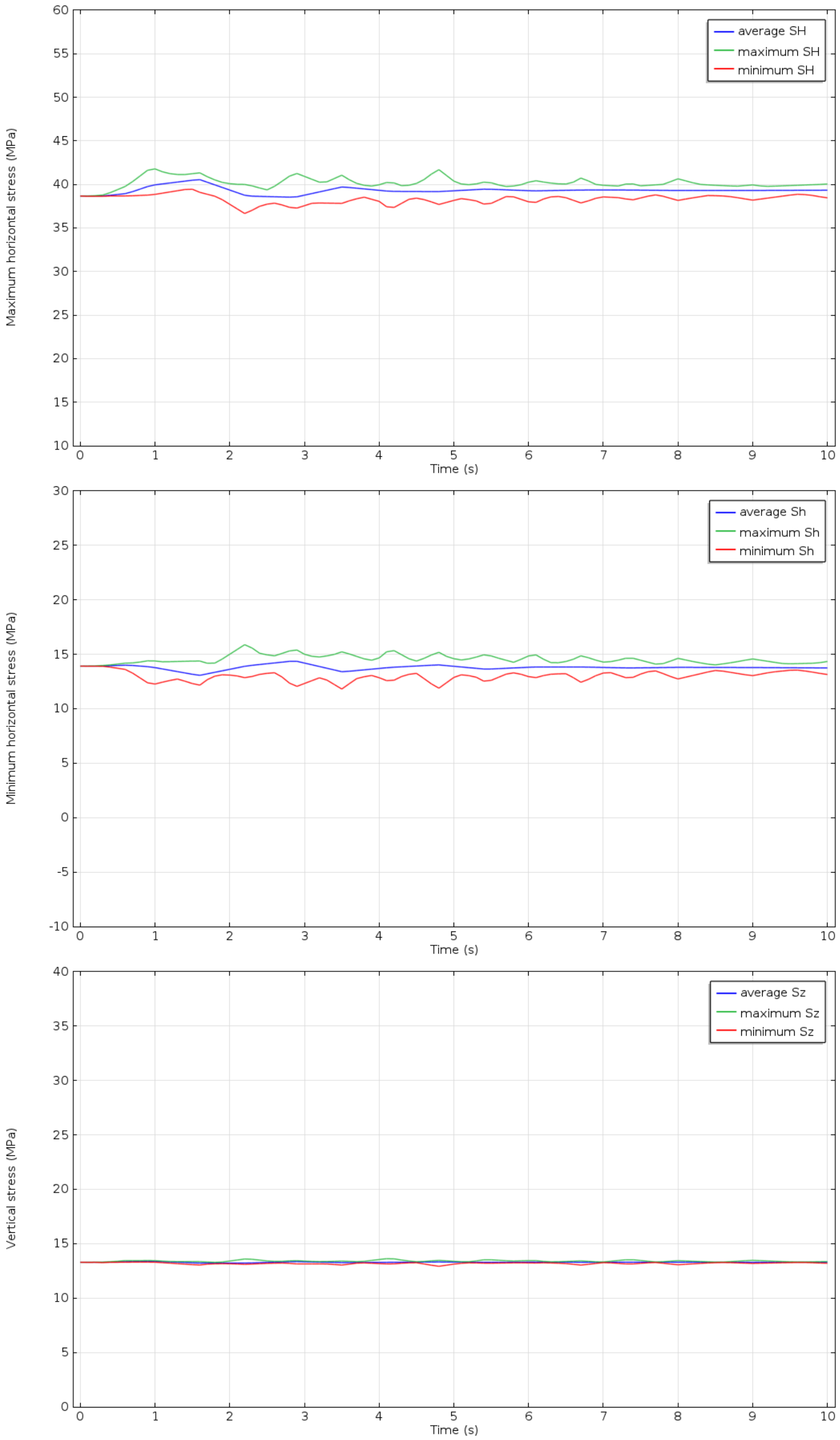

Figure 5.10. Maximum, minimum and average stresses in direction of the background principal stresses as monitored in the repository plane at 500 m depth during the proximal M6 earthquake (green rupture area) and background stresses according to the #4 geomecon stress model.

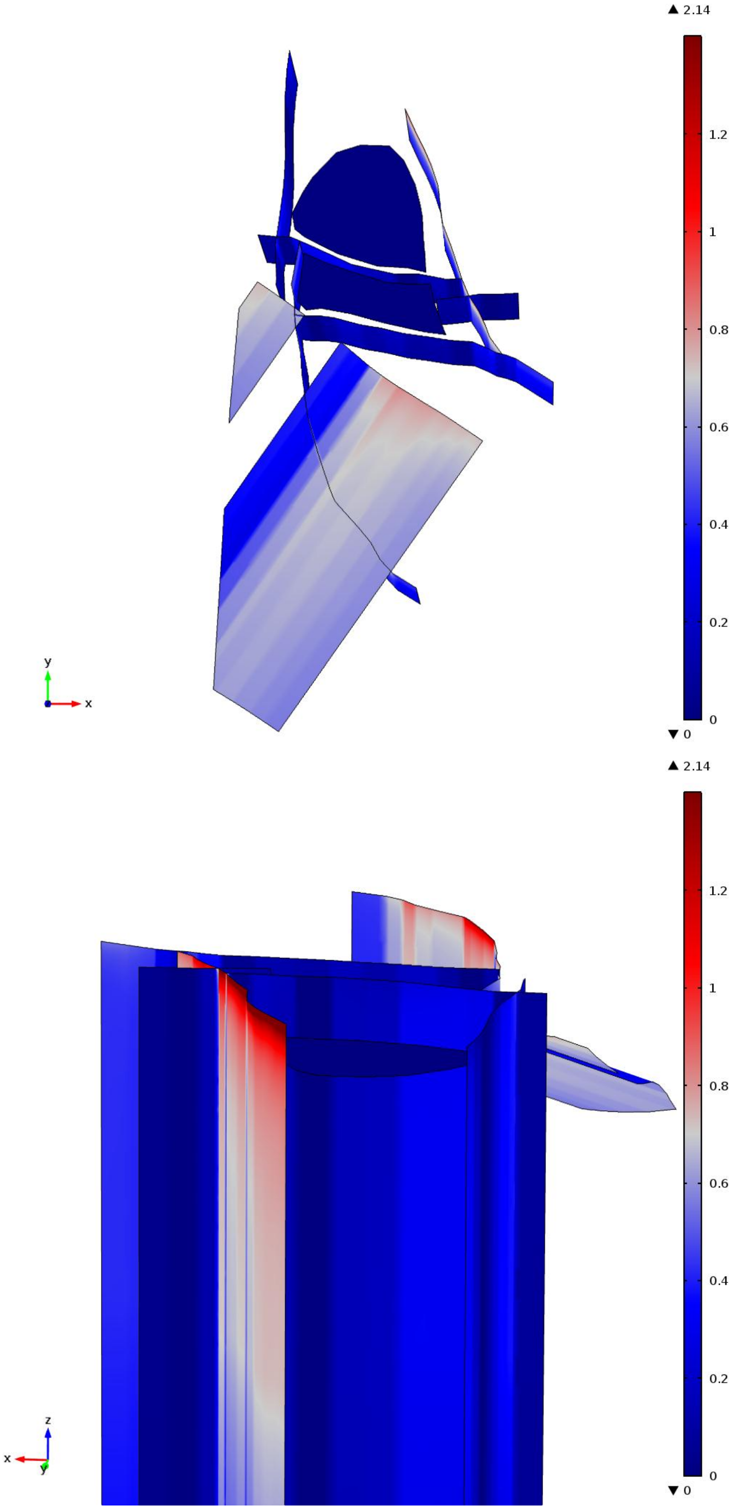

Figure 5.11. Reactivation potential at 2.9 s after the proximal M6 earthquake (green rupture area) in (top) a view from the top on the model and (bottom) a view from NW and background stresses according to the #4 geomecon stress model.

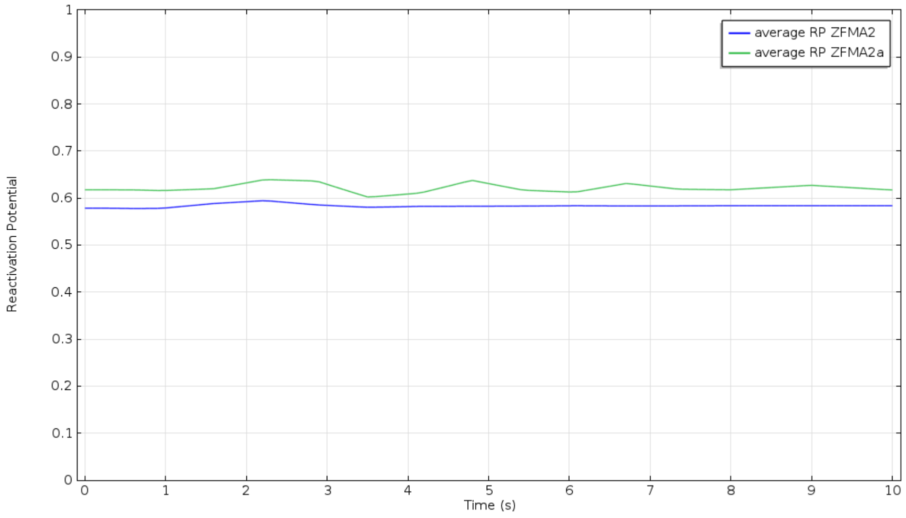

Figure 5.12. Average *rp* for ZFMA2 and ZFMA2a during the proximal M6 earthquake (green rupture area) and background stresses according to the #4 geomecon stress model.

Distal M6 earthquake

This earthquake of magnitude M6 (blue rupture area) is located in the model at maximum possible distance to the repository and is realised by simulating a displacement on a part of the Forsmark deformation zone that defines the South-Western boundary of the Forsmark tectonic lens. The maximum displacement amounts to 0.5 m in the centre of the rupture area and is decreased to zero at the edges of the plane. The total length of the rupture surface is 24.91 km. Figures 5.13 and 5.14 show the resulting displacements and stress increments, respectively, in direction of the principal stresses as monitored at a central point on the repository plane (cf. Figure 3.3).

The stress increments are considerably smaller than for the M7 earthquake and also only a fraction of those due to the proximal M6 earthquake. The maximum stress increase is in direction of SH and amounts to 0.12 MPa at about 5.5 s after rupture. The resulting maximum, minimum and average stresses in each direction of the background principal stresses within the whole repository plane are shown in Figure 5.15. The evaluation of the resulting reactivation potential reveals values that are basically unchanged from the initial reactivation potential (Figure 5.16, cf. Figure A2.13). The same observation is made for the average *rp* on ZFMA2 (Figure 5.17).

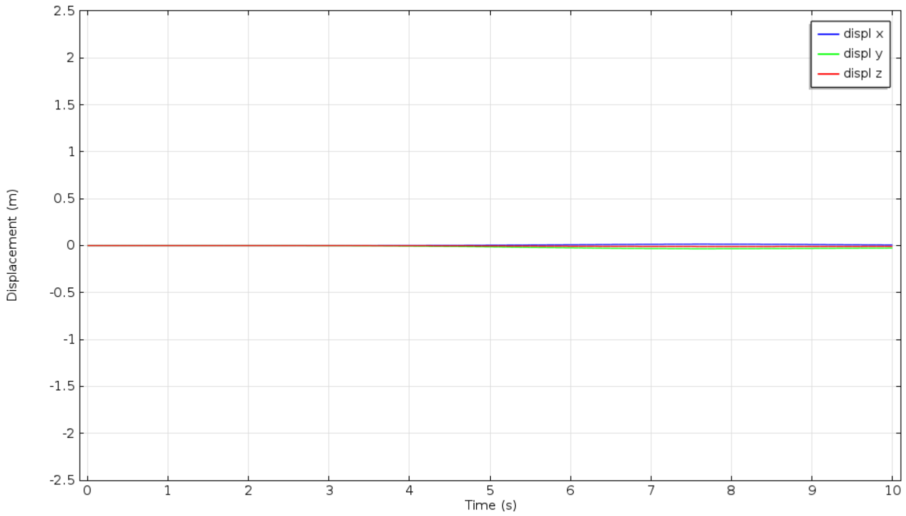

Figure 5.13. Displacements in the direction of the background principal stresses as monitored in the repository plane during the distal M6 earthquake (blue rupture area) at 500 m depth and background stresses according to the #4 geomecon stress model.

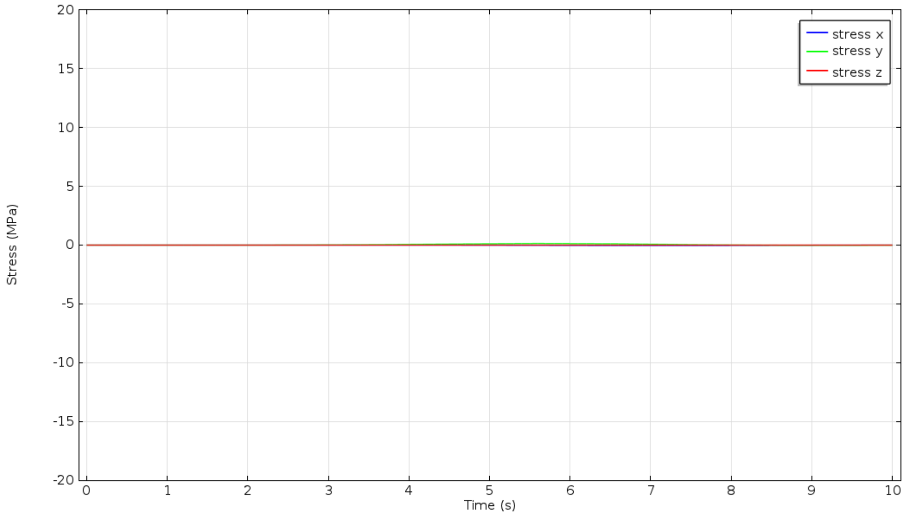

Figure 5.14. Displacements and stress increments in the direction of the background principal stresses as monitored in the repository plane during the distal M6 earthquake (blue rupture area) at 500 m depth and background stresses according to the #4 geomecon stress model.

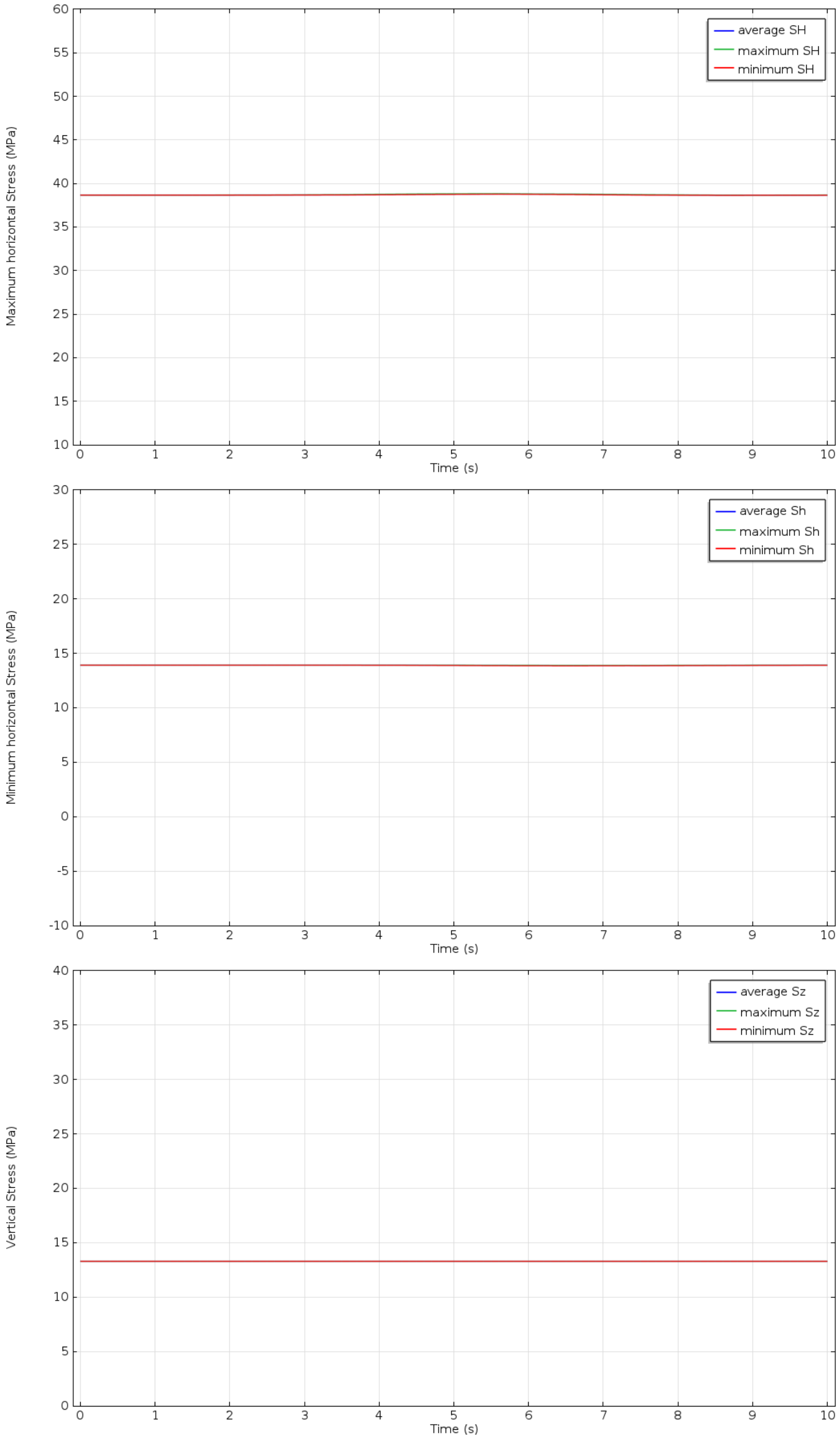

Figure 5.15. Maximum, minimum and average stresses in direction of the background principal stresses as monitored in the repository plane at 500 m depth during the distal M6 earthquake (blue rupture area) and background stresses according to the #4 geomecon stress model.

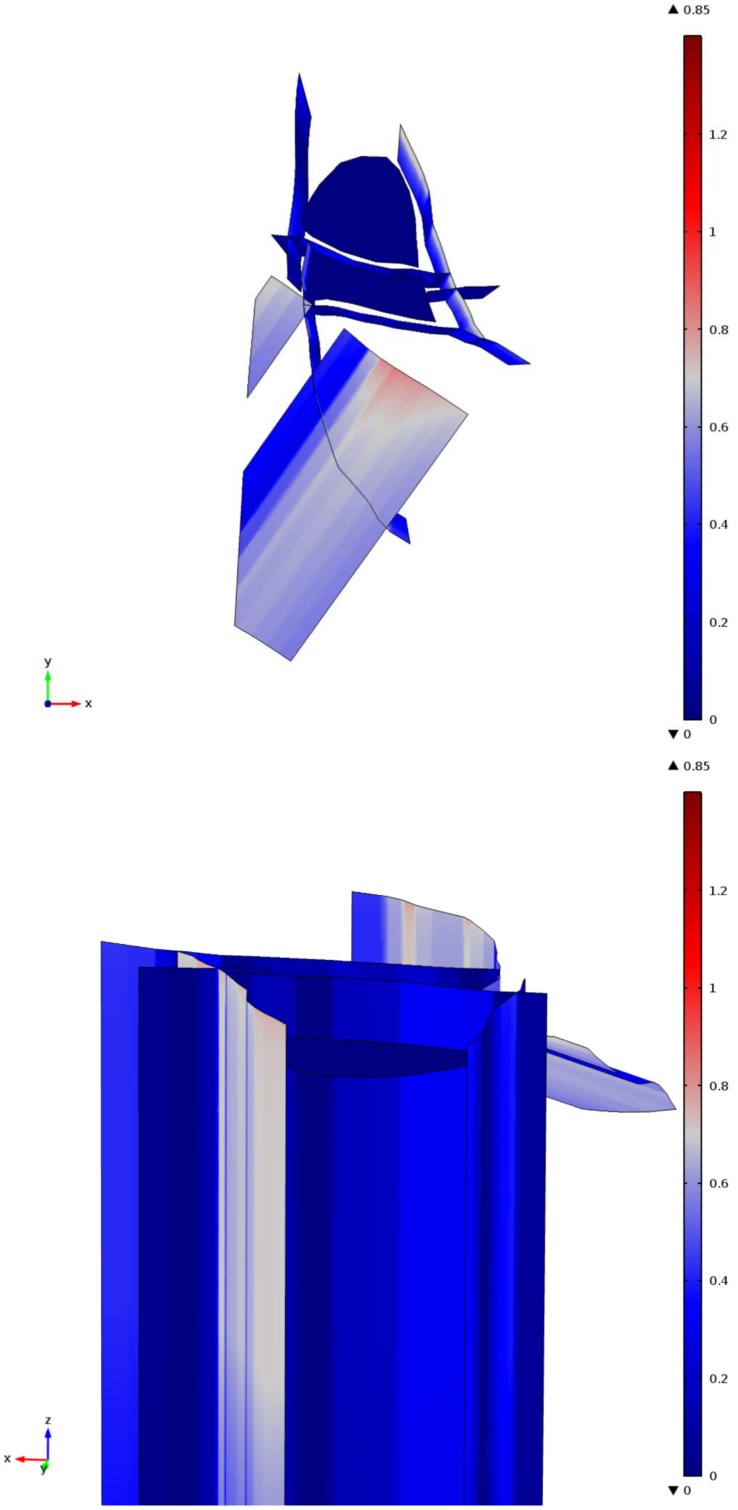

Figure 5.16. Reactivation potential at 4.0 s after the distal M6 earthquake (blue rupture area) in (top) a view from the top on the model and (bottom) a view from NW and background stresses according to the #4 geomecon stress model.

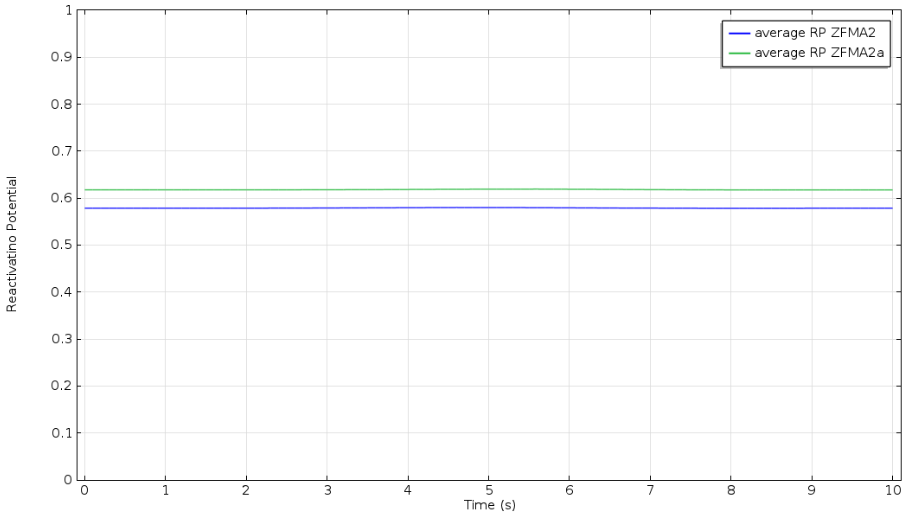

Figure 5.17. Average *rp* for ZFMA2 and ZFMA2a during the distal M6 earthquake (blue rupture area) and background stresses according to the #4 geomecon stress model.

5.3.3. Analysis of the reactivation area of deformation zones

Figure 5.18 and Table 5.2 summarise the area of each fault and the repository at the most critical time step, where the reactivation potential is larger than 0.7. Furthermore, the areas are given in Table 5.2 in percent with regard to the total size of the fault. The given size and the related percentage hold only for the chosen geometry and boundary conditions.

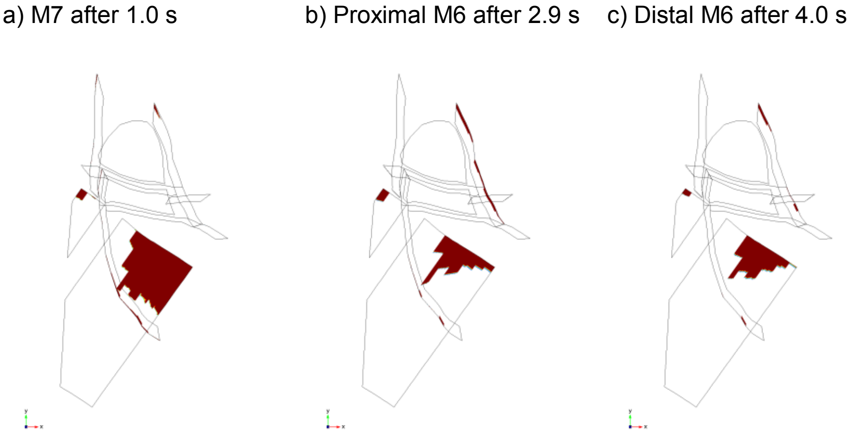

Figure 5.18. Area with *rp* > 0.7 for: a) M7, b) proximal M6, and c) distal M6 earthquake realisations using the #4 geomecon stress field evaluated at the most critical time steps.

Table 5.2. Maximum reactivation area of the local deformation zones where *rp* > 0.7. The specific values hold only for the chosen model boundary (#4 geomecon stress field) conditions and geometry.

	M7 at 1 s [km^2]	**% of the area**	**Proximal M6 at 2.9 s [km^2]**	**% of the area**	**Distal M6 at 4 s [km^2]**	**% of the area**
Repository	0,000	0,0	0,000	0,0	0,000	0,0
ZFMA2a	0,059	6,7	0,071	8,1	0,032	3,7
ZFMA2	2,516	24,7	0,931	9,1	1,012	9,9
ZFMNW1200	0,572	1,2	0,000	0,0	0,000	0,0
ZFMNW0809A	0,827	1,6	7,602	14,4	2,925	5,6
ZFMWNW0123	4,669	6,1	2,030	2,6	0,894	1,2
ZFMENE0060A	0,012	0,0	0,000	0,0	0,000	0,0
ZFMENE0060A	0,016	0,1	0,000	0,0	0,000	0,0
ZFMENE0062A	0,070	0,1	0,000	0,0	0,000	0,0

5.3.4. Analysis of the induced movements on deformation zones

The secondary maximum shear displacement of deformation zones and for the repository plane, acting as a plane of weakness, induced by the simulated earthquakes M7, proximal and distal M6, is given in Tables 5.3, 5.4, and 5.5. The deformation zones and the repository are modelled as thin elastic layers as described in Appendix 2.4. The tables show the results for the case of very low stiffness values, i.e. as for the Singö deformation zone in Table A2.2. The results for thin elastic layers with the high stiffness values, i.e. as for the fracture domain FFM01 in Table A2.2, the maximum shear displacements are well below 2 mm for all faults and the repository plane.

The maximum shear displacement of about 2 m is observed for zone ZFMNW0809A during the M7 earthquake. For the two M6 earthquakes, the maximum shear displacement falls down to approximately 0.2 m and 0.005 m for the proximal and distal earthquake, respectively.

Figure 5.19 shows a plot of the induced secondary shear displacements given in Tables 5.3 to 5.5 versus to the horizontal distance from the point of maximum displacement on the host fault. Also the displacements on the host faults are presented for a distance equal to zero for the three modelled earthquakes. It can be observed that the overall size of the shear displacements decreases with decreasing magnitude of the triggering earthquake and increasing distance from it. Within the data of a single event (e.g. proximal or distal M6), the correlation is week. This is due to the fact that the deformation zones are close to each other and the correlation is perturbed by effects of deformation zone orientation. However, since the zones have similar sizes and similar distances to the point of maximum displacement on the host fault, the plot is still significant for showing the decrease of the induced movements with increasing distance from the host faults.

Table 5.3. Maximum shear displacements and distance to the earthquake recorded during the M7 earthquake.

	Maximum shear displacement [mm]	**Distance from earthquake (max. displacement on host fault) [m]**
Repository	91.26	11524
ZFMA2a	138.6	12060
ZFMA2	353	9711
ZFMNW1200	838.6	13892
ZFMNW0809A	2009.9	11725
ZFMWNW0123	2217	10594
ZFMENE0060A	640.9	12605
ZFMENE0060B	275	10966
ZFMENE0062A	920	10981

Table 5.4. Maximum shear displacements and distance to the earthquake recorded during the proximal M6 earthquake.

	Maximum shear displacement [mm]	**Distance from earthquake (max. displacement on host fault) [m]**
Repository	3.85	2679
ZFMA2a	18.7	4380
ZFMA2	26.44	5138
ZFMNW1200	62.2	3251
ZFMNW0809A	183.52	1614
ZFMWNW0123	74.25	4191
ZFMENE0060A	29.49	2853
ZFMENE0060B	38.89	3020
ZFMENE0062A	55.06	3778

Table 5.5. Maximum shear displacements and distance to the earthquake recorded during the distal M6 earthquake.

	Maximum shear displacement [mm]	Distance from earthquake (max. displacement on host fault) [m]
Repository	0.11	22353
ZFMA2a	0.67	21593
ZFMA2	3.08	18852
ZFMNW1200	5	23464
ZFMNW0809A	3.69	21279
ZFMWNW0123	6.8	17638
ZFMENE0060A	4.9	22311
ZFMENE0060B	1.1	21277
ZFMENE0062A	5.28	20365

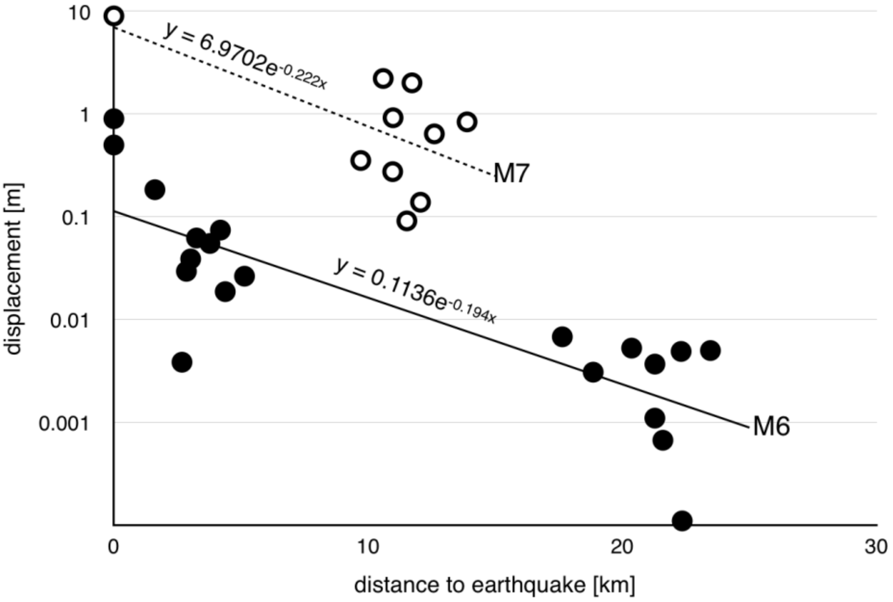

Figure 5.19. Shear displacements versus horizontal distance to the point of maximum displacement on the host fault. Circles mark data from the M7 earthquake, black points are data from the two M6 events (proximal and distal). The displacements on the host faults are shown together with the induced secondary displacements.

5.3.5. Analysis of the potential for deformation zone growth

The static analysis of the growth of deformation zone as a consequence of an earthquake on a regional fault is problematic since the specific stress state applied to a deformation zone varies in reality, and a particular stress state only acts in a single point and propagate with time. The evaluation via the intensity factor K_{II} value according to Sec. 2.3.3 can therefore be regarded as conservative. For the analyses below, the points in time with the maximum stress difference in horizontal principal stress directions are taken for the proximal M6 and the M7 earthquakes while the vertical stress is not changed. The principal stress magnitudes are assumed to be SH = 43 MPa and Sh = -0.7 MPa for the M7 event, and SH = 37.5 MPa and Sh = 12 MPa for the proximal M6 event, respectively. The results are valid for the repository depth only.

Figure 5.20 to 5.23 show the K_{II} values for selected deformation zones when subjected to the peak horizontal stress difference as measured in the repository plane during the M7 and the proximal M6 earthquake. The results are consistent with the general analysis of the reactivation potential. However, as already stated above, those K_{II} values actually correspond to small areas of the deformation zones and at a particular point in time.

During the M7 earthquake, all the applied background stress fields lead to the same deformation zones showing growth potential. These zones are ZFMA2, WNW and NW striking deformation zones. ENE striking deformation zones remain stable. For the proximal M6 earthquake, ZFMA2 and WNW striking deformation zones show growth potential with background stresses according to the #4 geomecon stress model. If background stresses according to the #1 to #3 SKB stress models are applied, only ZFMA2 has potential for growth. For friction coefficients as low as 0.4, the WNW striking deformation zones show growth potential also for these background stress conditions.

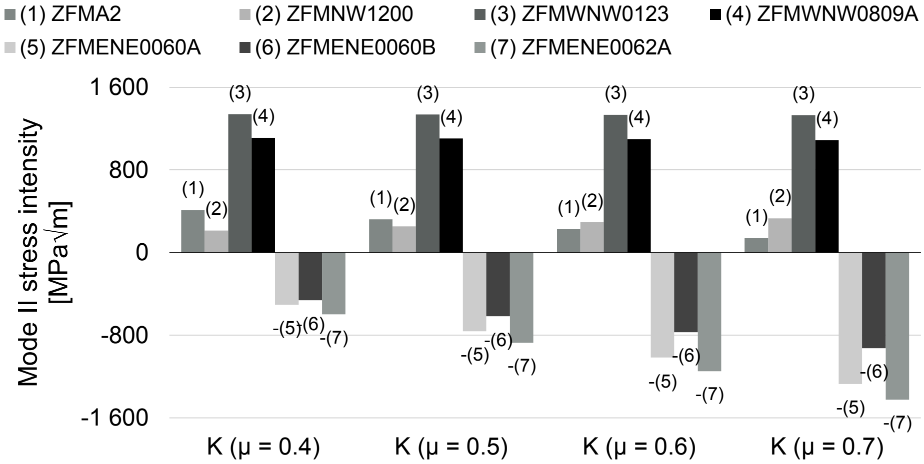

Figure 5.20. K_{II} values for the time of peak induced stresses (1.0 s) after the M7 earthquake (red rupture area). Background stresses are as in the #4 geomecon stress model at 500 m depth. Assuming that K_{II} is indicative for growth of deformation zones, it is evident that only the ENE striking deformation zones will not tend to grow, even assuming the highest frictional strength. Most prone to growth are deformation zones that show a WNW strike.

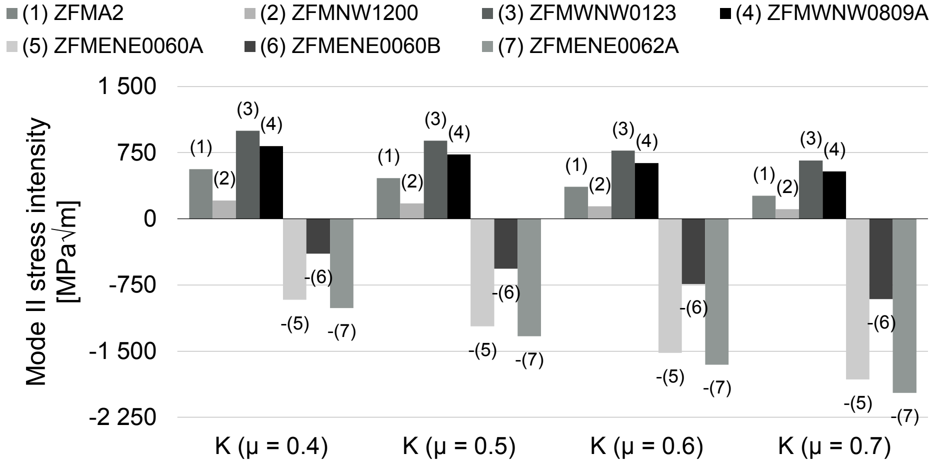

Figure 5.21. K_{II} values for the time of peak induced stresses (1.0 s) after the M7 earthquake (red rupture area). Background stresses are as in the #1 to #3 SKB stress models at 500 m depth. Assuming that K_{II} is indicative for growth of deformation zones, it is evident that only the ENE striking deformation zones will not tend to grow, even assuming the highest frictional strength. Most prone to growth are deformation zones that show a WNW strike.

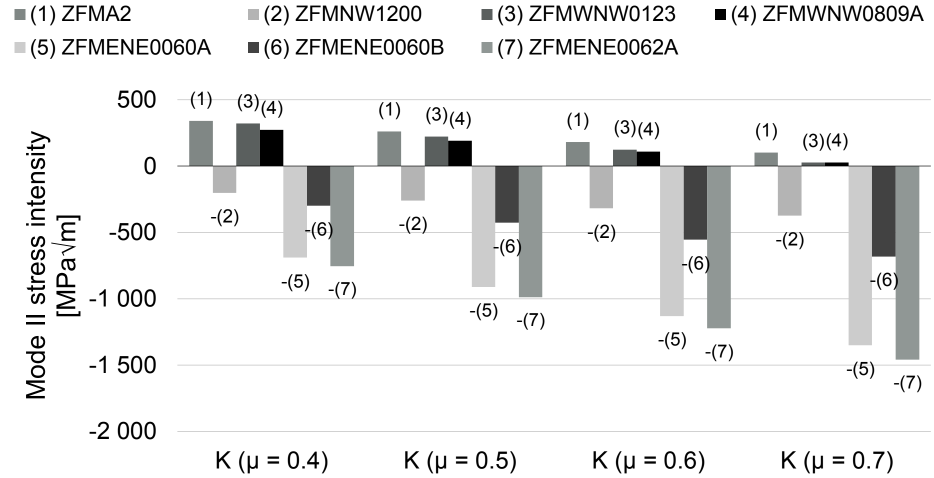

Figure 5.22. K_{II} values for the time of peak induced stresses (2.9 s) after the proximal M6 earthquake (green rupture area). Background stresses are as in the #4 geomecon stress model at 500 m depth. Assuming that K_{II} is indicative for growth of deformation zones, it is evident only the ENE striking deformation zones and ZFMNW1200 will not tend to grow, even assuming the highest frictional strength. Most prone to growth is deformation zone ZFMA2, followed by zones that strike WNW.

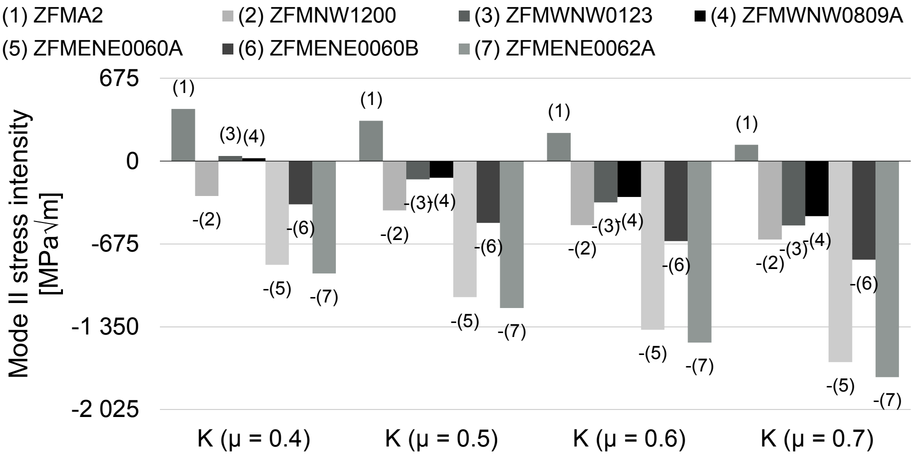

Figure 5.23. K_{II} values for the time of peak induced stresses (2.9 s) after the proximal M6 earthquake (green rupture area). Background stresses are as in the #1 to #3 SKB stress models at 500 m depth. Assuming that K_{II} is indicative for growth of deformation zones, it is evident only ZFMA2 will tend to grow. If the frictional strength is very low (μ = 0.4) also WNW striking deformation zones show a tendency to extend.

Since the stress increments induced by the distal M6 earthquake are small in the vicinity of the repository, the K_{II} analysis yields results comparable to the base case where only background stresses are applied.

5.3.6. Analysis of the repository as a plane of weakness

The repository plane consistently shows zero reactivation potential as shown in Figures 5.6, 5.10 and 5.14. This is the result of the assumption that the principal stresses lie in the horizontal and vertical planes as described in Sec. 2.3.5. The simulations reveal that there is a minor secondary displacement along the repository plane caused by the earthquakes. This results from the repository plane being treated like as a thin elastic layer, which allows for secondary displacements. The actual stiffness of the repository is unknown and is assumed conservatively the same as for the deformation zones. The results should thus be treated with cautiousness. Especially since the modelling approach is not validated for the repository. The M7 earthquake resulted in ca. 91 mm displacement parallel to the repository plane while the M6 earthquakes lead to a maximum displacement of ca. 4 mm for the proximal event.

5.3.7. Analysis of fault-jump potential

In this section the Authors present an approach for evaluating the potential of a fault jump via simulations with the software roxol^{TM}. roxol is a code based on the principles of fracture mechanics and is designed to predict the evolution of fracture networks for user defined loading conditions (Backers et al., 2014b, SSM Technical Note 2014, in preparation). The applicability to large scale problems is therefore not fully assessed. However, large scale deformation zones can be understood as volumes with increased fracture intensity compared to the surrounding rock mass

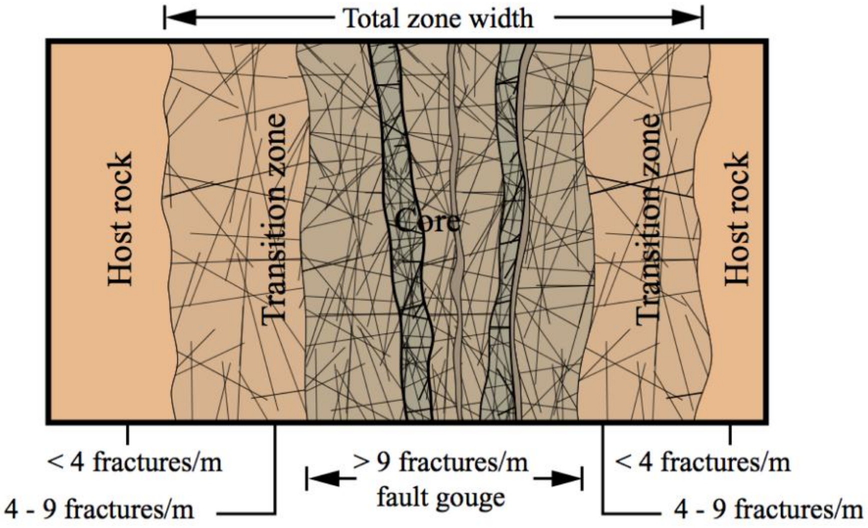

Figure 5.24. Schematic illustration of the structure of a brittle deformation zone (from Munier et al., 2003, SKB R-03-07, Figure 2-1).

(Figure 5.24) with sets of fractures that show preferred orientation. The Authors therefore consider the presented approach valid, especially since a literature review revealed that this topic has not found much attention from the scientific community so far and there are presently no proposed solutions.

The deformation zone geometry around the repository reveals one T-termination between deformation zones ZFMENE0060A and ZFMWNW0123 (cf. Figure 3.3), where a potential fault jump might pose a risk to the repository integrity. Fault jump denotes the growth of a fault-end that is truncated against another fault, beyond the other fault. For the following analysis the geometry was significantly simplified. This generalisation has the advantage of a future possible extrapolation to other localities at the site where fault jump might be identified as a risk. A potential jump of deformation zone ZFMWNW0123 would lead to an intrusion into the repository volume. Therefore, the stress redistributions at the T-termination, for stresses as they occur during the simulated earthquake of magnitude M7 on the Singö fault are investigated.

Model setup

The 2D model is built by a 400 m × 400 m square with the orthogonal deformation zone termination at its approximate centre, representing a horizontal cross section through the critical deformation zones at repository depth. The coordinate system of the model is aligned to the direction of the far field principal stresses with SH parallel to the model x-axis and and Sh parallel to the y-axis, respectively. The two deformation zones are modelled as straight planes parallel to these coordinate axes (Figure 5.25).

The fault zones are represented by single fractures of 174 m and 240 m length and fracture networks around them, corresponding to zone ZFMWNW0123 and ZFMENE0060A, respectively. Eleven different realisations of the deformation zones were used in order to incorporate a variety of possible deformation zone features (Table 5.6). In general, these models consist of a core of the deformation zone including potential slip planes, and a fractured damage zone or transition zone according to the general structure of brittle deformation zones (Figure 5.24). In the realisations, the single major fractures represent the core, whilst a network of smaller fractures of 10-25 m length account for the fractured damage zone (Figure 5.26). The deformation zone thickness estimated Stephens et al. (2007, SKB R-07-45) was between 10 and 64 m for both deformations zones. In the simulations, the thickness was assumed to range between 8 and 15 m. In the context of a fault-jump scenario, a deformation zone of smaller width should undergo larger stress concentrations and thus be more prone to potential slip movements and fault growth.

The same boundary conditions were used for all simulations. They comprised displacement boundaries (“roller boundaries”) on the top and right boundary of the model, as well as static stresses on the bottom and left boundary. Different stress conditions were assigned to the two segments of the left boundary on each side of deformation zone ZFMWNW0123 to simulate the shear loading. On the upper side, 36.5 MPa were applied while on the lower side, only 31 MPa were applied. These stress conditions were derived by the large scale simulation of a M7 earthquake. The stresses acting in the direction of the horizontal principal stresses of the far field during the earthquake were extracted for one observation point on each side of ZFMWNW0123. The most critical stress state related to a possible fault jump is the state of maximum shear stress acting on ZFMWNW0123, i.e. in the x-direction of the model. In the earthquake simulation, this state occurs at 2.1 s after the main rupture. Accordingly, the stresses in x-direction at the observation points were used for the respective boundaries. For the stress boundary condition acting from the bottom in the y-direction, the mean value of 12 MPa at the observation points was used.

Note that other stress states with a similarly high shear stress in x-direction occurred at 2.8 s and 3.4 s for the same M7 earthquake. In these cases, the stress magnitudes are smaller in the x-direction, while the stresses acting in y-direction normal to ZFMWNW0123 are of larger magnitudes. Thus, both stress states should be more stable than the one used for the simulations here.

Table 5.6. Summary of the geometric features and their combination in the different simulations (SM) of a fault jump at a T-termination (y: yes, n: no).

SM No.	Continuous core fracture	Fracture length [m]	No. of fractures	Fracture orientation [°]	Fracture zone width [m]
1	y	25	42	0/90 ± 10	15
2	n	25	40	0/90 ± 10	15
3	y	10	65	0/90 ± 10	8
4	n	10	63	0/90 ± 10	8
5	y	10	65	15/75 ± 2	10
6	n	10	63	15/75 ± 2	10
7	y		2	0/90 ± 10	0
8	horizontal	10	64	0/90 ± 10	8
9	horizontal	10	64	15/75 ± 2	10
10	y	10	122	0/15 ± 4 90/75 ± 4	12
11	horizontal	10	121	0/15 ± 4 90/75 ± 5	12

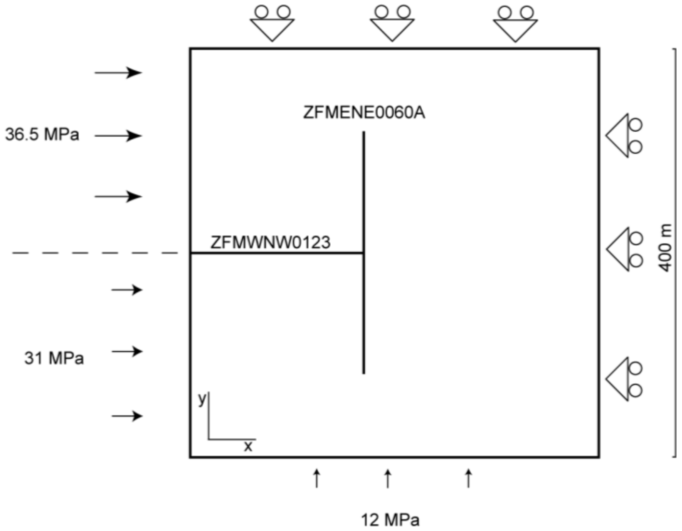

Figure 5.25. Boundary conditions for the T-termination analyses. The top and right sides of the model are defined as displacement boundaries (“roller boundaries”), while static stresses are applied on the bottom and left sides. Different stress conditions were assigned to the two segments of the left boundary on each side of deformation zone ZFMWNW0123 as derived from the simulation of the M7 earthquake.

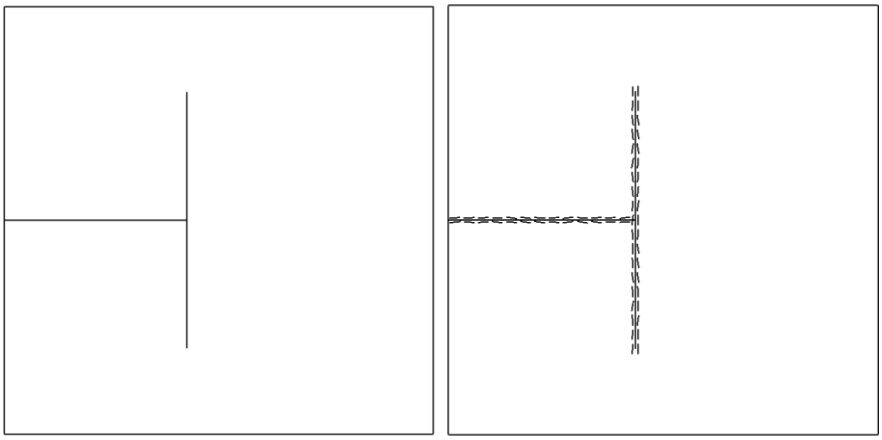

Figure 5.26. General examples of the geometry of the realisations, with two large single fractures (left), and smaller fractures of varying orientation representing the fault core and the damage zone (right).

Simulation results for a fault jump at a T-termination

The results are presented in terms of the resulting maximum shear stress in the model. Figure 5.27 to 5.37 show the maximum shear stress distribution around the modelled geometries.

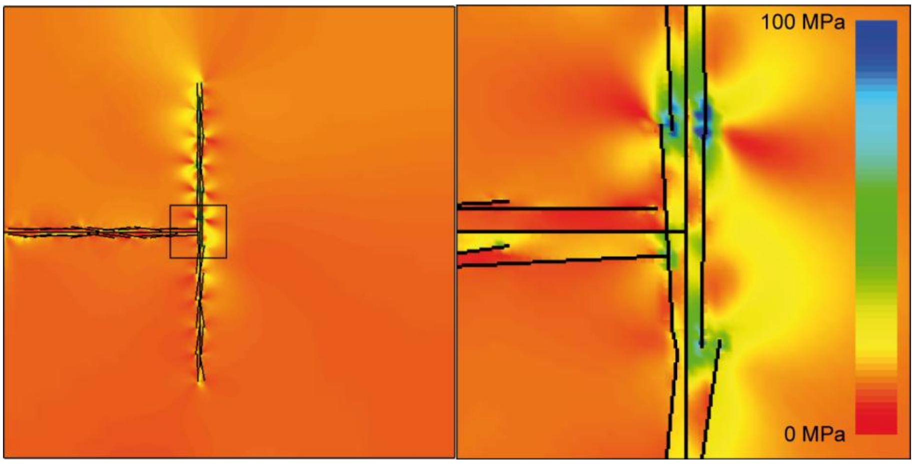

Figure 5.27. Fault jump model No. 1. The detail in the left figure (50 x 50 m) is magnified in the right figure. The maximum resulting shear stress around the T-termination is 19.2 MPa.

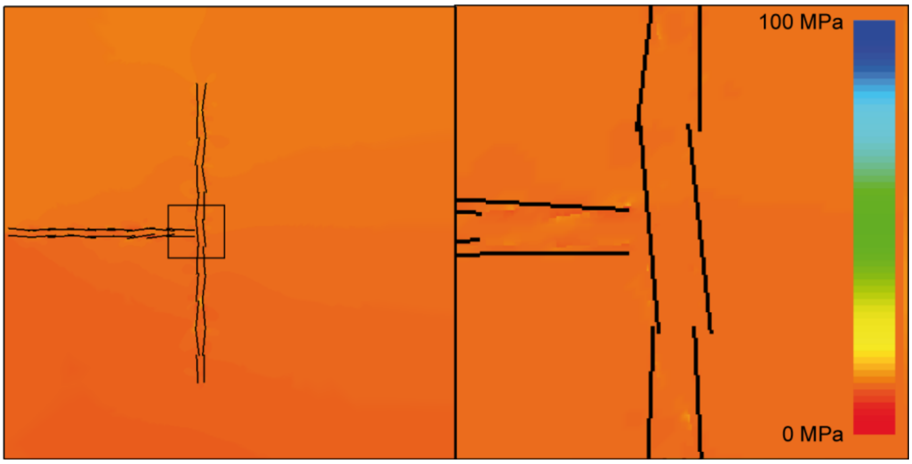

Figure 5.28. Fault jump model No. 2. The insert in the left figure (50 x 50 m) is magnified in the right figure. The maximum resulting shear stress around the T-termination is 11.7 MPa.

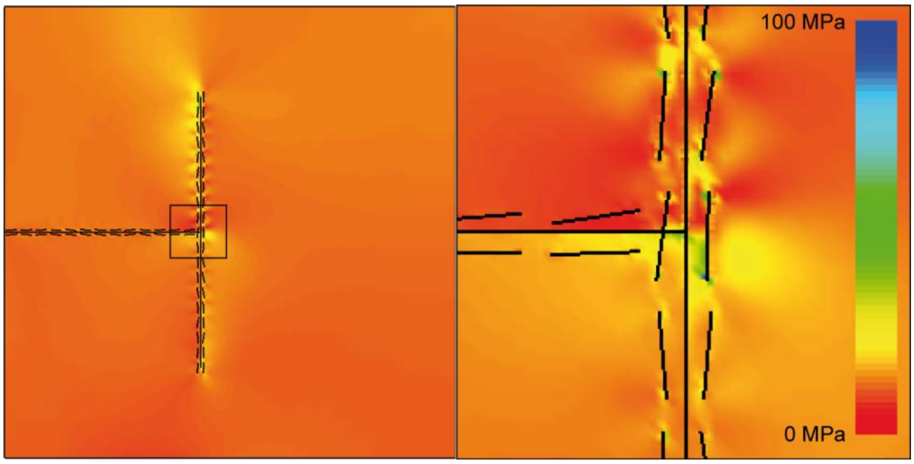

Figure 5.29. Fault jump model No. 3. The insert in the left figure (50 x 50 m) is magnified in the right figure. The maximum resulting shear stress around the T-termination is 20.3 MPa.

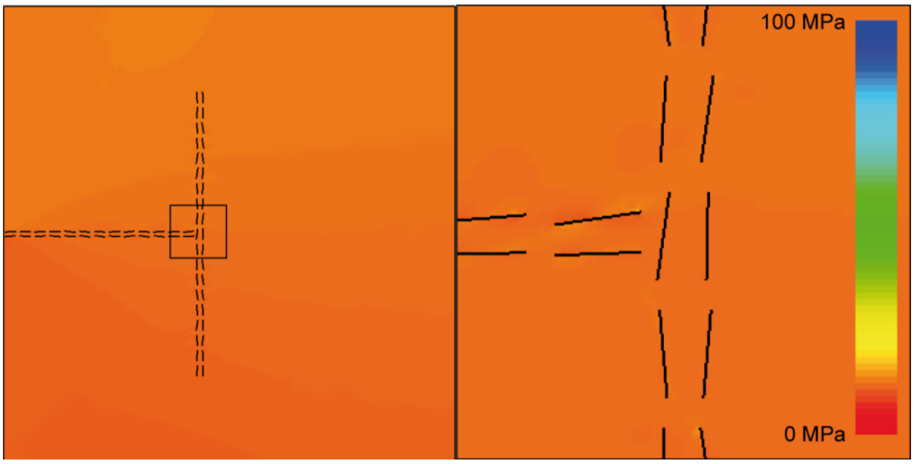

Figure 5.30. Fault jump model No. 4. The insert in the left figure (50 x 50 m) is magnified in the right figure. The maximum resulting shear stress around the T-termination is 11.7 MPa.

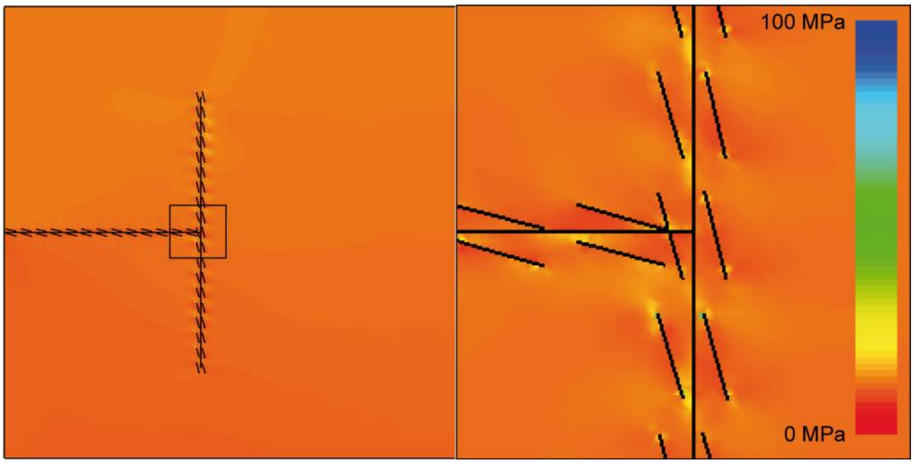

Figure 5.31. Fault jump model No. 5. The insert in the left figure (50 x 50 m) is magnified in the right figure. The maximum resulting shear stress around the T-termination is 12.1 MPa.

Figure 5.32. Fault jump model No. 6. The insert in the left figure (50 x 50 m) is magnified in the right figure. The maximum resulting shear stress around the T-termination is 12.2 MPa.

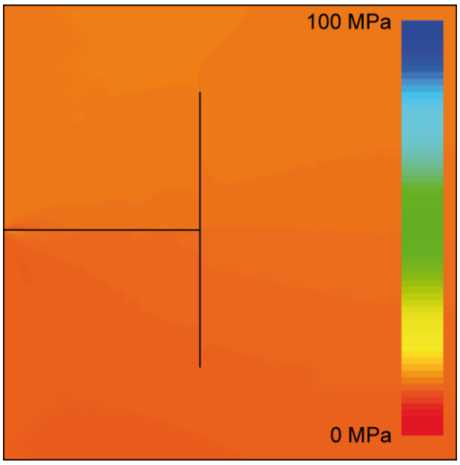

(Magnigication intentionally not shown)

Figure 5.33. Fault jump model No. 7. The maximum resulting shear stress around the T-termination is 12.2 MPa. The insert in the left figure is not needed due to too uniform stresses.

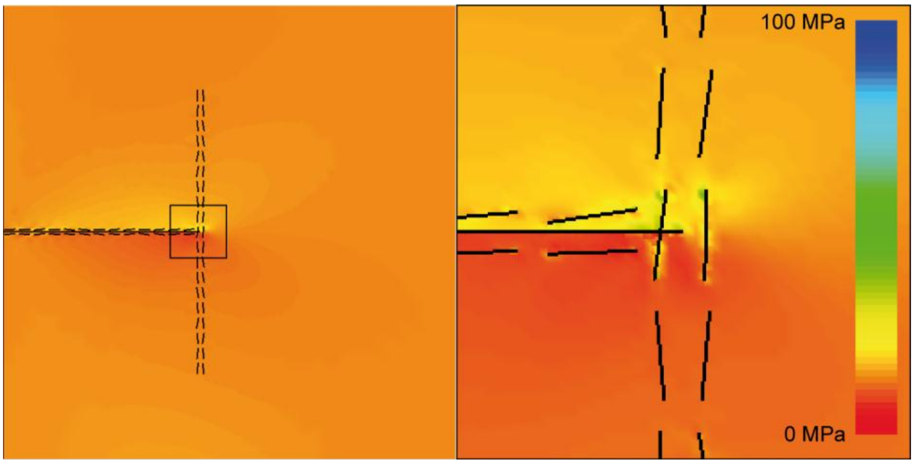

Figure 5.34. Fault jump model No. 8. The insert in the left figure (50 x 50 m) is magnified in the right figure. The maximum resulting shear stress around the T-termination is 15.5 MPa.

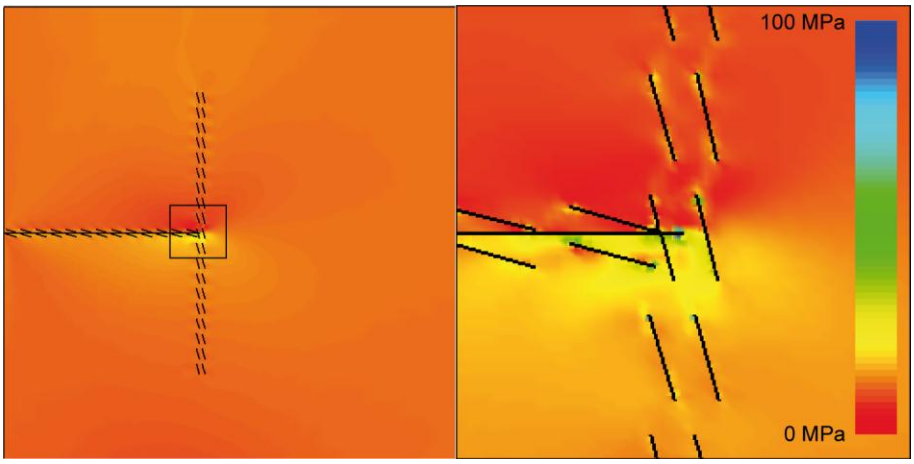

Figure 5.35. Fault jump model No. 9. The insert in the left figure (50 x 50 m) is magnified in the right figure. The maximum resulting shear stress around the T-termination is 18.1 MPa.

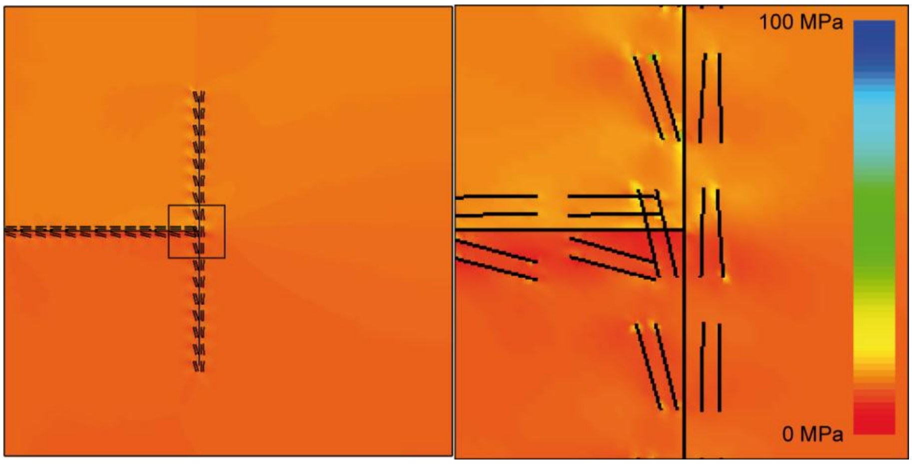

Figure 5.36. Fault jump model No. 10. The insert in the left figure (50 x 50 m) is magnified in the right figure. The maximum resulting shear stress around the T-termination is 12.2 MPa.

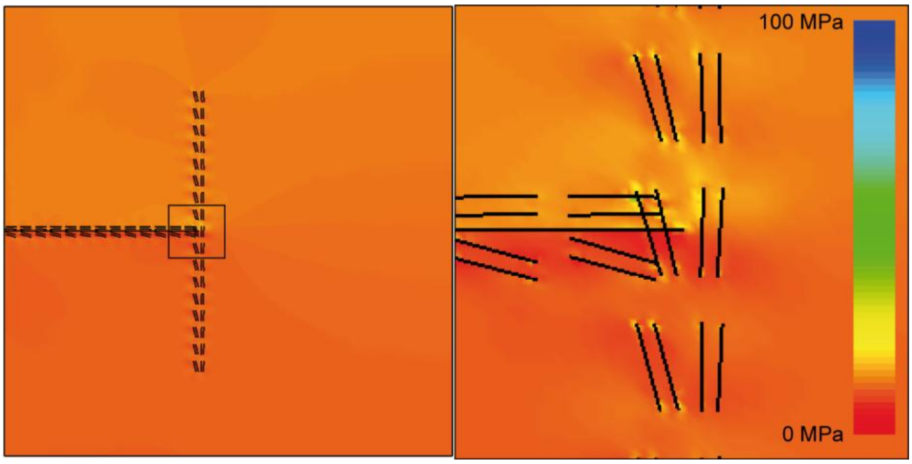

Figure 5.37. Fault jump model No. 11. The insert in the left figure (50 x 50 m) is magnified in the right figure. The maximum resulting shear stress around the T-termination is 13.8 MPa.

The results show that throughout the different combinations of fracture elements, there is no configuration that results in especially high shear stresses at the T-termination between ZFMENE0060A and ZFMWNW0123 or beyond. The highest shear stresses generally evolve at free fracture tips and where fracture tips approach each other. Therefore a coalescence of the individual fractures in the deformation zones might happen. However, there is no clear indication for a propagation of the tip of ZFMWNW0123 beyond its present termination. It can be observed, however, that those simulations that include the fault core as a singular element show overall higher shear stresses.

Limitations of the simulation of a fault jump at a T-termination

There are some limitations to this modelling approach of a fault jump over a T-termination:

- The model only considers the horizontal plane and neglects the stress increments in z-direction caused by the earthquake;
- The deformation zones feature an array of fractures; the degree of their interlink is not known. If the deformation zone is mostly consisting of linked fractures, the stress concentration at the T-termination may be larger and hence the potential for a propagation of the zone beyond the arrester position against the other zone;
- The modelling has not included a distinct fracture network as potential nucleus for deformation zone evolution on the other side of the T-termination. From an existing DFN fracture reactivation and coalesce might lead to formation of a new deformation zone extension. This issue is analysed in Backers et al. (2014b, SSM Technical Note 2014, in preparation);
- The problem of fault jump cannot be fully understood by a geomechanical evaluation only. The fault-jump potential should, amongst others, be largely influenced by the mineralogy of the involved faults, especially the fault in the arresting position. An arresting fault that is completely healed should represent less of a barrier than a recently active fault.

5.4. The Consultants' assessment on the influence of an earthquake on the deformation zone stability and growth

The simulations of three different earthquakes reveal that the impact on deformation zone stability scales (a) with magnitude and (b) with distance of the rupture area to the respective deformation zones. Thereby, it was found that there is a massive difference between the effects of magnitude M7 and M6 regarding the induced stress increments and deformation zone stability. For the M7 earthquake, the maximum measured horizontal stress increment is about 9 MPa, while for the proximal M6 earthquake that increment is only 2 MPa. The stress increments measured after the distal M6 event is even smaller, 0.12 MPa, and does not affect the stability of the deformation zones close to the repository.

For the M7 and the proximal M6 earthquake, a change in deformation zone stability is observed. Both events produce *rp* values above any reasonable assumptions of friction coefficients, and thus would certainly lead to unstable conditions. But it was also observed that those high reactivation potentials are very localised and restricted to small patches on the respective affected deformation zones. The simulations show that those patches are mainly restricted to shallow depths (<100 m). This effect depends on the fact that the magnitudes of the background stresses are very small at the shallow depth and are of the same order of magnitude as the earthquake induced stress increments. Thus, conclusions can be drawn that the stability of the zones impacted by an earthquake on the regional deformation zones generally increases with depth.

From a scoping Fracture Mechanics approach analysis, it was concluded that there is little potential for deformation zone jump at the T-termination of deformation zones.

6. The Consultants' overall assessment on the probability and extent of blind faults and fault-end growth at Forsmark

The following statements can be concluded from the assessment:

Thermal phase

- The thermal phase stabilises sub-vertical deformation zones with orientations tangential to the repository circumference;
- During the thermal phase deformation zones that are affected by the differential stress change due to the heating, i.e. dipping zones and non-tangential vertical deformation zones, might exhibit an increase in reactivation potential.

Glacial phase

- During the glaciation, the effect of ice retreat is leading to instability on the shallow dipping deformation zone ZFMA2a, independently of the assumed stress model;
- During glaciation, some areas of the vertical deformation zones might become reactivated depending on the stress model;
- If the newly proposed stress model by Backers et al. (2014a, SSM Technical Note 2014:10) is adopted, also the forebulge might introduce massive reactivation of vertical deformation zones striking WNW;
- During glaciation, certain parts of the regional deformation zones are subject to potential reactivation that can lead to large magnitude earthquakes. This aspect is further analysed in the following.

Earthquake scenario

- An earthquake that nucleates on a regional deformation zone that defines the Forsmark tectonic lens leads to significant instability of the deformation zones around the repository. Thereby, only small areas of the deformation zones become critical at the same point in time. Those areas shift along the secondary deformation zones as the seismic waves propagate;
- The maximum observed reactivation potential during a seismic event decreases with decreasing earthquake magnitude and increasing distance from the rupture area to the zone experiencing the secondary movement;
- The repository horizon does not appear to be a plane of weakness. In all analyses, the reactivation potential is extremely low on the horizontal plane at repository depth;
- Fault jump appears to be unlikely from the performed analyses of T-intersections between deformation zones.

It should be mentioned that, besides reactivation of deformation zones considered here, an earthquake on one of the large deformation zones can trigger both a new earthquake at another deformation zone, and or a large displacements on target fractures in the repository. The impact of the combination of primary and secondary events has not been considered here.

Table 6.1 summarises the results of fault-tip stress intensity analyses that have been performed for all loading scenarios. Because those analyses reflect the results from the numerical simulations quite well, they can serve for a general overview of the most critical times during long-term evolution of the repository for the most critically oriented deformation zones. However, the fault-tip stress intensity analysis has strong limitations for the application to large scale problems (cf. Sec. 2.3.3). It considers only the average orientation and stability of the deformation zones at 500 m depth. The reader should also keep in mind that the most critical group of gently dipping deformation zones are underrepresented in Table 6.1, with only one deformation zone (ZFMA2). Many blind-faults, if any of significant size, are present at Forsmark and will fall into this category. Regarding the reactivation potential of faults of unknown orientation, the box-plots in Chapter 2 should be consulted, which show the maximum reactivation potential independently of the presence of deformation zones with a certain orientation.

In general, it can be concluded that most of the analyses by SKB appear to be adequate. For the thermal and glacial phase, the conclusions drawn by SKB are generally in line with the results of this assessment. However, the results here show that induced seismic events might appear in the post-glacial phase, and SKB addressed this issue only marginally.

The Consultants' assessment has shown that fault jump appears not to be an issue with the given assumptions. Another conclusion is that the repository itself seems not to act as a plane of weakness. However, the analyses have shown that the deformation zones show large secondary displacements of up to 2 m and become unstable during seismic events of large magnitude on a regional deformation zone, if soft deformation zone properties are chosen. This might lead the fractures in the deformation zones to interlink and create increased pathways for fluids.

Any secondary shear movements on target fractures in the repository volume were not addressed in this assessment.

Table 6.1. Summary of results form the fault tip stress intensity analyses for the #4 geomecon and the #1-3 SKB stress models. “+” indicates that no fault growth was predicted while a “-” indicates that fault instability and growth is predicted.

	Base case	**Thermal**	**Glaciation**					**Earthquake**		
			T1	**T2**	**T3**	**T4**	**T5**	**M7**	**M6 proximal**	**M6 distal**
#4 geomecon stress model										
ZFMA2	+	-	+	-	+	+	-	-	-	+
ZFMNW1200	+	+	+	+	+	+	+	-	+	+
ZFMWNW0123	+	+	+	+	-	+	+	-	-	+
ZFMWNW0809A	+	+	+	+	-	+	+	-	-	+
ZFMENE0060A	+	+	+	+	+	+	+	+	+	+
ZFMENE0060B	+	+	+	+	+	+	+	+	+	+
ZFMENE0062A	+	+	+	+	+	+	+	+	+	+
#1-3 SKB stress models										
ZFMA2	-	-	+	-	-	+	-	-	-	-
ZFMNW1200	+	+	+	+	+	+	+	-	+	+
ZFMWNW0123	+	+	+	+	+	+	+	-	+	+
ZFMWNW0809A	+	+	+	+	+	+	+	-	+	+
ZFMENE0060A	+	+	+	+	+	+	+	+	+	+
ZFMENE0060B	+	+	+	+	+	+	+	+	+	+
ZFMENE0062A	+	+	+	+	+	+	+	+	+	+

7. References

Backers T, Meier T, Gipper P and Stephansson O, 2014a. Rock Mechanics - Confidence of SKB's models for predicting the occurrence of spalling - Main Review Phase. SSM Technical Note 2014:10, Swedish Radiation Safety Authority (SSM), ISSN: 2000-0456.

Backers T, Meier T, Gipper P, Stephansson O, 2014b. Rock Mechanics - Assessing the likelihood and extend of fracture growth in the KBS-3 repository at Forsmark – Main Review Phase. SSM Technical Note 2014 (in preparation). Swedish Radiation Safety Authority (SSM).

Brown ET, Hoek E, 1978. Trends in relationships between measured in situ stresses and depth. Int. J. Rock Mech. Min. Sci. & Geomech. Abstr. 15: pp 211–215.

Byerlee J, 1978. Friction of rocks. Pure and Applied Geophysics 116: 615-626.

Heidbach O, Tingay M, Barth A, Reinecker J, Kurfeß D, Müller B, 2008. The World Stress Map database release 2008. doi:10.1594/GFZ.WSM.Rel2008, 2008.

Freeman T T, Chalaturnyk R J, Bogdanov I I, 2008. Fully Coupled Thermo-Hydro-Mechanical Modeling by COMSOL Multiphysics, with Applications in Reservoir Geomechanical Characterization. Proceedings of the COMSOL Conference 2008 Boston.

Jaeger J C, Cook N G W, Zimmermann R W, 2007. Fundamentals of Rock Mechanics, fourth ed. Blackwell Publishing, Oxford, UK.

Johnston, A C, 1994. Seismotectonic interpretations and conclusions from the stable continental region seismicity database, in The Earthquake of Stable Continental Regions. Volume 1: Assessment of Large Earthquake Potential, Johnston A C, Coppersmith K J, Kanter L R and Cornell C A (Editors), Electric Power Research Institute.

Lagerbäck R, Sundh M, 2008. Early Holocene faulting and paleoseismicity in northern Sweden. Research Paper C 836. SGU – Sveriges Geologiska Undersökning.

Lawn B, 1993. Fracture of Brittle Solids – Second Edition, 378 pp. Cambridge: Cambridge University Press.

Leonard M, 2010. Earthquake Fault Scaling: Self-Consistent Relating of Rupture Length, Width, Average Displacement, and Moment Release. Bull. Seismol. Soc. Am. 100, no. 5A, 1971-1988.

Lund B, Zoback M D, 1999. Orientation and magnitude of in situ stress to 6.5 km depth in the Baltic Shield. In: International Journal of Rock Mechanics and Mining Sciences, vol 36: pp 169–190.

Lundborg N, 1967. The strength-size relation of granite. Int. J. Rock Mech. Min. 4:269-272.

SKB TR-90-30. Slunga R, 1990. The earthquakes of the Baltic shield. Swedish Nuclear Fuel and Waste Management Company (SKB).

SKB TR-97-07. La Pointe P, Wallmann P, Thomas A, Follin S, 1997. A methodology to estimate earthquake effects on fractures intersecting canister holes. Swedish Nuclear Fuel and Waste Management Company (SKB).

SKB TR-00-08. La Pointe P R, Cladouhos T T, Outters N, Follin S, 2000. Evaluation of the conservativeness of the methodology for estimating earthquake-induced movements of fractures intersecting canisters. Swedish Nuclear Fuel and Waste Management Company (SKB).

SKB R-00-15. Andersson J, Ström A, Almén K-E, Ericsson LO, 2000. Vilka krav ställer djupförvaret på berget? Geovetenskapliga lämplighetsindikationer och kriterier för lokalisering och platsutvärdering (in Swedish). Swedish Nuclear Fuel and Waste Management Company (SKB).

SKB R-01-15. Munier R, Hermansson J, 2001. Metodik för geometrisk modellering. Presentation och administration av platsbeskrivande modeller (in Swedish). Swedish Nuclear Fuel and Waste Management Company (SKB).

SKB TR-02-24. Bäckblom G, Munier R, 2002. Effects of earthquakes on the deep repository for spent fuel in Sweden based on case studies and preliminary model results. Swedish Nuclear Fuel and Waste Management Company (SKB).

SKB R-03-07. Munier R, Stenberg L, Stanfors R, Milnes A G, Hermanson J, Triumf C-A, 2003. Geological Site Descriptive Model. A strategy for the model development during site investigations. Swedish Nuclear Fuel and Waste Management Company (SKB).

SKB TR-04-02. Börgesson L, Johannesson L-E, 2003. Earthquake induced rock shear through a deposition hole. Effect on the canister and the buffer. Swedish Nuclear Fuel and Waste Management Company (SKB).

SKB R-05-35. Sjöberg J, Lindfors U, Perman F, Ask D, 2005. Evaluation of the state of stress at the Forsmark site. Preliminary site investigation Forsmark area - version 1.2. Swedish Nuclear Fuel and Waste Management Company (SKB).

SKB R-06-48. Fälth B, Hökmark H, 2006. Seismically induced slip on rock fractures. Results from dynamic discrete fracture modeling. Swedish Nuclear Fuel and Waste Management Company (SKB).

SKB TR-06-23. Näslund J-O, 2006. Ice sheet dynamics, in climate and climate related issues for the safety assessment SR-Can. Swedish Nuclear Fuel and Waste Management Company (SKB).

SKB R-06-67. Bödvarsson R, Lund B, Roberts R, Slunga R, 2006. Earthquake activity in Sweden. Study in connection with a proposed nuclear waste repository in Forsmark or Oskarshamn. Swedish Nuclear Fuel and Waste Management Company (SKB).

SKB R-07-06. Glamheden R, Hansen LM, Fredriksson A, Bergkvist L, Markström I, Elfström M, 2007. Mechanical modelling of the Singö deformation zone. Site descriptive modelling Forsmark stage 2.1. Swedish Nuclear Fuel and Waste Management Company (SKB).

SKB R-07-26. Martin CD, 2007. Quantifying in situ stress magnitudes and orientations for Forsmark Design Step D2. Swedish Nuclear Fuel and Waste Management Company (SKB).

SKB R-07-31. Glamheden R, Fredriksson A, Röshoff K, Karlsson J, Hakami H, Christiansson R, 2007. Rock mechanics Forsmark. Site descrpitive modelling Forsmark stage 2.2. Swedish Nuclear Fuel and Waste Management Company (SKB).

SKB R-07-45. Stephens M B, Fox A, La Pointe P, Simeonov A, Isaksson H, Hermanson J, Öhman J, 2007. Geology Forsmark. Site descriptive modelling Forsmark stage 2.2. Swedish Nuclear Fuel and Waste Management Company (SKB).

SKB P-07-206. Ask D, Cornet F, Fontbonne F, 2007. Forsmark site investigation. Stress measurements with hydraulic methods in boreholes KFM07A, KFM07C, KFM08A, KFM09A and KFM09B. Swedish Nuclear Fuel and Waste Management Company (SKB).

SKB P-07-234. Ask D, 2007. Evaluation of overcoring stress measurements in boreholes KFM01B, DBT-1 and DBT-3 and hydraulic stress measurements in boreholes KFM01A, KFM01B, KFM02A and KFM04A at the Forsmark site. Forsmark site investigation. Swedish Nuclear Fuel and Waste Management Company (SKB).

SKB TR-08-05. Site description of Forsmark at completion of the site investigation phase. SDM-Site Forsmark, 2008. Swedish Nuclear Fuel and Waste Management Company (SKB).

SKB TR-08-11. Fälth B, Hökmark H, Munier R, 2010. Effects of large earthquakes on a KBS-3 repository. Evaluation of modelling results and their implications for layout and design. Swedish Nuclear Fuel and Waste Management Company (SKB).

SKB R-08-65. Sundberg J, Wrafter J, Ländell M, 2008. Thermal properties Forsmark Modelling stage 2.3. Complementary analysis and verification of the thermal bedrock model, stage 2.2. Swedish Nuclear Fuel and Waste Management Company (SKB).

SKB TR-09-15. Lund B, Schmidt P, Hieronymus C, 2009. Stress evolution and fault stability during the Weichselian glacial cycle. Svensk Kärnbränslehantering AB.

SKB TR-09-17. Hartikainen J, Kouhia R, Wallroth T, 2010. Permafrost simulations at Forsmark using a numerical 2D thermo-hydro-chemical model. Swedish Nuclear Fuel and Waste Management Company (SKB).

SKB TR-10-23. Hökmark H, Lönnqvist M, Fälth B, 2010. THM-issues in repository rock. Thermal, mechanical, thermo-mechanical and hydromechanical evolution of the rock at the Forsmark and Laxemar sites. Svensk Kärnbränslehantering AB.

SKB TR-10-49. Climate and climate-related issues for the safety assessment SR-Site. Swedish Nuclear Fuel and Waste Management Company (SKB).

SKB TR-11-01. Long-term safety for the final repository for spent nuclear fuel at Forsmark. Main report of the SR-Site project. Swedish Nuclear Fuel and Waste Management Company (SKB).

Slunga RS, 1991. The Baltic Shield earthquakes.Tectonophysics, 189, pp 323-331.

Stephansson O, Ljunggren C, Jing L, 1991. Stress measurements and tectonic implications for Fennoscandia. Tectonophysics, 189, pp 317–322.

Stirling M, Rhoades D, Berryman K, 2002. Comparison of earthquake scaling relations derived from data of the instrumental and preinstrumental era. Bull. Seismol. Soc. Am. 92, No. 2, 812–830.

Ugural A, Fenster S K, 2011. Advanced Mechanics of Materials and Applied Elasticity, fifth ed. Prentice Hall, 2011.

Wells D L, Coppersmith K J, 1994. New empirical relationships among magnitude, rupture length, rupture width, rupture area and surface displacement. Bull. Seism. Soc. Am. 84(4): pp 974–1002.

APPENDIX 1

Coverage of SKB reports

Table A1.1: Reports covered in the assignment.

Reviewed report	Reviewed Sections	Comments
SKB P-07-206, Forsmark site investigation. Stress measurements with hydraulic methods in boreholes KFM07A, KFM07C, KFM08A, KFM09A and KFM09B	5.3, 5.4, 6, 7, 8	
SKB R-03-07, Geological Site Descriptive Model. A strategy for the model development during site investigations.	2	
SKB R-06-48, Seismically induced slip on rock fractures. Results from dynamic discrete fracture modeling.	6	
SKB R-06-67, Earthquake activity in Sweden. Study in connection with a proposed nuclear waste repository in Forsmark or Oskarshamn.	complete report	
SKB R-07-06, Mechanical modelling of the Singö deformation zone. Site descriptive modelling Forsmark stage 2.1.	12	
SKB R-07-26, Quantifying in situ stress magnitudes and orientations for Forsmark Design Step D2.	complete report	
SKB R-07-31, Rock mechanics Forsmark. Site descrpitive modelling Forsmark stage 2.2.	complete report	
SKB R-07-45, Geology Forsmark. Site descriptive modelling Forsmark stage 2.2.	1, 2, 3, 5	

SKB R-08-65, Thermal properties Forsmark Modelling stage 2.3. Complementary analysis and verification of the thermal bedrock model, stage 2.2.	
SKB TR-90-30, The earthquakes of the Baltic shield.	complete report
SKB TR-97-07, A methodology to estimate earthquake effects on fractures intersecting canister holes.	4, 5
SKB TR-00-08, Evaluation of the conservativeness of the methodology for estimating earthquake-induced movements of fractures intersecting canisters.	4
SKB TR-02-24, Effects of earthquakes on the deep repository for spent fuel in Sweden based on case studies and preliminary model results.	4, 5
SKB TR-06-23, Ice sheet dynamics, in climate and climate related issues for the safety assessment SR-Can.	3.5
SKB TR-08-05, Site description of Forsmark at completion of the site investigation phase. SDM-Site Forsmark, 2008.	2.2.2, 2.3, 6, 7, 11.3, 11.4
SKB TR-08-11, Effects of large earthquakes on a KBS-3 repository. Evaluation of modelling results and their implications for layout and design.	complete report
SKB TR-09-15, Stress evolution and fault stability during the Weichselian glacial cycle.	complete report
SKB TR-10-23, THM-issues in repository rock. Thermal, mechanical, thermo-mechanical and hydromechanical evolution of the rock at the Forsmark and Laxemar sites.	complete report

SKB TR-11-01, Long-term safety for the final repository for spent nuclear fuel at Forsmark. Main report of the SR-Site project.	S1-S5, 4.3, 4.4, 4.5, 4.6, 10.2.2, 10.3.5, 10.4.4, 10.4.5 15.5.12	

APPENDIX 2

3D FEM Model

The 3D finite element (FEM) software COMSOL multiphyiscs (www.comsol.se) was used to evaluate the reactivation potential of existing deformation zones in the surrounding of the planned repository at Forsmark. The employed FEM package is capable of coupling thermo-hydro-mechanic processes, which are expected to affect the repository within its lifetime.

A2.1. Geometry

The geometry of the COMSOL model is based on maps of the repository showing the confining regional deformation zones (SKB TR-11-01, Figure 10-116 and 10-117) and surrounding local deformation zones within the local model area that exceed 3 km surface trace length (SKB TR-11-01, Figure 10-118). The modelled deformation zones are shown in Figure A2.1.

The basic model covers a volume of 25 km in width, 45 km in length and 5 km in depth as shown in Figure A2.2. The longest axis (y-axis) is in direction NW-SE and, hence, sub-parallel to the largest horizontal stress. The x-axis is oriented NE-SW, pointing towards the minimum horizontal stress. The z-axis is oriented vertically and is aligned with the vertical stress. The tectonic lens is located within the model volume, and is defined by the intersection of the Eckjarfjärden, Singö and Forsmark deformation zones. Deformation zones and splays of deformation zones outside the lens are not included in the model. For the sake of simplicity, deformation zones with dips larger then 80° are considered vertical.

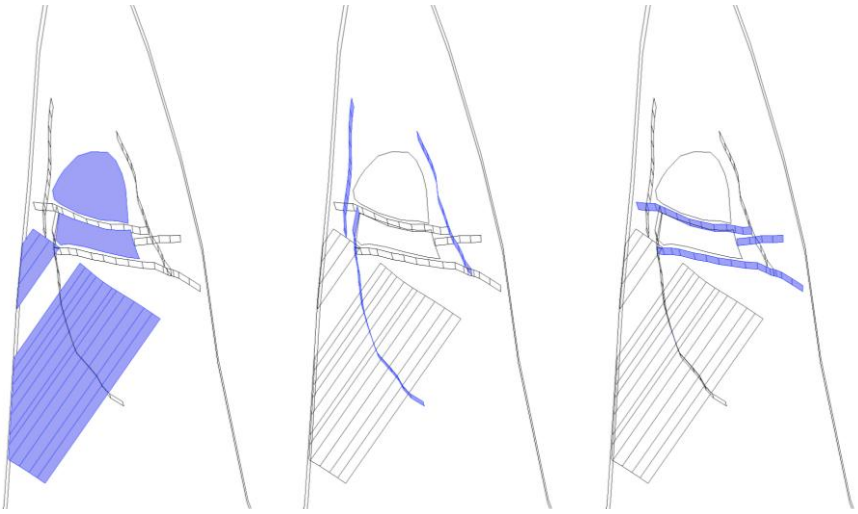

Figure A2.1. (Left) repository and patches of ZFMA2. (Middle) in blue from left to right ZFMNW1200, ZFMWNW0123, ZFMWNW0809A. (Right) in blue from top to bottom ZFMENE0060A, ZFMENE0060B, and ZFMENE0062A.

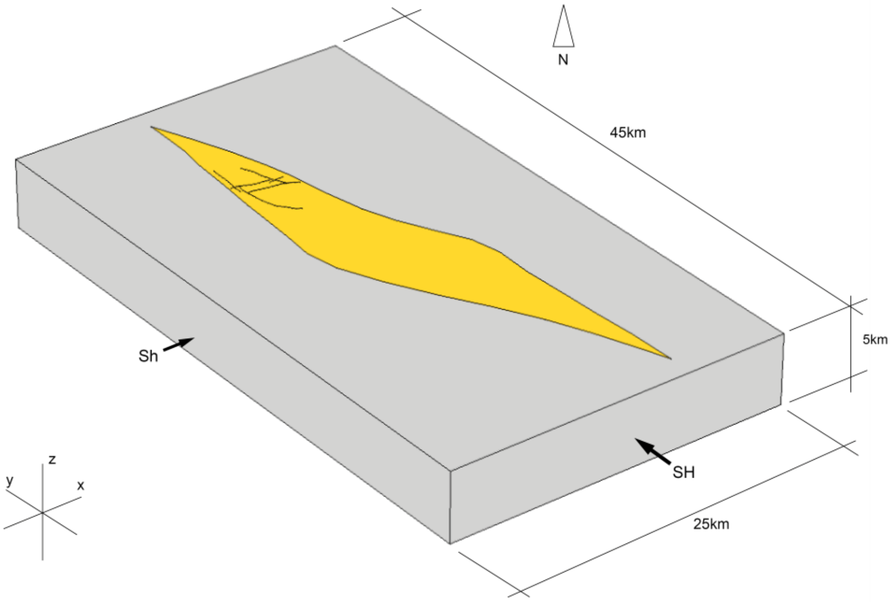

Figure A2.2. Set-up for the basic model with the Forsmark tectonic lens (yellow) embedded in a rectangular box with its longest axis pointing NW-SE. Black lines within the lens represent the deformation zones in the vicinity of the repository (cf. Figure A2.1).

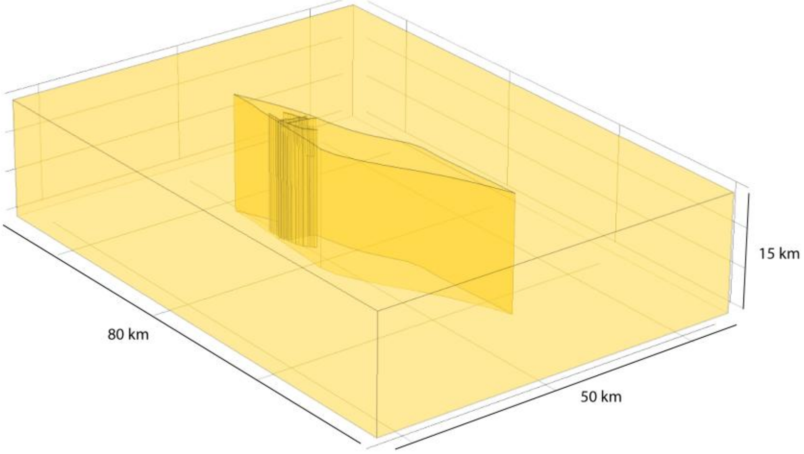

Figure A2.3. Set-up for the earthquake model with the Forsmark tectonic lens embedded in a rectangular box with its longest axis pointing NW-SE. The repository plane and the deformation zones that have been included are the same as for the basic model (cf. Figures A2.1 and A2.2).

The basic model geometry has been expanded for the simulation of earthquakes on the regional deformation zones that define the Forsmark tectonic lens. This has been done to avoid the effect of seismic wave reflection at the model boundaries. The geometry of the earthquake model is shown in Figure A.2.3.

A2.2. Mesh

The mesh of the basic model consists of 52,049 tetrahedral elements with a minimum element quality of 0.665. The quality of an element is a value between 0 and 1, where 0.0 represents a degenerated element and 1.0 represents a completely symmetric element. Deformation zones are modelled with a refined mesh with a minimum mesh quality of 0.8260. The mesh of the basic model is shown in Figure A2.5. Further refinements of the mesh did not lead to satisfactory results, since close to the deformation zones, sharp, complex structures with small intersection angles are formed, which make the creation of a refined mesh difficult and the calculation time unnecessarily long.

The mesh of the earthquake model consists of 137,589 tetrahedral elements with a minimum element quality of 0.635.

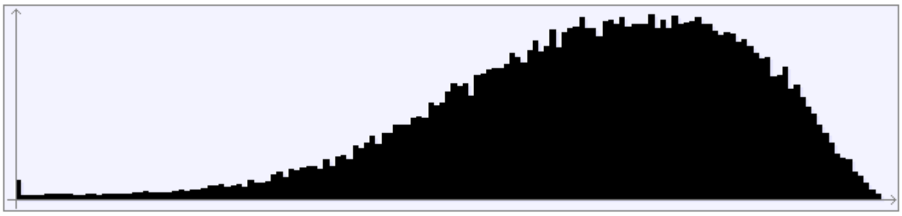

Figure A2.4. Histogram of element quality for the basic model.

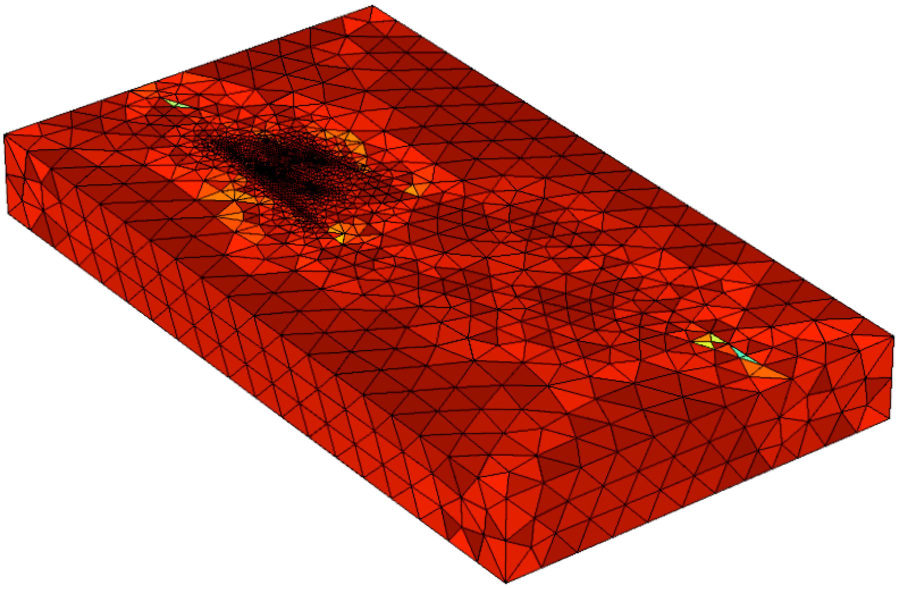

Figure A2.5. Meshed volume of the basic model consisting of 52,049 tetrahedral elements, which are refined close to deformation zones.

A2.3. Material properties

The rock mass is treated as linear elastic matrix with properties given in Table A2.1. The values are based on rock domain RFM029, which is the dominant rock domain in the Forsmark tectonic lens. It is composed mainly of medium-grained granites and granodiorites that underwent amphibolite-facies metamorphism. Subordinate rock types include pegmatitic granite, fine to medium grained metagranitoid and tonalite, and amphibolite which occur as isolated minor bodies, lenses and dyke-like sheets (Stephens et al., 2007, SKB R-07-45) are not considered in the model.

Table A2.1. Properties of the matrix representing the rock mass in the COMSOL model.

Parameter	**Value**
Density	2,500 kg/m^3
Ultrasonic velocity	4098 m/s
Young's modulus	35 GPa
Poisson's ratio	0.25
Thermal expansion coefficient	7.7*10^{-6} 1/K
Heat capacity	763 J/kgK
Thermal conductivity	3.57 W/mK

A2.4. Boundary conditions

Model outer boundaries

The outer, vertical and bottom boundaries are modelled as roller boundaries, where displacements are free in the plane but fixed in the out-of-plane direction. The upper boundary is free to move.

Two displacement functions with opposing directions but of the same magnitude were prescribed onto the fault surfaces in tangential direction. With time, the displacement was ramped up by a sinusoidal function, reaching the maximum displacement (given in Table 5.1) after 0.5 seconds. In space, the prescribed displacement peaked in the middle of the fault plane, which was ensured by a triangular distribution of the displacement.

Deformation Zones

For each segment of the deformation zones the direction cosine (*l, m, n*) with regard to the reference coordinate system (principal stress directions) are determined. The normal stress on the segment of the deformation zone is then given as:

$$\sigma_n = S_h^2 l^2 + S_H^2 m^2 + S_z^2 n^2 \qquad \text{Eq. (A2.1)}$$

with *l* = *cos(**n**, x)*, *m* = *cos(**n**, y)*, *n* = *cos(**n**, z)*, where ***n*** is the normal to the boundary. Similarly, the shear stress is given by:

$$\tau = \sqrt{(S_h - S_H)^2 l^2 m^2 + (S_H - S_z)^2 m^2 n^2 + (S_z - S_h)^2 n^2 l^2} \qquad \text{Eq. (A2.2)}$$

A full derivation of the shear and normal stress on an arbitrarily oriented plane is given in Ugural and Fenster (2011). The ratio between the shear and normal stress is the reactivation potential *rp* (see also Sec. 2.3).

In the earthquake analyses that allow for secondary displacements, all local deformation zones and the repository were modelled as thin-elastic layers with normal and shear stiffness parameters as given in Table A2.2. Thin-elastic layers are used to model thin or high aspect-ratio structures sandwiched between other relatively low aspect-ratio structures. On interior boundaries, the thin-elastic layer decouples the displacement between the two sides of the boundary. The two sides are then connected by elastic forces with equal size but opposite directions, proportional to the relative displacements and velocities as indicated by:

$$\sigma \vec{n} = \vec{k} \cdot \vec{u} \qquad \text{Eq. (A2.3)}$$

where ***n*** is the normal vector to the boundary, ***k*** is the spring constant in tangential and normal direction (MPa/mm), and ***u*** is the displacement vector. To determine the maximum shear displacement induced by the earthquake, the maximum displacement on the left and right side of the fault is subtracted at each time step. The highest difference is then located in space and the distance to the epicentre (location of the maximum displacement on host fault) is calculated.

Table A2.2. Properties of the deformation zones in the COMSOL model.

	Normal Stiffness (MPa/mm)	**Shear Stiffness (MPa/mm)**	**Reference**
Fracture domain FFM01	656	81	SKB TR-10-23, Table 4-3
Singö deformation zone	0.2	0.01	SKB R-07-31, Table 5-7 SKB R-07-06, Table 12-1

A2.5. Background stress models and initial conditions

Four background stress models as determined in Sec. 2.3.1 are employed in the COMSOL model for testing the likelihood of slip along deformation zones at present day. The pore pressure is subtracted from the given stress gradients and, hence, only effective stresses are considered in the model. The initial effective stresses obtained for the four stress fields are then used to calculate the changes of stability conditions for the different scenarios.

The reactivation potential *rp* as described in Chapter 2 was calculated along the tectonic lens and for the deformation zones in the proximity of the repository. As the steeply dipping deformation zones in vicinity of the repository share approximately the same orientations as the regional deformation zones, the *rp* for the two groups of zones are in the same order of magnitude. The conditions for the four initial stress models #1 to #4 are given in the following sections.

A2.5.1. #1 Reverse stress field

Principal stresses and temperature along a vertical monitoring line, passing through the centre of the repository, are shown in Figure A2.7. Using the #1 Reverse stress field, the regional deformation zones and the vertical deformation zones in the vicinity of the repository have a maximum *rp* of approximately 0.34.

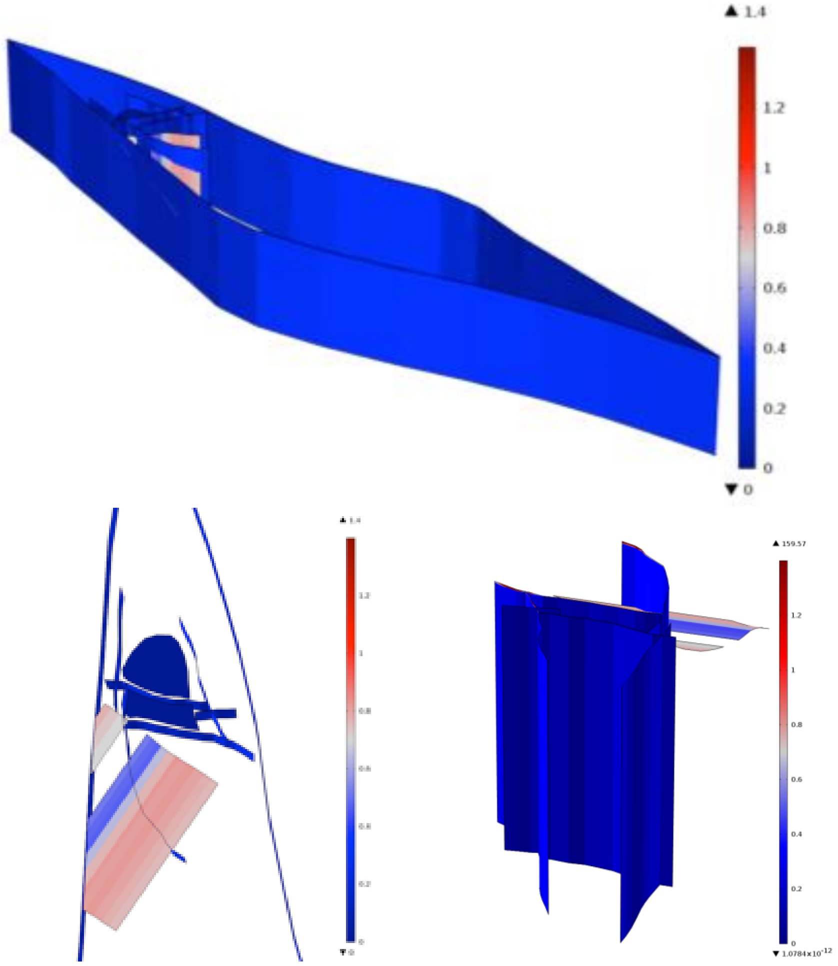

Figure A2.6. Reactivation potential for the #1 Reverse stress field model. (top) bird view, (bottom left) top view, and (bottom right) view from model north.

The shallow dipping deformation zone ZFMA2 has the highest *rp* of approximately 0.76 (Figure A2.6).

A2.5.2. #2 Mixed stress field

Principal stresses and temperature along a vertical monitoring line, passing through the centre of the repository, are shown in Figure A2.8. Using the #2 Mixed stress field the regional and the vertical deformation zones in the vicinity of the repository have a maximum *rp* of approximately 0.8 at depths greater 1,000 m. Above, the *rp* reduces to maximum 0.4 depending on the strike of the deformation zone. For the shallow dipping deformation zone ZFMA2 the highest reactivation potential is about 0.76 independently of depth (Figure A2.9).

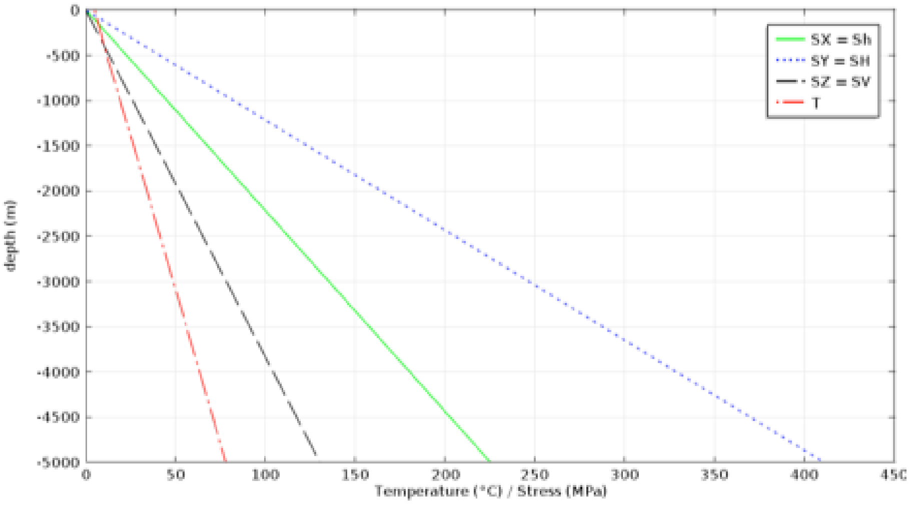

Figure A2.7. Stresses as a function of depth for the #1 Reverse stress field.

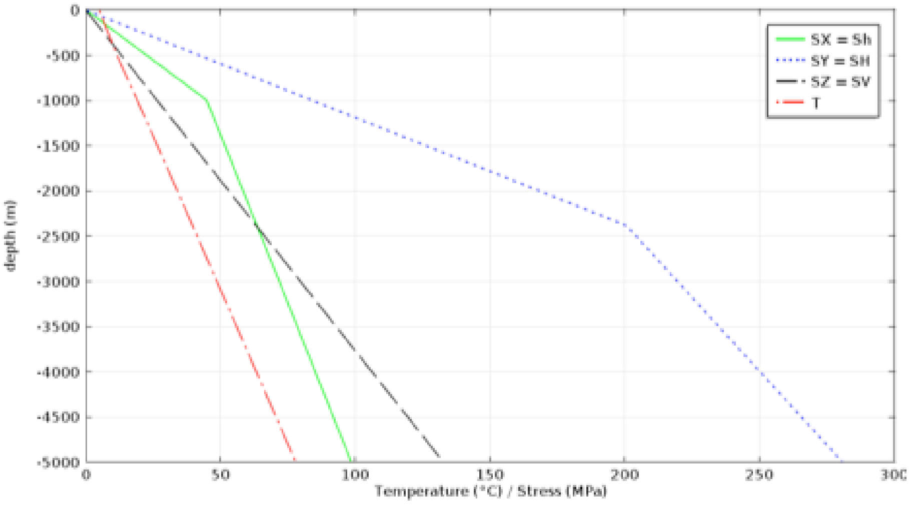

Figure A2.8. Stresses as a function of depth for the #2 Mixed stress field.

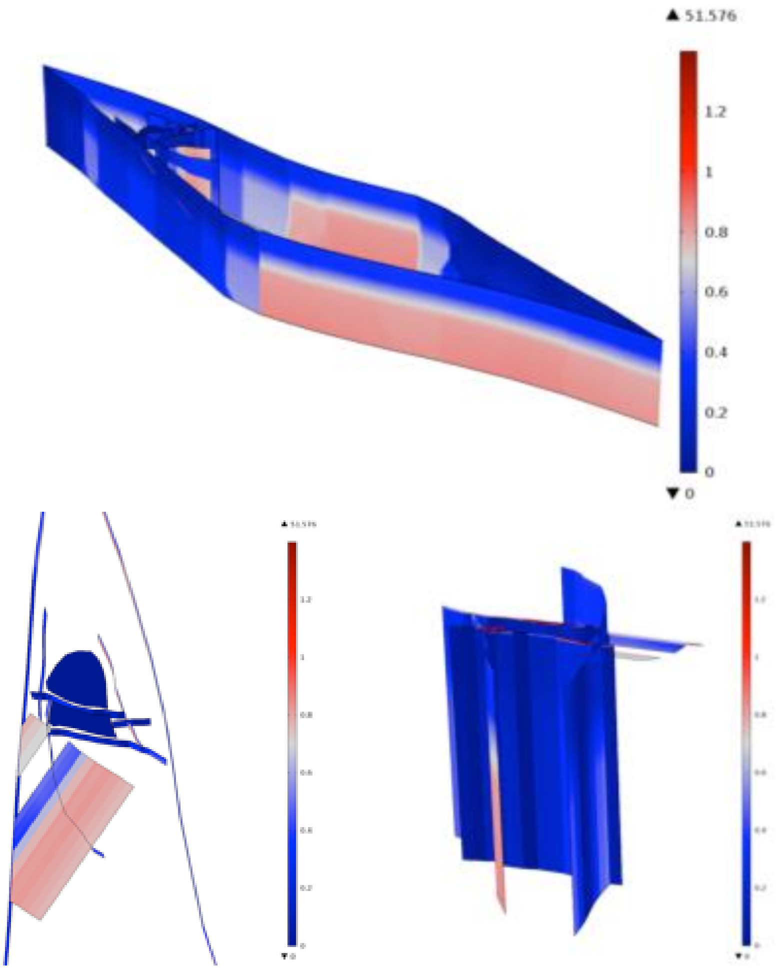

Figure A2.9. Reactivation potential for the #2 Mixed stress field model. (Top) bird view, (bottom left) top view, and (bottom right) view from model north.

A2.5.3. #3 Site stress field

Principal stresses and temperature along a vertical monitoring line, passing through the centre of the repository, are shown in Figure A2.10. The #3 Site stress field model represents the lowest *rp* among the simulated stress fields. Deformation zones show an increased *rp* of max. 0.6 within the first 100 m but reduce to values close to 0.2 within the first kilometre. Similar *rp* values are obtained for the steeply dipping deformation zones within the tectonic lens except ZFMA2 featuring a maximum *rp* of 0.8 at approximately 500 m depths (Figure A2.11).

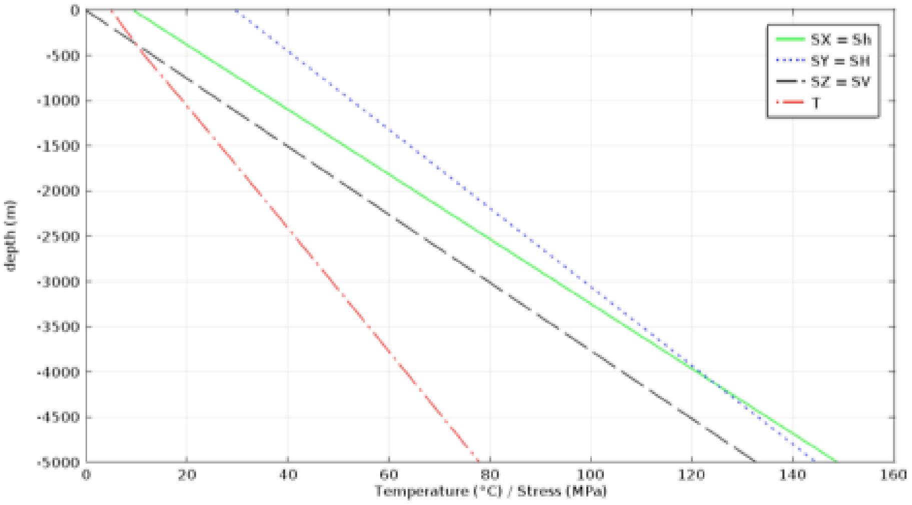

Figure A2.10. Stresses as a function of depth for the #3 Site stress field.

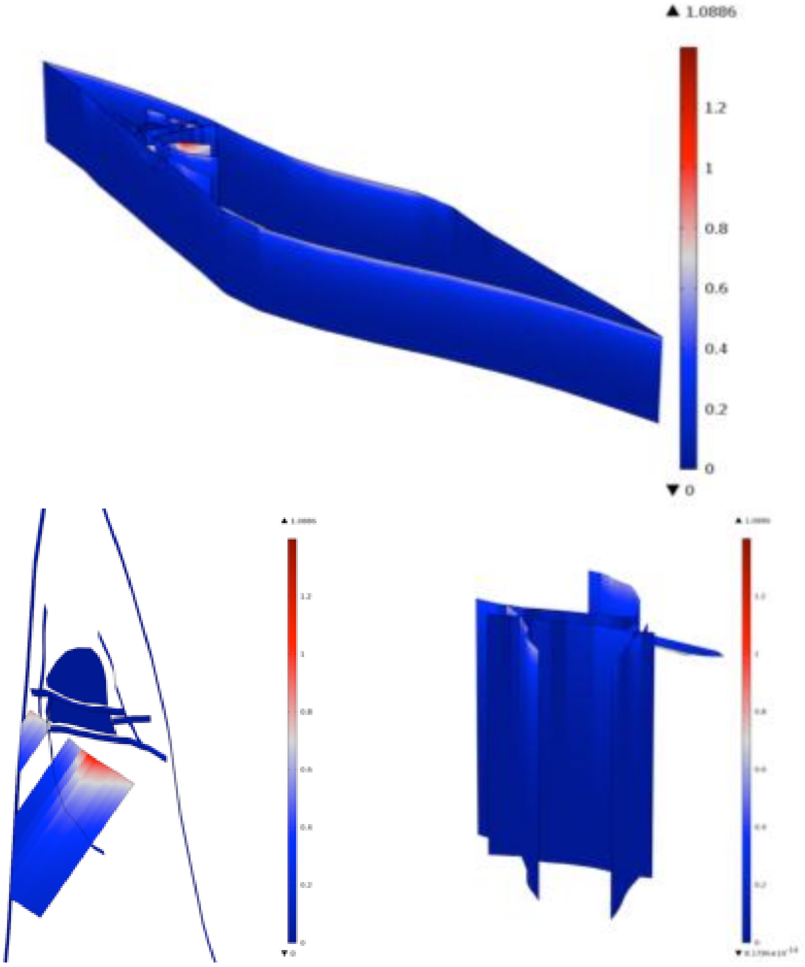

Figure A2.11. Reactivation potential for the #3 Site stress field model. (Top) bird view, (bottom left) top view, and (bottom right) view from model north.

A2.5.4. #4 geomecon stress field

Principal stresses and temperature along a vertical monitoring line, passing through the centre of the repository, are shown in Figure A2.12. Deformation zones confining the tectonic lens display a variety of *rp* between 0.2 and 0.75 depending on their strike and the depth. Among the tested stress fields the *rp* is greatest in the range from 0 to 3 km depth. Below 3 km the *rp* reduces slightly. Compared to the #3 Site stress field, the ZFMA2 has its highest reactivation potential at about 500 m of maximum 0.78 (Figure A2.13).

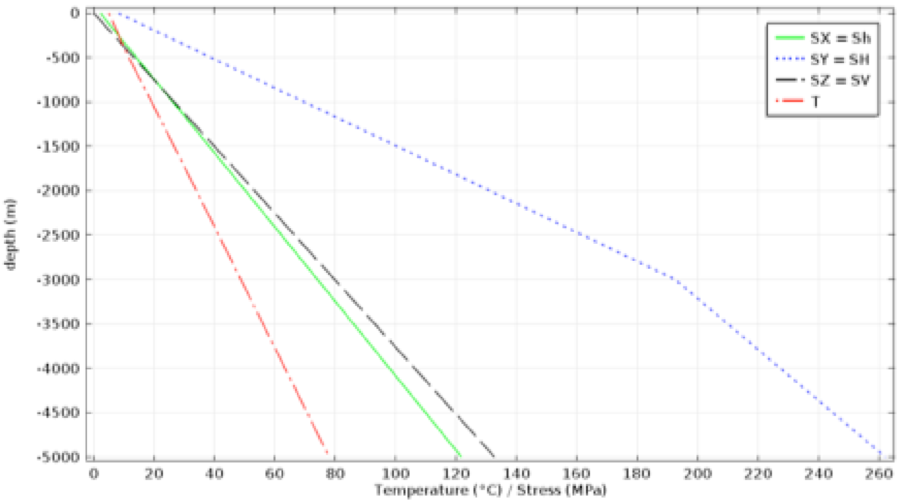

Figure A2.12. Stresses of the geomecon stress field as a function of depth for the #4 geomecon stress field.

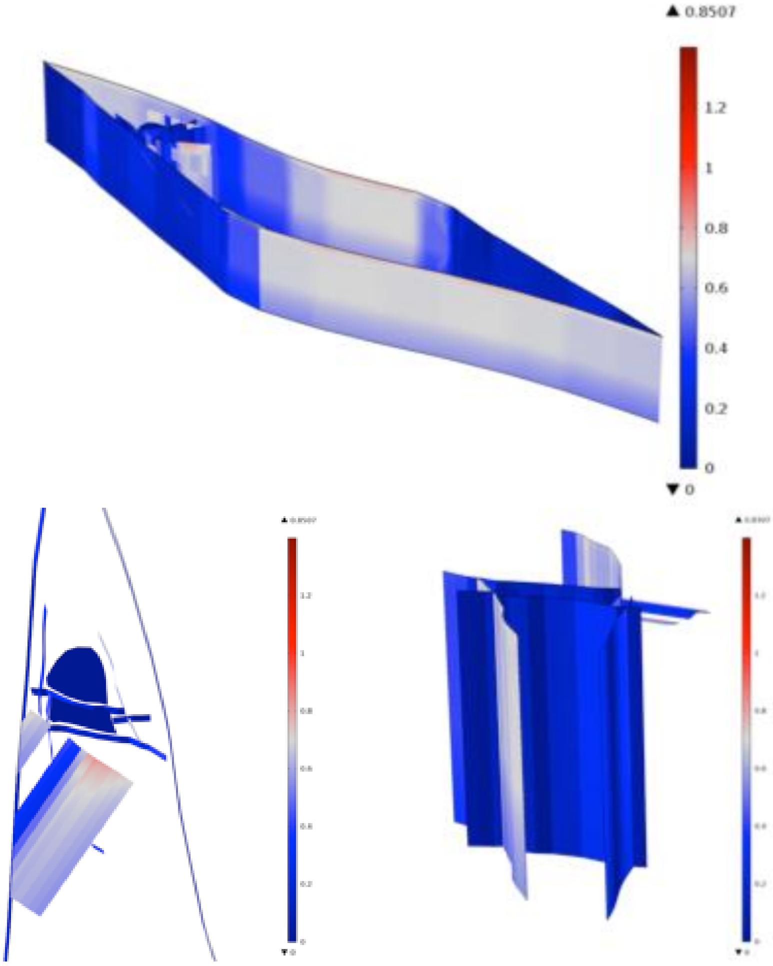

Figure A2.13. Reactivation potential for the #4 geomecon stress field model. (Top) bird view, (bottom left) top view, and (bottom right) view from model north.

A2.6. References

SKB R-07-06. Glamheden R, Hansen LM, Fredriksson A, Bergkvist L, Markström I, Elfström M, 2007. Mechanical modelling of the Singö deformation zone. Site descriptive modelling Forsmark stage 2.1. Swedish Nuclear Fuel and Waste Management Company (SKB).

SKB R-07-31. Glamheden R, Fredriksson A, Röshoff K, Karlsson J, Hakami H, Christiansson R, 2007. Rock mechanics Forsmark. Site descrpitive modelling Forsmark stage 2.2. Swedish Nuclear Fuel and Waste Management Company (SKB).

SKB R-07-45. Stephens M B, Fox A, La Pointe P, Simeonov A, Isaksson H, Hermanson J, Öhman J, 2007. Geology Forsmark. Site descriptive modelling Forsmark stage 2.2. Swedish Nuclear Fuel and Waste Management Company (SKB).

SKB TR-10-23. Hökmark H, Lönnqvist M, Fälth B, 2010. THM-issues in repository rock. Thermal, mechanical, thermo-mechanical and hydromechanical evolution of the rock at the Forsmark and Laxemar sites. Svensk Kärnbränslehantering AB.

Ugural A, Fenster S K, 2011. Advanced Mechanics of Materials and Applied Elasticity, fifth ed. Prentice Hall, 2011.

APPENDIX 3

2D Fracture Growth Model

The simulation of fracture extension requires the employed code to be able to handle discontinuities, and the related strain and structural changes involved in the propagation of fractures. While standard commercial codes are usually not capable of simulating fracture extension, there are a few that are in principle suitable for that purpose. These are fracod2d, Ycode, PFC and roxol[1]. Each code has its advantages, but also limitations for the application to the current issues (c.f. Backers, 2010):

- BEM-codes: Examples are the fracod2d (Shen et al., 2004) and DIGS. fracod2d has been shown to be capable of simulating fracture growth in brittle rocks quite satisfactory. The boundary element method (BEM) code has been applied frequently to rock fracturing, and the code is based on Fracture Mechanics principles. The fundamental building block is the discontinuity, rather than the element or particle, and fracturing is modelled as a chain of cracks. The path of crack growth is almost independent of the discretisation in the BEM, in contrast to the conventional finite element method. The BEM is well suited for large domains, but the level of complexity of the model is limited for non-linear material behaviour, inhomogeneity and anisotropy (Cruse, 1988). The simulations with fracod2d are, however, limited to about 20 fractures. The number of fractures relevant in the present simulation study is well above 50. Another example of the BEM approach is DIGS (Napier and Backers, 2006), but the code is not commercially distributed.

- Hybrid finite element/discrete element codes. Examples are the Ycode or ELFEN. Ycode has its strength in the simulation of landslides and similar. It is a hybrid approach. Hybrid methods have been introduced to combine the advantages of several methods and to overcome the limitations arising from employing one single method. Ycode is a hybrid finite element/discrete element code: each discrete element is discretised into finite elements. The finite element meshes define the shapes of discrete elements, the boundary stresses, displacements at their contacts and their deformability. Transition from continuous media to discontinuous media is realised by a “smeared crack model” (Munjiza, 2004; Mahabadi et al., 2009). However, remeshing is needed for the fractures to propagate. Also, it has the limitation that tuning of the physical models is needed, as it is a hybrid FEM/DEM code. In addition, the calculation speeds are very slow.

- PFC is well suited for generic studies to get a feeling for mechanisms, but its predictive capabilities are limited. A specific assumption about the basic composition of the material is made in the Particle Flow Code (PFC, Itasca). The rock material is represented as an assembly of bonded particles. The complex evolution of emergent failure patterns is then

---

[1] roxol and the roxol logo are registered trademarks of geomecon GmbH.

reduced to an explicit integration of the motion of each particle, subjected to the evolving forces imposed by neighbouring particles. Physical models, and hence experimental input data from laboratory, can be employed only in a limited way. Each parameter in the code has to be tuned, and the parameters mostly lack of physical meaning. Hence, the tuning has to be performed for each specific case to the results of a physical experiment post hum, ergo. Forward modelling is not physically based and hence, in the Authors' opinion, not suitable for the predictive simulation of DFN behaviour.

- eXtended Finite Element Method codes (XFEM). Example is roxol. Geomechanical tasks are generally of high geometrical complexity, and there are a vast number of publications on numerical modelling applications in rock engineering using finite element models. The finite element method (FEM) is widely applied because of its flexibility in handling material heterogeneity, anisotropy, boundary conditions, and non-linear material behaviour. Many commercial software packages are available, and almost any physical law can be implemented in such code with a limited effort. However, when applied to the simulation of fracture propagation, the finite element approach has the limitation that crack propagation requires a doubling of the edges and subsequent adaptive redefinition of the underlying finite element mesh. Also, because the crack tip causes a singularity in the stress field, the mesh density in the vicinity of the crack tip has to be increased. Consequently, the numerical implementation effort and computing time are greatly increased, and yet the fracture propagation paths remain mesh-dependent. The XFEM is an approach that has the capacity to resolve the above limitation of the FEM (e.g. Sukumar and Prévost, 2003; Budyn et al., 2004). The XFEM, not only removes the necessity of re-meshing, but locally improves the accuracy of the numerical solution by introducing a priori knowledge about the stress and displacement fields near the crack tip (Schroeder, 2008). roxol is based on FEM and hence has all the advantages of being able to simulate physical processes by dedicated equations. The fractures are simulated by some added shape functions on the FEM framework, and hence almost any model of rock and fracture behaviour can be simulated.

Based on this, roxol appears to be the code of choice for the current study and is used for further simulations. In addition to the aforementioned arguments, roxol allows the Consultants free extension of the software or the direct access to certain code modules when needed.

A3.1 The fracture network evolution simulator roxol™

geomecon[2] GmbH is developing a simulation software named roxol that can simulate fracture growth and related fracture network evolution in rock and rock mass. The development is based on Fracture Mechanics principles. For this purpose the basis was developed in recent years and the feasibility of the methodology was proven in first numerical campaigns.

---

[2] geomecon and the geomecon logo are registered trademarks of geomecon GmbH.

At this point the mathematical basis is laid out and was combined into an XFEM core software. The fundamental geomechanical models are adopted and implemented. The architecture of the code is based on a modular structure.

Currently the following functionalities are available:

- linear elastic materials
- orthotropic compliance matrix
- multiple material regions
- plane strain, plane stress, pure 2D
- stress boundaries (Neumann)
- displacement boundaries (Dirichlet)
- combination of stress and displacement boundaries
- fluid pressure on fractures
- variable stress on fractures and boundaries
- tensile fractures
- fractures under compression with contact and Coulomb friction
- fracture initiation criteria (Mohr-Coulomb, Mogi, Hoek-Brown, mean stress, deviatoric stress)
- definition of fracture initiation length and fracture initiation distances
- pre-existing fractures
- statistical fracture generation wizard
- fracture activation
- stress and stress intensity factor based fracture propagation criteria and combinations thereof (circumferential stress, principal stress, maximum shear stress, linear K_{IC} - K_{IIC} mixed-mode criterion, quadratic K_{IC} - K_{IIC} mixed-mode criterion)
- fracture interaction and coalescence
- simple fracture geometry export functions.

A3.2. Geomechanical models

The material law used in the simulations in the present study is isotropic linear elastic, defined by the Young’s moduli and Poisson’s ratios. The fractures are included in the geometrical model and fracture strength is modelled by Coulomb friction. The extension of fractures, hence fracture growth, is modelled by a linear combination of the stress intensities. If the linear combination of normalised fracture intensities ($K_I/K_{IC} + K_{II}/K_{IIC}$) reaches unity at some point close to the fracture tip, fracture extension takes place in the direction of the maximum. For a discussion of the model see Whittaker et al. (1992).

Fracture initiation or activation is not considered unless otherwise stated; it is anticipated that existing fractures will propagate. The properties for the rock mass are given in Table A3.1.

Table A3.1. Properties for the simulation of deformation zone extension with roxol.

Model parameters	Type / Values	Reference to SKB reports
Sxx	variable, reflecting stress models and evolution	
Syy	variable, reflecting stress models and evolution	
Szz	vertical stress, variable, reflecting stress models and evolution	
Young's moduli	76 GPa/76 GPa/76 GPa	SKB TR-08-05 Table 7-3
Poisson's ratios	0.23/0.23/0.23	SKB TR-08-05 Table 7-3
fracture cohesion	0.8 MPa	SKB TR-08-05 Table 7-4
fracture friction coefficient *)	0.72	SKB TR-08-05 Table 7-4
Mode I fracture toughness	3.8 MPam$^{1/2}$	Backers (2005)
Mode II fracture toughness	5.1 MPam$^{1/2}$	Backers (2005)

*) the used friction coefficients throughout all the analyses are static. This reflects the equilibrium condition before slip occurs. For this reason it is considered the correct choice of coefficients. The kinetic friction coefficients are in general lower but do not reflect the given model conditions.

A3.3. References

Backers T, 2010. Applications of fracture mechanics numerical modelling in rock engineering. first break. Volume 28, issue 3, pages 13 - 22.

Backers T, Meier T, Gipper P and Stephansson O. 2014. Rock Mechanics - Confidence of SKB’s models for predicting the occurrence of spalling - Main Review Phase. SSM Technical Note - Report number: 2014:10 ISSN: 2000-0456

Budyn E, Zi G, Moes N, Belytschko T, 2004. A method for multiple crack growth in brittle materials without remeshing. International Journal for Numerical Methods in Engineering, 61, 1741-1770.

Cruse T, 1988. Boundary Element Analysis in Computational Fracture Mechanics. Kluwer: Dordrecht.

Mahabadi O K, Grasselli G, Munjiza A, 2009. Numerical modelling of a Brazilian Disc test of layered rocks using the combined finite-discrete element method. In: Diederichs M, Grasselli G (Eds.) ROCKENG09: 3rd CANUS Rock Mechanics Symposium, Toronto, Paper 3894.

Munjiza A, 2004. The Combined Finite-Discrete Element Method. Wiley, Hoboken, NJ.

Napier J A L, Backers T, 2006. Comparison of numerical and physical experiment for understanding shear fracture processes. Pure and Applied Geophysics, 163, 1153-1174.

Schroeder A, 2008. Constraints coefficients in hp – fem. In: Kunisch K, Of G, Steinbach O (Eds.) Numerical Mathematics and Advanced Applications. Springer, Berlin, 183–190.

Sukumar N, Prévost J-H, 2003. Modeling quasi-static crack growth with the extended finite element method Part I: Computer implementation. International Journal of Solids and Structures, 40, 7513–7537.

Whittaker BN, Singh RN, Sun G, 1992. Rock Fracture Mechanics - Principles, Design and Applications, volume 72 of Developements of Geotechnical Engineering. Elsevier, Amsterdam - London - New York Tokyo, 1992.

Earthquake magnitude estimation based on trace lengths

Table A4.1. Magnitude estimation based on surface trace length of the deformation zones as presented by SKB. Magnitudes according to alternative databases are also shown. (Trace lengths are taken from Appendix 15 in Stephens et al., 2007, SKB R-07-45.)

Zone ID	Trace Length [km]	SKB	Wells & Coppersmith (1994)	Stirling et al. (2002)	Leonard (2010)	Johnston (1994)
Regional DZ						
ZFMWNW0004 (Forsmark zone)	70	7.2	7,2	7,2	7,4	7,2
ZFMWNW0001 (Singö zone)	30	6.8	6,8	6,9	6,8	6,7
ZFMNW0003 (Eckarfjärden zone)	30	6.8	6,8	6,9	6,8	6,7
ZFMWNW0854	29		6,8	6,9	6,8	6,7
ZFMNW0806	22	6.6	6,6	6,8	6,6	6,5
ZFMNW0002	18	6.5	6,5	6,7	6,4	6,4
ZFMNW1173	14		6,4	6,7	6,2	6,2
ZFMWNW0853	13		6,4	6,6	6,2	6,2
ZFMWNW0036	11	6.3	6,3	6,6	6,1	6,1
Local major DZ (steep)						
ZFMWNW0019	8,760	6.2	6,2	6,5	5,9	6,0
ZFMWNW0016	8,06	6.1	6,1	6,5	5,8	5,9
ZFMWNW0024	7,986	6.1	6,1	6,4	5,8	5,9
ZFMNW0017	7,923	6.1	6,1	6,4	5,8	5,9
ZFMWNW0023	7,665	6.1	6,1	6,4	5,8	5,9
ZFMNNE1134	7,284	6.1	6,1	6,4	5,8	5,8
ZFMNNE1133	6,284	6.0	6,0	6,4	5,7	5,8

Zone ID	Trace Length [km]	SKB	Wells & Coppersmith (1994)	Stirling et al. (2002)	Leonard (2010)	Johnston (1994)
ZFMNNE0828	5,932	6.0	6,0	6,3	5,6	5,7
ZFMNNE0860	5,922	6.0	6,0	6,3	5,6	5,7
ZFMNNE1132	5,478		5,9	6,3	5,6	5,7
ZFMWNW1127	5,394	5.9	5,9	6,3	5,5	5,7
ZFMNNE0929	5,203	5.9	5,9	6,3	5,5	5,6
ZFMWNW0123	5,086	5.9	5,9	6,3	5,5	5,6
ZFMWNW0836	4,498	5.8	5,8	6,2	5,4	5,6
ZFMNNE1135	4,361		5,8	6,2	5,4	5,5
ZFMEW0137	4,300	5.8	5,8	6,2	5,4	5,5
ZFMWNW0974	4,097		5,8	6,2	5,3	5,5
ZFMNE0808A	4,080	5.8	5,8	6,2	5,3	5,5
ZFMNE0065	4,068	5.8	5,8	6,2	5,3	5,5
ZFMNW0029	3,792	5.8	5,8	6,2	5,3	5,5
ZFMNW0805	3,694	5.7	5,7	6,2	5,3	5,4
ZFMWNW0062A	3,543	5.7	5,7	6,1	5,2	5,4
ZFMWNW0035	3,521	5.7	5,7	6,1	5,2	5,4
ZFMWNW0809A	3,347	5.7	5,7	6,1	5,2	5,4
ZFMNNW0823	3,273	5.7	5,7	6,1	5,2	5,4
ZFMNNE0842	3,157	5.7	5,7	6,1	5,2	5,3
ZFMNW1200	3,121	5.7	5,7	6,1	5,1	5,3
ZFMENE0060A	3,120	5.7	5,7	6,1	5,1	5,3
ZFMWNW0851	3,080		5,6	6,1	5,1	5,3
ZFMEW1156	3,025		5,6	6,1	5,1	5,3
ZFMWNW0835A	2,816		5,6	6,1	5,1	5,3
ZFMWNW1053	2,686		5,6	6,0	5,0	5,3
ZFMENE0810	2,672		5,6	6,0	5,0	5,3
ZFMENE0061	2,081		5,4	6,0	4,9	5,1
ZFMENE0401A	1,961		5,4	5,9	4,8	5,1
ZFMENE0159A	1,909		5,4	5,9	4,8	5,1
ZFMNNW0101	1,726		5,4	5,9	4,7	5,0
ZFMNNW0100	1,673		5,3	5,9	4,7	5,0
ZFMWNW2225	1,613		5,3	5,9	4,7	5,0
ZFMWNW0813	1,609		5,3	5,9	4,7	5,0

Zone ID	Trace Length [km]	SKB	Wells & Coppersmith (1994)	Stirling et al. (2002)	Leonard (2010)	Johnston (1994)
ZFMWNW1056	1,557		5,3	5,8	4,6	4,9
ZFMWNW0835A	1,532		5,3	5,8	4,6	4,9
ZFMENE2232	1,458		5,3	5,8	4,6	4,9
ZFMNNE2308	1,419		5,3	5,8	4,6	4,9
ZFMENE0103	1,399		5,2	5,8	4,6	4,9
ZFMWNW0809B	1,354		5,2	5,8	4,5	4,8
ZFMENE2248	1,298		5,2	5,8	4,5	4,8
ZFMNNE0725	1,274		5,2	5,8	4,5	4,8
ZFMENE2320	1,251		5,2	5,8	4,5	4,8
ZFMENE0060C	1,161		5,2	5,7	4,4	4,8
ZFMENE1061A	1,158		5,2	5,7	4,4	4,8
ZFMNE0808C	1,156		5,2	5,7	4,4	4,8
ZFMENE1208B	1,112		5,1	5,7	4,4	4,7
ZFMENE1192	1,090		5,1	5,7	4,4	4,7
ZFMENE1208A	1,081		5,1	5,7	4,4	4,7
ZFMENE0060B	1,070		5,1	5,7	4,4	4,7
ZFMENE0169	1,069		5,1	5,7	4,4	4,7
ZFMNNE0869	1,065		5,1	5,7	4,4	4,7
ZFMNNE2280	1,035		5,1	5,7	4,3	4,7
ZFMENE2254	1,021		5,1	5,7	4,3	4,7
ZFMENE2383	1,000		5,1	5,7	4,3	4,7
ZFMWNW1068	0,999		5,1	5,7	4,3	4,7
ZFMNNE2293	0,996		5,1	5,7	4,3	4,7
ZFMNNW0404	0,947		5,1	5,7	4,3	4,6
ZFMENE0159B	0,673		4,9	5,5	4,0	4,4
ZFMWNW0062B	0,616		4,8	5,5	4,0	4,4
ZFMNE0808B	0,445		4,7	5,4	3,7	4,2
ZFMENE1061B	0,436		4,7	5,4	3,7	4,2
ZFMENE0401B	0,358		4,6	5,3	3,6	4,1
ZFMWNW0062C	0,346		4,5	5,3	3,6	4,0

Zone ID	Trace Length [km]	SKB	Wells & Coppersmith (1994)	Stirling et al. (2002)	Leonard (2010)	Johnston (1994)
Local major DZ (gently dipping)						
ZFMA1						
ZFMA2	3,987	5.8	5,8	6,2	5,3	5,5
ZFMA3	3,234	5.7	5,7	6,1	5,2	5,4
ZFMA4	3,641	5.7	5,7	6,2	5,3	5,4
ZFMA5	2,842		5,6	6,1	5,1	5,3
ZFMA6	3,021		5,6	6,1	5,1	5,3
ZFMA7	3,510	5.7	5,7	6,1	5,2	5,4
ZFMA8	1,852		5,4	5,9	4,8	5,0
ZFMB1	3,224	5.7	5,7	6,1	5,2	5,4
ZFMB23						
ZFMB4						
ZFMB5						
ZFMB6						
ZFMB7						
ZFMB8	0,515		4,7	5,4	3,8	4,3
ZFME1						
ZFMF1						
ZFMJ1						
ZFMJ2	1,428		5,3	5,8	4,6	4,9
ZFMK1	2,331		5,5	6,0	4,9	5,2
ZFM886	1,724		5,4	5,9	4,7	5,0
ZFM871	1,163		5,2	5,7	4,4	4,8
ZFM1203	0,881		5,0	5,6	4,2	4,6

2014:58

The Swedish Radiation Safety Authority has a comprehensive responsibility to ensure that society is safe from the effects of radiation. The Authority works to achieve radiation safety in a number of areas: nuclear power, medical care as well as commercial products and services. The Authority also works to achieve protection from natural radiation and to increase the level of radiation safety internationally.

The Swedish Radiation Safety Authority works proactively and preventively to protect people and the environment from the harmful effects of radiation, now and in the future. The Authority issues regulations and supervises compliance, while also supporting research, providing training and information, and issuing advice. Often, activities involving radiation require licences issued by the Authority. The Swedish Radiation Safety Authority maintains emergency preparedness around the clock with the aim of limiting the aftermath of radiation accidents and the unintentional spreading of radioactive substances. The Authority participates in international co-operation in order to promote radiation safety and finances projects aiming to raise the level of radiation safety in certain Eastern European countries.

The Authority reports to the Ministry of the Environment and has around 315 employees with competencies in the fields of engineering, natural and behavioural sciences, law, economics and communications. We have received quality, environmental and working environment certification.

Strålsäkerhetsmyndigheten
Swedish Radiation Safety Authority

SE-171 16 Stockholm
Solna strandväg 96

Tel: +46 8 799 40 00
Fax: +46 8 799 40 10

E-mail: registrator@ssm.se
Web: stralsakerhetsmyndigheten.se